



**BACK-PRESSURE EFFECT ON SHOCK-TRAIN LOCATION IN A SCRAMJET
ENGINE ISOLATOR**

THESIS

Richard I. Paek, Captain, USAF

AFIT/GAE/ENY/10-M17

**DEPARTMENT OF THE AIR FORCE
AIR UNIVERSITY**

AIR FORCE INSTITUTE OF TECHNOLOGY

Wright-Patterson Air Force Base, Ohio

APPROVED FOR PUBLIC RELEASE; DISTRIBUTION UNLIMITED

The views expressed in this thesis are those of the author and do not reflect the official policy or position of the United States Air Force, Department of Defense, or the United States Government. This material is declared a work of the U.S. Government and is not subject to copyright protection in the United States.

AFIT/GAE/ENY/10-M17

**BACK-PRESSURE EFFECT ON SHOCK-TRAIN LOCATION IN A SCRAMJET
ENGINE ISOLATOR**

THESIS

Presented to the Faculty

Department of Aeronautics and Astronautics

Graduate School of Engineering and Management

Air Force Institute of Technology

Air University

Air Education and Training Command

In Partial Fulfillment of the Requirements for the
Degree of Master of Science in Aeronautical Engineering

Richard I. Paek, BS

Captain, USAF

March 2010

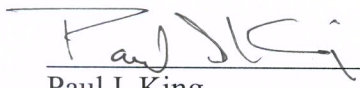
APPROVED FOR PUBLIC RELEASE; DISTRIBUTION UNLIMITED

**BACK-PRESSURE EFFECT ON SHOCK-TRAIN LOCATION IN A SCRAMJET
ENGINE ISOLATOR**

Richard I. Paek, BS

Captain, USAF

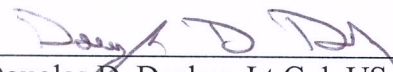
Approved:



Paul I. King

19 Mar 10

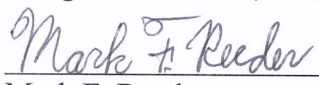
Date



Douglas D. Decker, Lt Col, USAF

19 MAR 10

Date



Mark F. Reeder

19 Mar 10

Date

Abstract

A scramjet consists of four main components: an inlet, an isolator, a combustor, and a nozzle. The isolator of the scramjet decelerates the incoming high Mach number flow to a lower Mach number and stabilizes the flow to a suitable condition before it enters the combustor. Because the combustion is not necessarily a steady phenomenon and may yield inconsistent heat release depending on the completeness of the combustion, pressures within the combustion zone can vary significantly. Variations in pressures caused by combustion can propagate forward and affect the flow field in the isolator and even create a large enough pressure blockage to un-start the inlet. Other factors that can influence the airflow in the isolator include changes in free stream conditions, vehicle geometry, and the vehicle's orientation with respect to the free stream velocity. As a result of these factors, the incoming flow to the inlet can change dramatically: as the airflow enters the isolator, a shock-train may develop upstream of the combustor. In this research, the shock-train location as affected by the back-pressure is examined experimentally. The back-pressure is artificially created by symmetric, top and bottom, ramps that can close the flow cross-sectional area in a controlled manner. Raising or lowering these ramps results in higher or lower back-pressures, respectively. Higher back-pressure moves the shock-train forward, with too high a back-pressure causing un-start. This experiment is conducted for a variation in Reynolds number, ramp angle, and two incoming Mach numbers. As a result, for Mach 1.8 case, a shock is imminent at the back-pressure ratio (i.e. back-pressure to stagnation pressure) of ~ 0.25 ,

and un-start occurs at the back-pressure ratio of ~ 0.55 . For the Mach 3 case, a shock is imminent at the back-pressure ratio of ~ 0.04 , and un-start occurs at the back-pressure ratio of ~ 0.28 . A higher Reynolds number affects these values by increasing them a little. This research also describes a hysteresis found in the shock-train characteristics. When restarting an un-started flow, the restart will occur at a lower back-pressure value than the one at un-start. In this research, the data is non-dimensionalized to collapse onto one graph. By using the Mach number ratio (i.e., Mach number at the test section when no shock is present to Mach number at various back-pressure), it is possible to find one ratio value when the shock-imminent and un-start occurs regardless of the different Mach number. The ratio for this particular test facility is found to be near 1.83.

Acknowledgments

In the journey of this research, I found myself deeply indebted to a number of people. First, I would like to thank my thesis advisors, Dr. King and Lt Col Decker who constantly provided the encouragement and wisdom to guide my efforts. I deeply appreciate your mentoring and enlightening. I only wish that I could have been a better student for you. I would also like to thank Capt John Hutzel and Maj Troy Hoeger for knowledge and research efforts. John, you were always there to keep me out of trouble. Special thanks also go to AFRL/RZ who was always interested in this research, for your support. I would like to extend a very special thanks to the AFIT machine shop. Most notably, the outstanding craftsmanship of the test section model is beyond reproach. Without their work, this research could not come alive. Last but certainly not least, I give my primary thanks to my family for support, love and patience. Mother, you were always there whenever I need you although you were going through some tough time. My sister and my brother-in-law, I really appreciate your care and help. Father, even though you are not here with us at this moment, my most gratitude goes to you. You taught me the value of family.

Richard I. Paek

Table of Contents

	Page
Abstract	iv
Table of Contents	vii
List of Figures	x
List of Tables	xvii
I. Introduction	1
General Issue	1
Problem Statement	2
Research Objectives	2
Investigative Questions	3
Methodology	3
Assumptions/Limitations	4
II. Literature Review	5
Scramjet Engine	5
History	6
Shock system	8
Isolator	11
Pressure measurements	12
Control of the shock	12
Un-start	13
Flight conditions	14
III. Methodology	17
Entire experiment apparatus set-up	17
2.5"x2.5" supersonic wind tunnel	19

	Page
The new test section	28
Main control computer	38
Endevco pressure transducers and amplifiers	46
Schlieren imaging setup	49
Actuator system	54
Safety pressure relief valves	57
Side project: making an actuator stand.....	57
IV. Analysis and Results.....	60
Overview	60
Ramp input to an actuator: constant increase in height.....	61
Hysteresis examination.....	76
Ramp speed effect.....	88
Reynolds number effect.....	90
Non-dimensionalization	92
Air flow symmetry test.....	100
Adding injection pressure upstream test	105
Comparison with other researches.....	107
V. Conclusions and Recommendations	116
Conclusions of Research	116
Significance of Research.....	119
Recommendations for Future Research	119
Appendix A. Test section window thickness calculation	122
Appendix B. Window deflection calculation.....	124
Appendix C. Test facility engineering drawings	125

	Page
Appendix D. Endevco pressure sensor/amplifier in-house calibration results	153
Appendix E. Unit conversion from MTS reading	154
Bibliography	173
Vita	176

List of Figures

	Page
Figure 1. Schematic of dual-mode scramjet engine with stations 1-5 labeled(1)	5
Figure 2. Schematic of Isolator Pre-Combustion Shock-train for Ram, Early Scram, and Late Scram Modes(1)	10
Figure 3. Picture of the 2.5’’x2.5’’ supersonic wind tunnel laboratory	17
Figure 4. Entire laboratory diagram	19
Figure 5. High air pressure compressor pump	20
Figure 6. Desiccant compressed air dryer	21
Figure 7. Vacuum tank (left) and pressure tank (right)	21
Figure 8. Main manual shut off valve	22
Figure 9. A small high pressure tank (black), air filter (gray), and stagnation chamber pressure control knob on the top of the air filter	23
Figure 10. Upstream solenoid valve	24
Figure 11. A regulation valve (black component on the left) and stagnation chamber (blue)	24
Figure 12. Mach 1.8 nozzle (left) and Mach 3 nozzle (right)	25
Figure 13. A new test section	25
Figure 14. Diffuser and downstream solenoid valve	26
Figure 15. Stokes vacuum pump	27
Figure 16. Stagnation pressure behavior during the test runs	28
Figure 17. First concept: adding a new section behind the existing section	29
Figure 18. Gearing mechanism to synchronize two ramps	32

	Page
Figure 19. Two ramps inside the wind tunnel	33
Figure 20. Clevis rod ends (left), wheel rod ends (center), T rod end (right).....	34
Figure 21. Top view of a top plate	35
Figure 22. Bottom view of bottom plate	35
Figure 23. The new test section drawn in the Solidworks software.....	36
Figure 24. (Continued) the new section drawn in the Solidworks software.....	37
Figure 25. The picture of the new test facility	38
Figure 26. A main control computer for 2.5”x2.5” supersonic wind tunnel	39
Figure 27. NI PXI-8196 Embedded Controller	40
Figure 28. NI PXI-6120 Simultaneous Sampling Multifunction I/O	41
Figure 29. NI PXI-6259 M series Multifunction DAQ.....	41
Figure 30. NI PXI-6070E Multifunction I/O	42
Figure 31. NI BNC-2120 boards	43
Figure 32. NI cDAQ-9172 and NI 9263	43
Figure 33. LabVIEW GUI panel for supersonic wind tunnel.....	44
Figure 34. LabVIEW internal structure	45
Figure 35. NI Measurement & Automation Explorer	46
Figure 36. Endevco 8530C-50 piezoresistive pressure transducers	47
Figure 37. Endevco Model 136 DC Amplifier	48
Figure 38. Reference pressure digital barometer for day-to-day calibration purpose.....	49
Figure 39. Schlieren imaging setup.....	50
Figure 40. Light source for schlieren imaging	50
Figure 41. Biconvex lens (left) and pinhole (right).....	51

	Page
Figure 42. Convex mirror	51
Figure 43. A knife edge and high speed camera	52
Figure 44. Schlieren imaging control and viewing computer.....	53
Figure 45. High speed camera interface software: PFV ver.2.4.3.8	53
Figure 46. Screenshots of PFV.2.4.3.8 software	54
Figure 47. Hydraulic pump (left) and actuator (right)	55
Figure 48. MTS software, desktop icon (left) and GUI (right)	56
Figure 49. Safety pressure relief valves	57
Figure 50. A stand for the hydraulic actuator, drawn in the Solidworks software.....	58
Figure 51. Final product: hydraulic actuator stand.....	59
Figure 52. Pressure profile in the test section with ramp input, $M=1.8$, $Re=1.28E07$ /m	63
Figure 53. Pressure profile in the test section with ramp input, $M=1.8$, $Re=1.436E07$ /m	64
Figure 54. Pressure profile in the test section with ramp input, $M=1.8$, $Re=1.659E07$ /m	64
Figure 55. Pressure profile in the test section with ramp input, $M=1.8$, $Re=1.712E07$ /m	65
Figure 56. Pressure profile in the test section with ramp input, $M=1.8$, $Re=1.719E07$ /m	65
Figure 57. Pressure profile in the test section with ramp input, $M=3$, $Re=7.8E06$ /m	66
Figure 58. Pressure profile in the test section with ramp input, $M=3$, $Re=1.185E07$ /m	66
Figure 59. Pressure profile in the test section with ramp input, $M=3$, $Re=1.7E07$ /m	67
Figure 60. Pressure profile in the test section with ramp input, $M=3$, $Re=2.3E07$ /m	67

Figure 61. Schlieren photo of shock-train ($M = 1.8$, $Re = 1.712 \text{ E}07 /m$, upstream is left)	
.....	68
Figure 62. Schlieren photo of shock-train ($M = 3$, $Re = 1.7 \text{ E}07 /m$, upstream is left)	69
Figure 63. Upstream versus back-pressure ratio ($M=1.8$, $Re\# = 1.28\text{E}07 /m$).....	71
Figure 64. Upstream versus back-pressure ratio ($M=1.8$, $Re\# = 1.436\text{E}07 /m$).....	72
Figure 65. Upstream versus back-pressure ratio ($M=1.8$, $Re\# = 1.659\text{E}07 /m$).....	72
Figure 66. Upstream versus back-pressure ratio ($M=1.8$, $Re\# = 1.712\text{E}07 /m$).....	73
Figure 67. Upstream versus back-pressure ratio ($M=1.8$, $Re\# = 1.719\text{E}07 /m$).....	73
Figure 68. Upstream versus back-pressure ratio ($M=3$, $Re\# = 7.8\text{E}06 /m$).....	74
Figure 69. Upstream versus back-pressure ratio ($M=3$, $Re\# = 1.185\text{E}07 /m$).....	74
Figure 70. Upstream versus back-pressure ratio ($M=3$, $Re\# = 1.7\text{E}07 /m$).....	75
Figure 71. Upstream versus back-pressure ratio ($M=3$, $Re\# = 2.3\text{E}07 /m$).....	75
Figure 72. Triangle input explanation	78
Figure 73. Shock-train start/un-start/restart/clean behavior in response to triangle input ($M=1.8$, $Re=1.196\text{E}07 /m$).....	79
Figure 74. Shock-train start/un-start/restart/clean behavior in response to triangle input ($M=1.8$, $Re=1.365\text{E}07 /m$).....	79
Figure 75. Shock-train start/un-start/restart/clean behavior in response to triangle input ($M=1.8$, $Re=1.568\text{E}07 /m$).....	80
Figure 76. Shock-train start/un-start/restart/clean behavior in response to triangle input ($M=1.8$, $Re=1.619\text{E}07 /m$).....	80
Figure 77. Shock-train start/un-start/restart/clean behavior in response to triangle input ($M=1.8$, $Re=1.621\text{E}07 /m$).....	81

	Page
Figure 78. Shock-train start/un-start/restart/clean behavior in response to triangle input (M=3, Re=7.15E06 /m)	81
Figure 79. Shock-train start/un-start/restart/clean behavior in response to triangle input (M=3, Re=8.95E06 /m)	82
Figure 80. Shock-train start/un-start/restart/clean behavior in response to triangle input (M=3, Re=1.419E07 /m)	82
Figure 81. Shock-train start/un-start/restart/clean behavior in response to triangle input (M=3, Re=1.895E07 /m)	83
Figure 82. Shock-train start/un-start/restart/clean behavior in response to triangle input (M=3, Re=2.212E07 /m)	83
Figure 83. Upstream pressure reading prior to un-start (M = 1.8, Re# = 1.619E07 /m) ..	86
Figure 84. Upstream pressure reading prior to un-start (M = 3, Re# = 2.212E07 /m)	86
Figure 85. Comparison of hysteresis diagram of shock-train	87
Figure 86. Ramp slope effect in hysteresis graph (M=1.8, Re=1.389E07 /m)	89
Figure 87. Ramp slope effect in hysteresis graph (M=1.8, Re=1.628E07 /m)	90
Figure 88. Reynolds number effect at M=1.8	91
Figure 89. Reynolds number effect at M=3	92
Figure 90. Hysteresis graph with Mach number ratio	93
Figure 91. Hysteresis graph of Mach ratio vs. $\Delta\%$ flow area	94
Figure 92. Mach 1.8 hysteresis graphs non-dimensionalized and combined	95
Figure 93. Mach 3 hysteresis graphs non-dimensionalized and combined	96
Figure 94. All hysteresis graphs are non-dimensionalized	96
Figure 95. Clean run with Mach 3 nozzle	98

	Page
Figure 96. Clean run with Mach 1.8 nozzle.....	99
Figure 97. Top and bottom symmetry test (M=1.8, Re=1.427E07 /m)	101
Figure 98. Top and bottom symmetry test (M=1.8, Re=1.665E07 /m)	101
Figure 99. Left and right symmetry test (M=1.8, Re=1.72E07 /m)	102
Figure 100. Left and right symmetry test (M=1.8, Re=1.773E07 /m)	102
Figure 101. Top and bottom symmetry test (M=3, Re=1.692E07 /m)	103
Figure 102. Top and bottom symmetry test (M=3, Re=2.388E07 /m)	103
Figure 103. Left and right symmetry test (M=3, Re=1.79E07 /m)	104
Figure 104. Left and right symmetry test (M=3, Re=3.205E07 /m)	104
Figure 105. Results of adding pressure in upstream	106
Figure 106. Schlieren image when the pressure added upstream.....	107
Figure 107. From Lin et al., shock-train locations for rectangular and round isolators at various back pressures in Mach 1.8 flow (27).....	108
Figure 108. Shock-train location versus P_b/P_1 in Mach 1.8 and $P_o=17$ psia.....	109
Figure 109. Comparison between Lin et al.'s and Paek.....	109
Figure 110. Shock-train location versus P_b/P_1 in Mach 3 and $P_o=31.7$ psia.....	110
Figure 111. Lin et al.'s graph – shifted and normalized shock train pressure profiles for I- 1 rectangular and I-2 round isolators in Mach 1.8 and 2.2 flow (27).....	112
Figure 112. From this research – shifted and normalized shock train pressure profile for rectangular isolator in Mach 1.8	113
Figure 113. From this research – shifted and normalized shock train pressure profile for rectangular isolator in Mach 3	113

	Page
Figure 114. From this research – shifted and normalized shock train pressure profile for rectangular isolator in Mach 1.8 and 3 combined	114
Figure 115. Ramp and T-bar and their relative motion.....	170
Figure 116. MTS reading increase VS. Ramp angle increase	171
Figure 117. MTS reading increase VS. %Area blocked increase	171
Figure 118. MTS reading increase VS. %Flow area decrease	172

List of Tables

	Page
Table 1. Constant slope input test conditions	62
Table 2. Actuator height and %flow area at shock-train imminent and un-start.....	70
Table 3. Test conditions for hysteresis experiments	77
Table 4. Start/un-start/restart/clean height summary	85
Table 5. Test conditions for ramp slope effect experiments.....	89
Table 6. Test conditions for symmetry tests.....	100
Table 7. Endevco pressure sensor/amplifier in-house calibration results.....	153
Table 8. Unit conversion from MTS reading.....	155

BACK-PRESSURE EFFECT ON SHOCK-TRAIN LOCATION IN A SCRAMJET ENGINE ISOLATOR

I. Introduction

General Issue

In a past development of a scramjet, proving the feasibility of the scramjet engine technology was the primary goal. Many past ground and flight experiments demonstrated the practicality of the scramjet. However, the technical maturity of the scramjet engine is still in progress and there is much room for improvement.

The Air Force Research Laboratory Propulsion Directorate (AFRL/RZ) at Wright Patterson Air Force Base has been looking at the engine un-start problem in a scramjet engine, especially the aerodynamics in the isolator of the scramjet engine. This problem can be caused by either pressure drop at the entrance of the isolator or pressure rise at the exit of the isolator. The pressure drop before the isolator can be caused by a high angle of attack of the vehicle that makes the flow-direction component of the airflow velocity towards the inlet decrease. The pressure rise behind the isolator can be caused by the irregular combustion pressure fluctuation at the combustor. To overcome this problem, the current scramjet engine isolator is designed long enough to contain the subsequent shock-train within the isolator's length and accommodate reasonable pressure variations in front of or behind the isolator. But, a long isolator brings another problem. The longer the isolator is, the more an air vehicle weighs and the more fuel it requires. Reducing the weight of an air vehicle ultimately improves the range of that vehicle for the same amount of fuel. Eventually, this improvement will be applied to long-range-rapid-attack

missiles or economic access-to-space programs. The AFRL/RZ requested the U.S. Air Force Institute of Technology to investigate this issue.

Problem Statement

Currently, scramjet engines do not have a feedback control system to stabilize the shock-train within the isolator. They have a lengthy isolator section designed with an extra margin of safety to contain the shock-train. As a result of pressure variations before and after the isolator, un-start can be imminent. This engine un-start problem leads to engine flame out and thrust loss. A lengthy isolator section also results in more weight on a hypersonic vehicle, thus, requiring more fuel, and consequently, reducing the air vehicle's flight range. Therefore, the problem to solve is how to make the shock-train reside within a shorter isolator. How does one control the shock-train position? Is it possible to build a feedback control system to do so? What further research is needed to design a feedback control system? Ultimately, answering these questions will enable technology to stabilize the supersonic aerodynamics inside the isolator and shorten the section's length. The particular problem for this research was to design a test facility to for this experiment and determine how the back-pressure affects the shock-train locations inside the isolator.

Research Objectives

The primary objective of this research is to find the back-pressure effect on the shock-train location in the isolator of the scramjet engine. For this research, the primary objective can be divided into two categories. The first one is to design, build, and set up the test facility to simulate the isolator of the scramjet engine. The new facility requires a

capability of applying back-pressure in a controlled manner and allowing the addition of a feedback control system later. The second category is to execute experiments to examine the steady-state behavior of the shock-train as a function of back-pressure.

Investigative Questions

What does it take to build a test facility to simulate the isolator of the scramjet isolator? Can this test facility produce a similar air flow condition as the real operating condition in the scramjet isolator? What is required to maintain the data integrity? How is the laboratory set up so that the research objectives are met? At what back-pressures are shocks and un-start imminent? What does the pressure distribution inside the isolator look like between those two points? How is the leading edge of the shock-train going to be determined from the collected data? Does shock-train location have a linear relationship with the back-pressure value? How does a change in Mach number or Reynolds number affect the shock-train location? If time allows, what does the dynamic behavior of the shock-train look like?

Methodology

A 2.5"x2.5" supersonic wind tunnel was used for this research. A new test section was built to simulate the scramjet isolator. An adjustable ramp was installed in the floor and one in the ceiling of tunnel downstream of the test section to create a back-pressure. Pressure transducers and amplifiers were installed along the top and bottom of the test section. Further a schlieren camera collected visual data through windows in the sides of the test section. A LabVIEW program operated the tunnel and provided position

commands the MTS actuator that controlled the two ramps. Refer to Chapter II Methodology for more detail.

Assumptions/Limitations

Currently, there are two nozzles in this laboratory. One produces a Mach 1.8 flow to the test section and the other produces a Mach 3 flow.

One of the assumptions made was that the flow was isentropic throughout the wind tunnel when calculating the flow Mach and Reynolds numbers within the test section. The available information for this calculation is a stagnation chamber pressure and temperature as well as static pressure measurements from the test section top and bottom. Also, ideal gas behavior was assumed for the air in the test section.

II. Literature Review

Scramjet Engine

A scramjet engine allows a vehicle to fly at hypersonic speeds while its combustion occurs at supersonic speeds. The turbojet engine has rotating parts, which limit its maximum speed because there is a limitation on how fast airflow can travel through compressor and turbine blades. Ideally, for maximum velocity, the airflow inside the engine would not slow down; therefore, the rotating blades must be rethought. An evolution toward this ideal, from the turbojet engine, is the ramjet engine, in which the rotating parts are removed. In a ramjet, the airflow inside the engine slows down to a subsonic flow for combustion. Still, a ramjet does not allow a vehicle to fly at high hypersonic speeds so the next evolution toward the ideal is to keep the airflow supersonic throughout the engine. When a vehicle flies in a hypersonic speed, airflow within the engine cannot be slowed down dramatically since drops in the airflow velocity convert the flow's kinetic energy to thermal energy. Then, the air itself would be excessively hot and result in ineffective combustion, resulting in thrust degradation. One way to avoid this problem is to have the combustion occur at supersonic speeds. The figure below shows the general schematic of a scramjet engine.

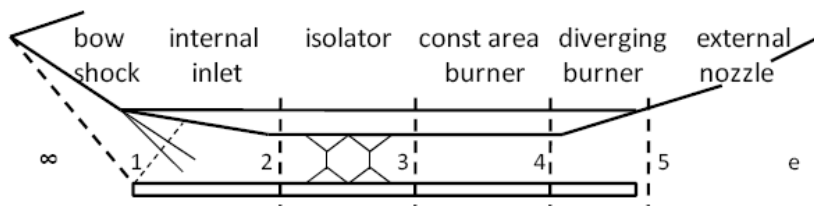


Figure 1. Schematic of dual-mode scramjet engine with stations 1-5 labeled(1)

At supersonic or hypersonic speeds, the nose of the air vehicle creates an oblique (or bow, if it is a blunt body) shock and the airflow speed drops across the oblique shock. When this airflow reaches the inlet of the ramjet/scramjet engine, the cowl lip creates another oblique shock and airflow is slowed down even more. The air finally reaches the combustor after crossing several oblique shocks in the inlet and isolator. The scramjet mixes hydrogen or hydrocarbon fuel with oxygen from the air to generate thrust through combustion.(2) Mixing the fuel and oxidizer in the combustor and burning them at a supersonic speed is still one of the challenges when designing a scramjet because the supersonic airflow does not allow enough time for that to happen.(2) This problem leads to a longer combustor section which ultimately results in more aircraft weight.(3) Currently, there are many ongoing research efforts on mixing fuel and oxygen in a scramjet combustor more effectively.

History

Genesis of the scramjet engine goes back to one century ago. In 1913, René Lorin in France brought an idea of employing ram pressure in propulsion hardware. In 1928, Albert Fono in Hungary was first to patent a ramjet engine (granted in 1932). In 1935, René Leduc in France designed a ramjet powered aerial vehicle and attempted his first flight on 21 April 1949.(4)

NASA's interest in the hypersonic air-breathing propulsion area goes back 60 years. The interest started from the hydrocarbon-fueled conventional ramjet (CRJ) engine concept and later progressed to scramjets. World War II also stimulated the

technology needs for high-speed flight. The first supersonic flight was accomplished in 1947 with the Bell X-1.(5)

In the 1960's, the interest in scramjets grew as did the understanding of their technical challenges. In that time, a comparison study between CRJ and scramjet was done and proved that the scramjet was more effective in hypersonic speed. In 1964, the Hypersonic Research Engine (HRE) program was initiated by NASA and its goal was to flight-test the scramjet engine on the X-15 rocket-powered vehicle. In April 1965, the U.S. Air Force initiated the Scramjet Incremental Flight Test Vehicle (IFTV) program and its goal was to show the acceleration of the vehicle with 4 hydrogen fuel scramjets.(2) During this decade, the US and UK were the major players in the scramjet propulsion community.(5)

In 1986, the U.S. Air Force and NASA began a serious hypersonic flight research program called the National Aerospace Plane (NASP) program. The goal of this program was to build and flight-test an air-breathing single-stage-to-orbit (SSTO) reusable spacecraft, X-30. It made a great contribution towards developing a rectangular, airframe-integrated scramjet. This program was cancelled without conducting a flight test. The goal of this program was to build a full scale operational SSTO vehicle and it was too big a jump in technology development, and the cost overran.(2) Australia also started scramjet research led by Professor Ray Stalker in 1981. In 1987, the University of Queensland in Australia built the T4 ground test facility. The T4 facility is the world's first facility that can produce the full range of a scramjet operating environment and measure the distinctive parameters inside the scramjet engine.(4)

In 1996, the Hyper-X program was initiated by NASA and built the X-43 series of prototype vehicles. First flight test was attempted in June 2001, but was not successful due to a booster failure. The second flight was successfully conducted at Mach 7 in March 2004. The third flight was also successful at Mach 10 in November 2004 and set a Guinness world record for the fastest air-breathing engine.(2)

In September 2001, the Defense Advanced Research Projects Agency (DARPA) made the first successful ground test flight at the Arnold Engineering Development Center in Tennessee. They tested a hypersonic scramjet projectile in a gun barrel tube.(4)

Currently, beside the U.S. military and NASA, other countries like UK, Australia, France, Russia, and India are making progress in the hypersonic propulsion area.(5) The implementation of this technology can be a hypersonic cruise missile, bomber, SSTD, or hypersonic transportation.

Shock system

A shock-train is a system of series of oblique or normal shocks, which is a very complex flow structure. Through a shock-train, the pressure rises and Mach number decreases.(6) The majority of the pressure rise occurs at the first oblique or normal shock, and then the pressure rises gradually thru the subsequent shocks.(7) There is a boundary layer between the wall and the shock-train. The boundary layer is thick at the leading edge of the shock-train and becomes thinner towards the downstream direction. The information from downstream can only propagate forward through the boundary layer because flow in the boundary layer is subsonic.(8)

In one experiment, once the shock-train propagated forward out of isolator, the so-called 'un-start' condition, pressure inside the isolator started fluctuating vigorously and its fluctuation frequency was dominant at 124 Hz.(8) According to Rodi et al, this frequency was very close to the natural resonant frequency of their dual-mode configuration. His method to find the resonant frequency was to calculate the ratio of the speed of sound at the flow stagnation temperature to the out-and-back travel length from the inlet entrance to throttle throat, assuming that the exit of the isolator was open. The natural resonant frequency from his calculation came out to be 275 Hz, which was more than twice the observed dominant frequency.(9)

The shock-train length is dependent upon the following factors: incoming flow conditions, isolator geometry, and the pressure ratio at the exit and entrance of the isolator.(10)

There are three criteria for detecting the leading edge of shock-train examined in the study by Lee et al: first, a location where the normalized pressure magnitude upstream of combustion increases by 1.5 times, second, a location where the normalized pressure standard deviation level upstream of combustion increases by 1.5 times, and third, the normalized pressure standard deviation reaches its maximum value. The study shows that the second criteria occurs earlier than other two, and then, first and third in this sequence. The frequency content of the pressure signal with power spectra analysis is another method to detect the shock-train leading edge. When the frequency content of the pressure signal changes significantly, it indicates the vicinity of shock-train leading edge. So, a change in spectral content of measured pressure means that the shock-train leading edge reached the measuring location.(10)

According to Torrez et al., in an early scram mode, the separated boundary layer inside the isolator reduces the effective supersonic airflow area and combustion pressure is expected to be constant during this mode. As you can see in the second picture in Figure 2, the separated boundary layer is getting thinner in the downstream direction so the effective flow area is increasing which results in decrease in static pressure, but heat addition causes the static pressure to rise at the same time.(1)

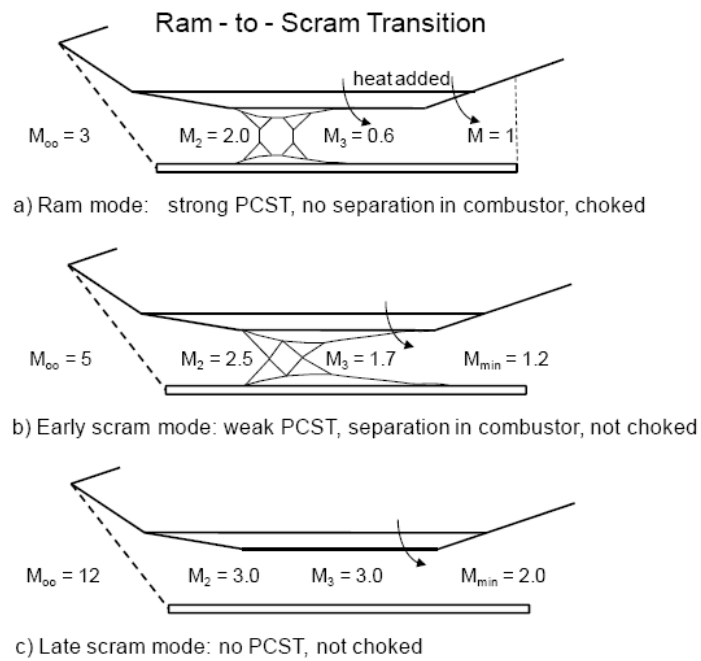


Figure 2. Schematic of Isolator Pre-Combustion Shock-train for Ram, Early Scram, and Late Scram Modes(1)

There are three methods to calculate the shock-train strength: the empirical method of Billing et al., the constant impulse function method of Heiser and Pratt, and the full CFD solution of Baurle and Eklund.(1)

According to Wagner, a typical shock-train propagation speed is 26 m/s from the laboratory frame of reference.(8) On the other hand, its velocities have been measured to range between 10 to 27 m/s by Weiting(11) and from 55 to 70 m/s by Rodi et al.(9) One journal indicates that the speed is affected by the heat release rate.(12)

Isolator

The name, isolator, came from its function, which is to isolate the incoming airflow at the inlet from any perturbations in the combustor, which may cause an engine un-start.(10) Its job is also to slow down and stabilize the incoming flow for ideal combustion condition.

The isolator plays a very critical role in a dual-mode scramjet engine. In order to avoid the high pressure in the combustor causing a un-start, an isolator contains the shock-train. For a scramjet, airflow is still supersonic after the shock-train and, for a ramjet it is subsonic which reduces the sensitivity of the inlet against combustor pressure perturbations. The performance of the isolator very closely relies on static pressure rise, total pressure recovery, shock system stability and exit flow uniformity, which are affected by the incoming free stream. Uniform incoming flow structure to the isolator yields uniform flow to a combustor. Ideal flow structure in an isolator would be one where the entire shock-train from leading edge to last shock is contained in the isolator region. For maximum performance, the maximum pressure rise through the isolator should be less than or equal to the pressure rise thru one normal shock.(8)

Without a high pressure from a combustor, there is no shock-train.(13) Why does the shock-train look like crossing oblique shocks? According to Reinartz et al., 'The high

back-pressure leads to the separation of the upper and lower boundary layer and generates a shock wave pattern of two crossing oblique shock waves.’(7)

Pressure measurements

A few pressure measurement methods were found in other papers. One of them is to use the time resolved measurements of pressure in the isolator to examine the shock-train leading edge detection. The second one is to look at 150% of the normalized pressure standard deviation level upstream of combustion influences. This gives the earlier warning of approaching shock-train from the downstream in the isolator. The third method is to monitor the peak in the normalized pressure standard deviation and this method is proved to be the most conservative one.(10)

Control of the shock

In the NASA Hyper-X program, X-43A was equipped with a Propulsion System Controller (PSC) to reduce the risk of inlet un-start. This device monitors isolator pressure signals as an indicator for shock train location to help predict un-start.(14)

Other research shows that scheduling of the engine pressure ratio to an empirically defined value was an effective way to control the shock-train location. The drawback of this method is that sensor noise and reference value uncertainties can degrade the controller performance. This method does not only require significant margin for error, but also relatively complex compensation to adapt to the changes in flight environment and vehicles orientation with respect to free stream. AuBuchon, et al argue that the control system should not just look at specific reference values or limits.(15)

According to Häberle et al., ‘the existing boundary layer separation due to shock interaction in the inlet throat can lead to inlet un-start. Therefore, an optional pressure boundary layer bleed has been integrated at the throat. The passive bleed reduces the lip shock induced separation bubble in the throat significantly.’(16)

Reinartz et al. used a ramp method to create a back-pressure. In their inlet experiments, at Mach 3 condition, he observed a serious flow separation over the ramp and the boundary layer covered one third of duct height. This big separation was not acceptable. So their team attached a wire behind the ramp, so that air flow over the ramp may attach to the ramp more and reduce the flow separation.(7)

Un-start

There are several things that can cause a un-start: high combustion pressure, heat addition resulting in boundary layer separation, too large inlet contraction ratio, and ignition of entrained hydrogen in the combustor sidewall boundary layer and subsequent separation.(8) (9) (17)(18)(19) Un-start is characterized by high thermal and pressure loads, loss of air mass capture, and an increase in drag.(10)

When un-start occurs, hot combusted gas propagates forward and can damage aircraft components which may lead to the loss of aircraft.(8) A bigger contraction ratio inlet causes more dramatic combustor pressure losses and abrupt un-start. Conversely, a lower contraction inlet causes gradual un-start. Pressure fluctuations become large and irregular during un-start which is also influenced by the inlet geometry.(9)(19)(12) Usually pressure spikes and significant increases in pressure root-mean-square values and inflection points occur right before the un-start.(19)(12)

There also seems to be something like a pause during un-start. Wagner et al. stated “the throttle induced shock system seemed to stop its upstream propagation momentarily in the isolator while the upstream shock-induced separated flow became stronger. After this pause, upstream propagation ensued and the condition of un-start was complete.”(8) His data indicates the shock-train transient behavior happened within 9 ms.

Flight conditions

Usually, the hypersonic vehicle geometry is determined by the cruise flight condition; at that condition, the vehicle is designed to have a bow shock impinge upon the engine inlet lip. This leads to maximum mass flow into the engine. If the vehicle is cruising at a slower speed, there may be mass flow spillage as the shock is ahead of the inlet lip.(20)

One study shows the experiments were done with Reynolds number between $1.07E05$ to $2.89E05$. In the higher Reynolds number range, the oblique shock generated by the inlet lip propagates downstream uninterrupted beyond the exit plane and the airflow in the isolator just expands continuously. Because of its own favorable pressure gradient, the shear layer remained attached. But at the lower Reynolds number range, the induced shock became stronger and impinged on the internal surface to create another high pressure gradient due to the interaction between shock and boundary layer. As a result, the airflow separated and the pressure propagation expanded upstream. At a Reynolds number near or less than $1.07E05$, the flow inside the isolator showed the shock-train transient behavior and led to a choking condition.(21)

Shang pointed out some Mach number and Reynolds number effect on the flow structure inside the isolator. He mentioned, “the lower the entrance Reynolds number, the greater is the induced pressure by the pressure interaction at the leading edge. In this case, the coalescing shock also has a steeper oblique angle to move the shock impingement upstream and leads to reflected shock wave downstream. The stronger adverse pressure gradient within the constant area duct unavoidably generates flow separation and consequently to a choking un-start.”(21)

In Shang’s experiment, he assumes that the flight region of the scramjet is at high altitude, so that the flow is laminar. Therefore, the turbulent effects were not a player in his investigation. In his experiment, he set his stagnation pressure at 580 Torr (7.47kPa, 11.2 psi) and temperature at 300K with an incoming Mach number of 5.15, which results in air number density of $1.57 \times 10^{-7} \text{ cc}$ and Reynolds number of $7.55 \times 10^5/\text{m}$. In his investigation, the real gas effect was not considered. At a lower Reynolds number, the oblique shock angle was steep, impinged on the sidewalls, and bounced off in the downstream direction. But at the higher Reynolds number, the oblique shock angle was shallow so it went to the exit of the isolator without bouncing off the wall.(21)

In Mirmirani et al.’s research, they had a flight condition of Mach number 10 at an altitude of 30 km, where the standard atmospheric temperature and pressure are $T_1=227\text{K}$ and $P_1=1172 \text{ Pa}$ respectively. A corrected specific heat ratio was $\gamma=1.36$ for hypersonic flight condition. They used oblique shock relations for their calculations. Their combustion process was simply modeled by Rayleigh flow theory, one-dimensional compressible flow with heat addition.(2)

It is important to recall how the air behaves at the molecular level at both supersonic and hypersonic speed. In supersonic speed, Mach 5 or less, the diatomic molecule, air, has five degrees of freedom. Those are three translational and two rotational modes. As the Mach number becomes greater than 5, the temperature across the normal shock increases and the inert degrees of freedom are energized. They are vibration, dissociation, and ionization, which significantly change the aerothermodynamics properties of air. Then the air no longer behaves as ideal gas; instead, it has real gas effects.(3)

In hypersonic flight, the temperature rises across the shock and thickens the boundary layer around the vehicle. This might damage the aircraft structure and alter the pressure distribution around the body. As the boundary layer become thicker, the flow sees the aircraft bigger than its actual size. This makes the shock at the leading edge become stronger, and the skin friction increases by induced pressure gradients. High Mach number increases the skin friction drag and this may increase the total drag by twice.(3)

III. Methodology

Entire experiment apparatus set-up

The laboratory is located in Bldg 640 Room 273 of the Air Force Institute of Technology (AFIT), Wright Patterson Air Force Base. A 2.5"x2.5" supersonic wind tunnel was used for this research. This wind tunnel and other peripherals occupy 17 ft x27 ft floor space. See the picture below.



Figure 3. Picture of the 2.5"x2.5" supersonic wind tunnel laboratory

The 2.5"x2.5" supersonic wind tunnel facility consists of the following components: a vacuum pump, a vacuum tank, two compressor pumps, an air dryer, a high pressure dry air tank, a main control computer with LabVIEW software, and National

Instruments data acquisition system. These are the main components driving this tunnel are not shown in the picture above, but are described later in this section. The components shown in the picture are schlieren set-up, a high speed camera, a computer that controls the camera with PFV software, a MTS hydraulic actuator, a hydraulic pump, a computer that controls the MTS hydraulic actuator with interface software, a hydraulic actuator stand, pressure transducers and amplifiers. The detailed list and their descriptions are written below. To better understand the laboratory system, a symbolic diagram is drawn and shown below.

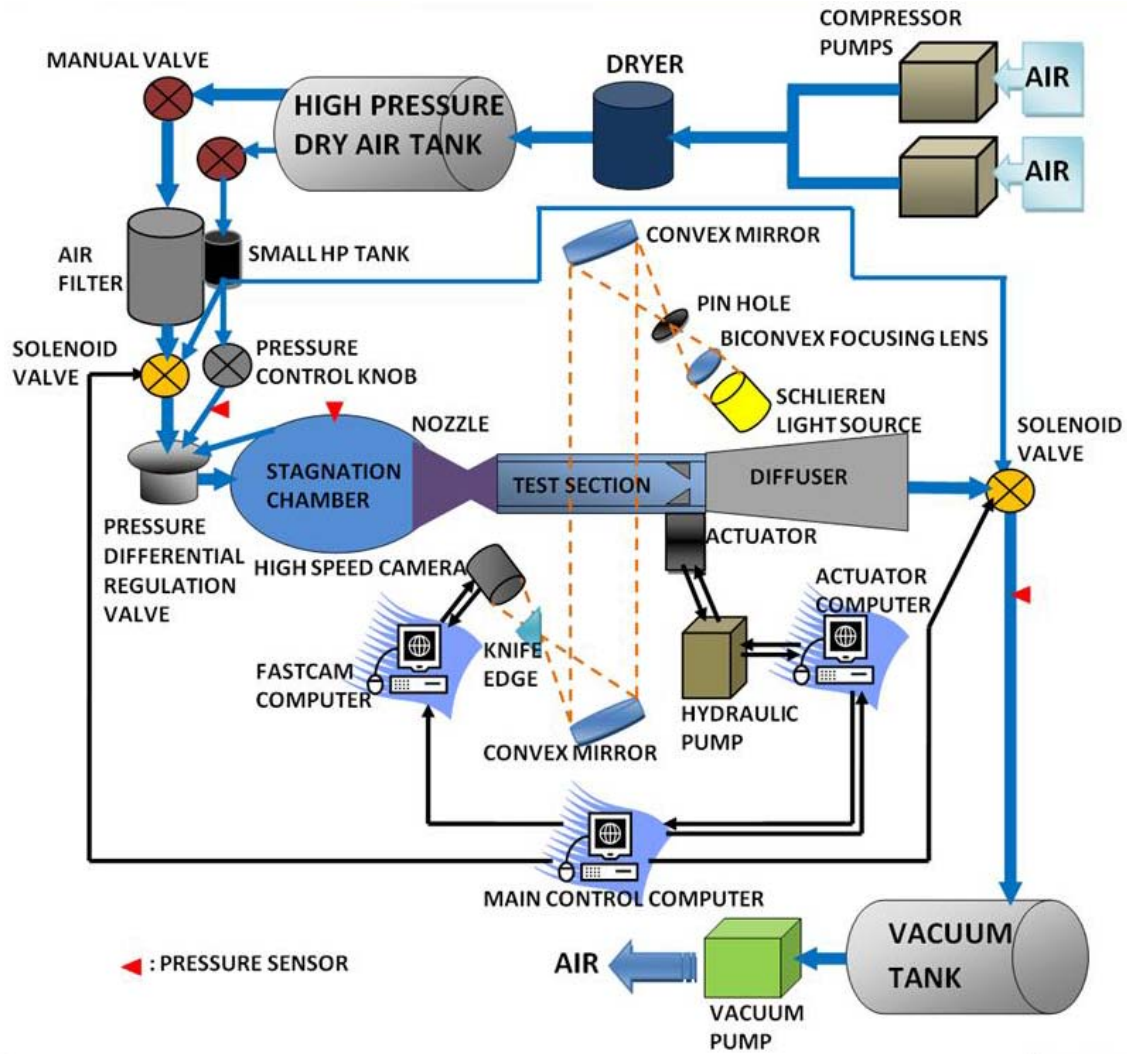


Figure 4. Entire laboratory diagram

2.5'x2.5' supersonic wind tunnel

At the very upstream of this supersonic wind tunnel, there are two compressor pumps, which bring air from the atmosphere and pressurize it into a tank outside the building. A picture of a compressor pump is shown in the Figure 5 below.



Figure 5. High air pressure compressor pump

This compressor is made by Ingersoll Rand Industrial Technologies Inc. and its model number is UP6-50PE-200. It can produce the maximum pressure of 200 psig. The next component that air goes thru is the desiccant compressed air dryer, which makes the air free of moisture and suitable for experimental use. This dryer is made by Donaldson and its model number is AHLD-350. The volumetric flow rate of gas for this dryer is rated at 350 standard cubic feet per minute (SCFM).



Figure 6. Desiccant compressed air dryer

Once the air goes thru this dryer, next it goes to the pressure tank outside the building. The volume of the tank is approximately 6,000 gallons. The pressure tank is shown in Figure 7 below.



Figure 7. Vacuum tank (left) and pressure tank (right)

The next component that air sees is the main manual shut off valve. This valve is regularly shut down at the end of the test day for safety purpose or when calibrating sensors.



Figure 8. Main manual shut off valve

Then air goes to a small high-pressure tank and, in parallel, to an air filter until the user begins a test run. A black knob on the top of the air filter controls the stagnation chamber pressure, which results in different Reynolds number of the air flow in the test section.(22)



Figure 9. A small high pressure tank (black), air filter (gray), and stagnation chamber pressure control knob on the top of the air filter

When the wind tunnel is started, the main control computer sends electronic signals to two solenoid valves. The downstream solenoid valve opens first, and then the upstream solenoid valve opens next. This sequence prevents the test section from being pressurized. Also, when the tunnel stops, the upstream solenoid valve closes first, and then the downstream solenoid valve closes next for the same reason. This logic sequence is built in the LabVIEW program in the main control computer. The picture below shows the upstream solenoid valve.



Figure 10. Upstream solenoid valve

After the air goes through the opened upstream solenoid valve, it goes to a regulation valve, and then stagnation chamber. The stagnation chamber is shown below. In the stagnation chamber, the velocity of the air is supposed to be zero, so the pressure measured at the stagnation chamber is the total pressure.

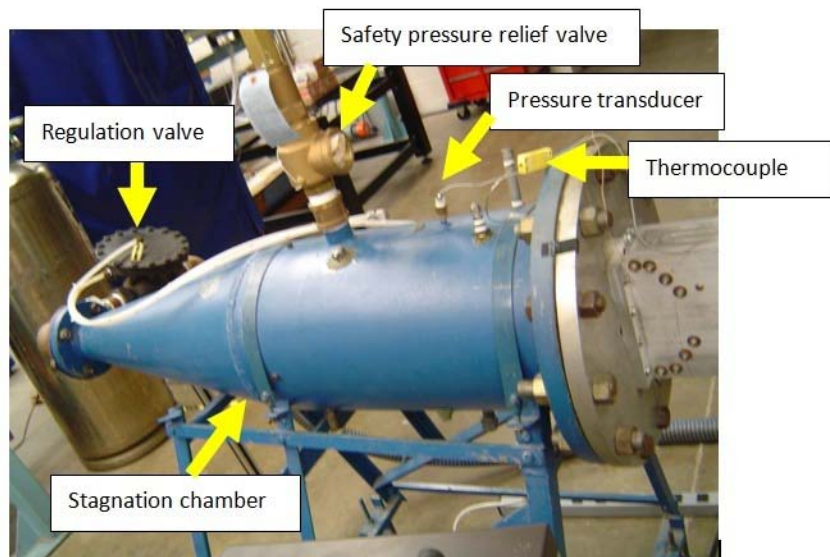


Figure 11. A regulation valve (black component on the left) and stagnation chamber (blue)

Then the air goes thru the diverging nozzle, which generate a desired Mach number of the incoming airflow to the test section. There are two diverging nozzles in the laboratory; one can produce Mach 1.8 and the other one can produce Mach 3 speed. Those nozzles are shown below.

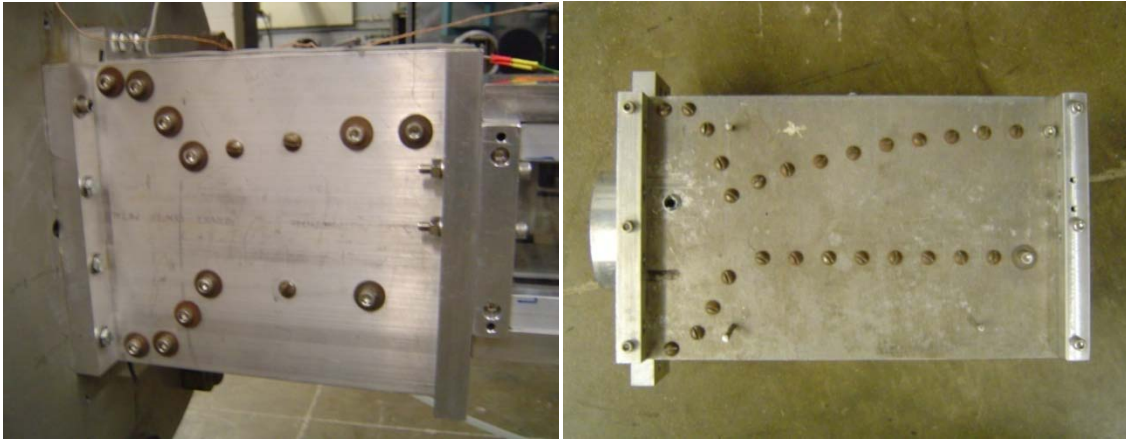


Figure 12. Mach 1.8 nozzle (left) and Mach 3 nozzle (right)

After going thru the nozzle, the air enters the test section. Figure 13 below shows the test section. This test section is specially designed for this research and is designed to simulate the scramjet isolator. The design process, fabrication process, and more detail about the test section are written later in this section.

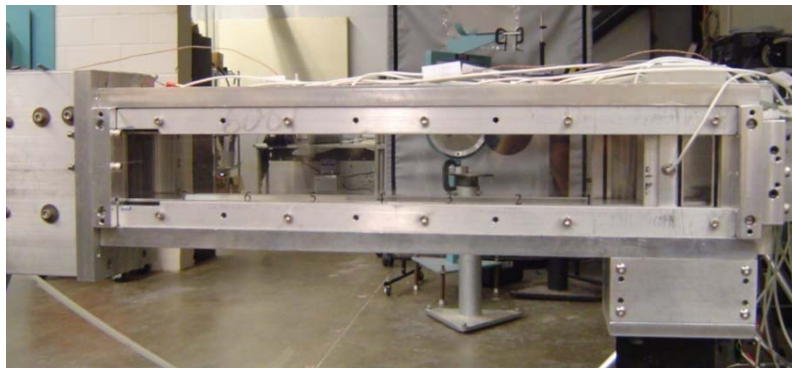


Figure 13. A new test section

Once the air exits the test section, it goes to the diffuser, a downstream solenoid valve, and then the vacuum tank outside the building. See pictures below.

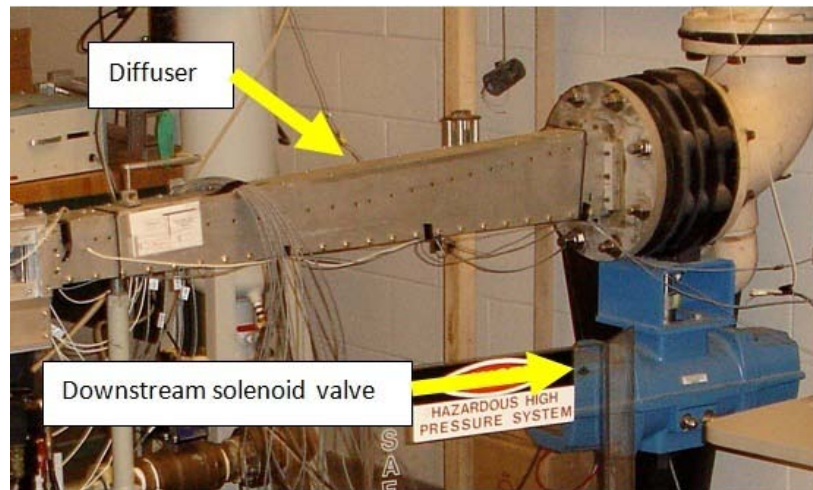


Figure 14. Diffuser and downstream solenoid valve

The volume of the vacuum tank is also approximately 6,000 gallon and the picture of the vacuum tank is in Figure 7. The air in the vacuum tank is forced out by the vacuum pump and it returns to the atmosphere. The vacuum pump is made by Stokes Vacuum Inc. It has two motors: one main motor with 10 H.P. and a turbo pump motor with 20 H.P. The vacuum pump is shown below.



Figure 15. Stokes vacuum pump

There is one unique characteristic about this wind tunnel. With Mach 1.8 nozzle, prior to test runs, the upstream regulator pressure valve (Figure 9) was set at approximately from 18 to 49 psia. After the wind tunnel started and air flow became stabilized, the total pressure measured at the stagnation chamber (Figure 11) was approximately from 14 to 18 psia. However, with Mach 3 nozzle, the upstream regulator pressure valve was set at from approximately 18 to 49 psia, and the pressure measured at the stagnation chamber was approximately from 14 to 44 psia. This phenomenon indicates that the throat area of the Mach 1.8 nozzle may be greater than the throat area of either the regulator valve (Figure 9) or the main shut-off valve (Figure 8), so the smaller throat area at either regulator valve or main shut-off valve does not supply enough air mass flow which results in low total pressure in the stagnation chamber. This phenomenon brings an importance of monitoring the stagnation chamber pressure during

the test runs to see whether the total pressure was steady or transient during the runs. The Figure 16 below shows the total pressure value at the stagnation chamber with respect to time. As you can see, the total pressure remain constant throughout the tests; therefore, there is no transient effects by total pressure in this wind tunnel. To note, the R.V.P in the figure's legend means the pressure setting at the regulator valve.

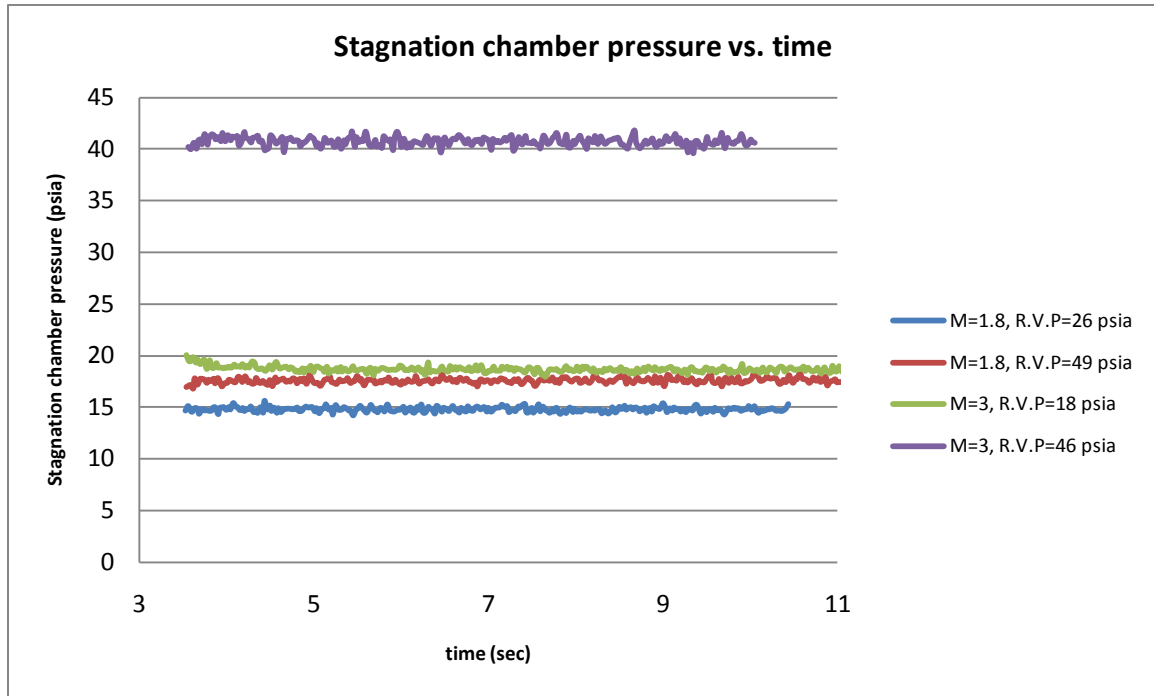


Figure 16. Stagnation pressure behavior during the test runs

The new test section

Probably the biggest challenge in this research was designing and fabricating the new test section. A lot of engineering studies were required during this process. First, a previous test section was carefully examined to see if it can be used for this research. To serve this research's purpose, the old test section did not only require a significant modification, but it also did not satisfy all this research's needs. For example, its length

in flow direction was too short, so it might not have covered the entire range of the shock train from the leading edge to a terminating shock. One idea came up was to put an additional section on the downstream side of the original section and install a mechanism to create a back-pressure. But, two different sections do not allow one smooth surface and any gaps or non-smoothness at the joint of two surfaces can create shock waves. Moreover, the old test section was not designed to hold any positive gauge pressure. In this research, the pressure in the test section might become high by raising the back-pressure. Moreover, the joint between the old section and the additional section can block the schlieren view. This first idea is shown below.

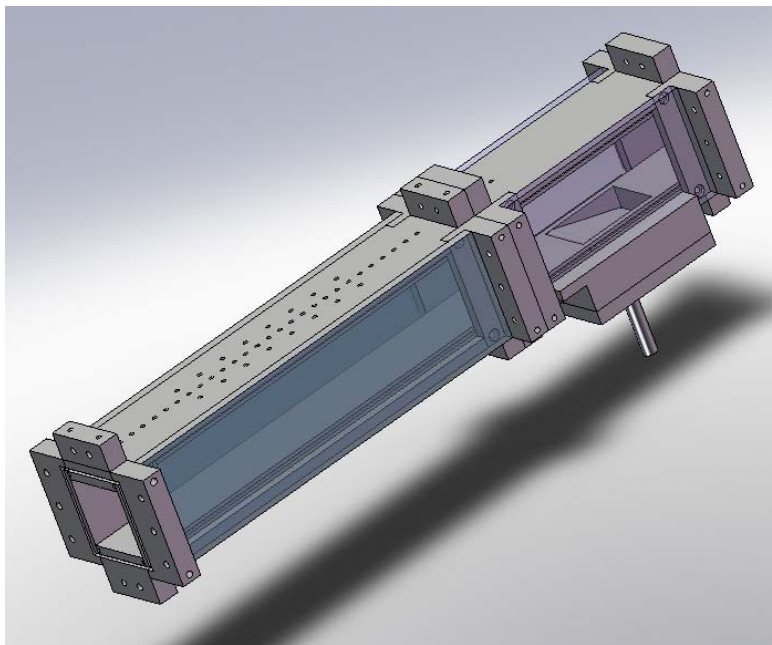


Figure 17. First concept: adding a new section behind the existing section

After in-depth examination and consideration, the decision was to take a risk of re-inventing the wheel. Then, so many questions followed. How long does the test section have to be? What kind of mechanism should be used to produce the back-

pressure? How strong does the test section have to be in order to hold the high pressure caused by the back-pressure inside the test section? Where should the sensors be mounted? How far should the sensors be spaced? What kind of material should be used for the test section? How about the window? How thick does the window have to be? And so on. The questions were countless. Some of the questions could be answered from other researchers' work. Some questions were answered because of the limitation of the current laboratory's configuration. For example, the maximum length of the test section cannot exceed 2 feet; otherwise, the walkway beside the wind tunnel is blocked and violates the safety code of the building.

Aluminum 6061-T6 was chosen for the test section material because aluminum is fairly light, strong, and used a lot for aerospace applications.(23) The material for the window was chosen to be cast acrylic because it is safer to handle and easier to fabricate than glass. Also, it provides outstanding optical clarity even at greater thicknesses, which is very important for schlieren video.

For a safety concern, the required minimum window thickness was calculated. The calculation is shown in Appendix A. The calculation shows that the window thickness has to be at least 0.729 inch. For optical use, i.e., schlieren imaging, it was also important to know the window deflection subject to the pressure because it affects the light refraction thru the window. Its calculation is shown in Appendix B. The results say that the maximum deflection of the window under 35.5 psig pressures would be 0.00211 inch. Both these calculations were based on the assumption that the maximum pressure at the test section is 35.5 psig. This case is only possible when the upstream pressure is set at 35.5 psig and the downstream of the tunnel is completely blocked. According to

the experiments on this tunnel in the past, the maximum gauge pressure inside the tunnel was -12 psig. Assuming the maximum pressure of 35.5 psig is conservative.

What to use to create a back-pressure brought some good discussion. At the very beginning, there was a debate over a pneumatic method versus a mechanical ramp method. The pneumatic method idea was turned down because it might not be able to produce constant steady pressure and also the valve mechanism's speed does not seem to keep up with the dynamic speed of the shock-train and the feedback control system. Moreover, the air from the pneumatic system can have significant non-linearities. Hence, the mechanical ramp method was chosen.

The size of the ramp was the next problem to solve. After a discussion with the previous researcher who used this tunnel, he noted that when he placed a test object with a diameter of 1 inch in the test section, he observed the shock-train propagated forward. The cross section area of 1 inch diameter object is 0.785 square inch. There is also a mount for the test object and it blocks some flow area as well. The wind tunnel cross-section area is 6.25 square inches. It means that at least 12.57% of area blockage can create the shock-train. From that number and engineering educated estimate, the ramp width was chosen to be 1 inch.

The hydraulic actuator has an extension range of 1.5 inches, but its reading is accurate only within middle 1 inch region. This number helps determine the location of the ramp's pivot point, the length of the ramp, and the maximum ramp angle.

The idea of using two ramps, top and bottom, was brought up for creating a symmetric flow. Though this is good idea, it also brings a new challenge. In order to move two ramps simultaneously and synchronize them, the gears are necessary.

However, a drawback about the gear is that it creates backlash in motion. Therefore, two big high precision gears were chosen and cut in Japanese-fan-shapes, so that the required number of gears and space around them can be reduced. Small dimension around the test section only allows the small gears, and then four gears are required to connect them. The more gears there is, the bigger the backlash is. Cutting two big gears into Japanese fan shapes does not only reduce the number of gears, but also makes the big gears fit in a small area. Because high precision gears were chosen, almost no backlash was noticeable.

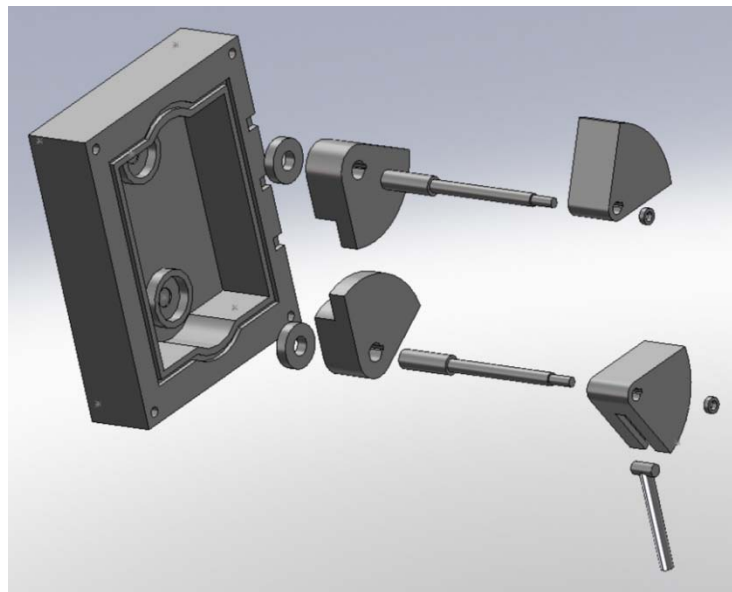


Figure 18. Gearing mechanism to synchronize two ramps

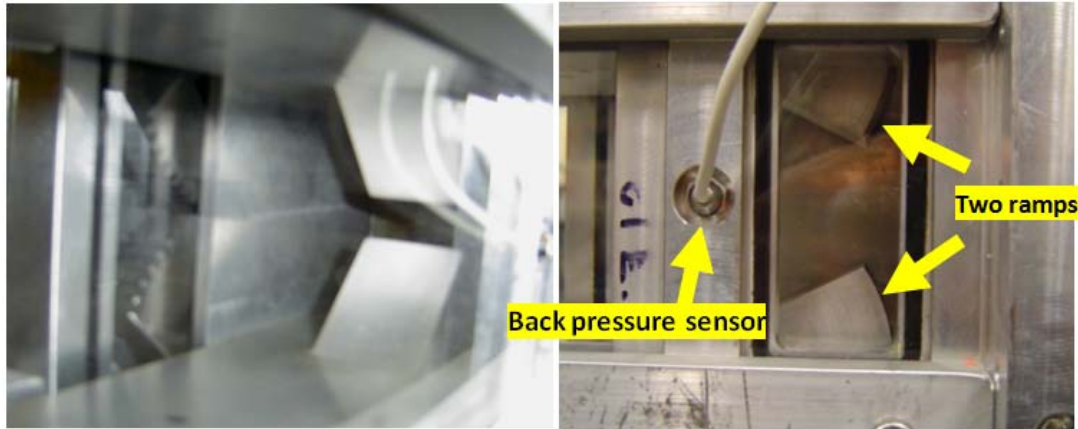


Figure 19. Two ramps inside the wind tunnel

There are some moving parts in this test facility, i.e., ramps, gears, an actuator, and shafts. Eventually, these parts will be moving at high frequency after the control system is installed. Wear-and-tear would be another problem to encounter. So, ball bearings are installed at almost every rubbing surface. High precision miniature-size ball bearings were chosen for this facility.

Sealing was another challenge. To keep the integrity of the airflow inside the test section, there must not be any air leaks in any joints in the test section. O-ring seals were used at almost every contacting surface. Sealing between the test section and the hydraulic actuator was another challenge. Making the joint parts precisely and using O-rings was a key to the success.

There were some design variables already determined due to the dimension of the other existing parts of the wind tunnel. The new test section had to mate with the upstream diverging nozzle and the downstream diffuser, and the inside cross section area had to be 2.5"x2.5." The hole locations for bolts, hole size, thread size, etc. on those

front and back end, were already determined. Other dimensions had to be worked around those fixed parameters.

Many ideas about how to link the actuator and the ramp together came up. Some of the ideas on the actuator end are shown below.

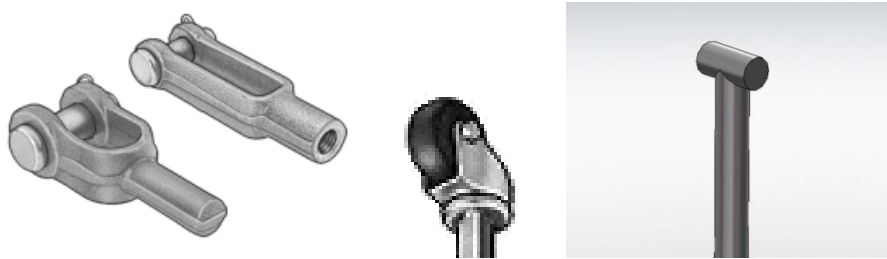


Figure 20. Clevis rod ends (left), wheel rod ends (center), T rod end (right)

The T-shape rod end was chosen because it reduces the complexity of the design, fits in a tighter space, and is easy to assemble and disassemble. When considering the future research, when the feedback control system will be used, there might be a time when the feedback control system goes unstable. Then, the actuator will move up and down out of control. In order to prevent the actuator from pulling, pushing, and breaking the ramp and other parts, the T-bar was chosen. T-bar disengages from the ramp when the actuator is all the way up or down. T-bar will slide out the back end of the ramp at those two situations. See Figure 115 in Appendix E for better understanding.

Figuring out the pressure sensor locations and their numbers was another difficult task because the goal of this research was to find where the shock-train would occur. Also, the oscillation amplitude of the shock-train was unknown. The number of sensors and location of them were limited by the physical space around the test section. The goal was to try to put as many as possible as close as physically possible. The pictures below

show the number and the locations of pressure transducer locations on a top plate and a bottom plate. They are the holes in the rectangular box.

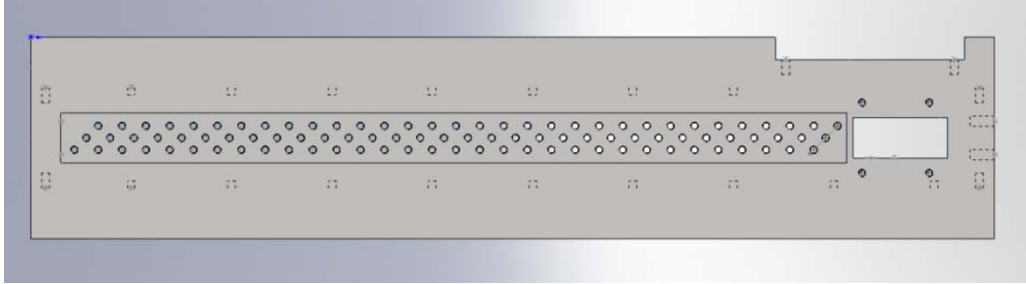


Figure 21. Top view of a top plate

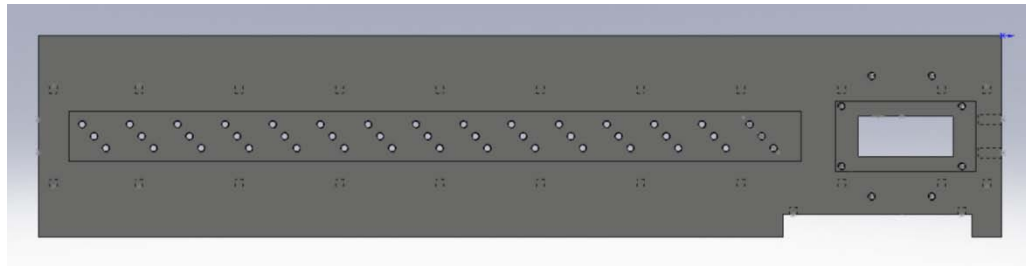


Figure 22. Bottom view of bottom plate

In order to communicate with the model makers at the machine shop, Solidworks software was used. Solidworks is an outstanding, sophisticated, professional, versatile, and visually beautiful program. But learning such a program by oneself was a challenge and requires significant time. Besides, the design for this project involves many complex geometries and moving parts. Drawing them in the Solidworks program was a very time-intensive effort. The final drawing of the test facility in Solidworks program is shown below. In addition, the engineering drawings are attached in the back of the report in Appendix C.

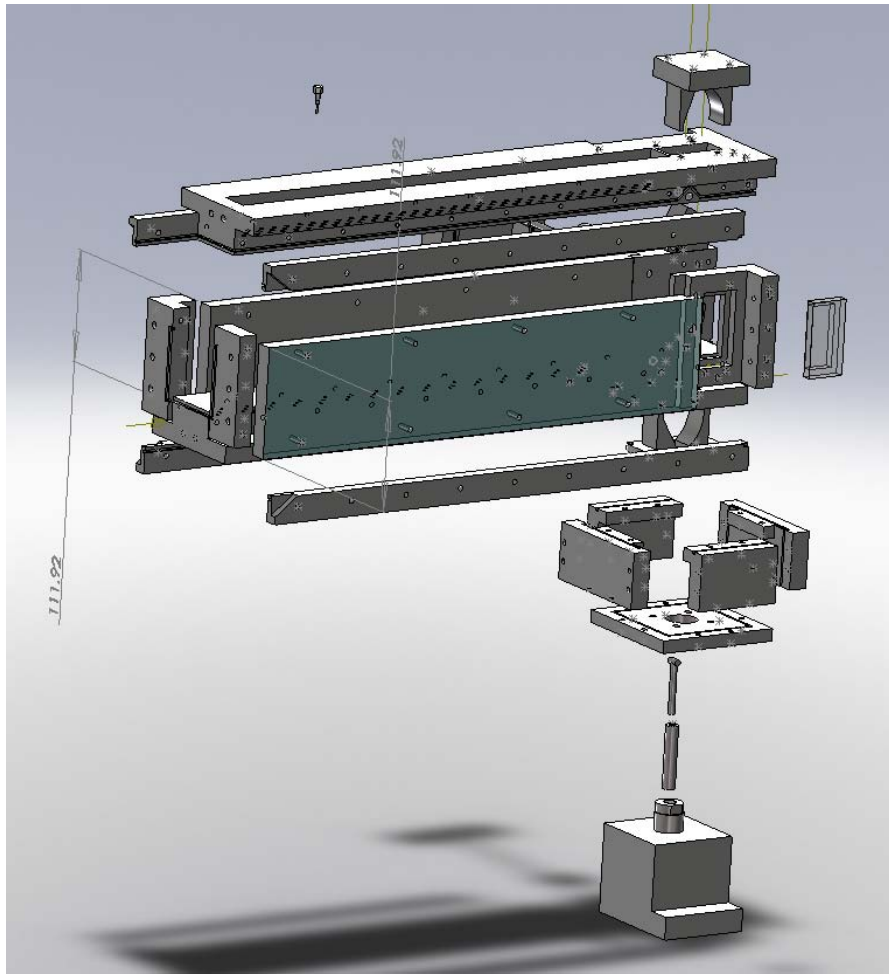


Figure 23. The new test section drawn in the Solidworks software

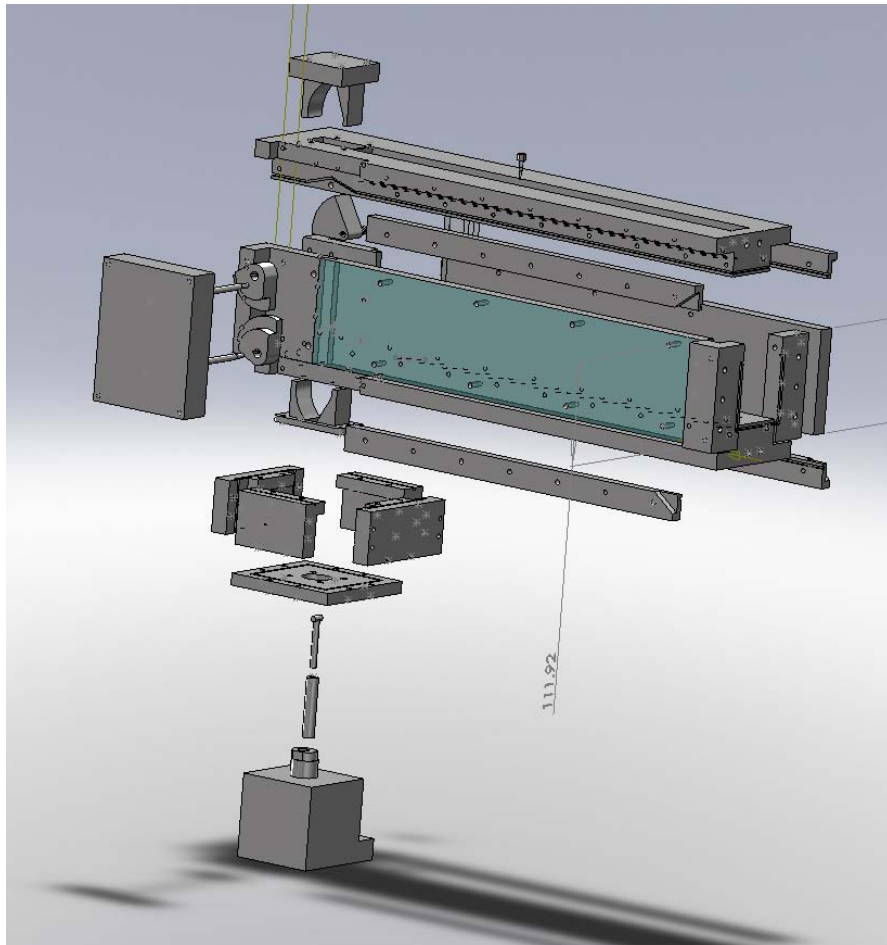


Figure 24. (Continued) the new section drawn in the Solidworks software

Also, the finished test section is shown in the picture below.

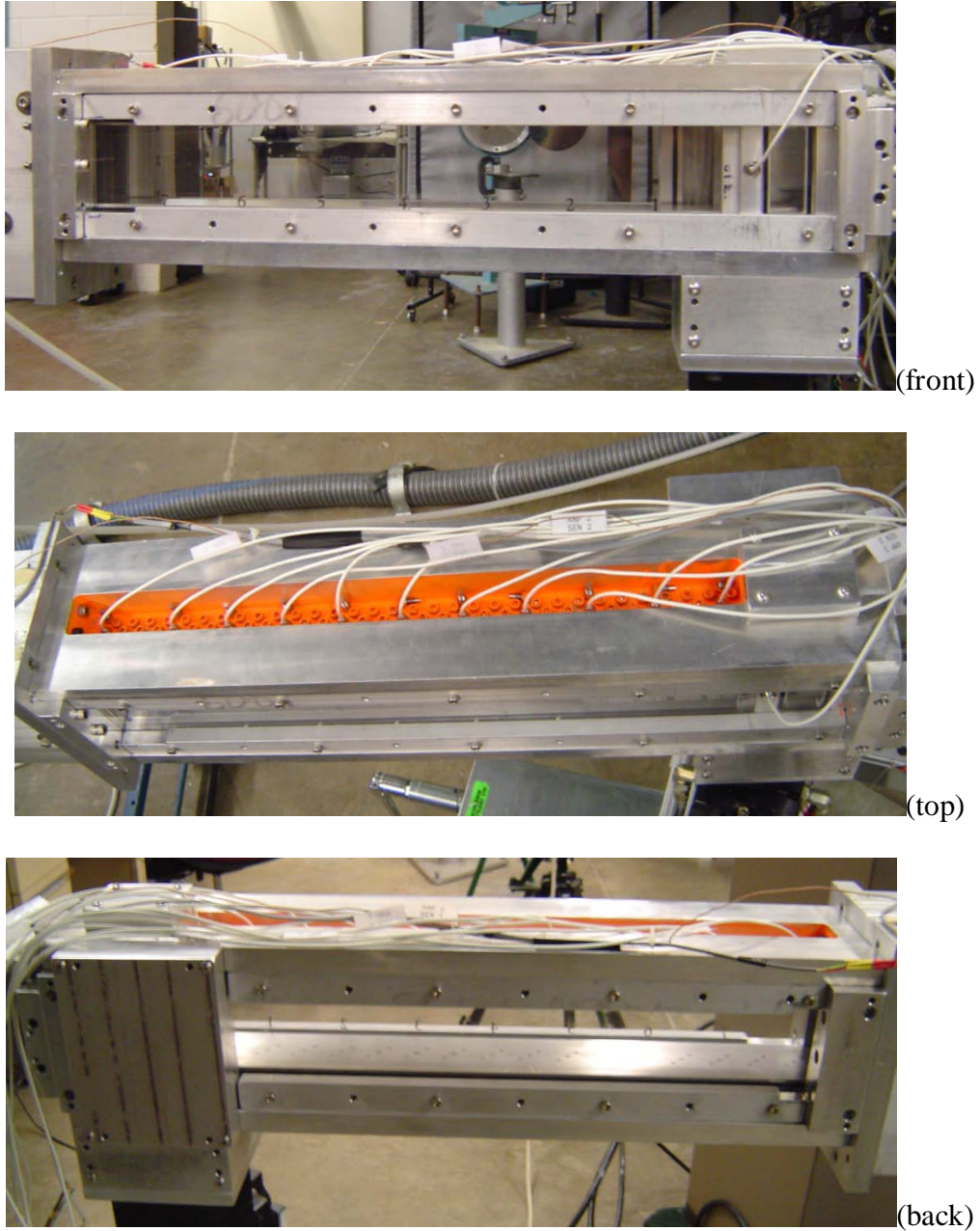


Figure 25. The picture of the new test facility

Main control computer

There was a main control computer already prepared for the 2.5"x2.5" supersonic wind tunnel in this laboratory. See the picture below.

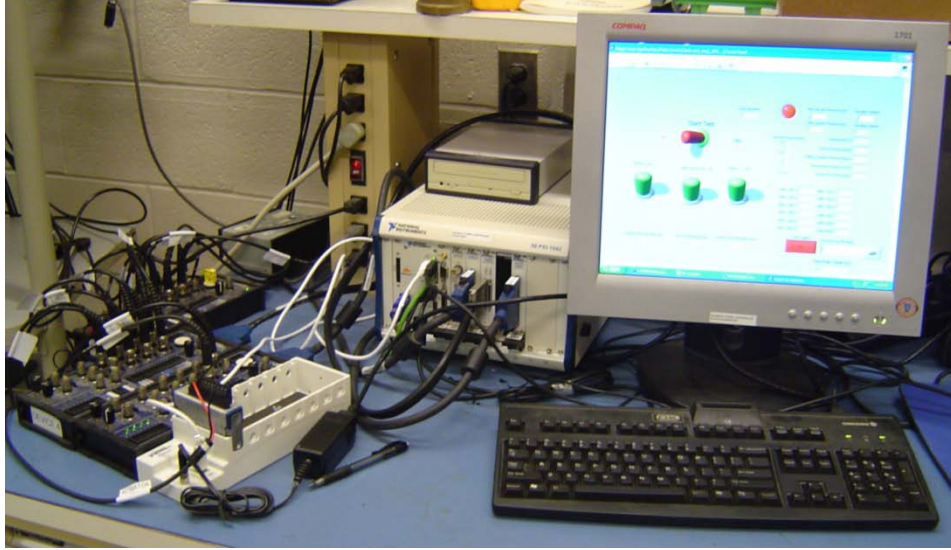


Figure 26. A main control computer for 2.5"x2.5" supersonic wind tunnel

This computer has the following components.

- A monitor, a keyboard, and a mouse
- NI PXI-1042 8-slot chassis
- NI PXI-8196 Embedded Controller
- NI PXI-6120 Simultaneous Sampling Multifunction I/O
- NI PXI-6259 M series Multifunction DAQ
- NI PXI-6070E Multifunction I/O
- NI PXI-1409 Image Acquisition
- External CD drive
- 68 pin cables (x3) and USB cables (x1)
- NI BNC-2120 boards (x3)
- NI cDAQ-9172 and NI 9263
- LabVIEW software

- NI Measurement & Automation software

A NI PXI-8196 Embedded Controller is the motherboard of this computer. It has 512 MB (2 x 256 MB DIMMs) dual-channel DDR2 RAM standard and 2GB maximum memory, 2.0 GHz Pentium M 760 processor, Windows OS and drivers, ExpressCard/34 slot and 4 USB 2.0 ports, Integrated hard drive, GPIB, serial, 10/100/1000 BaseTX (Gigabit) Ethernet, and other peripherals.(24)



Figure 27. NI PXI-8196 Embedded Controller

A NI PXI-6120 Simultaneous Sampling Multifunction I/O board was used for data acquisition of pressure and actuator position readings. It can take 4 simultaneously sampled analog inputs at 1MS/s per channel with warp mode enabled. It has onboard memory of 64 MS, extended input ranges up to +/-42V, and onboard anti-aliasing filters. It also has two 16-bit analog outputs that can send 4 MS/s per single channel or 2.5 MS/s per dual channel. It has 8 digital I/O lines, two 24-bit counters, analog and digital triggering.(24)



Figure 28. NI PXI-6120 Simultaneous Sampling Multifunction I/O

A NI PXI-6259 M series Multifunction DAQ is used for data acquisition of pressures. It has four 16-bit analog outputs (2.8 MS/s), 48 digital I/O, 32-bit counters, and NI-MCal calibration technology for increased measurement accuracy. It also has NIST-traceable calibration certificate, more than 70 signal conditioning options, correlated DIO (32 clocked lines, 10 MHz), analog and digital triggering.(24)



Figure 29. NI PXI-6259 M series Multifunction DAQ

A NI PXI-6070E Multifunction I/O was used for data acquisition of pressure and temperature, and analog output triggering to run the wind tunnel and start the camera. It

has 1.25 MS/s rate, 12-bit resolution, 16 analog inputs, 2 analog outputs, 8 digital I/O lines, two 24-bit counters, and analog triggering.(24)



Figure 30. NI PXI-6070E Multifunction I/O

A NI PXI-1409 Image Acquisition and an external CD drive were installed to this computer but were not used for this experiment.

The NI BNC-2120 board is a shielded connector block with signal-labeled BNC connectors. This device simplifies the connection of analog signals, some digital signals, and two user-defined connections to the DAQ device.(24) A picture of this unit is shown below.



Figure 31. NI BNC-2120 boards

The command output for a hydraulic actuator goes through a NI cDAQ-9172 and a NI 9263. The NI cDAQ-9172 is a compact DAQ chassis. It can run analog input modules at different rates. It has 8 slots for I/O modules. One NI 9263 module was installed in NI cDAQ-9172 chassis. The NI 9263 has 4 simultaneous channels, collects 100 kS/s with 16-bit resolution, and outputs ± 10 V analog signal.(24) Pictures of these units are shown below.



Figure 32. NI cDAQ-9172 and NI 9263

The information and specifications stated above were found at the NI official website.(24)

The LabVIEW software installed in this main computer was used to operate the wind tunnel, collect data, and trigger the camera. Figure 33 below shows the GUI panel of LabVIEW for the supersonic wind tunnel.

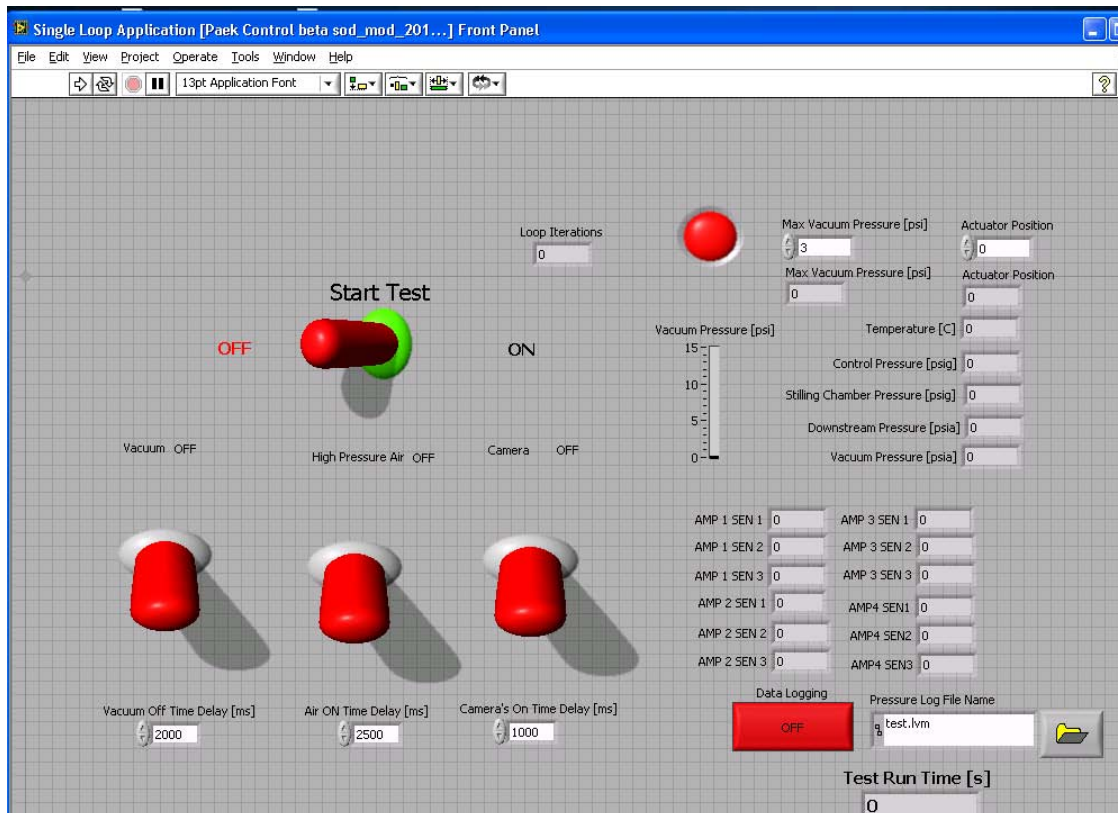


Figure 33. LabVIEW GUI panel for supersonic wind tunnel

Behind this front panel, there is a logic circuit panel and this is shown below.

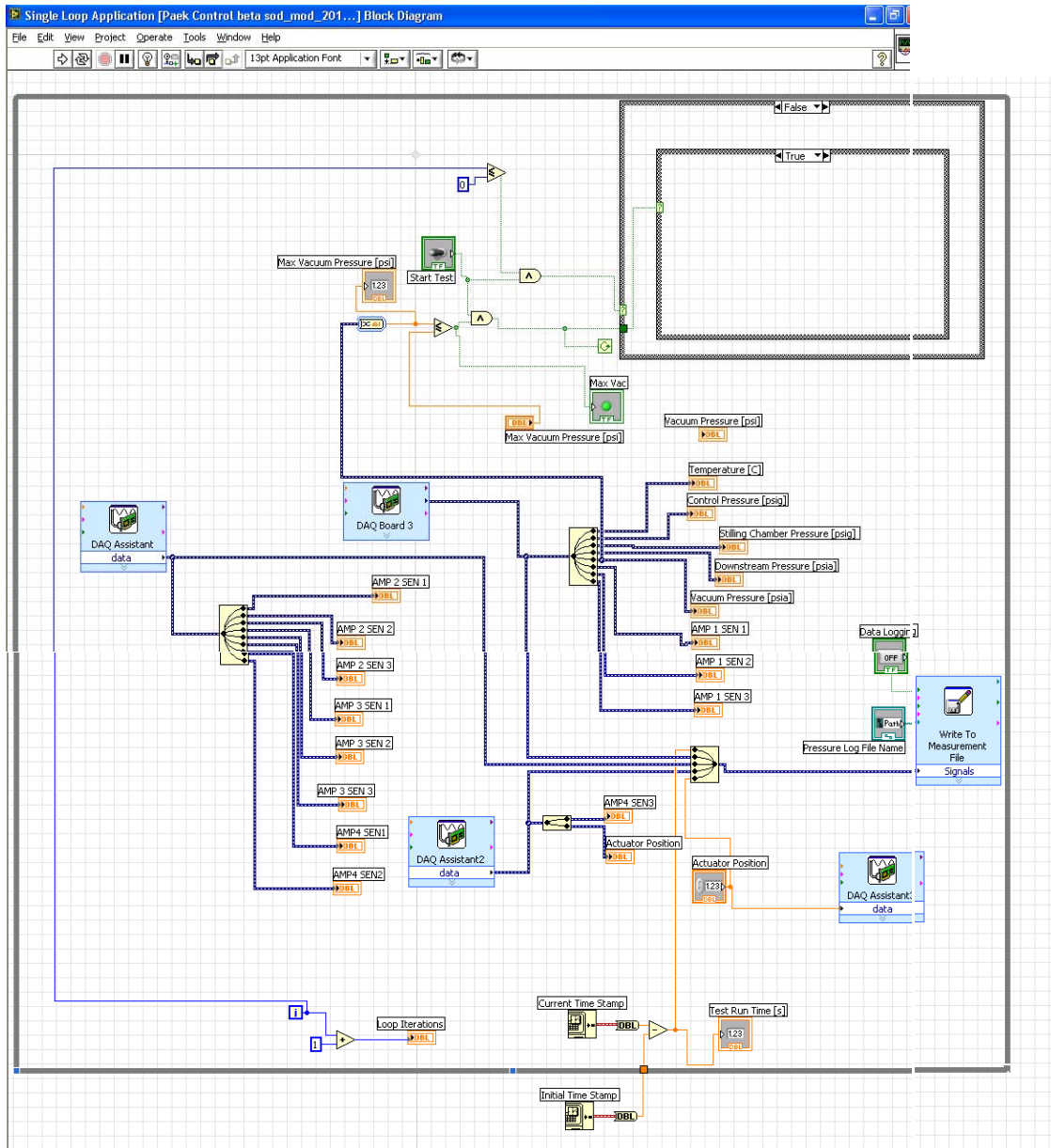


Figure 34. LabVIEW internal structure

Also, the NI Measurement & Automation Explorer software was used to install/uninstall, troubleshoot, and configure NI software or drivers. The screenshot of this program is shown below.

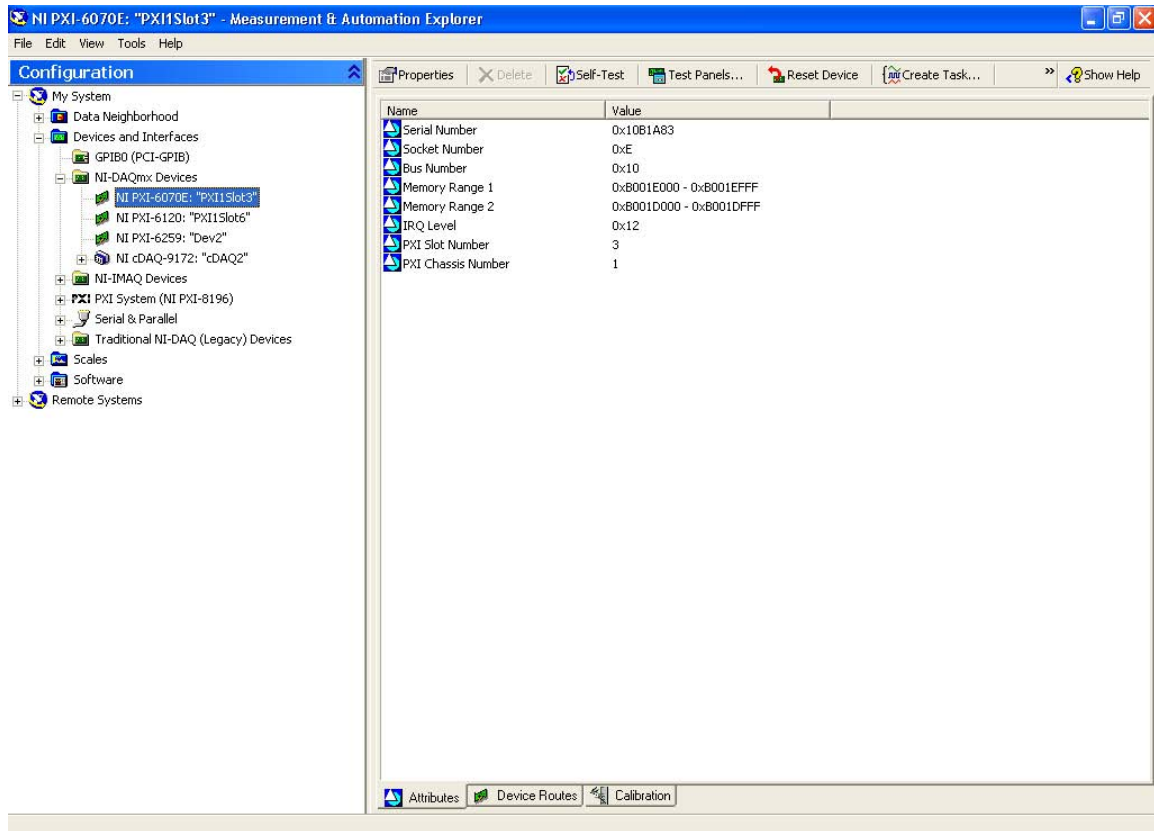


Figure 35. NI Measurement & Automation Explorer

Endevco pressure transducers and amplifiers

There were already four Endevco pressure transducers and four DC amplifiers installed in the wind tunnel for the operation purpose. Twelve additional Endevco 8530C-50 piezoresistive pressure transducers are purchased for the experimental purpose. They have a measurement range of 0 – 50 psi, 4.5 mV/psi sensitivity, 1 ms of warm-up time, and diaphragm burst pressure of 250 psi min. It also has full scale output of 225mV typical at 10.0Vdc, active four-arm piezoresistive bridge electrical configuration, noise of 5 microvolts rms typical, DC to 50,000 Hz and 50 microvolts rms maximum, DC to 50,000 Hz. It weighs 2.3 gram and cable weighs 9 grams/meter.(25)

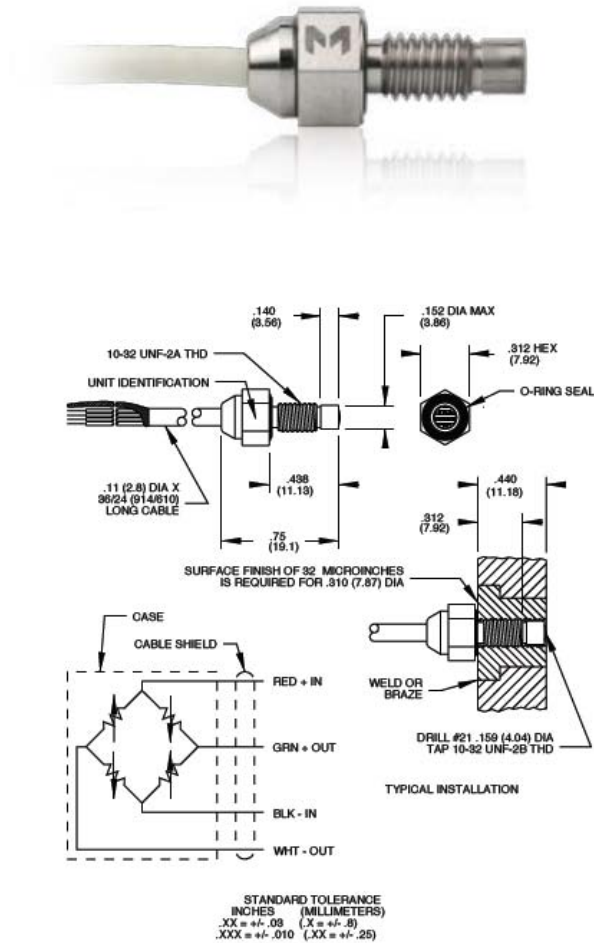


Figure 36. Endevco 8530C-50 piezoresistive pressure transducers

Four additional Endevco Model 136 DC Amplifiers were acquired for this experiment. Each one has three DC channels, 200 kHz bandwidth (-3dB corner), gain range from 0 to 1000 depending on the input voltage, built-in 4-pole Butterworth low-pass filter, linear output of 10V peak, current output of 10 mA minimum, output noise of 1mV rms maximum from 10 Hz to 50kHz with 1 kOhm load, accuracy of $\pm 0.5\%$ of full scale maximum with DC to 1kHz and filters disabled, linearity of 0.1% of full scale with best fit straight line at 1kHz reference, power dissipation of 10 Watts, and weight of 4 lbs.(25) A picture of these amplifiers is shown in a Figure 37 below.



Figure 37. Endeveco Model 136 DC Amplifier

The product information and specifications are available at the Endeveco official website.(25)

Upon receiving Endeveco products, a calibration was done on the sensors although the factory specification sheets were provided with the calibration results. After in-house calibration was complete, it was found that their results do not exactly match with the factory calibration data. Additionally, although the sensors themselves had linear behavior, the DC amplifiers were showing non-linear input-output relationships. Moreover, the digital readout on the DC amplifier has +/- 10% error. So the engineers had to find the direct relationship between pressures acting on the sensor versus the voltage outputs from the amplifier and kept in mind not to trust the digital readout on the DC amplifier. The pressure sensor/amplifier calibration results are shown in Appendix D. Also, a daily calibration was done at the very beginning of a test day to adjust any offsets due to any day-to-day pressure and temperature fluctuations. For this calibration, the reference pressure digital barometer was used in the laboratory and it is shown in the picture below.

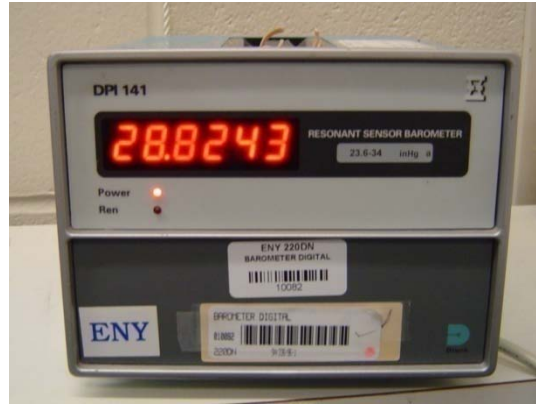


Figure 38. Reference pressure digital barometer for day-to-day calibration purpose

Schlieren imaging setup

Schlieren imaging equipment was available in the laboratory, but engineers had to configure it. The schlieren setup consists of following components.

- Light source: OSRAM HBO Mercury Short Arc lamps, 130W/2
- Biconvex focusing lens
- Pinhole
- Two convex mirrors (focal point: 80 inches)
- Knife edge
- High speed camera

The schlieren setup is shown in the diagram below.

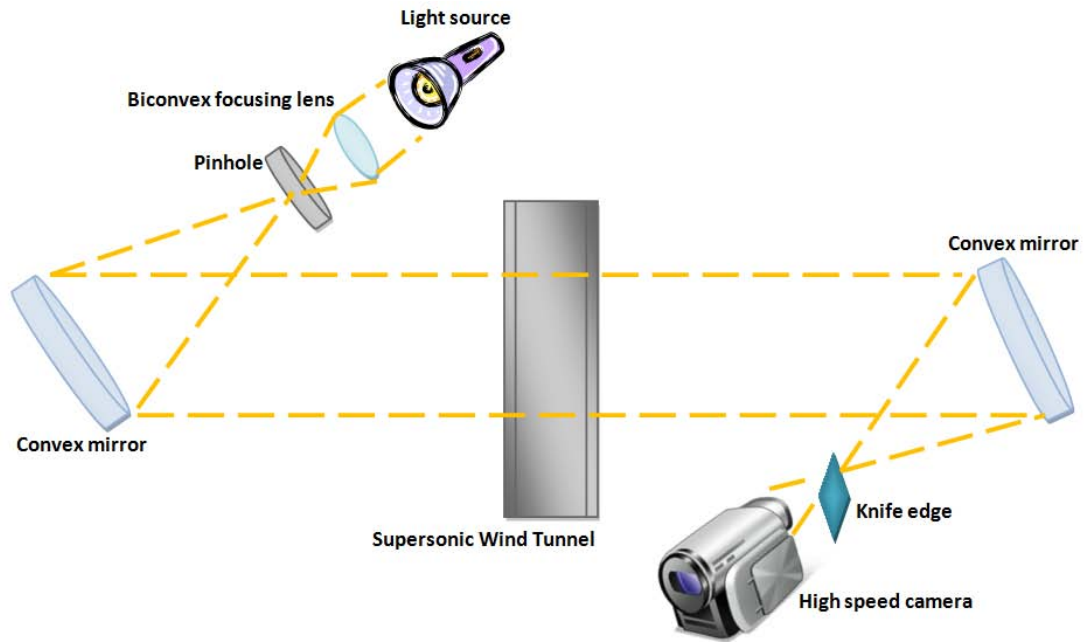


Figure 39. Schlieren imaging setup

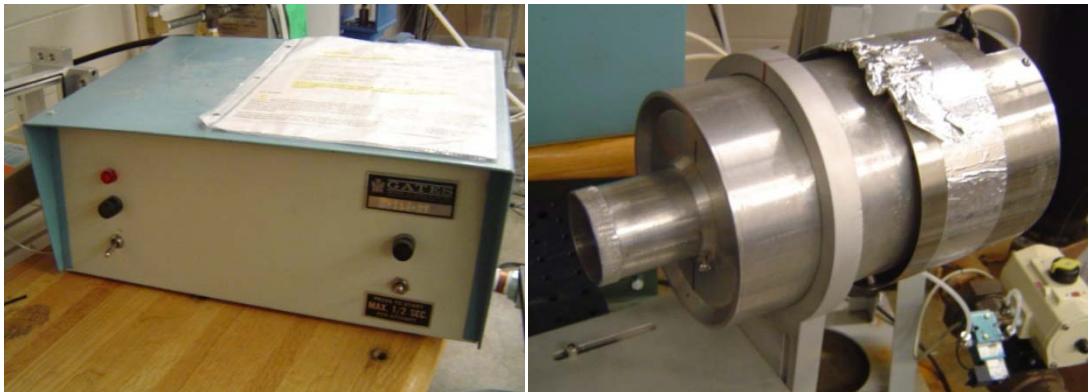


Figure 40. Light source for schlieren imaging



Figure 41. Biconvex lens (left) and pinhole (right)

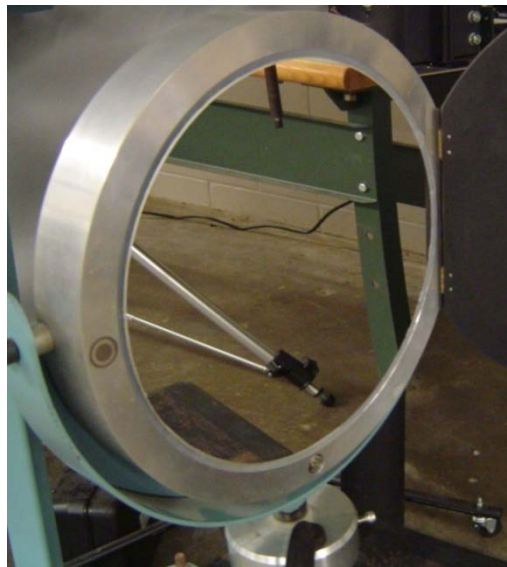


Figure 42. Convex mirror



Figure 43. A knife edge and high speed camera

The high speed camera is made by Photron and its model number is FASTCAM-X 1280PCI. It provides an 1,280x1,024 pixel image at frame rate to 500 frames per second, and at reduced resolution up to 16,000 fps. Electronic global shutter is as fast as 7.8 μ s. The knife-edge was set vertical because research focuses on the horizontal movement of the shock-train.

There is a separate computer station connected to the FASTCAM, which receives and records the video from the camera. The PFV ver.2.4.3.8 is the interface software for the high-speed camera. They are shown in the picture below.



Figure 44. Schlieren imaging control and viewing computer

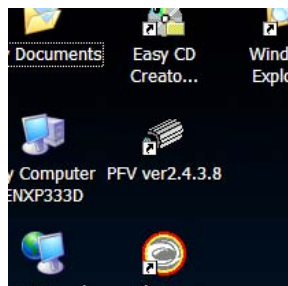


Figure 45. High speed camera interface software: PFV ver.2.4.3.8

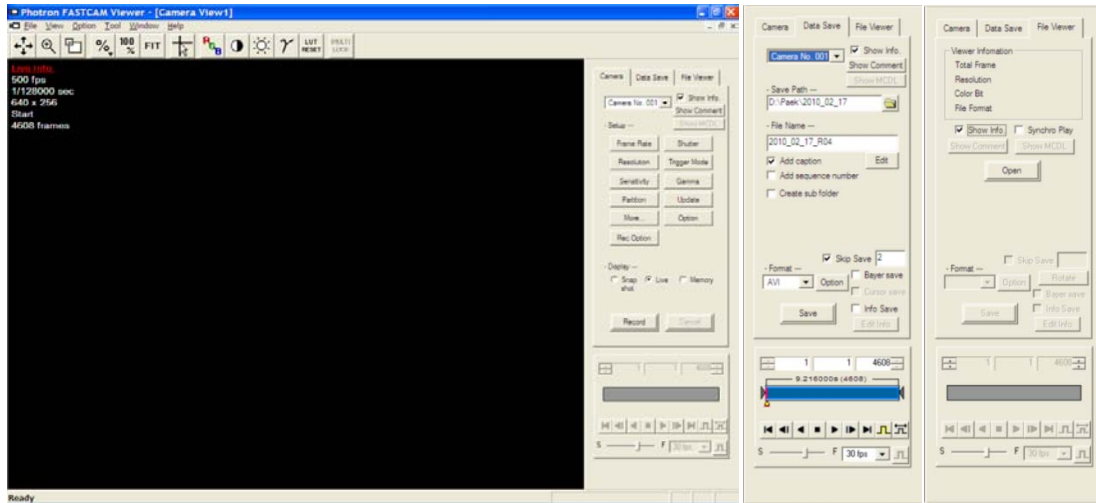


Figure 46. Screenshots of PFV.2.4.3.8 software

In the Figure 46 above, there are three menu taps on the right side of the screen, which allow a user to operate the camera, edit/save the video, and view the multiple videos. This software has a standby mode feature. When it is set at standby mode, it is waiting for a signal from the external source (main control computer for this experimental case). This feature allows a user to record the images automatically, remotely, and in a controlled timely manner with a single click of button.

Actuator system

The actuator system is composed of four main components. They are a hydraulic actuator, hydraulic fluid pump, a control computer, and interface software. The hydraulic actuator, the pump and the interface software are made by MTS Systems Corporation.

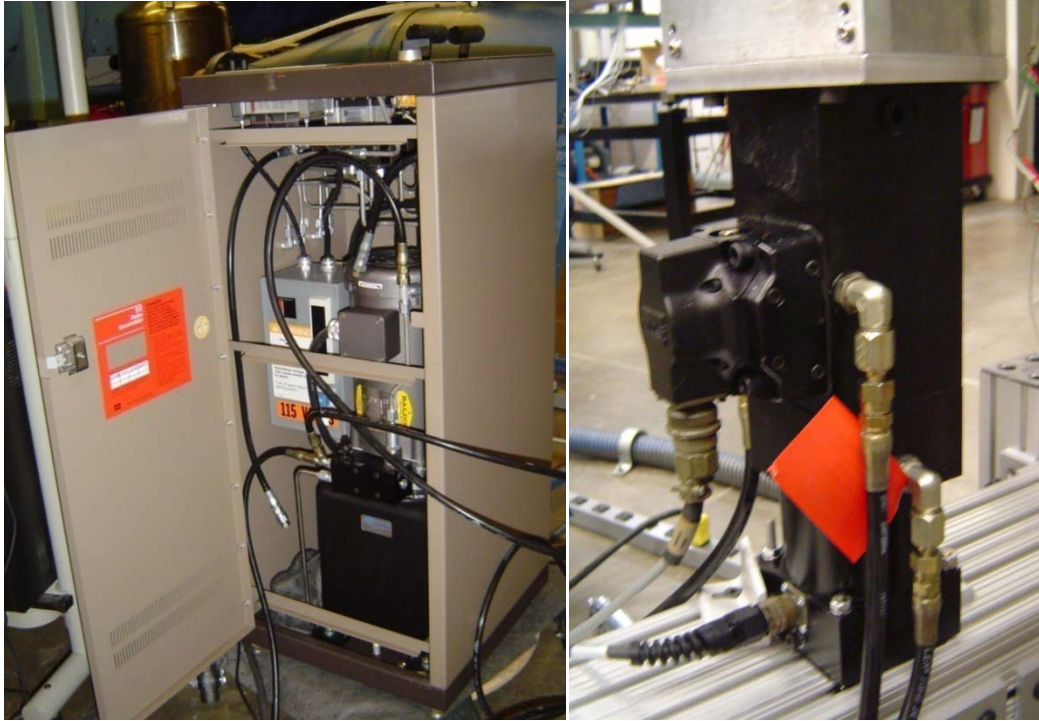


Figure 47. Hydraulic pump (left) and actuator (right)

The pictures above show the hydraulic pump and actuator used in these tests. The model number of the actuator is 242.01 and it can produce a force of 1 kip (= 5kN) over an effective area of 0.42 square inch. The model number of the pump is 685.03 and it is a 3,000 psi hydraulic grip supply.

The actuator control computer is linked to the main control computer, so the actuator position can be controlled and monitored by the main computer.

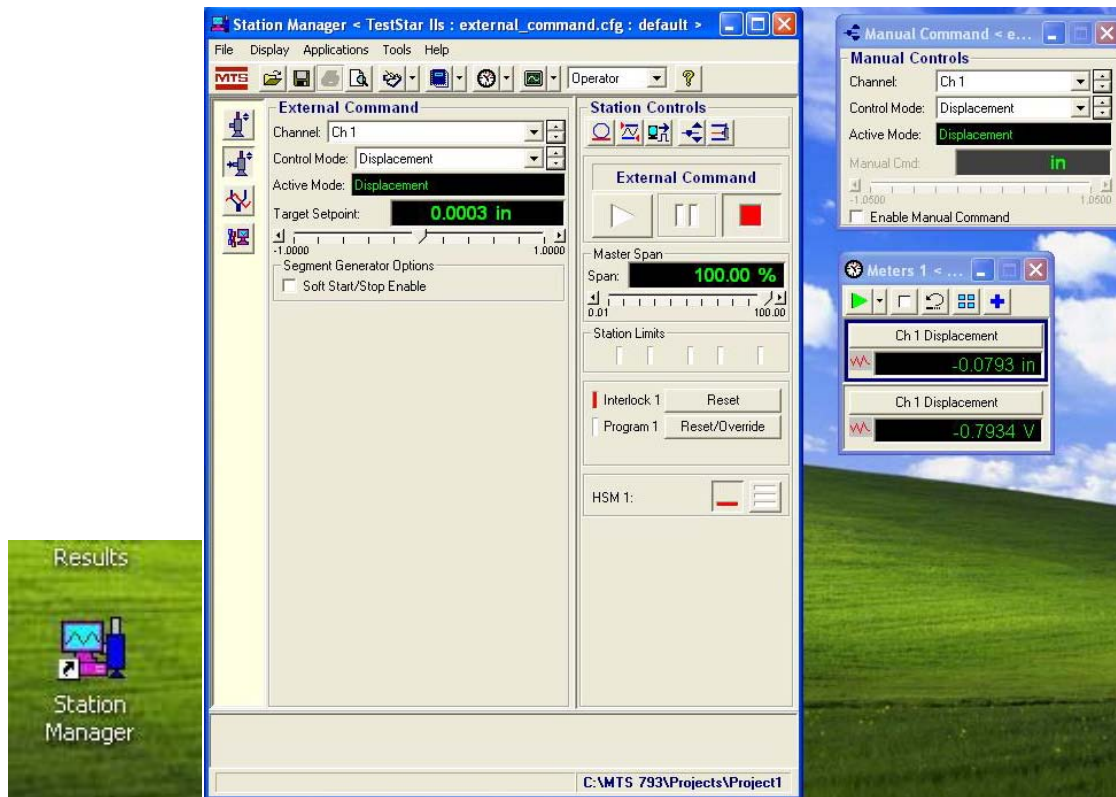


Figure 48. MTS software, desktop icon (left) and GUI (right)

The MTS software provides multiple capabilities. An actuator can be controlled by a real time manual command, a programmed command, or an external command. A Proportional-Integral-Derivative (PID) feedback controller is built in this software, so the position of the actuator can be accurately measured and controlled. Moreover, the PID gains in the software can be adjusted by a user, so the user can change the dynamics of the actuator. The MTS software also provides many types of preprogrammed inputs: step input, sinusoidal inputs, triangle inputs, ramp inputs, etc. The dynamics of the actuator can be customized in every aspect.

Safety pressure relief valves

There are two safety pressure relief valves in this supersonic wind tunnel. One is located on the stagnation chamber and the other one is located at the end of the diffuser. They both are pop-off type valves.

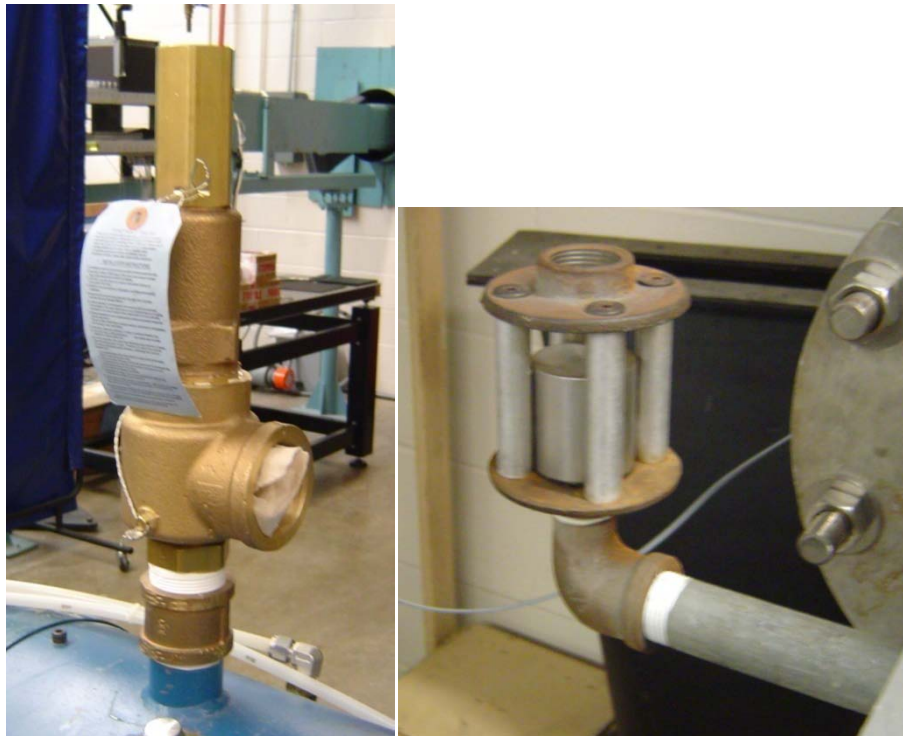


Figure 49. Safety pressure relief valves

Side project: making an actuator stand

In order to position the actuator at the right place and height, a stand was needed. First, small height adjustable carts or tables were looked at, but the space under the test section is very tight. So, the next option was to create new one. The 80/20 Inc. parts were suggested to use by lab technicians. First, the design schematic was done in the Solidworks program. By doing this way, it is easy to visualize the structure of the stand

and estimate the required material accurately. Once the design was done, the parts were acquired and assembled.

The stand should be height-adjustable, and able to handle hydraulic weight and its vibration. The actuator can be operated under very high frequency. In order to dampen out the vibration, rubber padding was inserted under an actuator. To raise and lower the heavy hydraulic actuator conveniently, a motorcycle jack was acquired. And there were 4 brakes installed on the stand to hold it at a fixed height. Pictures below show the Solidworks drawing and the final product.

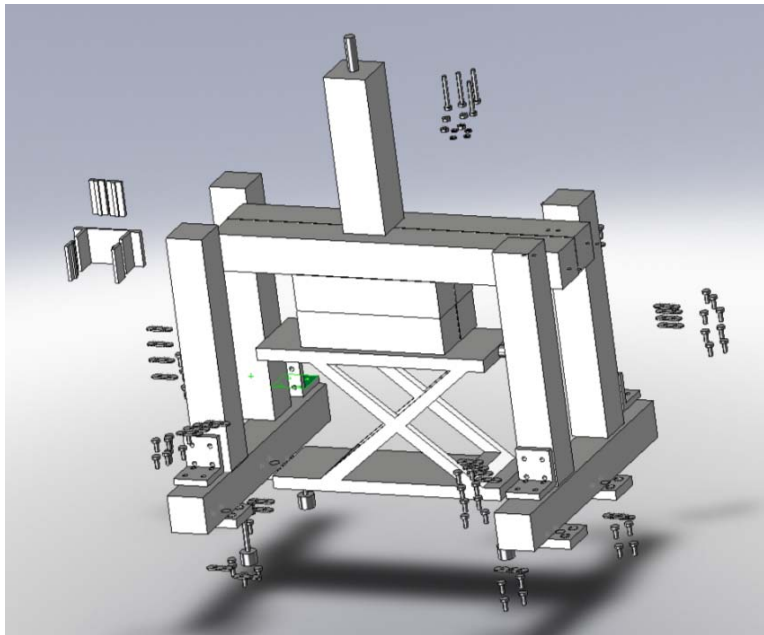


Figure 50. A stand for the hydraulic actuator, drawn in the Solidworks software

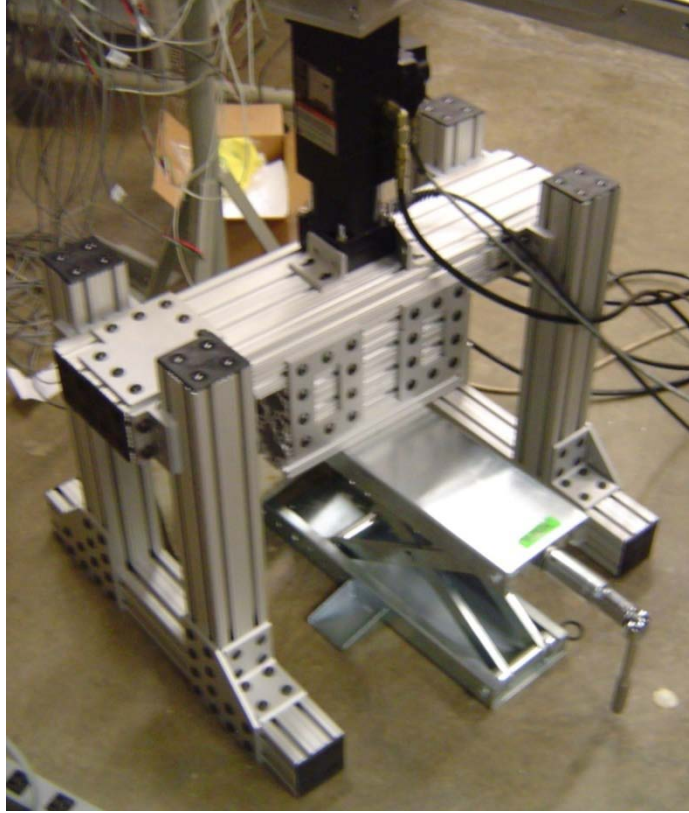


Figure 51. Final product: hydraulic actuator stand

IV. Analysis and Results

Overview

In the very beginning of the test phase, the test section was delivered. When and where the shock-train occurs in terms of the actuator height and its back-pressure value were of initial interest. After many test runs at a few different Reynolds numbers and two different Mach numbers, a rough idea of when and where the shock-train occurs in terms of actuator heights was determined.

The first method tried was a static ramp test. In this test, the ramp height was preset before the running the wind tunnel, and the tunnel was run with a fixed ramp height. An advantage of this approach is that one eliminates any dynamic or time-transient effects by ramp. One drawback of this approach, however, is that the airflow condition near the simulated isolator un-start point is uncertain. The simulated isolator un-start here means that the back-pressure caused by raising the ramps, creates the shock-train in the test section and causes it to propagate forward out of the test section. For example, compare two cases where the ramp was already raised before the wind tunnel started versus where the ramp was raised after the tunnel was already running. In the first case, the ramp was raised to a 35 degree angle, the tunnel started, and the shock-train appeared in the middle of test section. Next, the ramp was raised by a small increment, e.g., 36 degree angle, the tunnel was started, and one observed that the shock-train propagated all the way upstream. Let's compare this condition to the second case. The tunnel was started and running, the step input of 35 degree angle was introduced, and the shock-train appears in the middle of test section. Next, similarly, the tunnel was started

and running, and then the 36 degree step input was introduced. This time the shock-train stayed in the test section rather than propagated forward. The difference between two cases would be that the first case with the ramp angle of 36 degree choked the tunnel from the very beginning and the second case did not. Therefore, the second case seems to be a correct way to proceed because a stable test environment should be reached before any object is introduced. The second case also allows for airflow to stabilize before the object is introduced.

This issue was more apparent with the Mach 3 nozzle. With Mach 3 air flow, the shock-train was statically stable up to duct height 4 or 5 (10 to 12.5 inches) from the ramp at specific ramp heights. When trying to hold the shock-train beyond 4 or 5 duct heights, the simulated isolator un-started as the tunnel was starting. With Mach 1.8 nozzle, this issue was not a concern because shock-train had its own stable static positions throughout the test section with its corresponding ramp height. In other words, the stable shock-train could be held at any location in the test section, and there appeared no location where the shock-train goes to un-start with Mach 1.8 speed. A longer test section would possibly allow one to find the unstable point for the shock-train.

Ramp input to an actuator: constant increase in height

The next approach was to give the ramp a continuing increase in height after the tunnel started. This method prevents the tunnel from a un-start from the beginning, but would not be a truly static test, rather a quasi-static test. Quasi-static effects will be discussed later in the Analysis and Results.

In order to mitigate the quasi-static effect, the ramp was raised as slow as possible. The slope of the ramp input was determined by the three factors: the height where the shock-train first appear, the height where the shock-train became unstable, and the wind tunnel run time, which is roughly 5 to 6 seconds. Because the heights where the shock-train imminent and un-start conditions occur are different for different Reynolds and Mach numbers, the ramp input (the starting height, slope, and end height) must be adjusted in accordance with each test condition. In this constant-increasing-height test, 9 different test conditions were executed and those conditions are shown in Table 1 below:

Table 1. Constant slope input test conditions

Test No.	Mach number	Reynolds number (1/m)	Actuator command input (See a NOTE below for the unit)
1	1.8	1.280 E07	Starting height: 0 inch / Slope: 0.11 in/sec / end height: 0.22 inch
2	1.8	1.436 E07	Starting height: 0 inch / Slope: 0.11 in/sec / end height: 0.22 inch
3	1.8	1.659 E07	Starting height: 0.04 inch / Slope: 0.072 in/sec / end height: 0.22 inch
4	1.8	1.712 E07	Starting height: 0.05 inch / Slope: 0.072 in/sec / end height: 0.23 inch
5	1.8	1.719 E07	Starting height: 0.04 inch / Slope: 0.072 in/sec / end height: 0.22 inch
6	3	7.8 E06	Starting height: 0.36 inch / Slope: 0.012 in/sec / end height: 0.446 inch
7	3	1.185 E07	Starting height: 0.36 inch / Slope: 0.012 in/sec / end height: 0.5 inch
8	3	1.7 E07	Starting height: 0.37 inch / Slope: 0.012 in/sec / end height: 0.467 inch
9	3	2.3 E07	Starting height: 0.35 inch / Slope: 0.019 in/sec / end height: 0.476 inch

NOTE: The unit of the actuator height is in inches in MTS digital reading. Refer to Appendix E for conversion to other dimensions.

The calculation of Mach and Reynolds numbers are based upon the isentropic relationship and ideal gas law. The equations can be found in Chapter 8 of Anderson's 'Fundamentals of Aerodynamics' book. Total pressure and temperature in this experimental is those at the stagnation chamber. The static pressure is at the test section. The gamma of 1.4 and gas constant of 287 J/kg/K was used.

With the test conditions above, the test results are shown below. In each figure, the vertical axis is the ratio of static pressure over stagnation chamber pressure, and the horizontal axis is the distance from the leading edge of the ramp in inches. The legend in the figures above indicates the actuator height in the MTS reading (raw reading from the MTS software). The bold black * indicates the location of the leading edge of the shock-train from the schlieren video. They are put on the same plot to confirm if a match at the pressure data and visual data.

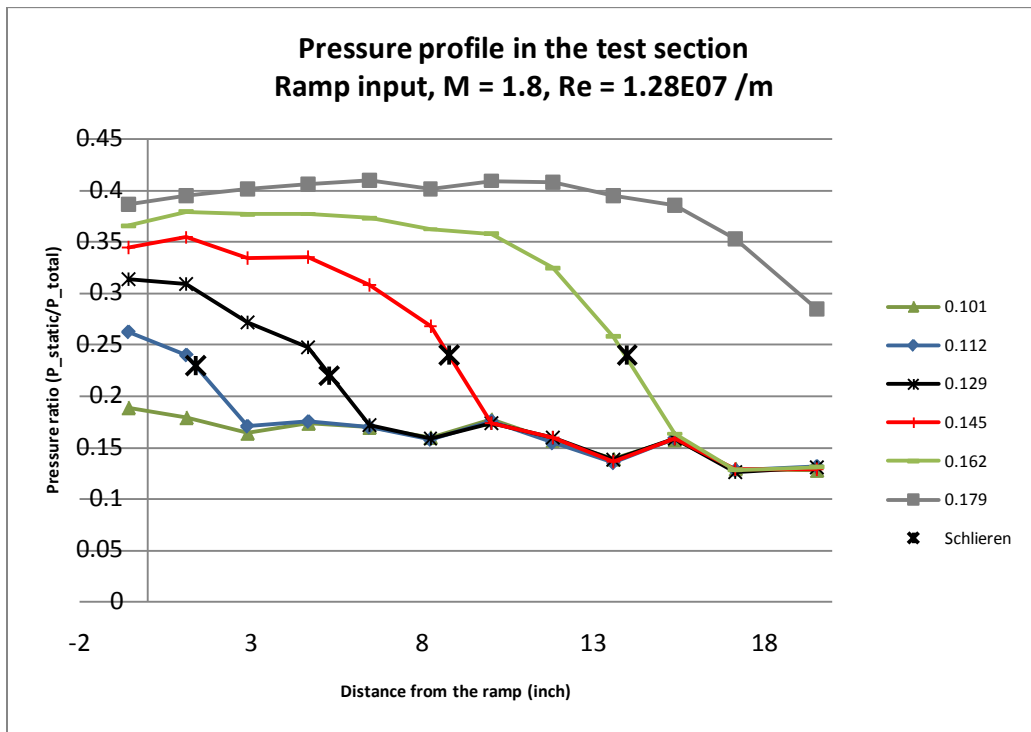


Figure 52. Pressure profile in the test section with ramp input, $M=1.8$, $Re=1.28E07 /m$

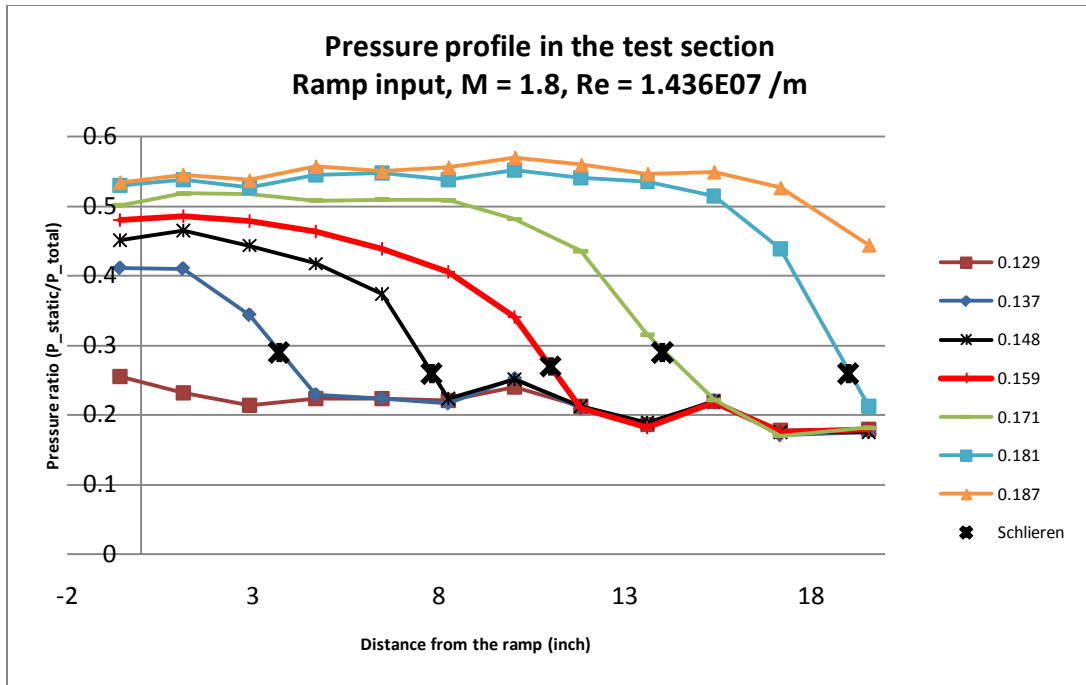


Figure 53. Pressure profile in the test section with ramp input, $M=1.8$, $Re=1.436E07 /m$

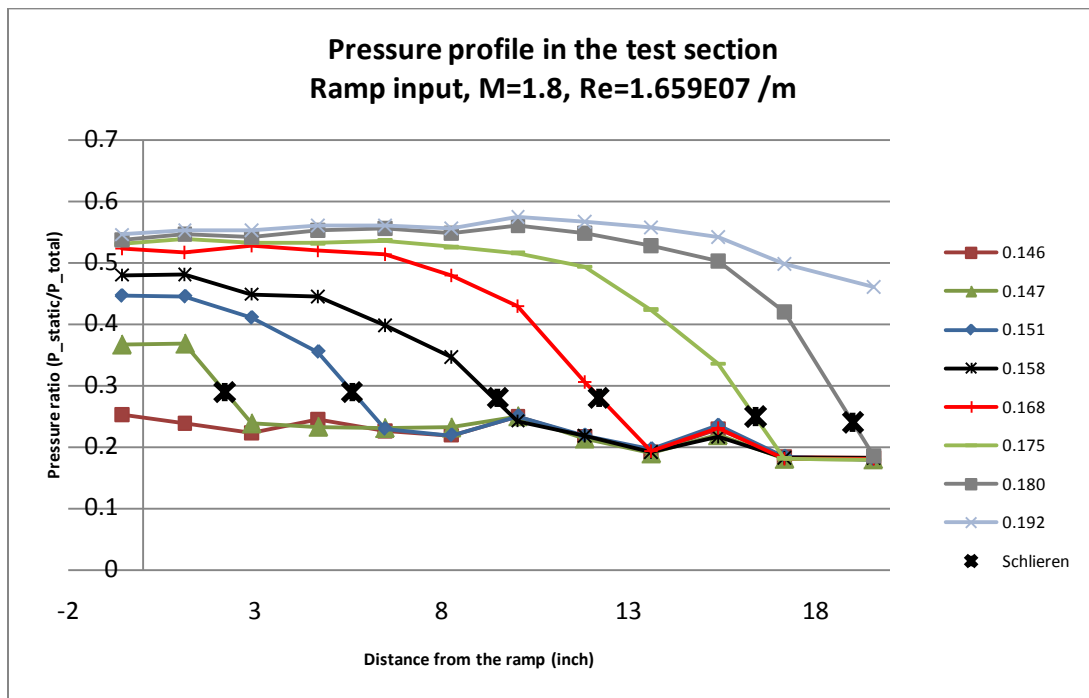


Figure 54. Pressure profile in the test section with ramp input, $M=1.8$, $Re=1.659E07 /m$

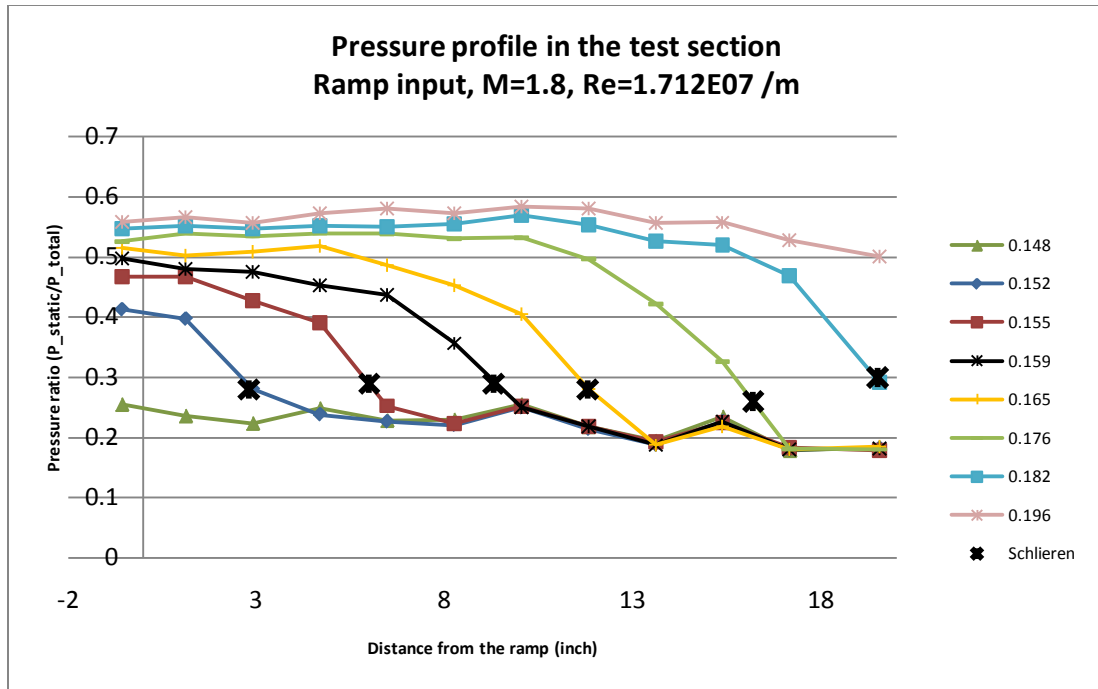


Figure 55. Pressure profile in the test section with ramp input, $M=1.8$, $Re=1.712E07 /m$

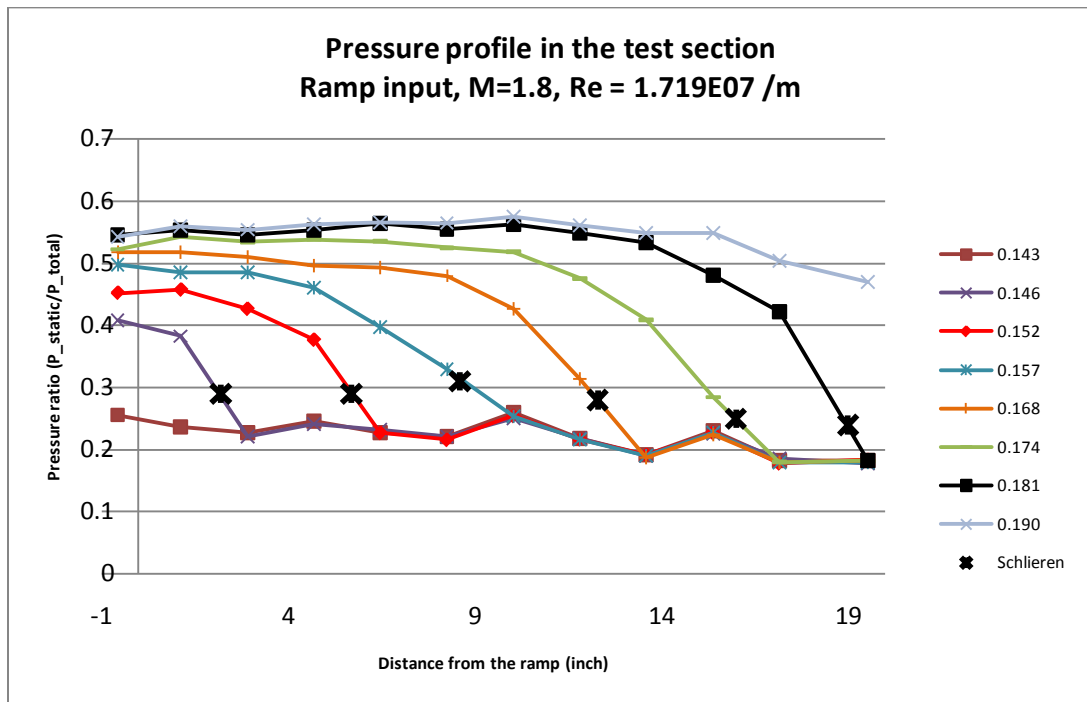


Figure 56. Pressure profile in the test section with ramp input, $M=1.8$, $Re=1.719E07 /m$

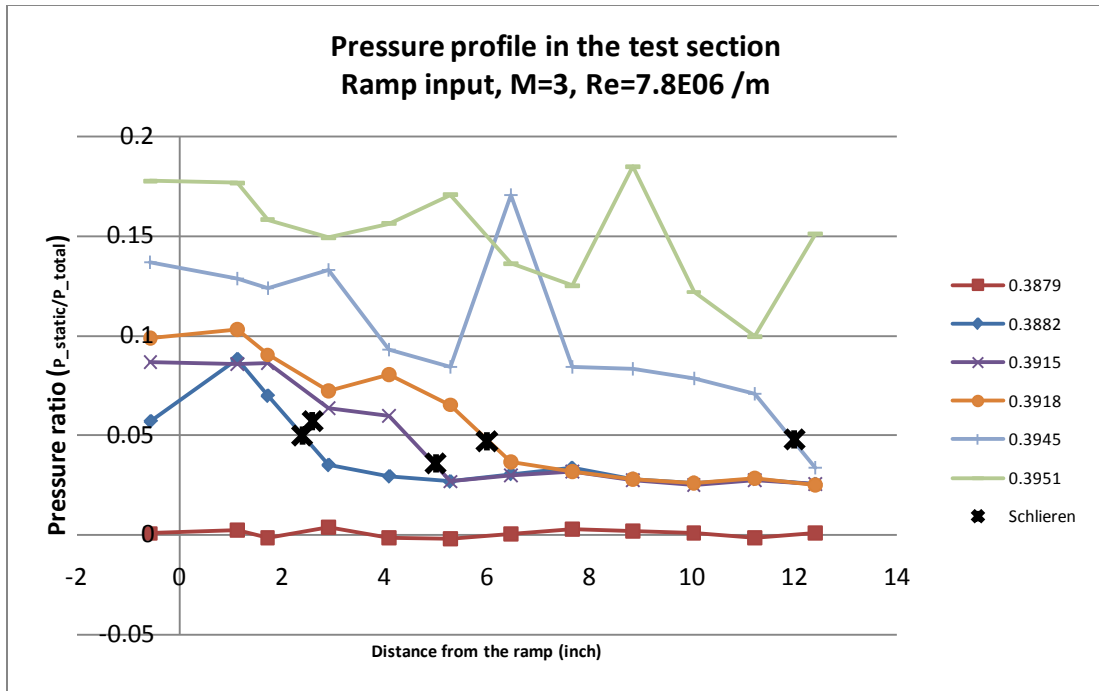


Figure 57. Pressure profile in the test section with ramp input, $M=3$, $Re=7.8E06 /m$

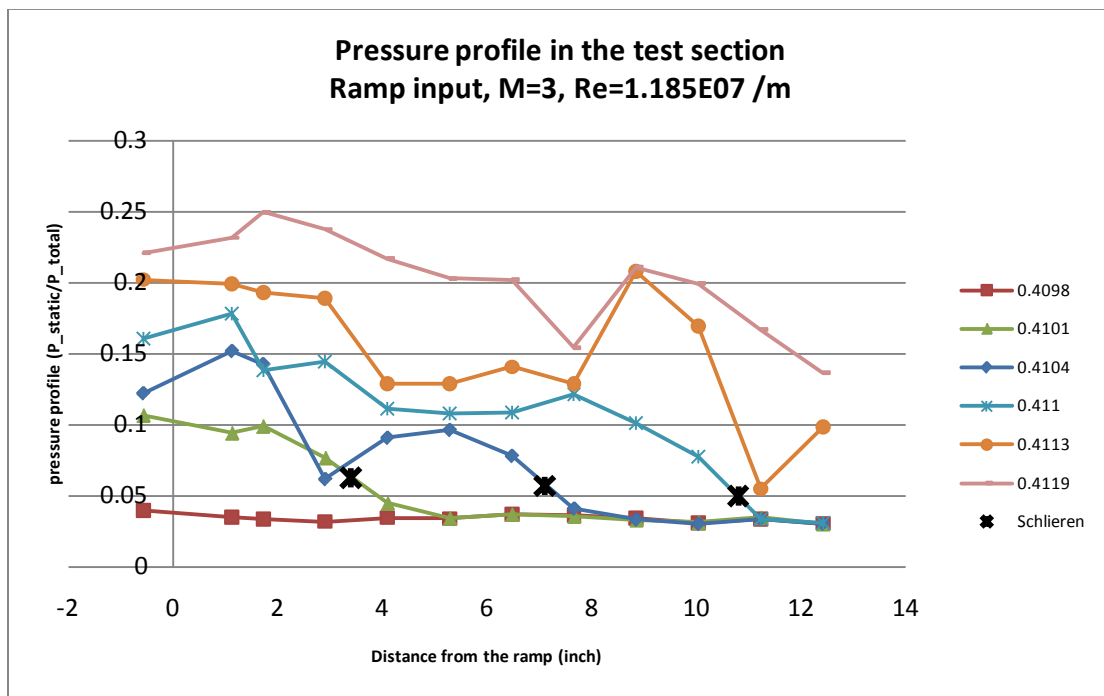


Figure 58. Pressure profile in the test section with ramp input, $M=3$, $Re=1.185E07 /m$

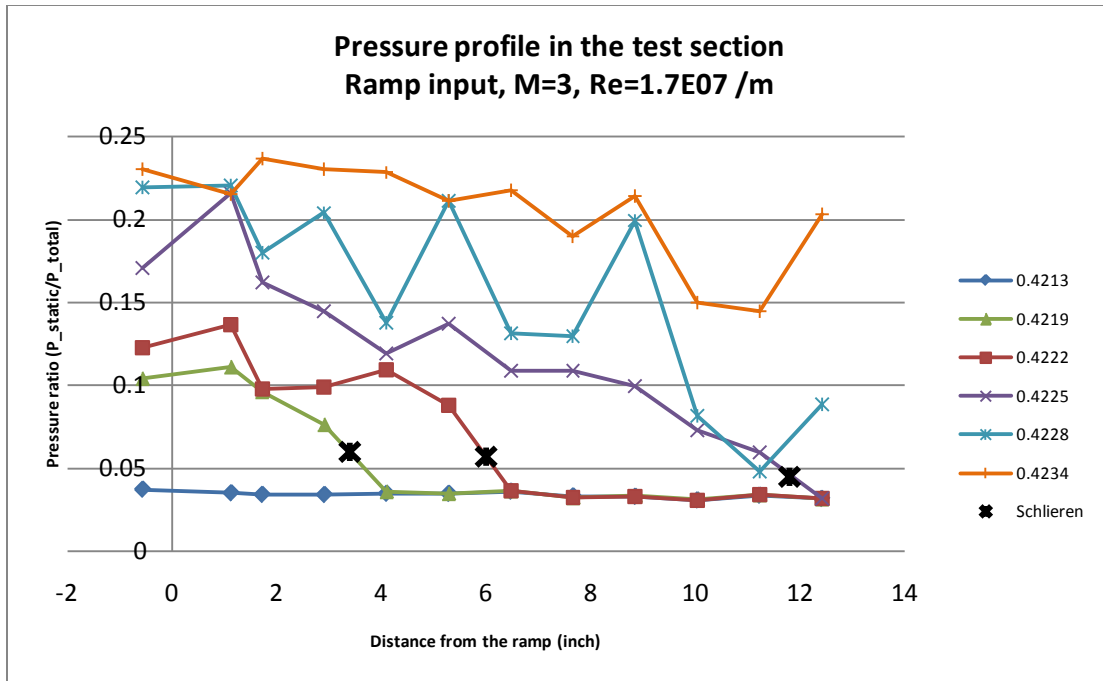


Figure 59. Pressure profile in the test section with ramp input, $M=3$, $Re=1.7E07 /m$

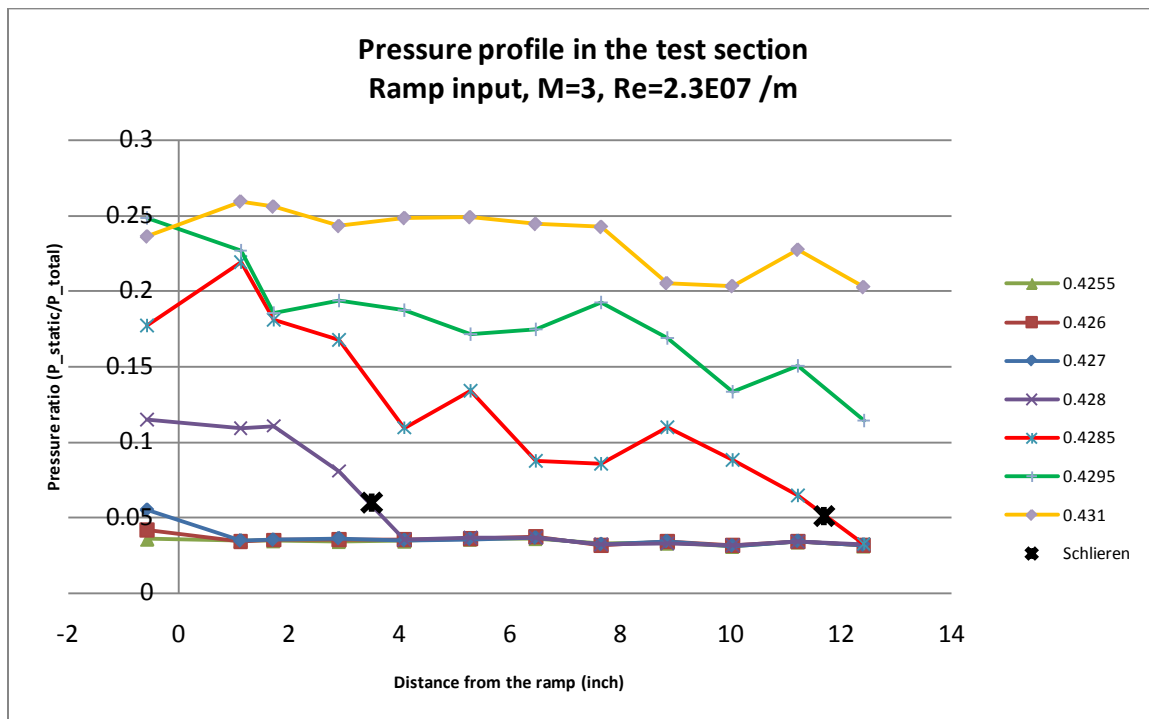


Figure 60. Pressure profile in the test section with ramp input, $M=3$, $Re=2.3E07 /m$

To note, actual data has more lines in the graphs, but a few of them are shown in Figure 52 through Figure 60 to help read the graph easier. Similar to the static test, one notices that the Mach 1.8 incoming flow case had stable shock-train locations with certain ramp heights throughout the test section as seen in the Figure 52 through Figure 56. In Figure 52 through Figure 56, the shock-train moves forward smoothly as the ramp height increases. On the other hand, with Mach 3 incoming flow, the shock-train had only a few stable locations and became unstable beyond a duct height 4 or 5. The shock-train's motion from one stable location to the next was very irregular, sudden, and jumpy. The higher Mach air flow seems to be very noisy or oscillatory and this behavior drives the flow unstable without much effort. From the schlieren video, the shock-train leading edge was oscillating in a flow direction within 0.1 – 0.2 duct heights for Mach 1.8 tests and within 0.2 – 0.4 duct heights for Mach 3 tests.

Schlieren photography in Figure 61 and Figure 62 show the shape of shock-train for two different Mach numbers.

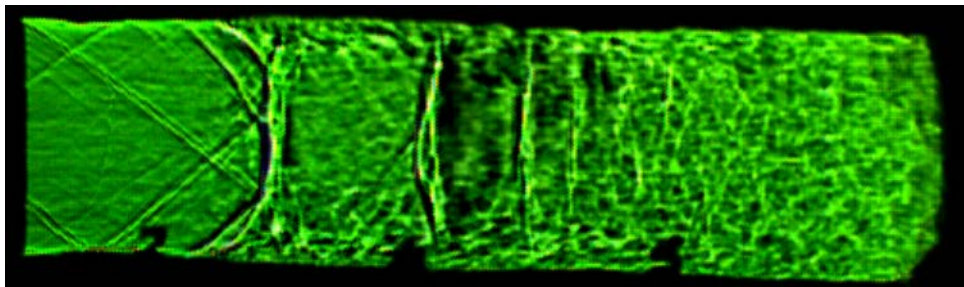


Figure 61. Schlieren photo of shock-train ($M = 1.8$, $Re = 1.712 \text{ E}07 / \text{m}$, upstream is left)

At Mach 1.8, the shock-train in Figure 61 looks like a train of normal or bow shocks. In Figure 61, the numbers along the bottom of the picture indicate the distance from the ramp in terms of a duct height. From the pressure ratio data in Figure 52 through

Figure 56, the Mach number after the shock-train is subsonic. Additionally, from static pressure, it can be noticed that the pressure ratio decreases towards downstream. This is indicative of frictional flow in a constant-area duct preceded by an isentropic nozzle (Fanno flow(26)). Subsonic flow in a constant-area duct preceded by an isentropic nozzle tends to speed up until it reaches sonic speed. The Mach number at the downstream end can be calculated using isentropic relationships with the stagnation pressure and temperature. In this test condition, the Mach number where the back-pressure sensor is located is calculated to be Mach 0.958.

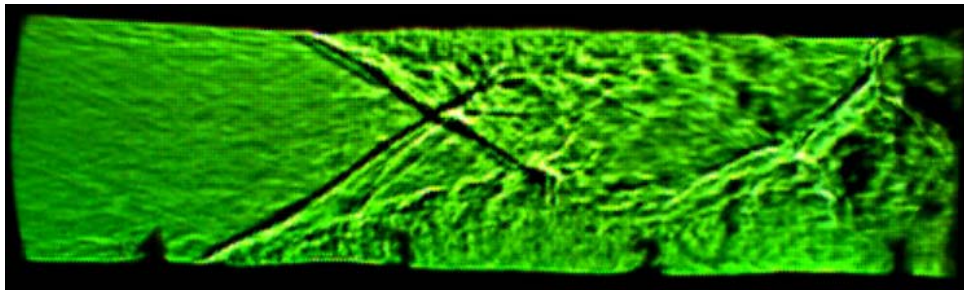


Figure 62. Schlieren photo of shock-train ($M = 3$, $Re = 1.7 \text{ E}07 \text{ /m}$, upstream is left)

Mach 3 flow in Figure 62 creates a shock-train with shallow angles, more like oblique shocks created by a wedge. Across each oblique shock, the Mach number drops and static pressure increases. The pressure ratio profiles in Figure 57 thru Figure 60 indicate that the air flow behind the shock-train is still supersonic and the pressure ratio increases towards the downstream. Again, this indicates Fanno flow behavior. The supersonic flow in a constant-area duct preceded by an isentropic nozzle tends to slow down until it reaches sonic speed.(26)

With Mach 1.8 incoming flow, the shock-train starts appearing at a smaller angle of the ramp; and with Mach 3 incoming flow, the shock-train starts appearing at a higher ramp angle. The detailed numerical values are tabulated below:

Table 2. Actuator height and % flow area at shock-train imminent and un-start

Test No.	Mach #	Reynold's number	MTS reading			Equivalent % flow area		
			Shock-train imminent	un-start	Δh	Shock-train imminent	un-start	$\Delta\%A$
1	1.8	1.280 E07	0.104	0.181	0.077	95.99	92.34	3.65
2	1.8	1.436 E07	0.131	0.187	0.056	94.78	92.02	2.76
3	1.8	1.659 E07	0.147	0.190	0.043	94.03	91.87	2.16
4	1.8	1.712 E07	0.149	0.192	0.043	93.93	91.76	2.17
5	1.8	1.719 E07	0.146	0.187	0.041	94.08	92.02	2.06
6	3	7.8 E06	0.387	0.395	0.008	78.98	78.35	0.63
7	3	1.185 E07	0.410	0.412	0.002	77.17	77.01	0.16
8	3	1.7 E07	0.422	0.424	0.002	76.21	76.05	0.16
9	3	2.3 E07	0.427	0.429	0.002	75.81	75.64	0.17

As shown in Table 2, at a lower Mach number, a shock-train starts at a smaller ramp angle and the height range from the shock-train imminent position to the un-start position is between 0.033 and 0.077 inches (in MTS reading). At a higher Mach number, the ramp has to be raised higher to start the shock-train and the range of the actuator height is only a few thousandths of an inch (in MTS reading). The shock-train is definitely more sensitive to the ramp angle (or back-pressure) in Mach 3 flow than in Mach 1.8 flow. In other words, small increases in the ramp angle can un-start the air flow at a higher Mach number.

Additionally, the Reynolds number plays a significant role here. At both high and low Mach flow, as the Reynolds number increases, the shock-train imminent position and the un-start position occurs at a higher ramp angle. Also, as the Reynolds number increases, the range of the actuator height from the shock-train imminent position to the un-start position decreases. The shock-train becomes more responsive to the ramp motion at the higher Reynolds number. See the Reynolds number effect section for more detail.

From Figure 52 to Figure 60, it might be interesting to look at the two farthest upstream sensors to find whether there is any precursor of a un-start. The graphs are drawn with the back-pressure ratio versus the pressure ratio from two farthest upstream pressure sensors and they are shown below.

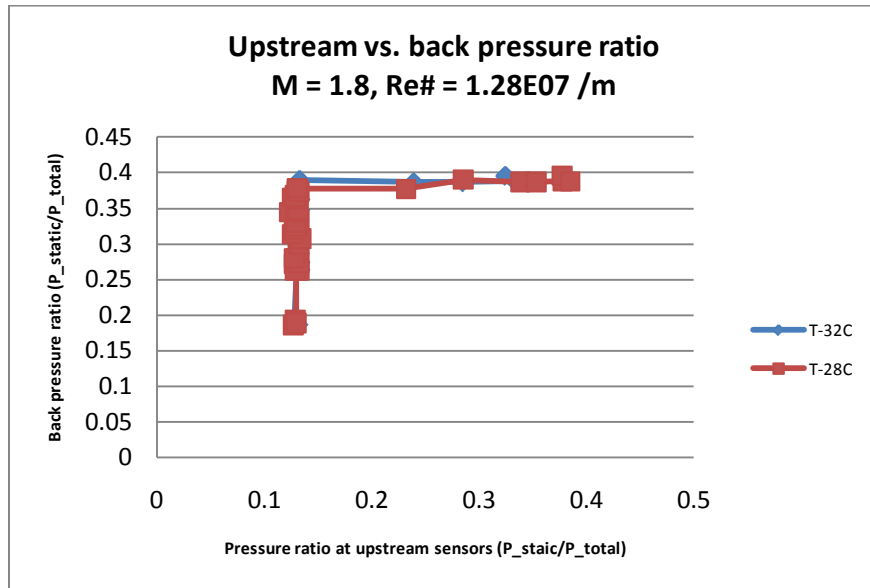


Figure 63. Upstream versus back-pressure ratio ($M=1.8$, $Re\# = 1.28E07 / m$)

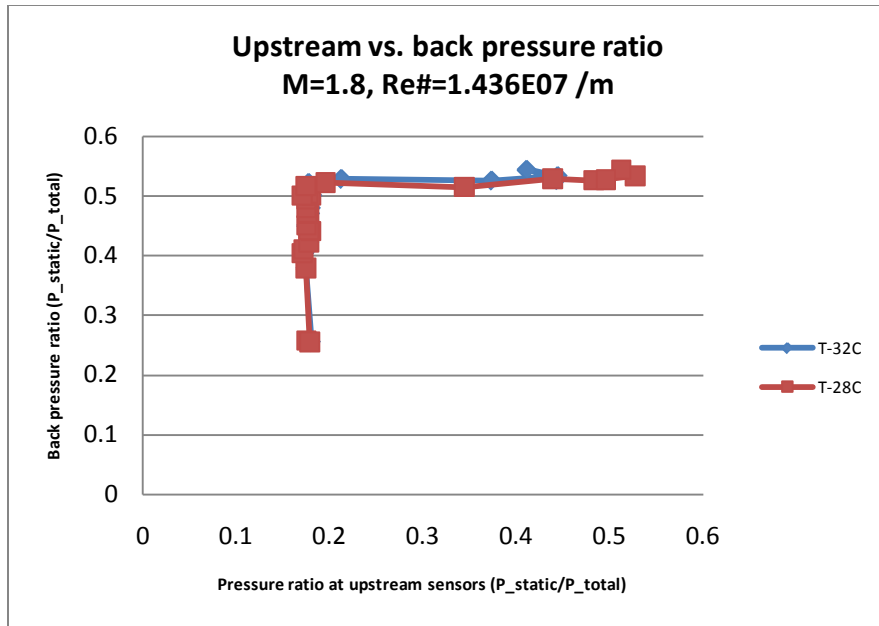


Figure 64. Upstream versus back-pressure ratio ($M=1.8$, $Re\# = 1.436E07 /m$)

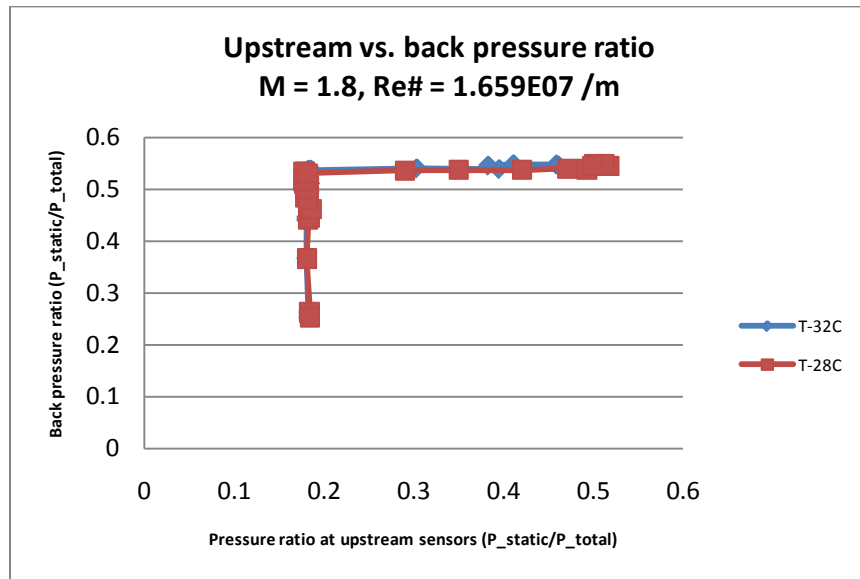


Figure 65. Upstream versus back-pressure ratio ($M=1.8$, $Re\# = 1.659E07 /m$)

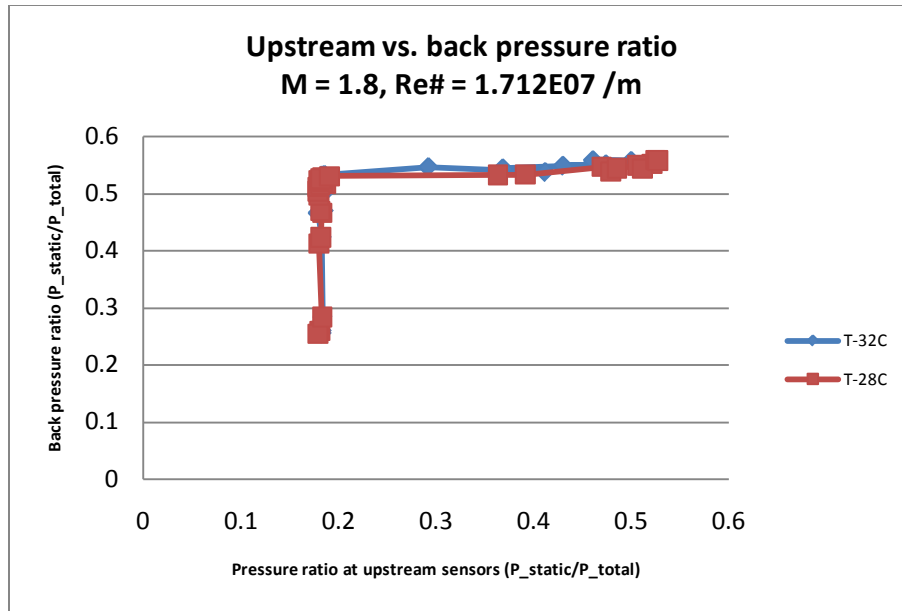


Figure 66. Upstream versus back-pressure ratio ($M=1.8$, $Re\# = 1.712E07 /m$)

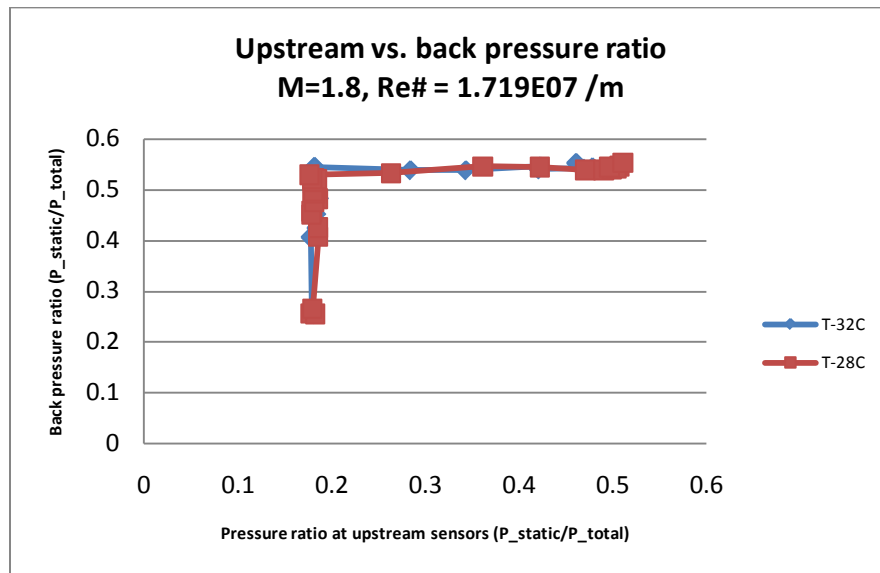


Figure 67. Upstream versus back-pressure ratio ($M=1.8$, $Re\# = 1.719E07 /m$)

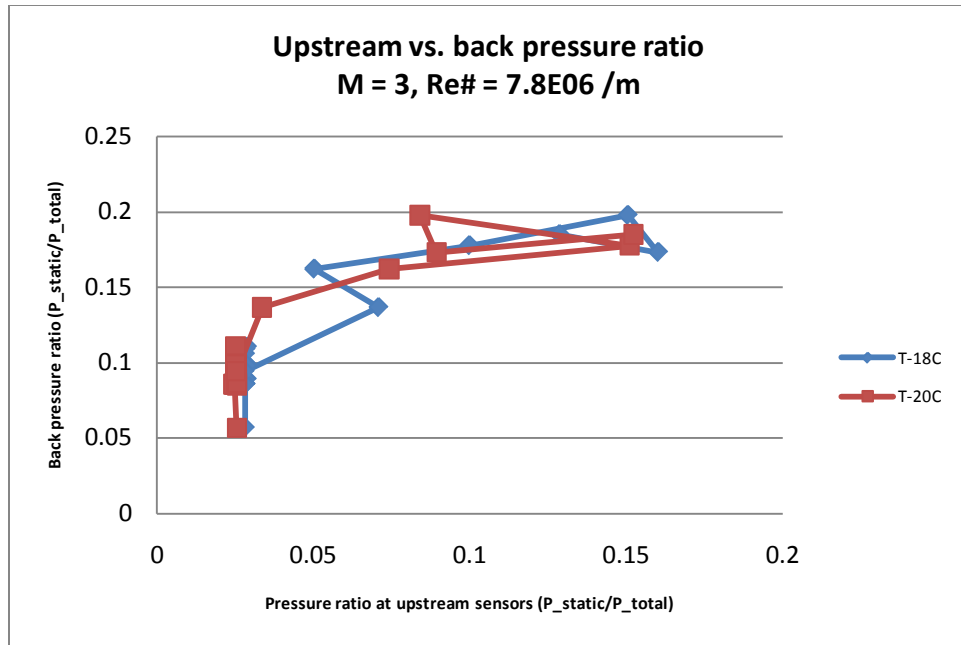


Figure 68. Upstream versus back-pressure ratio (M=3, Re# = 7.8E06 /m)

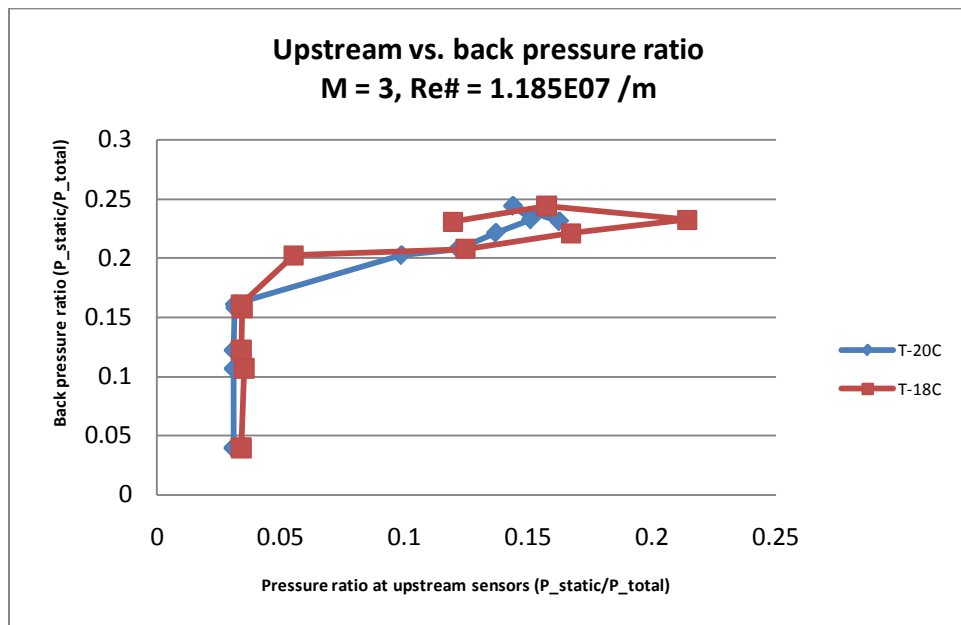


Figure 69. Upstream versus back-pressure ratio (M=3, Re# = 1.185E07 /m)

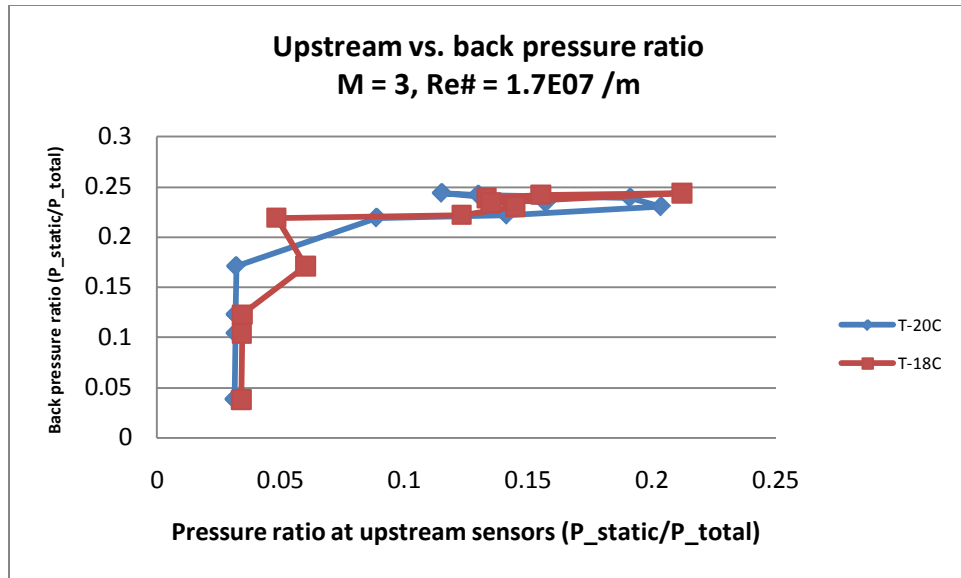


Figure 70. Upstream versus back-pressure ratio ($M=3$, $Re\# = 1.7E07 /m$)

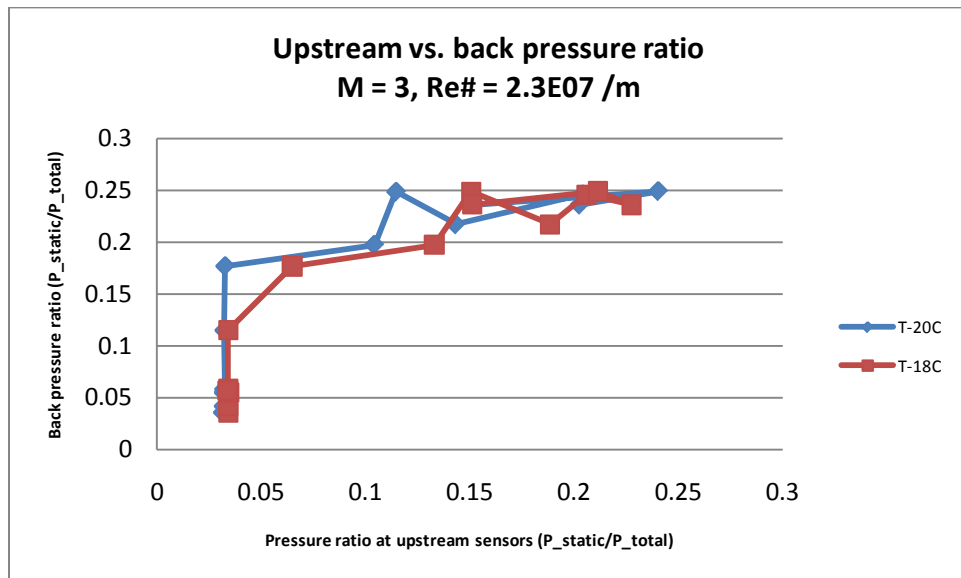


Figure 71. Upstream versus back-pressure ratio ($M=3$, $Re\# = 2.3E07 /m$)

In a legend, for example, ‘T-32C’ means that the sensor is located on a top plate, 32nd sensor hole from the ramp along a center line. In Figure 63 through Figure 67, Mach 1.8 air flow shows that the two far upstream sensors show sudden pressure rise when un-

start occurs. These two relationships do not seem to be a good method to use as precursor of a un-start. From Figure 68 to Figure 71, Mach 3 air flow shows some oscillatory behavior at two far upstream sensors near the un-start point. The oscillation in pressure reading is due to the oscillation of the shock-train leading edge in a flow direction. The two far upstream sensors in Mach 3 flow seems ok to be used as early warning indicators, however, one thousandths movement of an actuator make the shock-train go from start to un-start in a very short time. Again, this method does not work in Mach 1.8 cases.

Hysteresis examination

The next question was of hysteresis behavior. To determine hysteresis, a triangle voltage was input to the actuator, i.e., increasing ramp angle and followed by decreasing ramp angle. Because each test condition has different ramp heights where the un-start occurs and a different range of the actuator height from the shock imminent position to the un-start position, the triangle input was adjusted according to the test condition. The test conditions and the triangle inputs are shown below.

Table 3. Test conditions for hysteresis experiments

			Triangle input			
Test No.	Mach #	Reynolds # (/m)	Freq (Hz)	Phase Offset (deg)	Amplitude (MTS reading)	Offset (MTS reading)
1	1.8	1.196E07	0.25	250	0.11	0.11
2	1.8	1.365E07	0.25	250	0.11	0.11
3	1.8	1.568E07	0.2	270	0.09	0.13
4	1.8	1.619E07	0.2	270	0.09	0.14
5	1.8	1.621E07	0.2	270	0.09	0.13
6	3	7.15E06	0.2	270	0.045	0.38
7	3	8.95E06	0.2	270	0.04	0.39
8	3	1.419E07	0.2	270	0.04	0.4
9	3	1.895E07	0.2	270	0.05	0.4
10	3	2.212E07	0.2	270	0.05	0.4

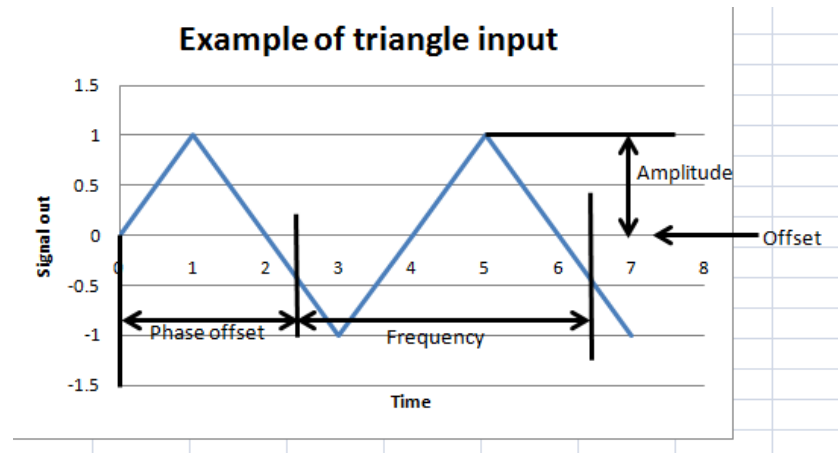


Figure 72. Triangle input explanation

In Table 3, the frequency means the $1/(\text{period time})$, the phase offset is where the triangle input starts, the amplitude means the peak value, and the offset means the center of the triangle input as shown in Figure 72.

The results are shown below. The x-axis is the run time and the y-axis is the pressure ratio for three sensors (downstream, upstream, and back-pressure sensors). Also, the y-axis is shared with the actuator height in inches (MTS reading). As the ramp rises, the green graph (back-pressure) responds first, and then the downstream sensors see that the shock-train is imminent. As the ramp increases, the upstream sensor sees a shock-train propagating forward and pressure reading peaks. As the ramp lowers (purple graph), the upstream sensor sees the shock-train moving back. Then, the downstream and back-pressure sensors see that the shock-train is near the ramps and disappears.

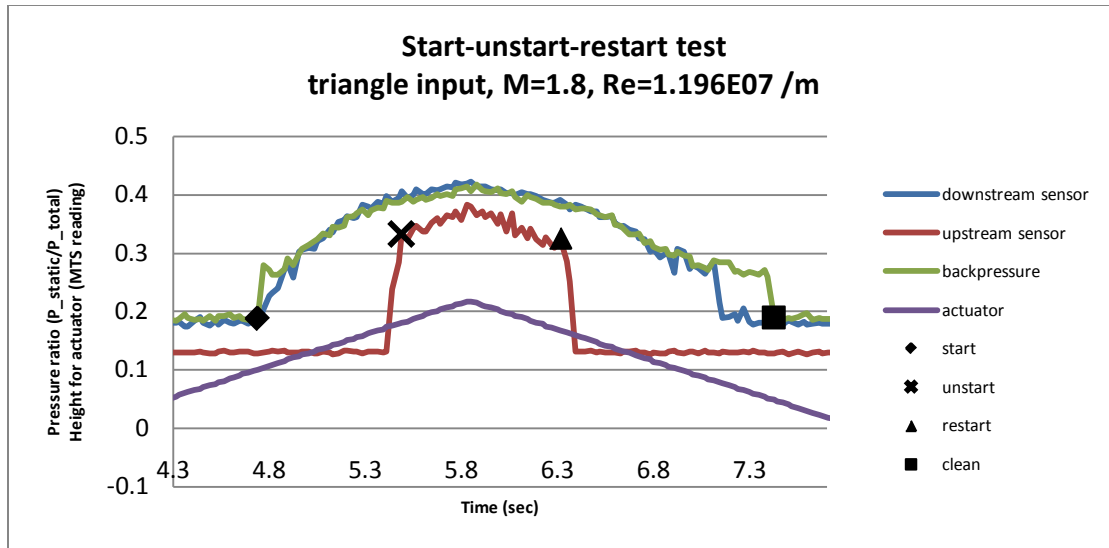


Figure 73. Shock-train start/un-start/restart/clean behavior in response to triangle input
($M=1.8$, $Re=1.196E07$ /m)

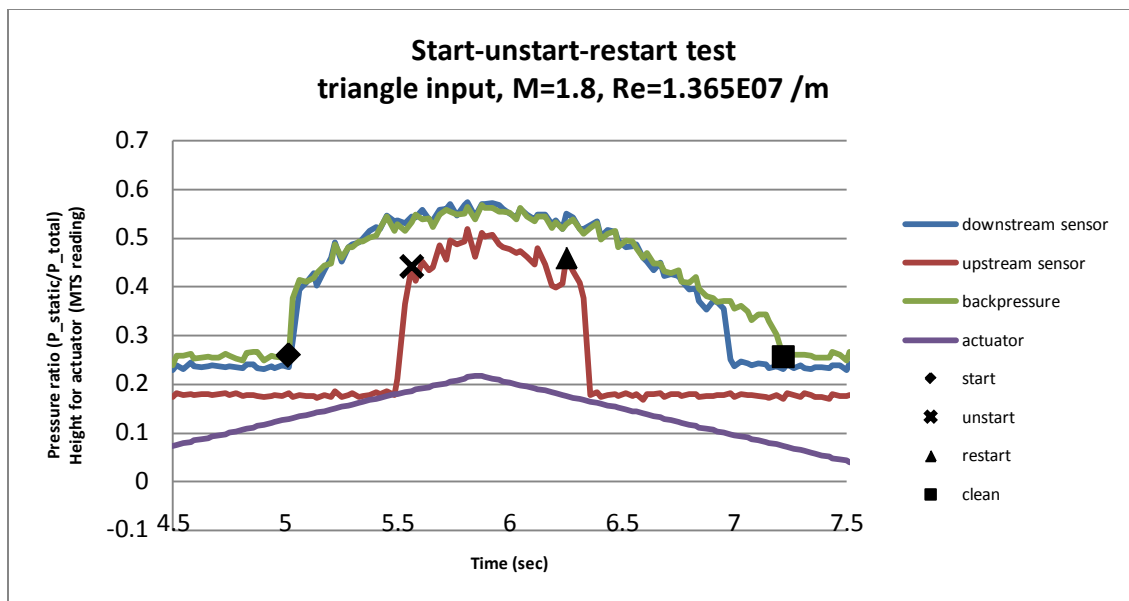


Figure 74. Shock-train start/un-start/restart/clean behavior in response to triangle input
($M=1.8$, $Re=1.365E07$ /m)

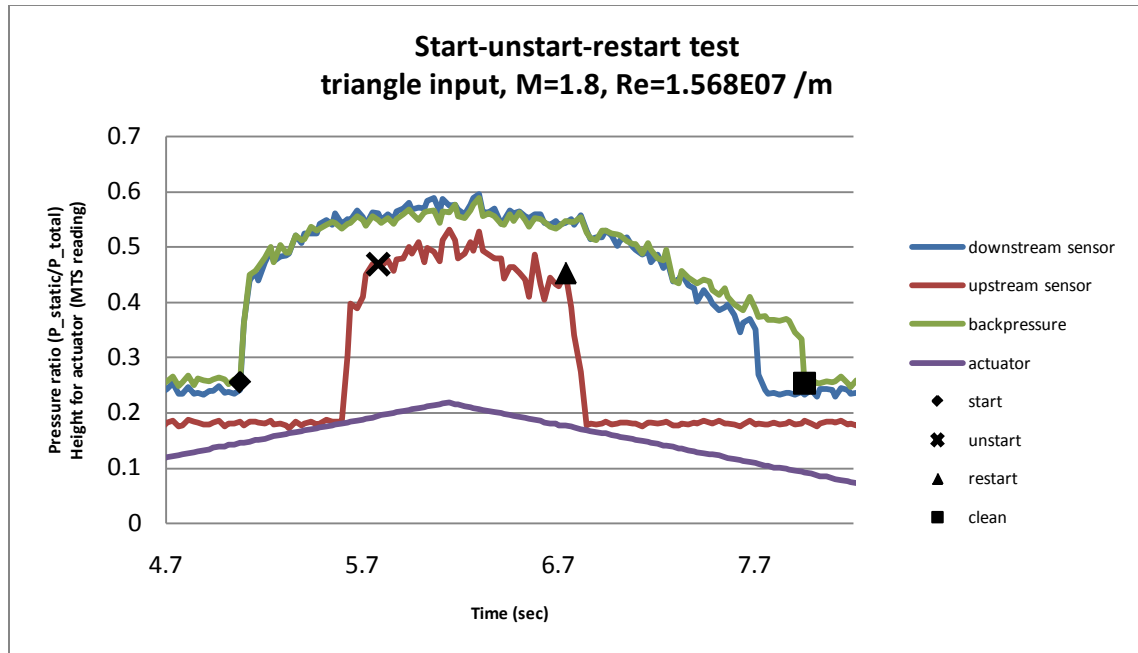


Figure 75. Shock-train start/un-start/restart/clean behavior in response to triangle input
($M=1.8$, $Re=1.568E07$ /m)

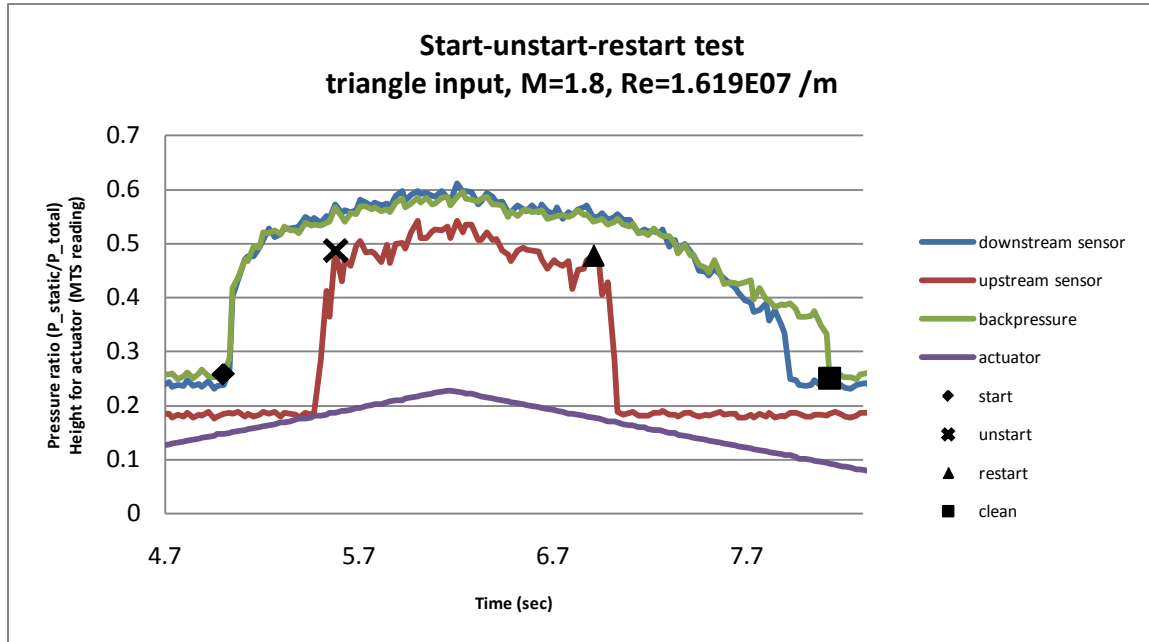


Figure 76. Shock-train start/un-start/restart/clean behavior in response to triangle input
($M=1.8$, $Re=1.619E07$ /m)

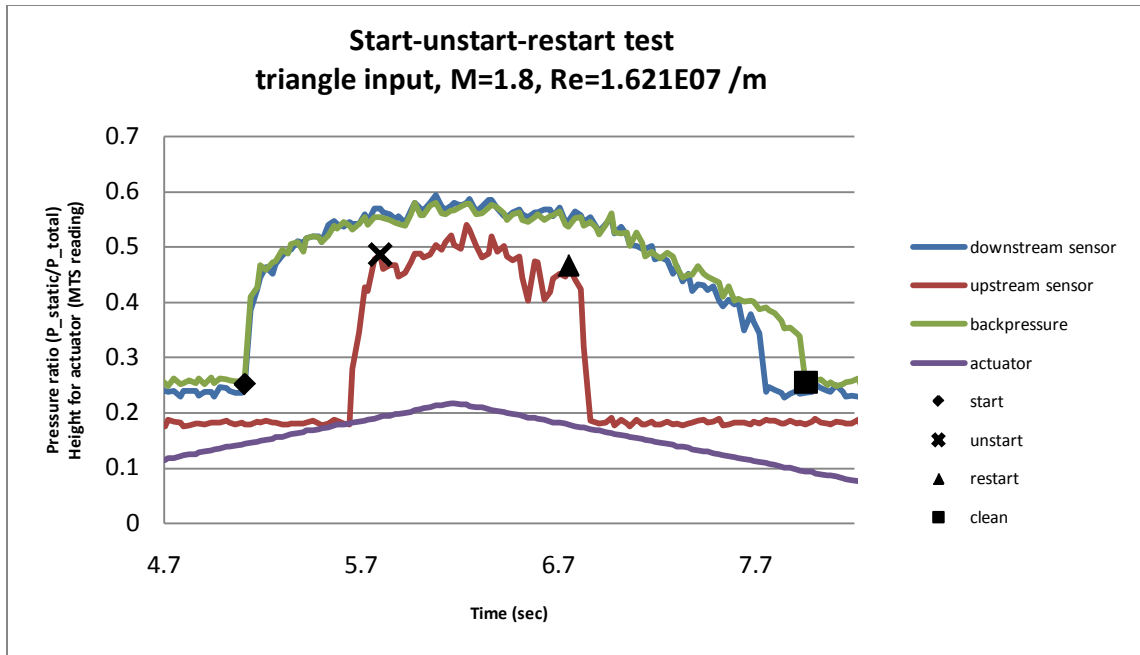


Figure 77. Shock-train start/un-start/restart/clean behavior in response to triangle input
($M=1.8$, $Re=1.621E07$ /m)

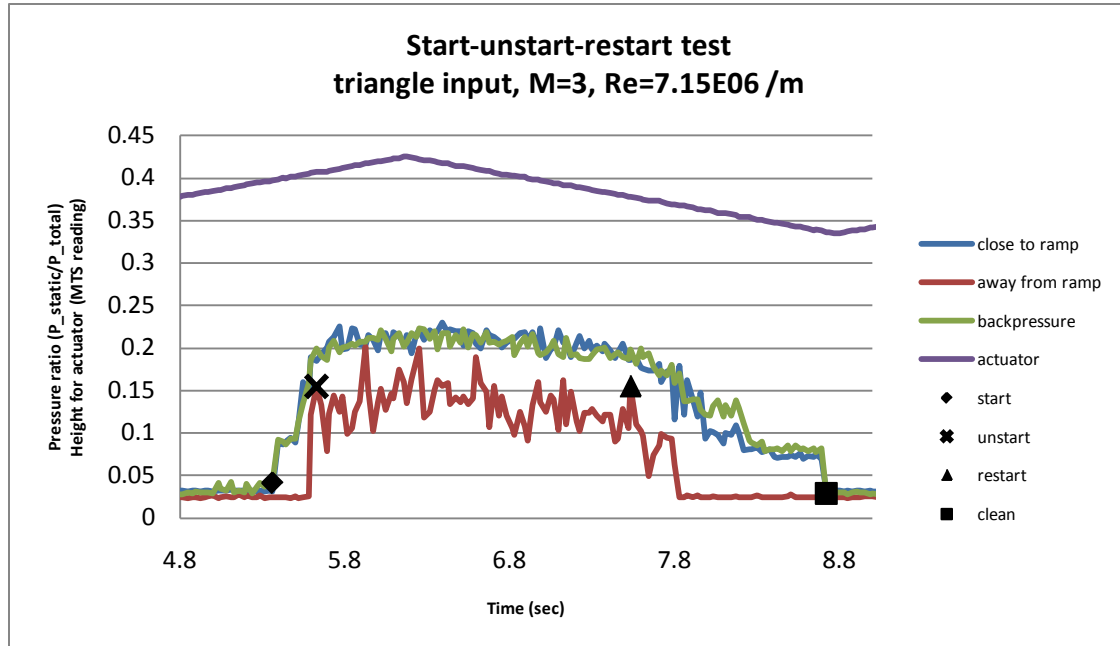


Figure 78. Shock-train start/un-start/restart/clean behavior in response to triangle input
($M=3$, $Re=7.15E06$ /m)

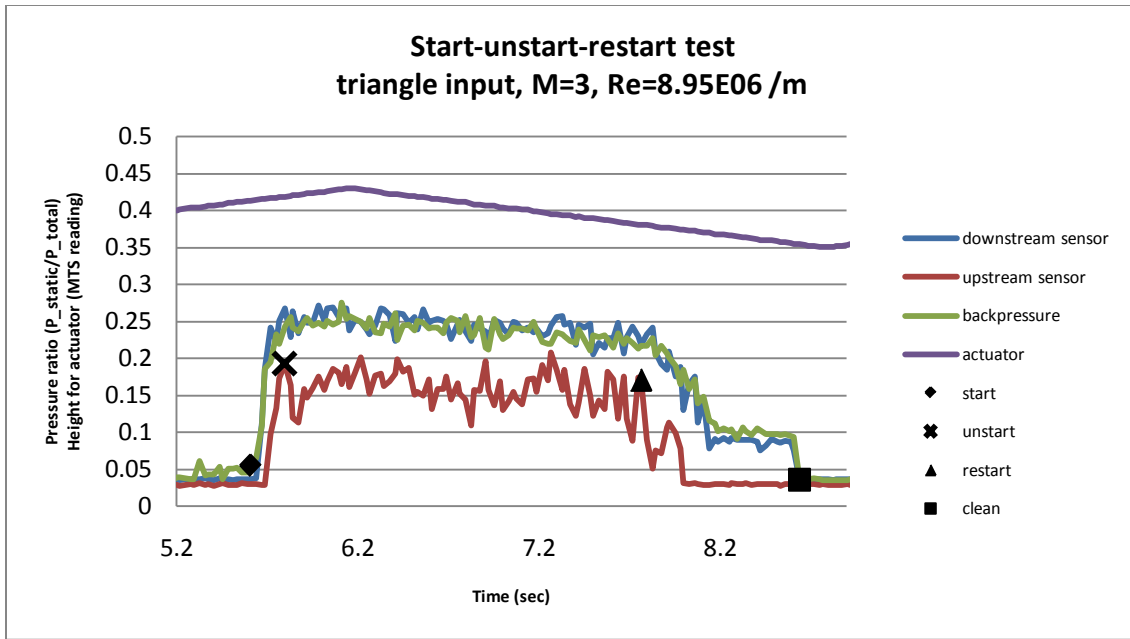


Figure 79. Shock-train start/un-start/restart/clean behavior in response to triangle input
($M=3$, $Re=8.95E06$ /m)

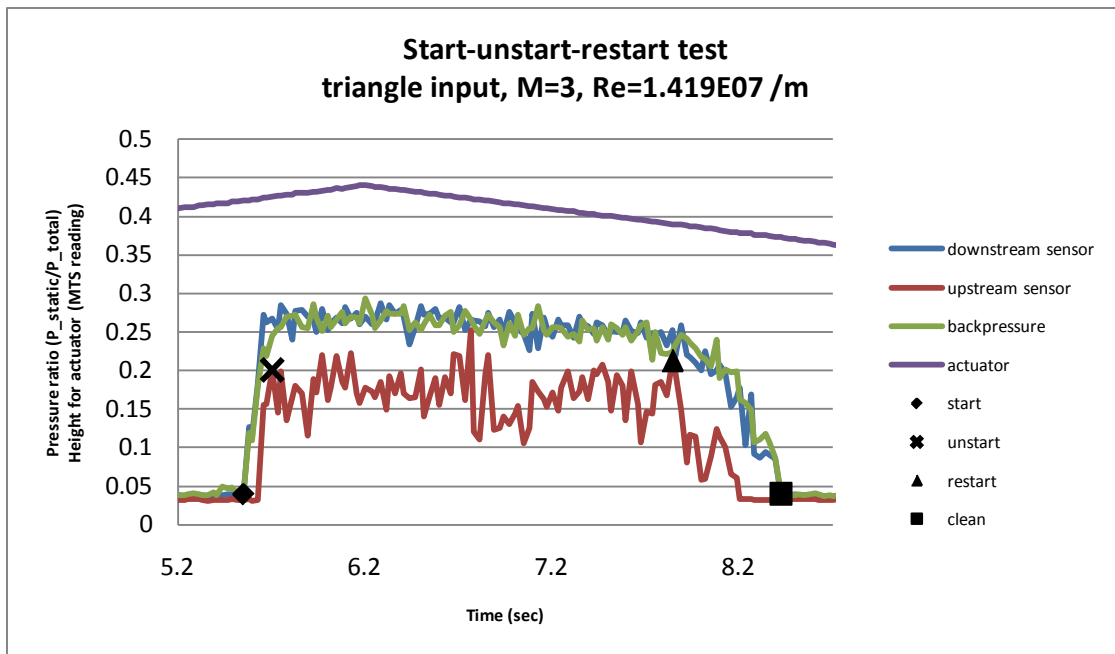


Figure 80. Shock-train start/un-start/restart/clean behavior in response to triangle input
($M=3$, $Re=1.419E07$ /m)

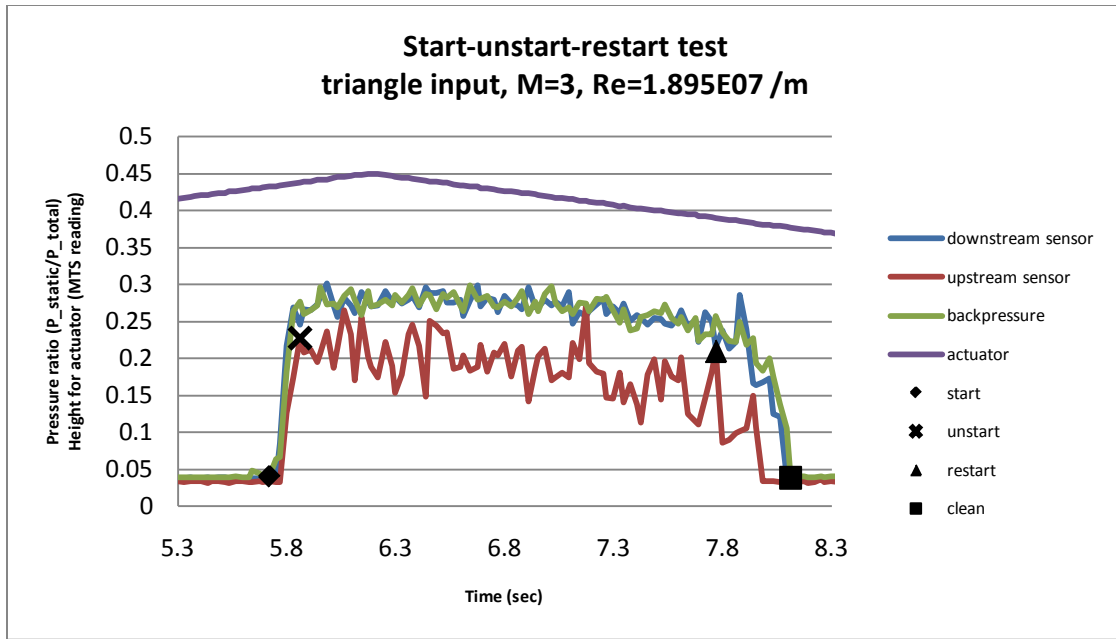


Figure 81. Shock-train start/un-start/restart/clean behavior in response to triangle input
($M=3$, $Re=1.895E07 /m$)

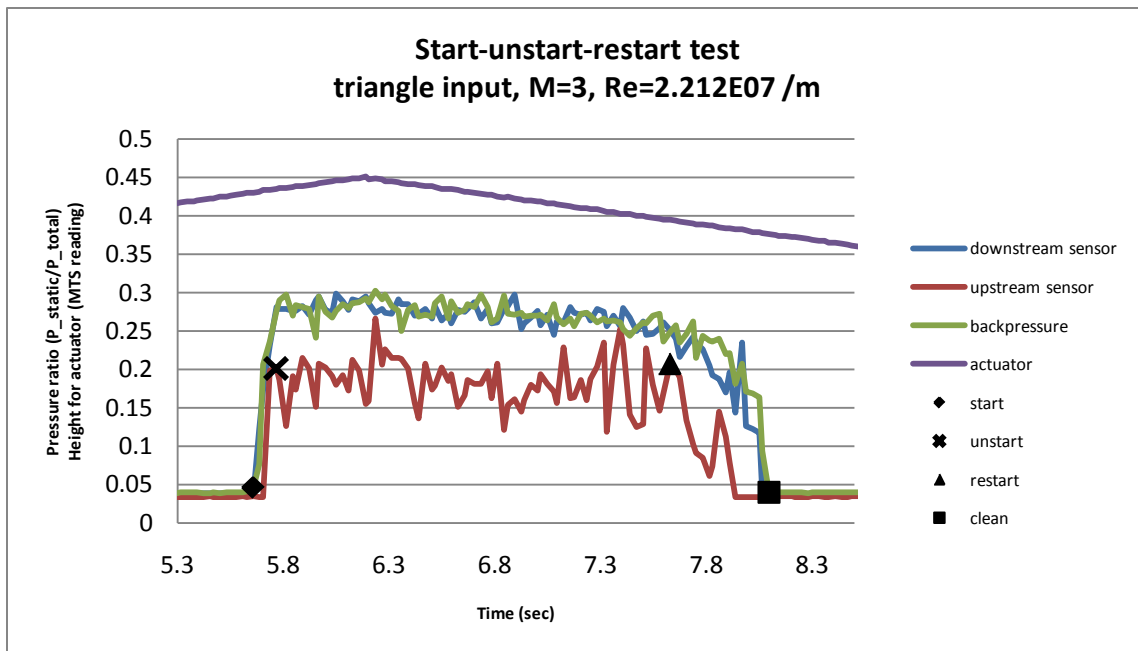


Figure 82. Shock-train start/un-start/restart/clean behavior in response to triangle input
($M=3$, $Re=2.212E07 /m$)

A speed of a triangle input signal to the actuator was slower for Mach 3 tests because it took only a few thousandths of inches of actuator height from a shock-train imminent to a un-start position. Going slowly from a shock-train imminent to a un-start was desired. This explains why the time difference from a un-start to restart position was longer in Mach 3 tests.

For the Mach 1.8 tests, the downstream sensor was placed at 1.1281 inches upstream of the leading edge of the ramp and the upstream sensor was placed at 19.5421 inches from the leading edge of the ramp, the furthest location where a sensor can be physically located.

For Mach 3 tests, the downstream sensor was placed at 1.1281 inches upstream of the leading edge of the ramp. The upstream sensor was placed at 12.4141 inches (approximately 5 duct heights) from the leading edge of the ramp since the un-start occurs when the shock-train reaches around 4 or 5 duct height for Mach 3 case. For both the Mach 1.8 and 3 cases, the back-pressure sensor is located on the side wall between the ramps (0.5636 inches downstream from the leading edge of the ramp).

From the Figure 78 thru Figure 82 above, the pressure data in Mach 3 flow was more noisy or oscillatory compared to the Mach 1.8 cases. This oscillatory behavior also can be observed in the schlieren video.

As can be seen in the Figure 73 and Figure 82, the un-start ramp heights are not the same as the restart ramp heights. The black X indicates where un-start occurred, and the black triangle indicates where restart occurred. At those points, the reading from the actuator (triangle shape graph) shows that the un-start height is slightly higher than the restart height. Similarly, the points where the shock-train starts (diamond mark) and

where it goes back to shock free (square mark) are not the same height, i.e., the shock-train starting point is higher than the clean (or shock free) point. This phenomenon can be observed in all the graphs above. So, there is a hysteresis in this shock-train behavior. The numerical values of the actuator height are shown in the Table 4 below.

Table 4. Start/un-start/restart/clean height summary

Test No.	Mach #	Reynolds # (/m)	Actuator Height (MTS reading)				ΔH (MTS reading)			
			start	un-start	restart	clean	start - un-start	un-start - restart	restart - clean	clean - start
1	1.8	1.196E+07	0.101	0.181	0.168	0.049	0.08	0.013	0.119	0.052
2	1.8	1.365E+07	0.129	0.187	0.175	0.073	0.058	0.012	0.102	0.056
3	1.8	1.568E+07	0.146	0.194	0.177	0.092	0.048	0.017	0.085	0.054
4	1.8	1.619E+07	0.148	0.187	0.178	0.093	0.039	0.009	0.085	0.055
5	1.8	1.621E+07	0.145	0.192	0.178	0.095	0.047	0.014	0.083	0.05
6	3	7.150E+06	0.397	0.407	0.378	0.337	0.01	0.029	0.041	0.06
7	3	8.950E+06	0.413	0.419	0.381	0.355	0.006	0.038	0.026	0.058
8	3	1.419E+07	0.42	0.425	0.39	0.373	0.005	0.035	0.017	0.047
9	3	1.895E+07	0.433	0.438	0.39	0.377	0.005	0.048	0.013	0.056
10	3	2.212E+07	0.431	0.435	0.395	0.377	0.004	0.04	0.018	0.054

From the numerical results, a small height change will cause the flow to go from start to un-start. But when it goes back from restart to clean, a significant change in height of the actuator is required.

In Figure 78 and Figure 79, the back-pressure oscillates a little before the shock-train initiates. The common parameter among those two test conditions is the low Reynolds number, i.e., below 10^7 /m. Nonetheless, the upstream pressure readings do not show any un-start precursor. For example, let's look at only the upstream pressure readings from Figure 76 and Figure 82. The following graphs show the zoomed-in view of the upstream pressure reading prior to the un-start.

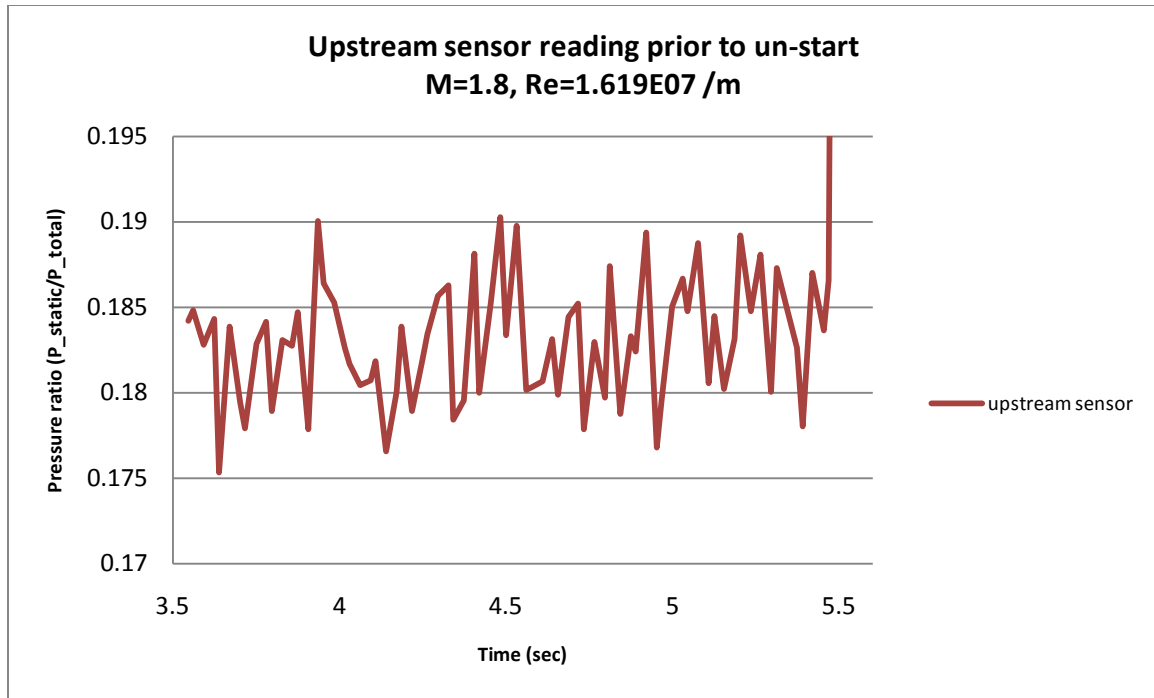


Figure 83. Upstream pressure reading prior to un-start ($M = 1.8$, $Re\# = 1.619E07 /m$)

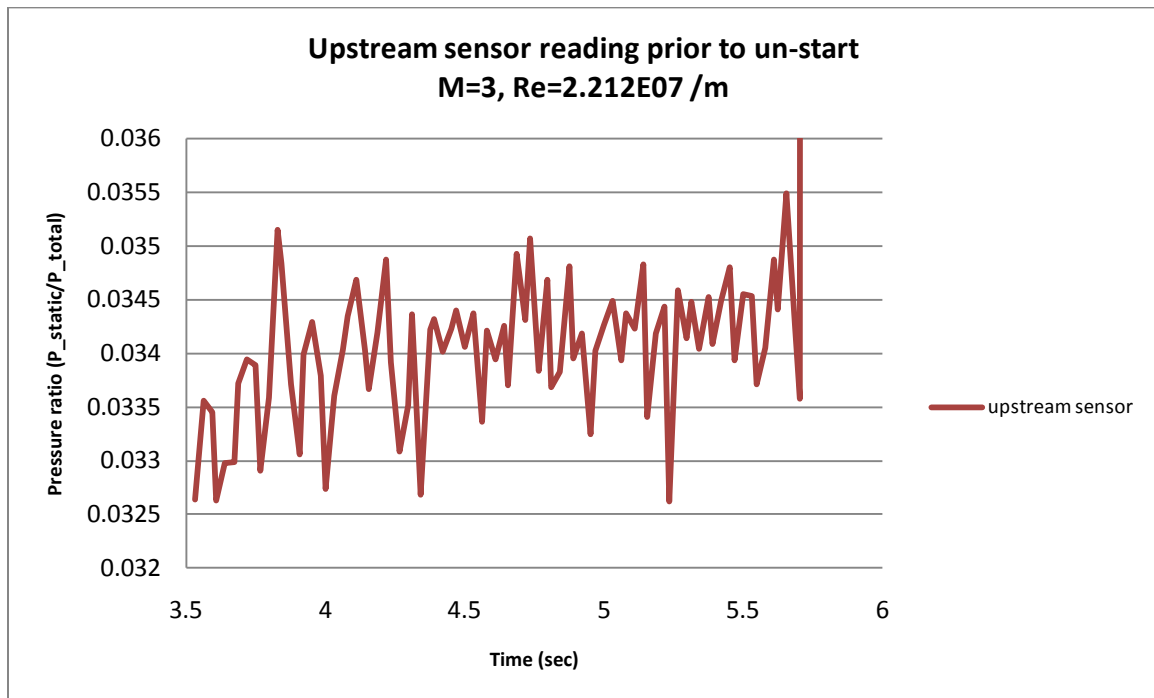


Figure 84. Upstream pressure reading prior to un-start ($M = 3$, $Re\# = 2.212E07 /m$)

As shown in Figure 83 and Figure 84, the upstream pressure readings do not show any energy content changes prior to the un-start. As far as the frequency content changes are concerned, more jagged lines can be observed from Figure 84 prior to the un-start. But, the data sampling rate was limited to a low number, so it is hard to determine the precursor of un-start from this data.

Figure 85 shows the back-pressure ratio (P_{BP}/P_{TOTAL}) versus the actuator height in MTS reading.

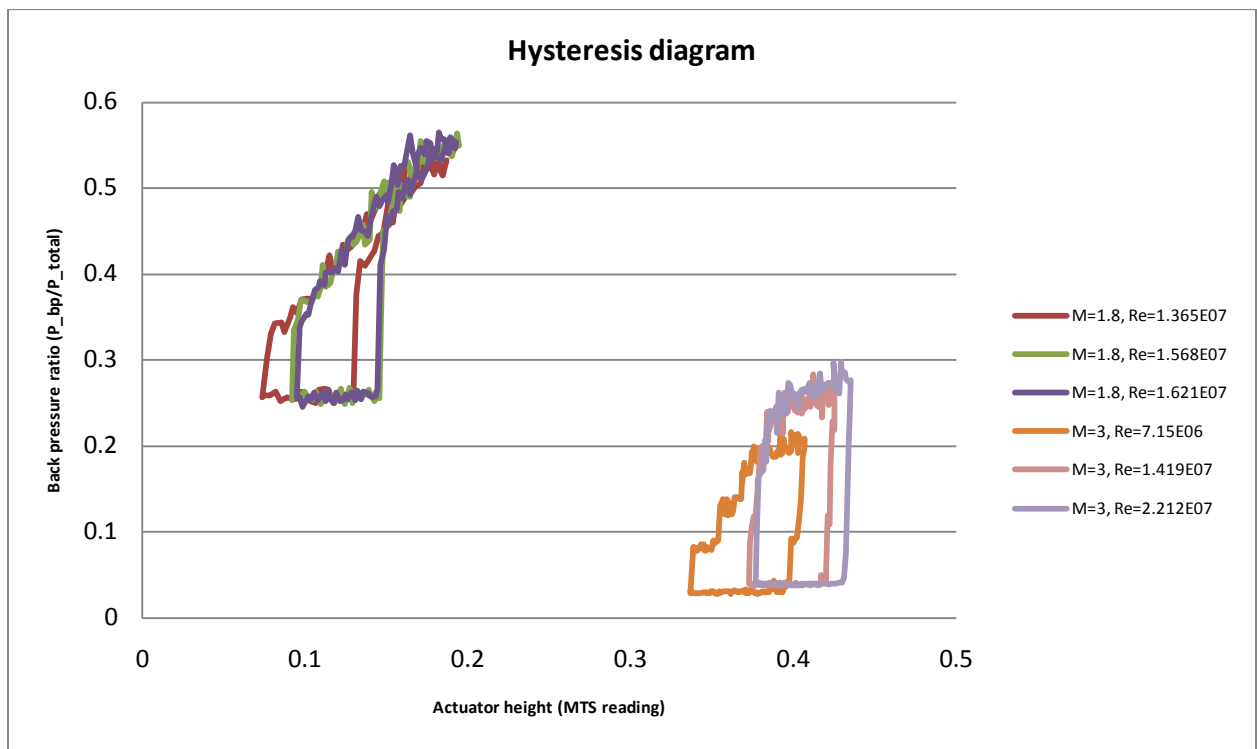


Figure 85. Comparison of hysteresis diagram of shock-train

As be seen in Figure 85, a trapezoidal shaped hysteresis graph formed from the data used to create Figure 73 through Figure 82 describes the shock-train behavior with respect to actuator height. The bottom right corner of the trapezoid is the shock-train imminent (start) position. The back-pressure rises towards the top right corner of the

trapezoid (un-start), then proceeds to top left (restart), and decreases to the bottom left corner for the shock free condition (clean).

In Figure 85, at Mach 1.8, the start and clean points occur at a back-pressure ratio of ~ 0.25 , and un-start and restart occurs at a back-pressure ratio of ~ 0.55 . At Mach 3, the hysteresis loop occurs at lower back-pressure ratio and higher actuator height. At Mach 3, start and clean occur at a back-pressure ratio of ~ 0.04 , and un-start and restart occurs at the back-pressure ratio of ~ 0.28 . One sees that the lines going from start to un-start and from restart to clean, i.e., the slant vertical lines in the hysteresis graph, vertical lines are steeper for Mach 3 than for Mach 1.8. In Mach 3 flow, the back-pressure increase per actuator height increase ($\Delta P_{BP}/\Delta h_{act}$) is greater.

Once again, the Reynolds number effect can be seen here. As the Reynolds number increases, it tends to move the graph toward the top right corner, i.e., towards higher back-pressure ratio and higher actuator height. The Reynolds number effect is explained more in the Reynolds number effect section later on the report.

Ramp speed effect

Because applying the constant increase in actuator height or the triangle wave input creates a non-static state (although it is a very slow increase called quasi-static here), one cannot ignore the dynamic effects of the ramp. For this investigation, the Mach number and the Reynolds number were fixed while the rate of increase in actuator height was varied. The test conditions are as follows.

Table 5. Test conditions for ramp slope effect experiments

Test No.	Mach #	Reynolds # (/m)	Ramp slope (MTS reading/sec)
1	1.8	1.389E07	0.088
2			0.22
3	1.8	1.628E07	0.088
4			0.22

The test results are shown in the Figure 86 and Figure 87 below.

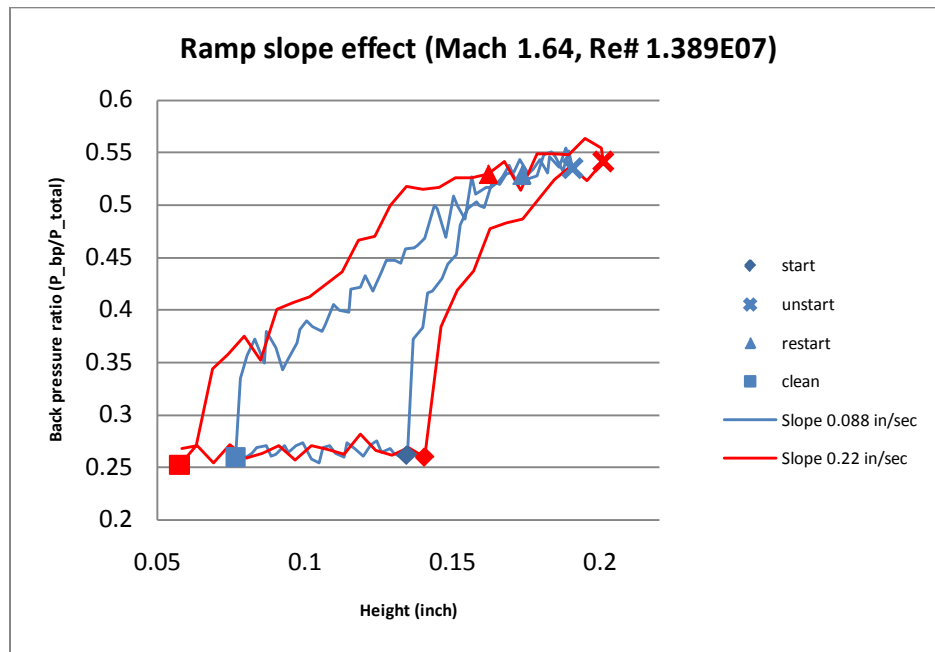


Figure 86. Ramp slope effect in hysteresis graph (M=1.8, Re=1.389E07 /m)

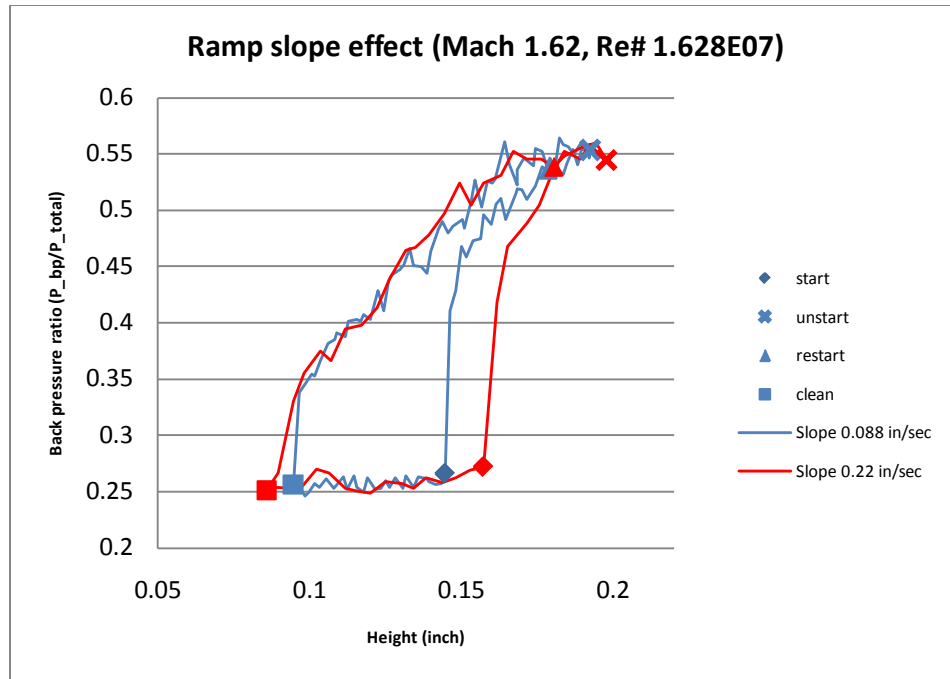


Figure 87. Ramp slope effect in hysteresis graph ($M=1.8$, $Re=1.628E07$ /m)

In Figure 86 and Figure 87, increasing ramp speed causes the hysteresis loop to be wider in the x-direction. That is, the clean and restart occurs at a lower height of the actuator and the start and un-start occurs at a higher actuator height. Thus, there is a lag or delay behavior in the shock-train's movement in relation to ramp angle changes.

Reynolds number effect

The Reynolds number has an important effect on the behavior of the shock-train. Figure 73 through Figure 82 are re-drawn for the Reynolds number versus back-pressure ratio in Figure 88 and Figure 89 below.

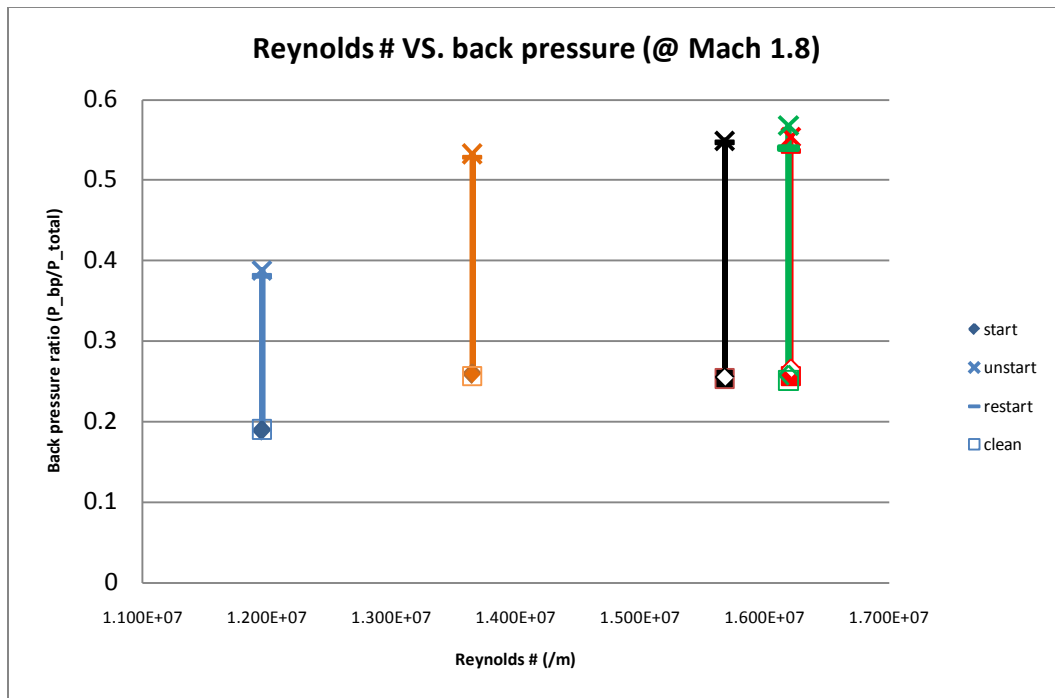


Figure 88. Reynolds number effect at M=1.8

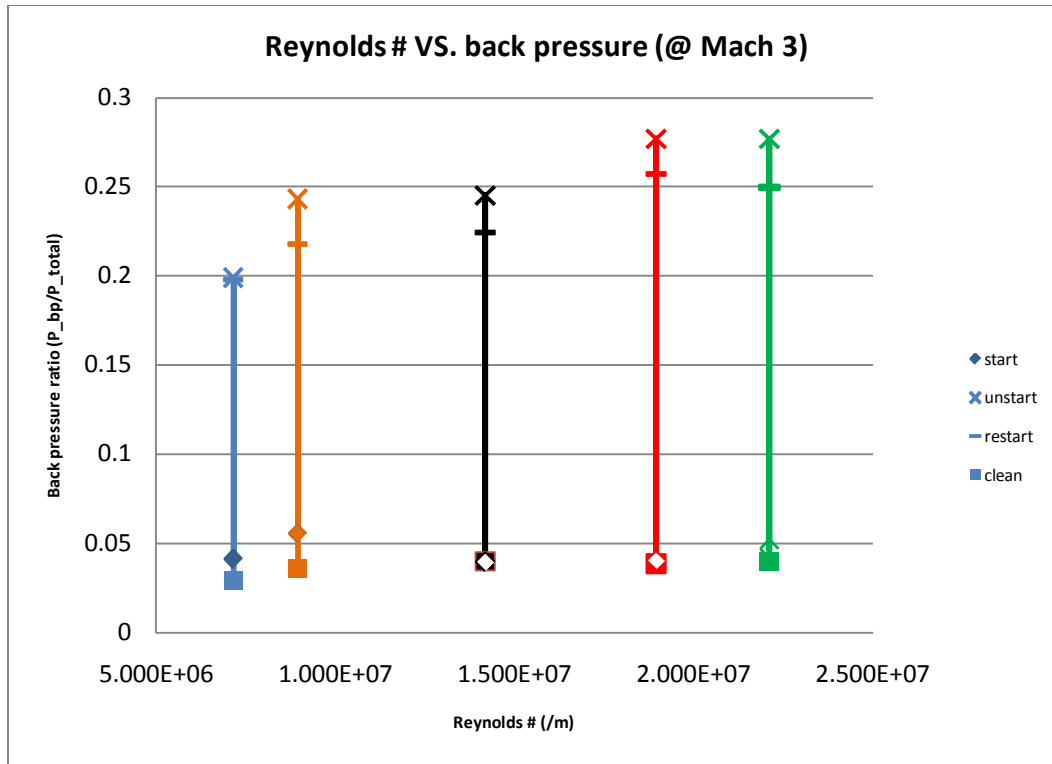


Figure 89. Reynolds number effect at M=3

The higher Reynolds numbers causes the un-start points to occur at a higher back-pressure; on the other hand, the start point does not seem to be affected as much.

Non-dimensionalization

In Figure 85, one can see two groups of graphs with respect to their Mach numbers. Mach 1.8 graphs are in the upper left region of the chart and the Mach 3 graphs are in the lower right region of the chart.

The ratio of Mach number in the test section at the shock free condition compared to the Mach number at the back-pressure location at any other condition eliminates the Mach number effect and groups the graphs together. The Mach number in the test section at shock free condition is constant, but the Mach number at the back-pressure

location for any condition throughout a run depends on ramp angle. The higher the ramp angle, the lower the Mach number, and vice versa. Two test conditions are selected: one for Mach 1.8 and a Reynolds number of 1.369×10^7 /m and the other for Mach 3 and a Reynolds number of 1.419×10^7 /m. The Mach numbers are different but their Reynolds numbers are similar.

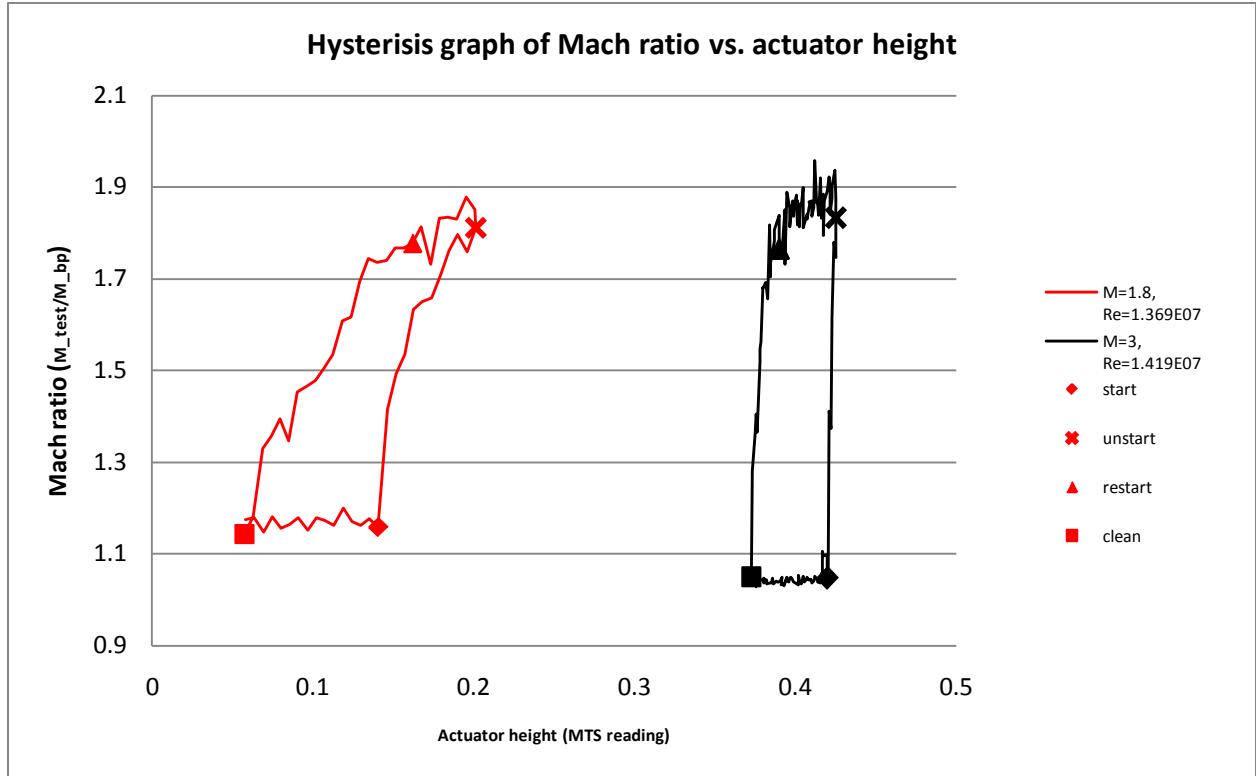


Figure 90. Hysteresis graph with Mach number ratio

Figure 90 shows that un-start occurs at a Mach number ratio of ~ 1.82 regardless of their Mach numbers, although start and clean points for the Mach 3 graph was a little lower than the Mach 1.8 graph. A next attempt was made to non-dimensionalize the x-axis. Rather than using the MTS reading, the difference in percent flow area is computed. Thus each value in x-direction (i.e., actuator height in the MTS reading) is

converted to the percent flow area using a conversion shown in Appendix E. The clean point (the square mark, lower left corner of the hysteresis graph) was set as a reference point. Any data point is expressed as the difference between the reference point and a given data point. Mathematically, it can be expressed as:

$$\Delta \% A_{flow,i} = \% A_{flow@clean} - \% A_{flow,i} \quad \text{Eqn. 1}$$

After non-dimensionalizing the x-axis using the method above, Figure 78 shows results.

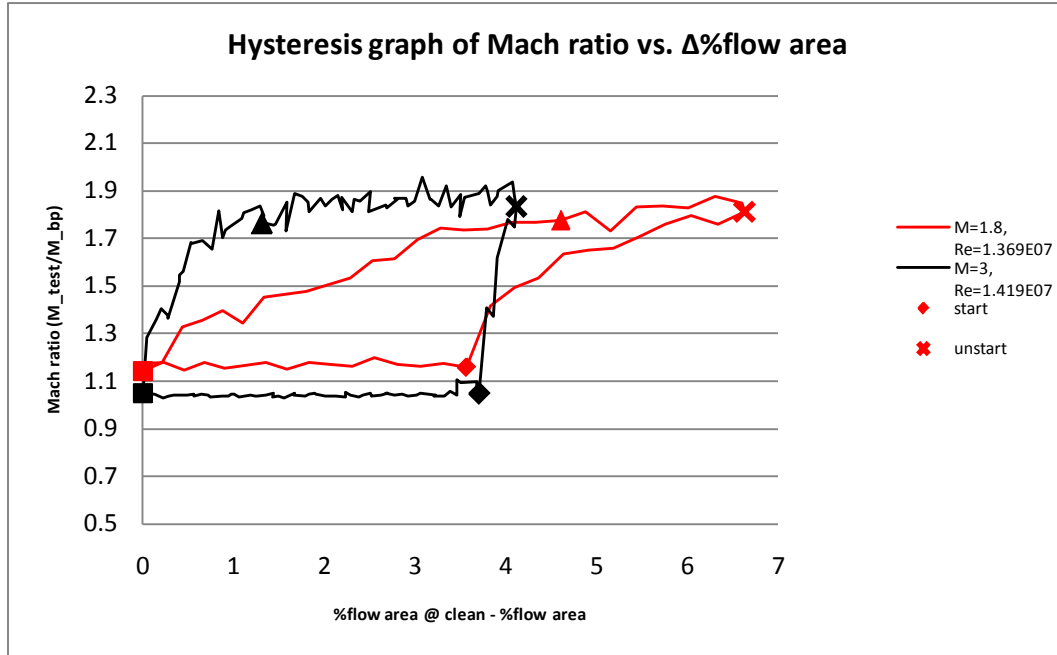


Figure 91. Hysteresis graph of Mach ratio vs. $\Delta\%$ flow area

Figure 91 shows that un-start and restart occurs at near Mach number ratio of 1.83 and shock-train appears and disappears within the 7% of flow area change regardless of the Mach number for this specific test facility. The numerical value of Mach number ratio, however, would be affected by the physical length of the test section because of the Fanno flow phenomenon.(26) To compare all the test conditions for Reynolds number

effect, the hysteresis graphs of different test conditions were created and non-dimensionalized by the method describe above. Figure 92 shows all the hysteresis graphs for the Mach 1.8 flow. Figure 93 shows all the hysteresis graphs for the Mach 3 flow. These are shown in Figure 94.

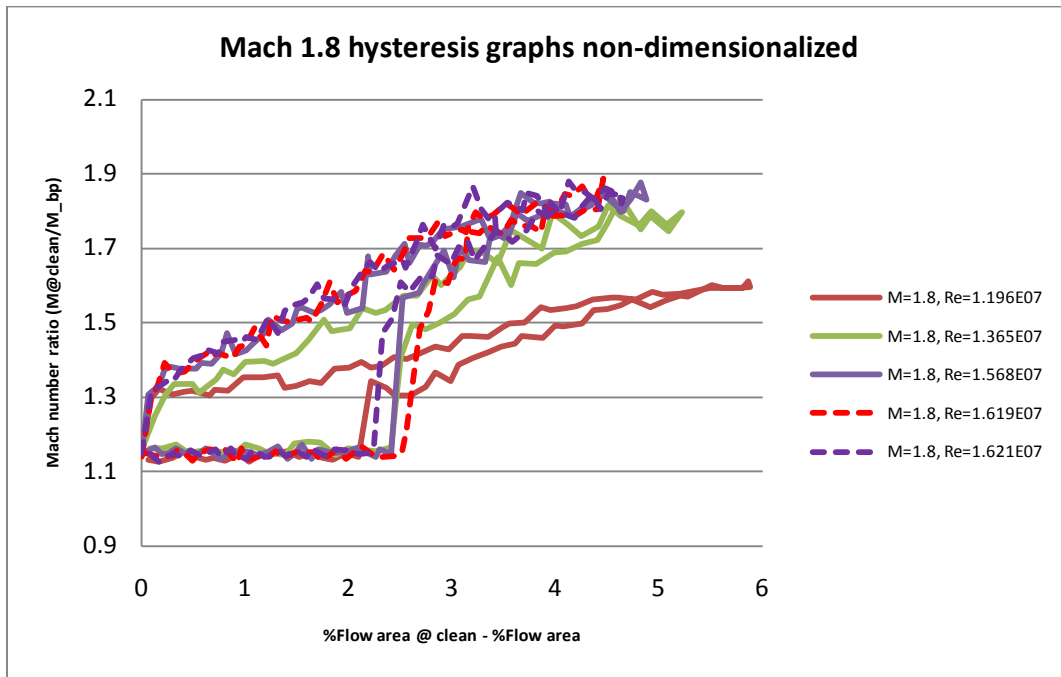


Figure 92. Mach 1.8 hysteresis graphs non-dimensionalized and combined

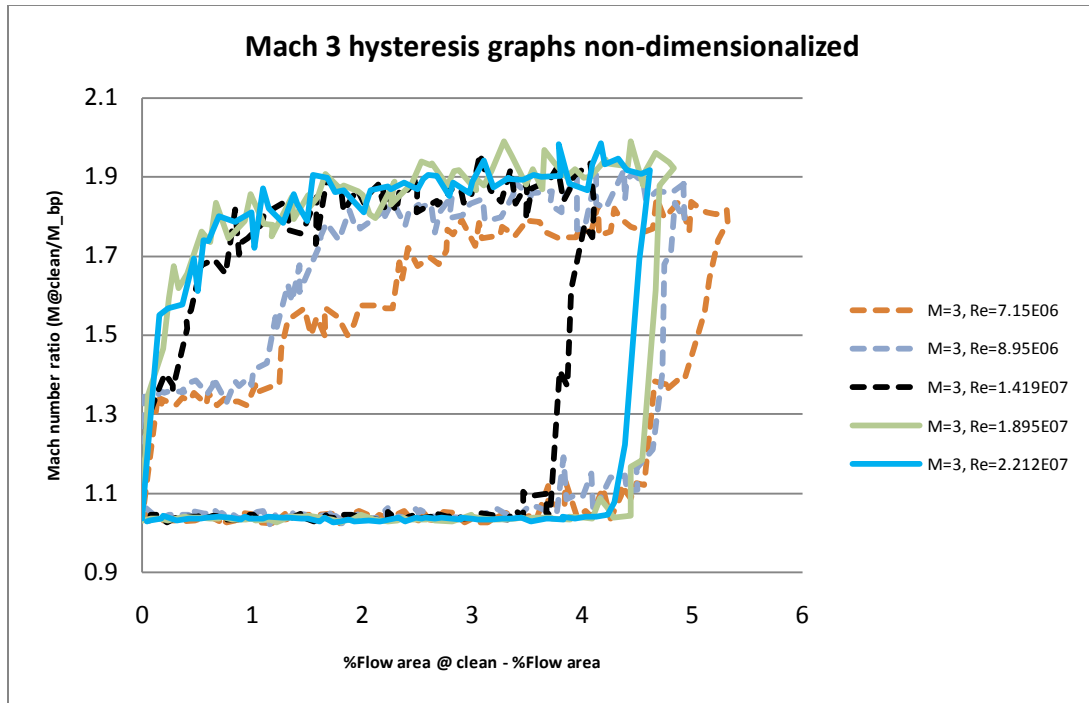


Figure 93. Mach 3 hysteresis graphs non-dimensionalized and combined

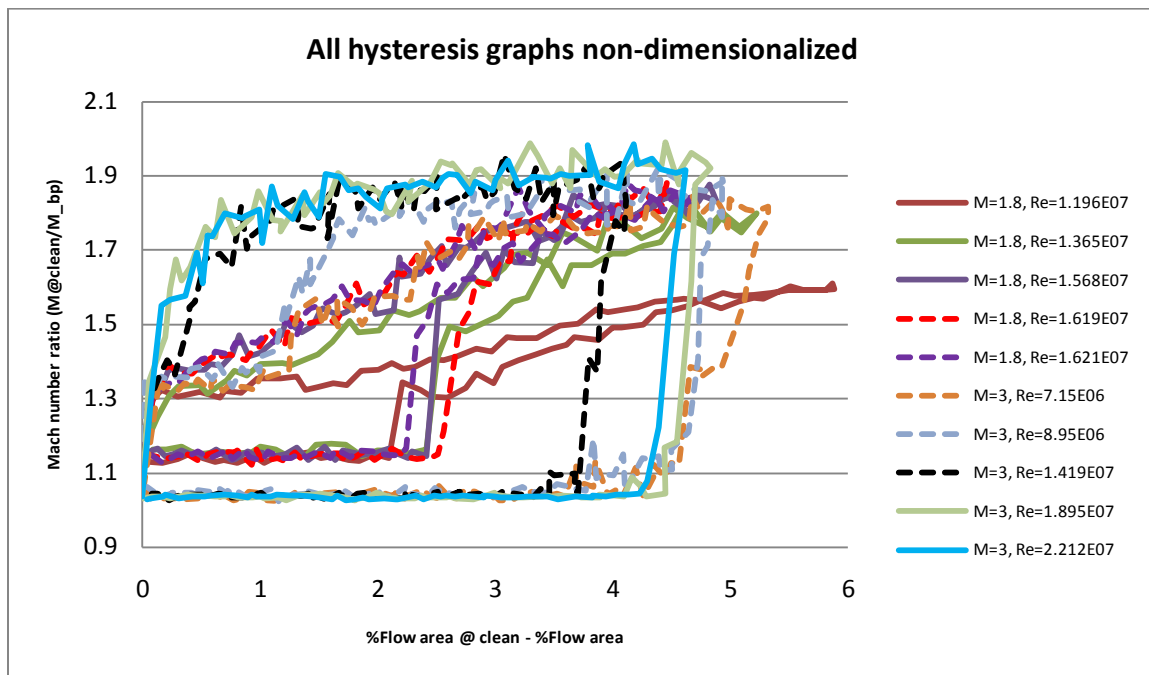


Figure 94. All hysteresis graphs are non-dimensionalized

In Figure 94, the Mach number ratio at the un-start points are between 1.8 and 1.95. The Mach number ratio at the start and clean points are approximately 1.03 for Mach 3 cases and 1.14 for Mach 1.8 cases. The bottom flat portions of the graphs for Mach 1.8 do not match with the one for Mach 3 because of two reasons.

First, the Mach number decreases as the flow travels in an adiabatic frictional constant-area duct due to the Fanno flow phenomenon.(26) It is interesting to calculate how much effect the Fanno line has here. The incoming Mach number toward the test section can be calculated using isentropic flow relationship with the total pressure and temperature at stagnation chamber and the static pressure at the test section. These values can be obtained by sensors. From this Mach number, the P_1/P_1^* can be found using the Table A4 in a ‘Compressible Fluid Flow’ book by Saad.(26) Here, subscript 1 indicates the upstream and 2 indicates the downstream. The L_1^* can be calculated with the Equation 5.35 on page 201 in Saad’s book. The L_2^* (L^* at downstream) is L_1^* subtracted by the physical distance between two sensors (one at L_1^* and the other at L_2^*). With the L_2^* value and a gamma of 1.4, the $4f L_2^*/D_H$ can be calculated, and then P_2/P_2^* can be found in the Table A4. Divide P_1/P_1^* by P_2/P_2^* , and then end up with P_1/P_2 . Since the experimental data is the measured static pressure at both places, the experimental P_1/P_2 is simply the static pressure ratio at those two locations. Next, compare the static pressure ratio of the Fanno line computation and the experimental data. For example, one of the Mach 3 tests shows that Fanno line computation yields $P_1/P_2 = 0.87738$, and the experimental data yields $P_1/P_2 = 0.85467$, in which case, their ratios are very close to each other. For a Mach 1.8 test, the Fanno line computation yields $P_1/P_2 = 0.86565$, and the experimental data yields $P_1/P_2 = 0.7625$. The reason why the Mach 1.8

case showed a bigger difference is due to the dimension difference between the upstream nozzle and the test section, and this is explained in detail in the next a few paragraphs.

Second, the newly built test section front cross section area does not exactly match the back end of the nozzle cross section area. This small difference in interior cross section dimension trips the incoming supersonic flow and creates weak shocks off the little gap between them. The shocks travel down the test section. Even though those shock lines fade as they march downstream, the Mach lines affect and slow down the air flow. In Figure 95 and Figure 96, the schlieren pictures show the weak Mach lines diagonally across the test section area when the tunnel is clean. Mach 3 air flow has a shallower angle of oblique shock lines and Mach 1.8 air flow has a steep angle of oblique shock lines that form diamond shapes throughout the tunnel. These shock lines causes small errors and result in differences between experimental values and theoretical values.

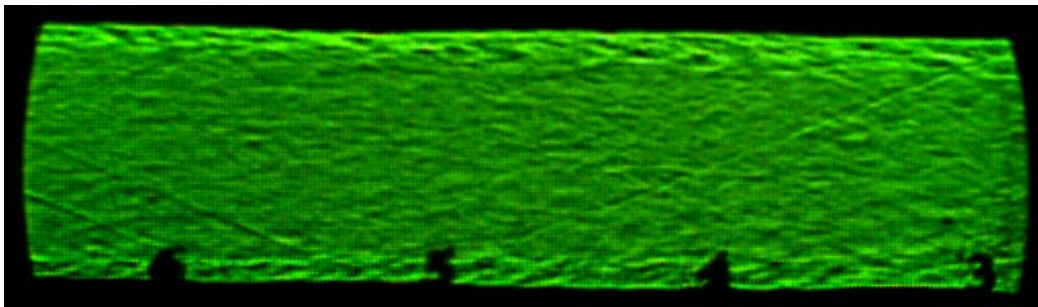


Figure 95. Clean run with Mach 3 nozzle

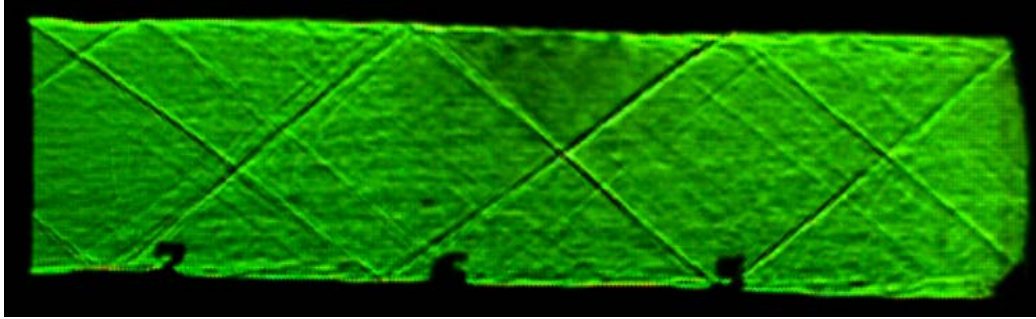


Figure 96. Clean run with Mach 1.8 nozzle

In Figure 94, the Reynolds number has a small effect. The higher Reynolds number tends to bring the hysteresis graphs a little higher, but not significantly.

In Figure 94, the graph with Mach 1.8 and Reynolds number $1.196E07$ /m has its un-start point much lower than the other cases. The same data is also used to show the effect of the Reynolds number in Figure 88. The upstream control pressure was set at a very low pressure. When the tunnel was running, the upstream stagnation pressure dropped even more and the tunnel was slowing down. That is why the one low Reynolds number graph has lower pressure values than other graphs. The test condition was not ideal in that case.

In Figure 73 and Figure 82, the ramp speed was not set at the same rate. Table 3 shows the test condition. So the width of the hysteresis loop is irrelevant.

As a result, regardless of the Mach number of the incoming air flow, the un-start would happen when the Mach number ratio of the shock free to the back-pressure location is near 1.85 for this specific test section. The percent flow area change from shock free to un-start is less than 6%. The Mach number ratio of 1.85 would be different for other test facilities because the Mach number downstream depends on the length of the tube and the friction on the inside wall of the duct.

Air flow symmetry test

This test investigates the integrity of the collected data, pressure sensor, and the test section, to help find any errors when analyzing the data. The eight test conditions are shown in Table 6.

Table 6. Test conditions for symmetry tests

Test No.	Mach #	Test type	Reynolds # (/m)
1	1.8	Top and bottom symmetry test	1.427E07
2			1.665E07
3		Left and right symmetry test	1.72E07
4			1.773E07
5	3	Top and bottom symmetry test	1.692E07
6			2.388E07
7		Left and right symmetry test	1.79E07
8			3.025E07

Eight test conditions were executed. In all eight tests, the ramp was slowly raised to a height between the start and un-start positions to ensure shock-train was present during the symmetry runs. The results are shown in Figure 97 through Figure 104.

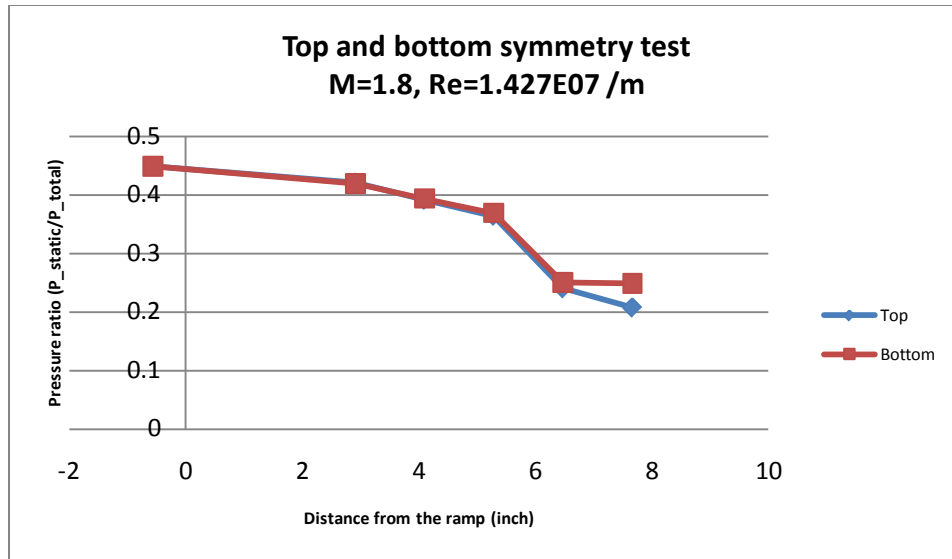


Figure 97. Top and bottom symmetry test (M=1.8, Re=1.427E07 /m)

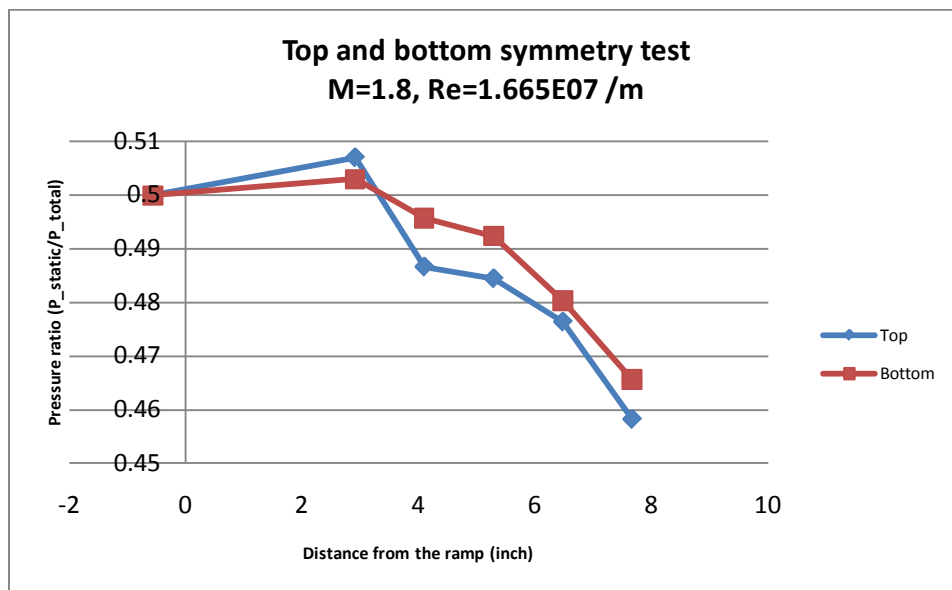


Figure 98. Top and bottom symmetry test (M=1.8, Re=1.665E07 /m)

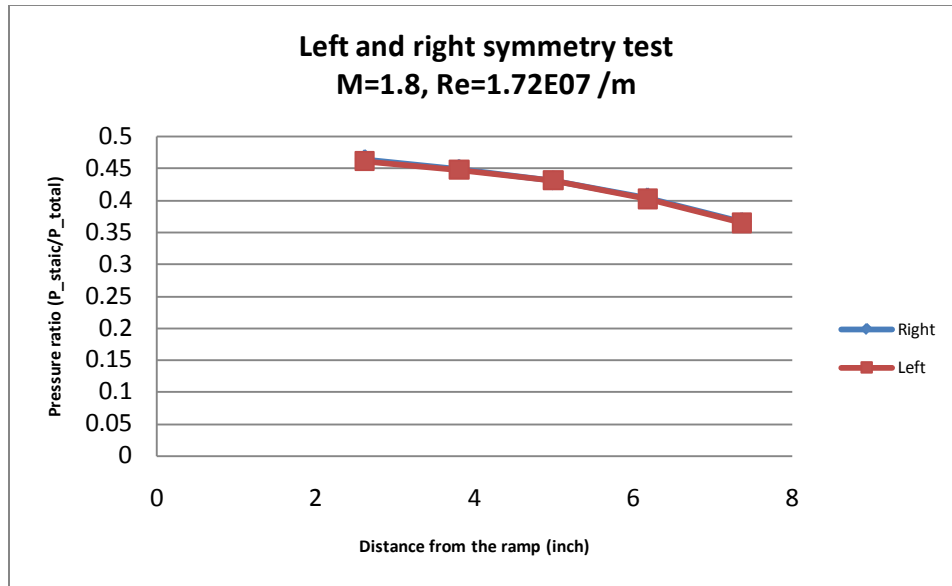


Figure 99. Left and right symmetry test (M=1.8, Re=1.72E07 /m)

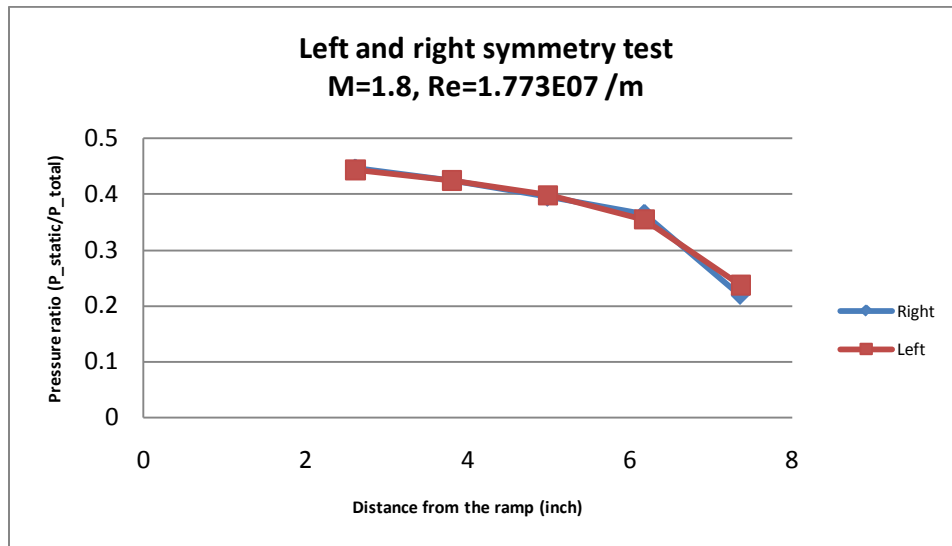


Figure 100. Left and right symmetry test (M=1.8, Re=1.773E07 /m)

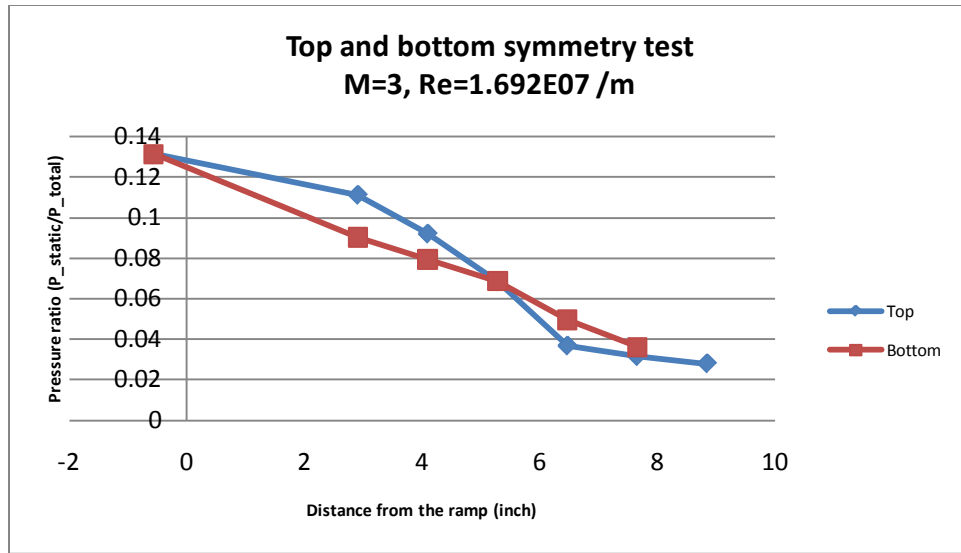


Figure 101. Top and bottom symmetry test (M=3, Re=1.692E07 /m)

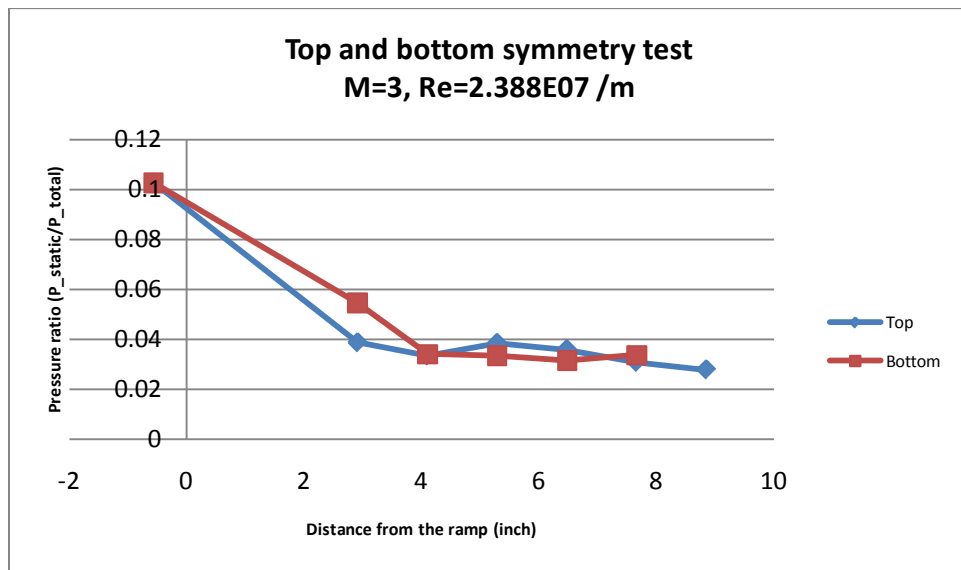


Figure 102. Top and bottom symmetry test (M=3, Re=2.388E07 /m)

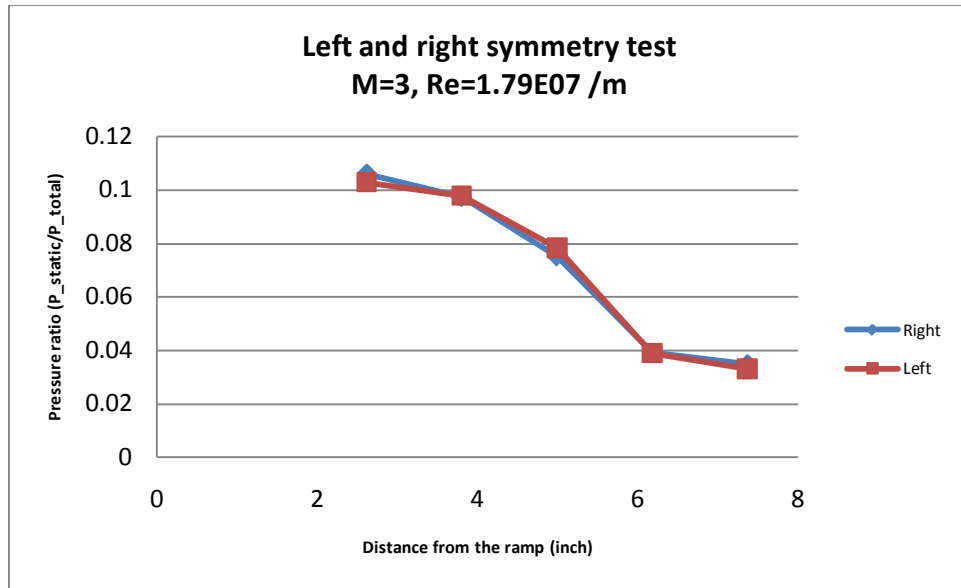


Figure 103. Left and right symmetry test (M=3, Re=1.79E07 /m)

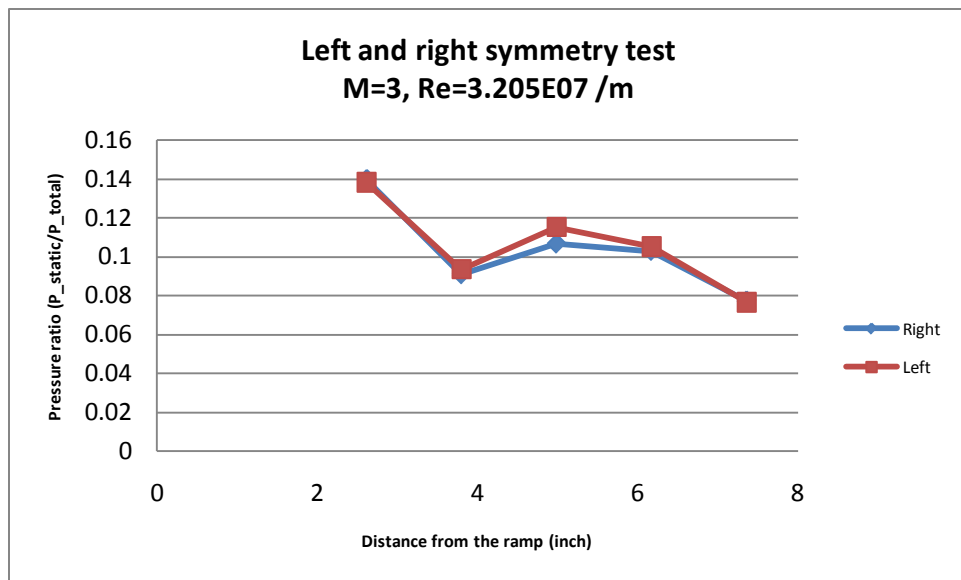


Figure 104. Left and right symmetry test (M=3, Re=3.205E07 /m)

In Figure 97 through Figure 104, the data are similar. The pressure ratio in the left and the right symmetry tests are nearly identical. From Figure 97 to Figure 104, a big

pressure rise or drop from one pressure sensor to the next one indicates that there is a shock between those two sensors. For example, in Figure 102, the big pressure difference between the second and third sensor from the left in the chart indicates that there is a shock-train leading edge presence. There are reasons for the minor differences in the top and bottom pressure readings. First, the upstream diffusing nozzle is not completely vertically symmetric. The Mach 3 nozzle is very asymmetric. It has a straight bottom and a diverging top. The Mach 1.8 nozzle is close to symmetric. To note, the exit flow uniformity from the inlet nozzle (i.e., incoming flow to the test section) was not investigated. The second reason is that the pressure data in Figure 97 through Figure 104 is time averaged. (PR = Pressure Ratio)

$$PR = \frac{Ave(\sum P_{static,i})}{Ave(\sum P_{total,i})} \quad \text{Eqn. 2}$$

Because the shock-train always oscillates within 0.2 – 0.4 duct heights depending on the Mach number and Reynolds number, there were some fluctuations in the pressure data. Third, the sensor itself has some noise. In conclusion, the air flow inside the tunnel is reasonably symmetric and should not be a problem for data integrity.

Adding injection pressure upstream test

One question arose as to whether upstream injection would push the shock-train back in the downstream directions. Air was input by opening one of the upstream pressure sensor plugs to allow the room pressure to enter the test section area which is below room pressure when the tunnel is running.

The additional pressure raised the overall pressure throughout the test section, including the back-pressure, and caused the test section to un-start at a lower ramp height

than when the pressure was not added. According to the results in Figure 85, when the tunnel is shock free, the back-pressure ratio is 0.25 for Mach 1.8 and 0.05 for Mach 3 flow, and un-start occurs at back-pressure ratio of 0.55 for Mach 1.8 and 0.27 for Mach 3 flow. Adding pressure upstream raises the overall pressure inside the tunnel, so it does not take much for the ramp to raise the back-pressure to its un-start point. Therefore, the shock imminent and un-start points occur at lower actuator heights.

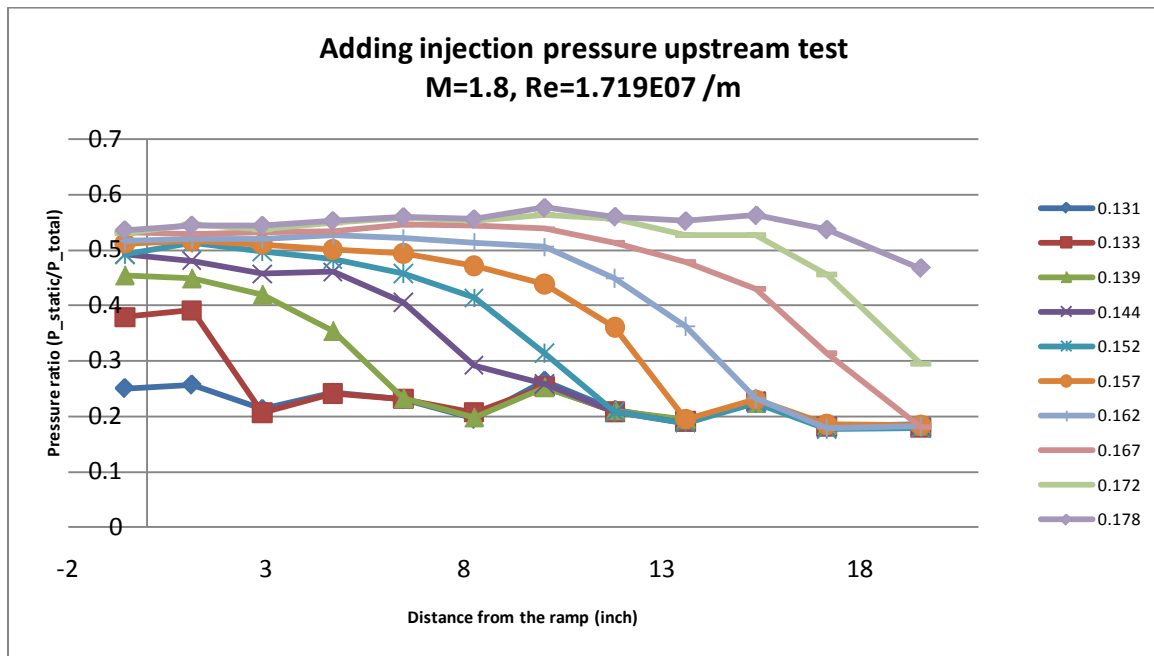


Figure 105. Results of adding pressure in upstream

As shown in Figure 105, adding pressure upstream causes the shock imminent point to occur at an actuator height of 0.131 and the un-start point to occur at an actuator height of 0.178 (in MTS reading). In Figure 56, without any additional pressure upstream, the shock imminent point occurred at a height of 0.149 and the un-start point occurred at a height of 0.191, which are higher values than the ones with injection.

In Figure 106, the injection pressure was added at approximately 6 ducts height away from the ramp on the top surface. As the atmospheric static air enters the test section, it encounters the supersonic flow and creates a shock wave. In Figure 106, two distinct oblique shocks from the open hole can be seen. The reason for two oblique shocks is that the actual shock wave is three dimensional. The wave upstream is the result of the leading edge of the curved shock and the second wave results from the outer edge of the curved shock. In Figure 106, the shock-train is at approximately 4.4 duct heights.

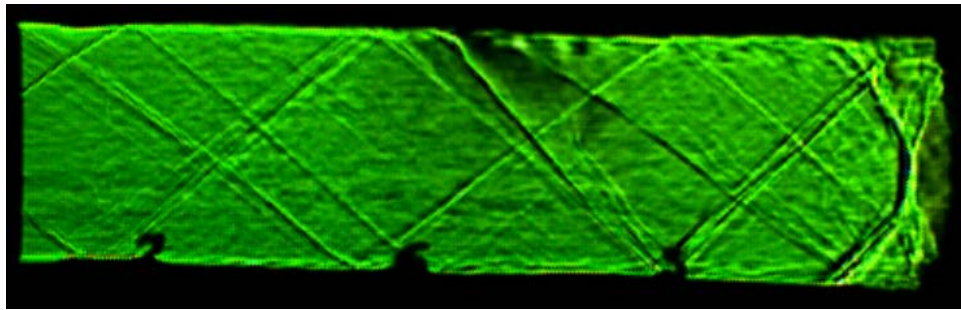


Figure 106. Schlieren image when the pressure added upstream

From work in the past, the shock-train can be made more stable by bleeding air out of the isolator because, by doing so the boundary layer will be thinned.

Comparison with other researches

From a research paper, 'Characterization of Shock Train Structures inside Constant-Area Isolators of Model Scramjet Combustors,' by Lin et al., the x- and y-axis variables in their graphs are different from the ones in this report.(27) One of the graphs in their paper was the shock-train location in x-axis versus the static back-pressure divided by the static upstream-pressure in y-axis, which is a Figure 3(a) in their paper.

This graph was chosen for a comparison study because its flow speed is Mach 1.8, which is also tested in this experiment as well. Their Figure 3(a) is shown below.

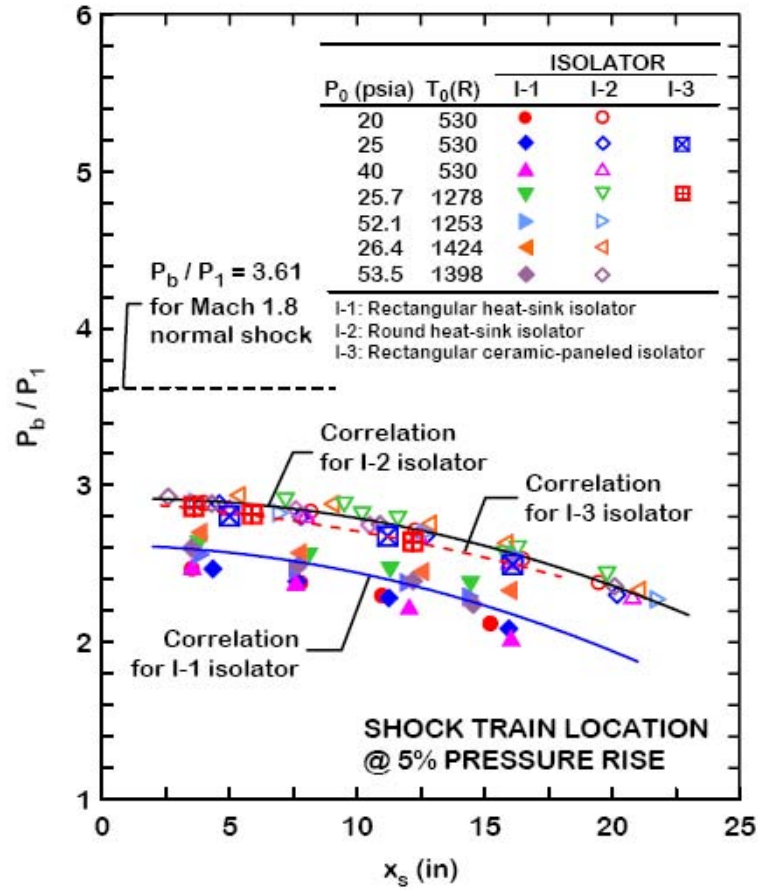


Figure 107. From Lin et al., shock-train locations for rectangular and round isolators at various back pressures in Mach 1.8 flow (27)

To compare with theirs, the result of the flow condition of Mach 1.8 and total pressure of 17 psia from this experiment was chosen. The graph is shown below in Figure 108.

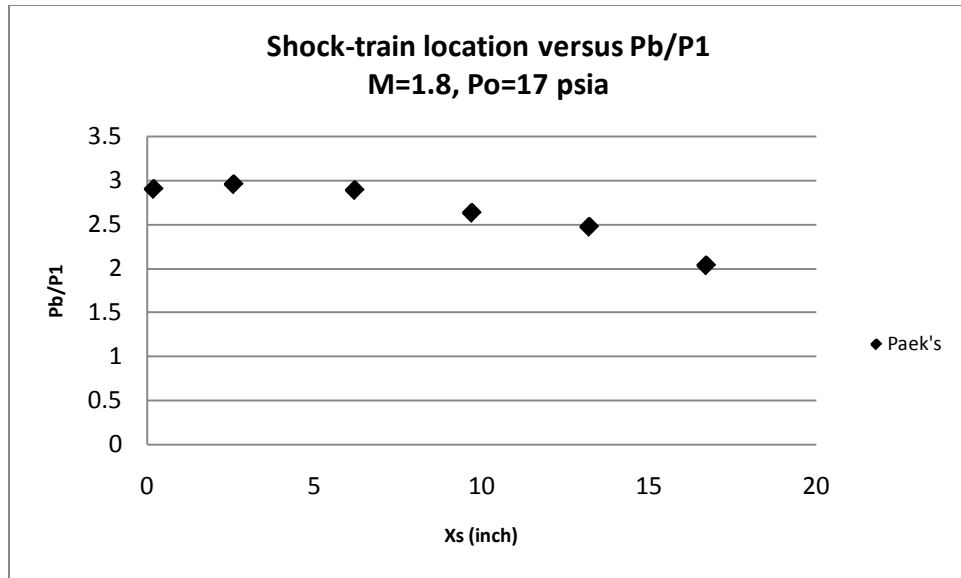


Figure 108. Shock-train location versus P_b/P_1 in Mach 1.8 and $P_o=17$ psia

The next graph shows the Figure 107 and Figure 108 overlaid together for a better direct comparison. Black diamond symbols indicate Paek's data.

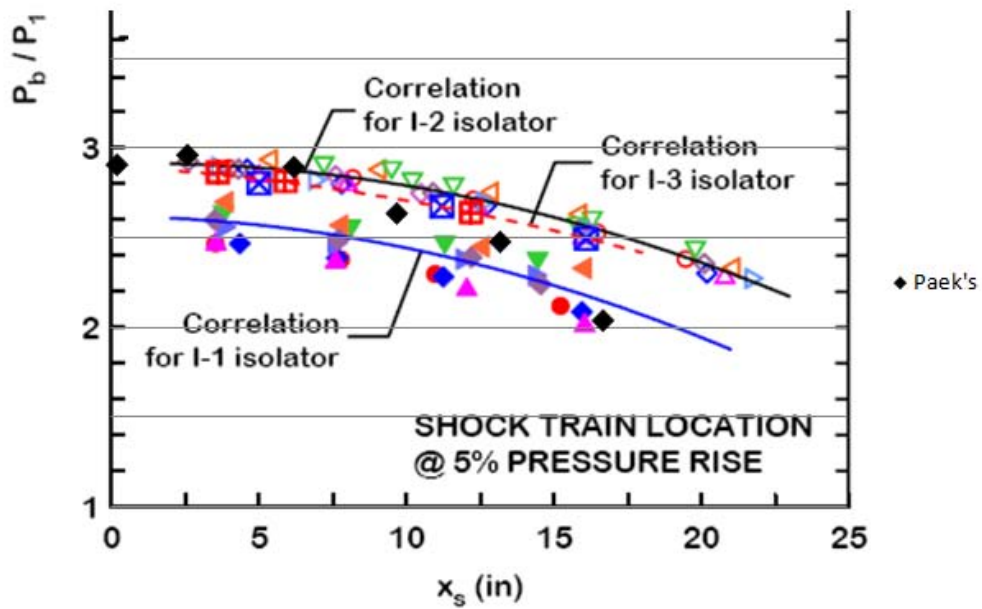


Figure 109. Comparison between Lin et al.'s and Paek

First of all, it is important to point out that the geometry of the cross section, an isolator length, and the surface roughness of Lin et al.'s isolators is different from Paek's. Nonetheless, those two data sets seem to agree with each other.

Since the Mach 3 flow was tested in this experiment, the same type of graph for Mach 3 flow was drawn and shown below. Since Lin et al. did not tested Mach 3 flow, no direct comparison can be made. Because the shock-train moved jumpy, sudden, and fast in Mach 3 flow case as the back pressure rose, there were a few stable shock-train locations recorded per one flow case. This explains a few data point in the Figure 110.

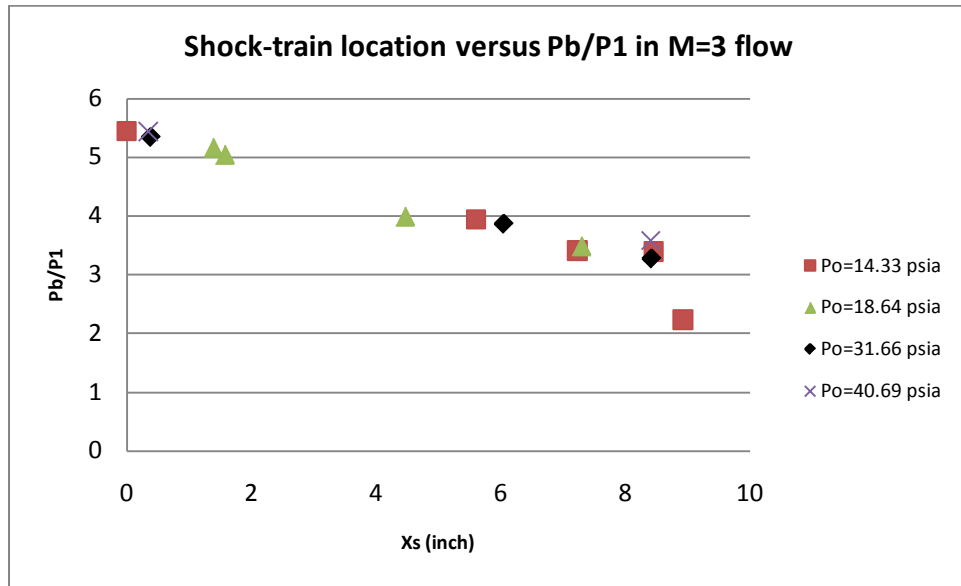


Figure 110. Shock-train location versus P_b/P_1 in Mach 3 and $P_o=31.7$ psia

Additionally, one of Lin et al.'s graphs demonstrated the one common characteristic from all the data they gathered. The data uses a free-stream distance from shock leading edge ($x' = x - x_s$) in an x-axis and $\left[\left(\frac{P_s}{P_o} \right) - \left(\frac{P_{s'}}{P_o} \right) \right] \frac{M_o^2}{(P_b/P_1)}$ in a y-axis. The nomenclatures are as follows.

M_0 = nominal Mach number at the upstream nozzle exit

P = pressure

x = pressure transducer location

x_s = shock train leading edge location

x' = free-stream distance from shock leading edge, $x' = x - x_s$

Superscript

' = condition at shock leading edge

Subscript

0 = total condition

1 = condition at the upstream nozzle exit

b = condition at extension piece exit

s = static condition

Their graph is shown in Figure 111 below.

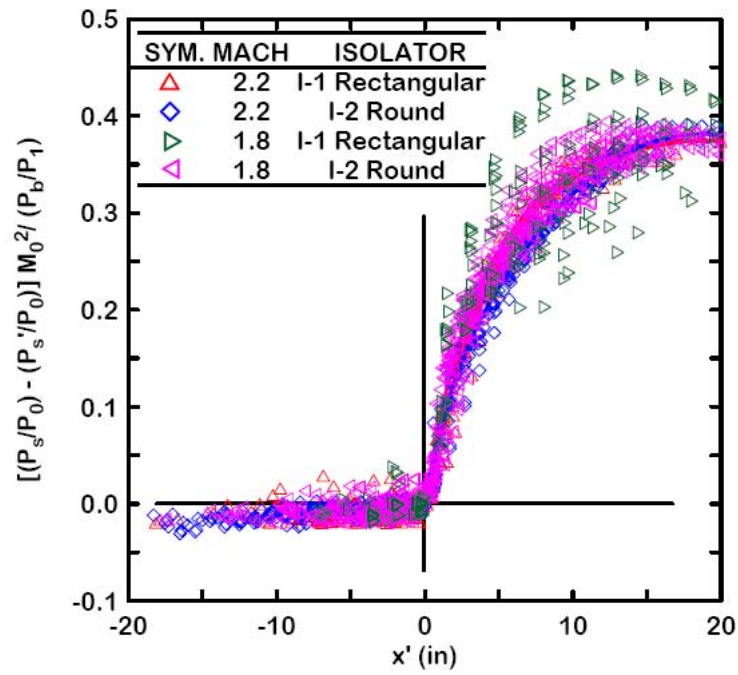


Figure 111. Lin et al.'s graph – shifted and normalized shock train pressure profiles for I-1 rectangular and I-2 round isolators in Mach 1.8 and 2.2 flow (27)

Using same x and y-axis as Lin et al., the data collected in this research was calculated and drawn on a chart. The graph is shown in Figure 112 and Figure 113 for Mach 1.8 and 3 cases respectively.

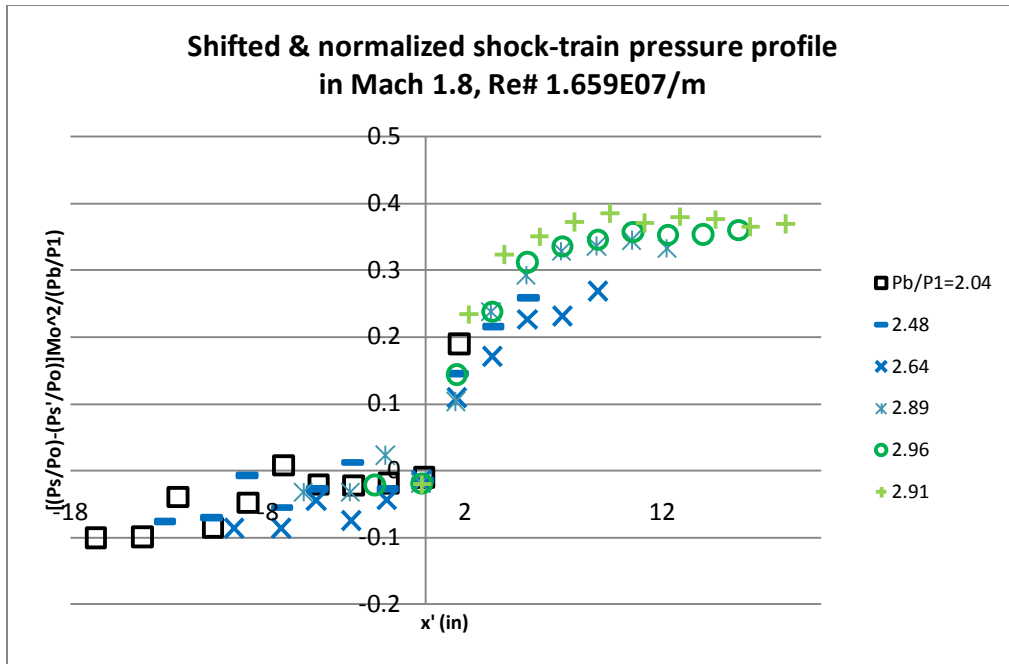


Figure 112. From this research – shifted and normalized shock train pressure profile for rectangular isolator in Mach 1.8

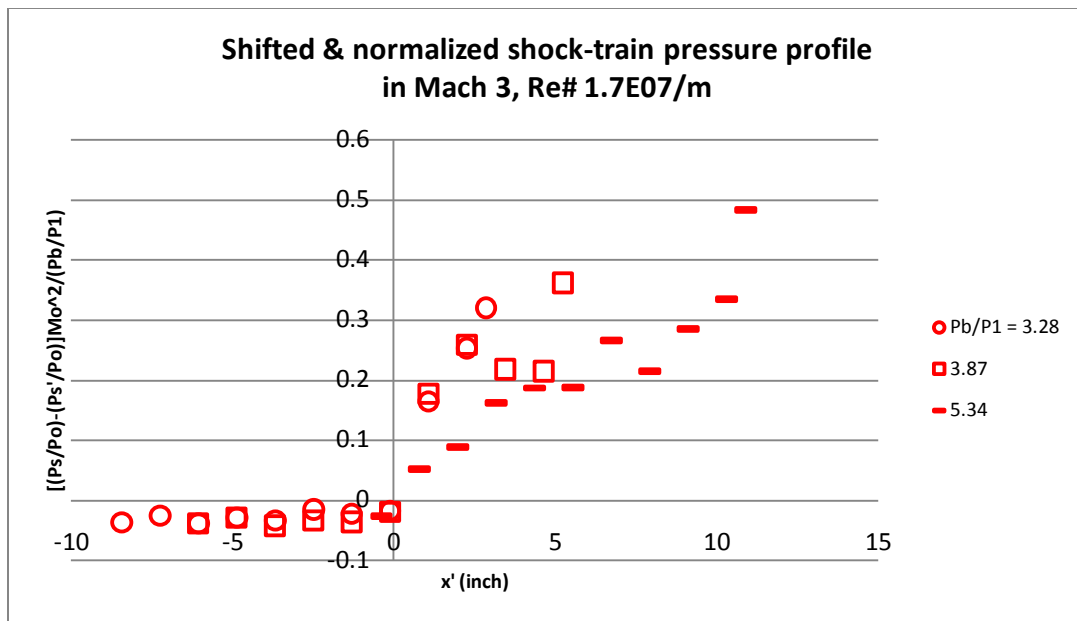


Figure 113. From this research – shifted and normalized shock train pressure profile for rectangular isolator in Mach 3

In Figure 113, one value (triangle symbol) peaks to $P_b/P_1 \approx 0.5$ at ~12 inch downstream from the shock-train leading edge. This is due to a great pressure fluctuation behind the shock-train at Mach 3 flow. As you can see in Figure 57 through Figure 60, the pressure profile behind the shock-train leading edge is very jagged. Lin et al. did not test at Mach 3 flow; therefore, this jagged pressure profile cannot be seen in their graphs.

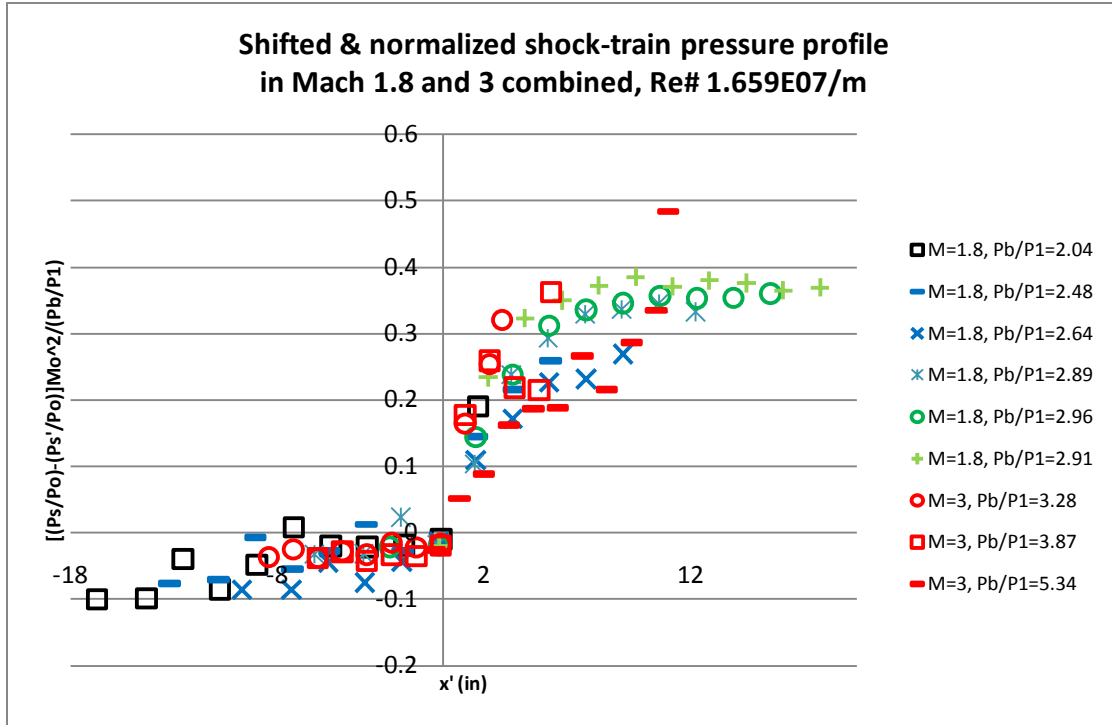


Figure 114. From this research – shifted and normalized shock train pressure profile for rectangular isolator in Mach 1.8 and 3 combined

One difference to notice in Figure 114 from Lin et al.'s graph is the amount of scatterings of the data in an upstream of the shock-train. In Lin et al.'s graph, the value in an upstream of the shock-train was between -0.03 and 0.03. The Paek's graph has a range of the values from -0.1 to 0.03. However, the values in a downstream of the shock-

train seem alike. Again, it is important to keep in mind that the geometry of the Lin et al.'s isolator is different from that of Paek's.

V. Conclusions and Recommendations

Conclusions of Research

From the conceptual idea to designing the experiment and its facility, to fabricating the test facility, and then to executing the experiments, there were a lot of findings. Designing a test section allowed abundant learning opportunities. Learning new software, Solidworks, and working with machine shop showed another side of engineering. During this process, continuous communication with machine shop experts accelerated the fabrication process and solved any type of design challenge.

While working on the design in the Solidworks, many engineering analyses were required. Material strength and stress/strain computation were required. As a result, the wind tunnel test section window thickness and its deflection with a respect to the pressure acting on it were calculated.

Once the test section was delivered and completely built, the experiment took place right away. The first phase of the experiment started with a fixed ramp position. This method can only yield useful data when test condition is away from the un-start condition. In other words, the results when the ramp was already raised were slightly different from when the ramp was introduced after the air flow was run and stabilized. It was important to stabilize air flow before introducing any objects into the test section.

In Mach 3 flow, the shock-train can be stable up to 4 or 5 duct heights from the ramp. Beyond this point, the shock-train was not stable at one location, rather it propagated forward. On the other hand, the Mach 1.8 flow was stable all the way up to the entrance of the test section, i.e., 7 or 8 duct heights. Also, in the higher Reynolds

number flows, the shock-train was more unstable and un-start would occur with a slight increase in the ramp height. The lower the Mach number, the more stable the shock-train. The lower the Reynolds number, the lower ramp height required to start the shock-train.

When changing a ramp input signal to the actuator during a run, data could be collected at one run, but this method introduced a quasi-static state. While the ramp was slowly raised, the shock imminent point, the un-start point, and the back-pressure values at those times were easily observable. At a lower Mach number, a smaller ramp angle started the shock-train and the range of actuator height from the shock imminent point to the un-start point was not as small. At a higher Mach number, a higher ramp angle was required to start the shock-train, and from there, a smaller angle increase caused the test section to un-start. A higher Mach number had a smaller ramp angle range when going from the shock imminent point to the un-start point compared to the lower Mach number. The flow Reynolds number also played a part. Similar to the Mach number effect, for a higher Reynolds number, the shock imminent point and the un-start point occurred at a higher ramp angle. Additionally, the range of the ramp angle from the shock imminent point to the un-start point decreased.

A triangle input signal to the actuator revealed important shock-train behavior. When the ramp was raised and lowered, the shock-train appeared, un-started, restarted, and disappeared. The most important discovery was that the ramp height at the un-start was not same as the height at restart. The height at the restart point was lower than that at the un-start point. In other words, there was a hysteresis in the aerodynamics of the shock-train movement. The back-pressure ratio versus actuator height showed a distinctive trapezoidal shape of the hysteresis. This hysteresis was also influenced by the

Mach number and Reynolds number. Where the back-pressure ratio is the y-axis and the actuator height is the x-axis, the higher Mach number moved the hysteresis graph to the bottom right corner, and the higher Reynolds number moved the hysteresis graph to the top right corner on the chart.

On dynamic runs, even though the ramp was very slowly moving up or up/down, the dynamic effect of the ramp cannot be ignored. Different ramp speeds were varied to observe the behavior of the shock-train. Surprisingly, faster ramp movement widened the hysteresis graph in x-direction, i.e., actuator height. This showed another non-linearity in the shock-train system: time delay between the ramp position and the shock train location changes. A further study of dynamic behavior of the shock-train is required to analyze on this delay behavior.

The coordinate system with a back-pressure ratio on the y-axis and the actuator height on the x-axis located the graph in several places depending on their Mach numbers. However, the Mach number ratio (Mach number at shock free condition to the Mach number at the back-pressure location) as a function of actuator height normalized the data. Also, the x-axis can be non-dimensionalized using the $\Delta\%$ flow area. This non-dimensionalization put all the graphs together with a slight variation depending on the Reynolds number. For this test facility, the Mach number ratio at the un-start point, regardless of the incoming Mach number, was near 1.85. This value would be different for a different test facility due to the dimensions of the duct.

Air flow inside the test section was found to be reasonably symmetric according to the symmetry test. It is found that, when injecting pressure upstream of the shock-train,

the shock imminent point and the un-start point occurred at a lower ramp height and made the shock-train system more unstable.

Significance of Research

The non-linearity of the aerodynamics of a shock train was discovered through quasi-static tests. When applying a triangle input to the actuator, it was observed that the un-start point was not the same as the restart point. The ramp height at the restart point was actually lower than that at the un-start point. Through this experiment, hysteresis graphs were created and hysteresis behavior was clearly noticeable.

Another non-linearity observed was the delay in the shock train system when the ramp speed was changed. This delay non-linearity widened the hysteresis graph in x-direction, i.e., actuator height. These two non-linear behaviors of the shock train emphasized the importance of further study of the dynamics of the shock train prior to building a feedback loop control system.

Recommendations for Future Research

When doing the experiment with the Mach 1.8 nozzle, the shock train was stable throughout the test section. One could not find a point where the shock train becomes unstable. A longer test section would be required to find the static unstable point.

Currently, in this laboratory, there are two different diverging nozzles. One nozzle produced approximately Mach 1.8 and the other produced approximately Mach 3 flow. Both nozzles were used throughout this research. It would be interesting to test with a Mach number somewhere between, e.g., Mach 2.4. Data collected with a Mach

2.4 nozzle would provide missing data between the two Mach numbers and present a better picture of Mach number effects.

The focus of this research was to investigate the static relationship of the back-pressure versus the shock train location. During this research, it was apparent that applying varying ramp inputs to the actuator while running tests created dynamic effects. Even though only a small portion of the dynamic study was touched on here, some important information about non-linearity was noted. It was strongly suggested that further study into shock train dynamics should be done before designing a feedback control system.

There were eleven pressure sensors available for test section measurement. Because the number of sensors was less than the number of points of interest, it was necessary to move the sensors around for different types of experiments. Repeatedly uninstalling and installing sensors could damage the sensors and test facilities, and might affect the integrity of the data. Having more sensors and keeping them in a fixed location would save a lot of test time in the future and maintain the integrity of the test configuration.

Each test-run-duration was approximately 4 to 9 seconds depending on a Mach or Reynolds number. A higher Mach number and a lower Reynolds number allows a longer run time. Time between runs, however, was 20 to 30 minutes because it took time for the vacuum pump to pump out the pressure from the vacuum tank. The test run time versus wait time needs to be improved. A 4 – 9 second run to a 20 – 30 minute recovery time ratio did not seem efficient.

As mentioned before, the inlet nozzles are not symmetric. The flow uniformity at the exit of the inlet nozzle needs to be investigated in order to help provide more accurate boundary conditions to the CFD analysts for future CFD works.

Appendix A. Test section window thickness calculation

The book, High-speed wind tunnel testing by Alan Pope(28), was used for wind tunnel test section calculation. The bottom of page 114 shows the window thickness calculation for a simply supported rectangular window. In this case, the four edges of a window would be fixed. The calculation for a window thickness for a simply supported window would yield thicker thickness than the one for fixed edge window. So this calculation would yield more thickness than what is required for the safety purpose.

t = long side of window (inch)

s = short side of window (inch)

$$t/s = 19.9228 / 4.4062 = 4.5215$$

From the Fig. 2:19 on page 115, the coefficient from ratio of long side to short side and Poisson's ratio (B) is 0.124. The maximum gauge pressure (p) would be 35.5 psig. Then, the maximum moment (M_{\max}) is

$$M_{\max} = B \cdot p \cdot s^2$$

$$M_{\max} = 0.1245 * 35.5 * 4.4062^2 = 90.4(in \cdot lb)$$

S_{\max} = maximum allowable stress, lb/inch² (S_{\max} occurs at the center of the window)

S_{\max} = modulus of rupture / safety factor

Modulus of rupture for the cast acrylic is 10200 psi.(29)(30)

Safety factor is 10

$$S_{\max} = 10200/10 = 1020 \text{ psi}$$

$$S_{\max} = (M_{\max} * c)/I$$

,where $c = \text{half the glass thickness} = t/2$ and $I = \text{moment of inertia for 1 inch wide strip} = t^3/12$

$$S_{\max} = (6 \cdot M_{\max})/t^2$$

$$\text{Hence, } t = \sqrt{\frac{6 \cdot M_{\max}}{S_{\max}}}$$

$$t = \sqrt{\frac{6 \cdot M_{\max}}{S_{\max}}} = \sqrt{\frac{6 \cdot 90.4}{1020}} = 0.729 \text{ inch}$$

In this calculation, 35.5 psig was chosen to be the maximum pressure acting on the window, but in this research, 35 psig would be never reached.

Appendix B. Window deflection calculation

Because the static pressure of the air flow inside the tunnel is acting on wind tunnel window, it is interesting to know how much deflection of the window the pressure causes. The book, Roark's formulas for stress and strain written by Warren C. Yong and Richard G. Budynas, was used as a reference.(31)

I chose the example of a rectangular plate with all edges fixed.

$$y_{\max} = \frac{\alpha q b^4}{E t^3}$$

y_{\max} = maximum deflection (inch)

α = coefficient from length and width ratio = 0.0284 for this case

q = pressure (psi) = 35.5 psi

b = short side length (inch) = 4.4062 inch

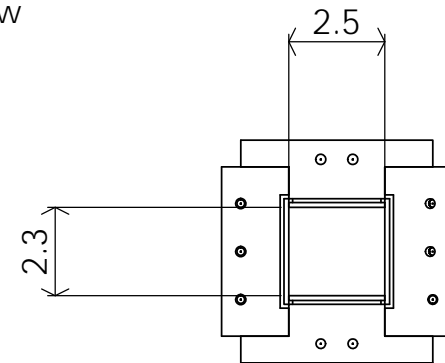
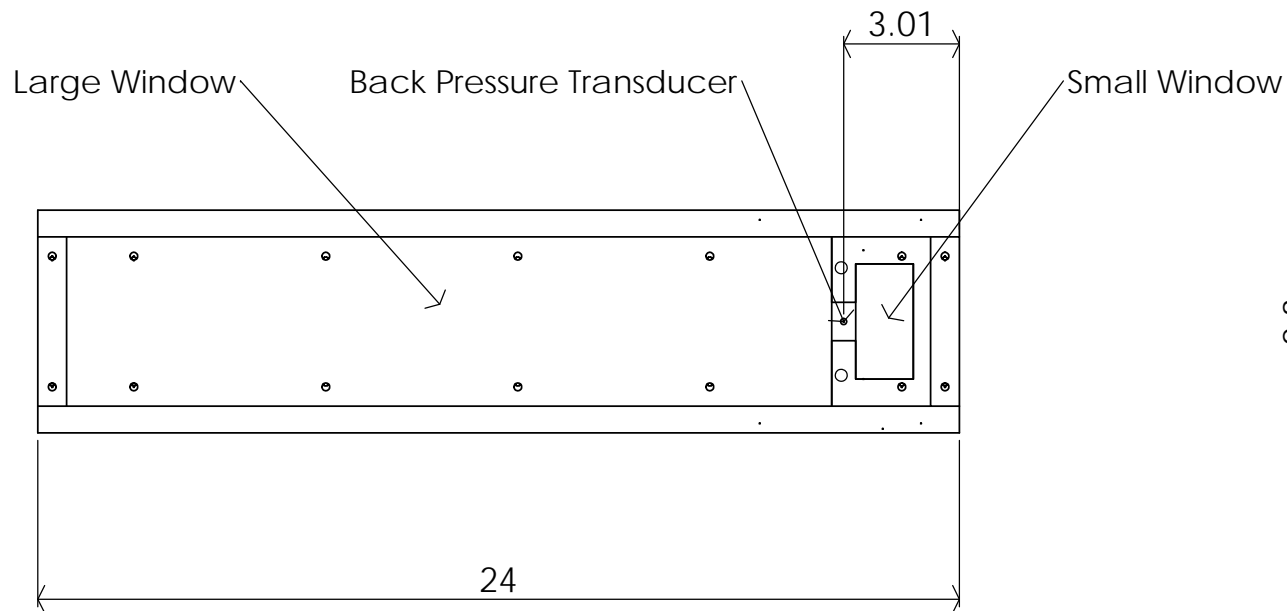
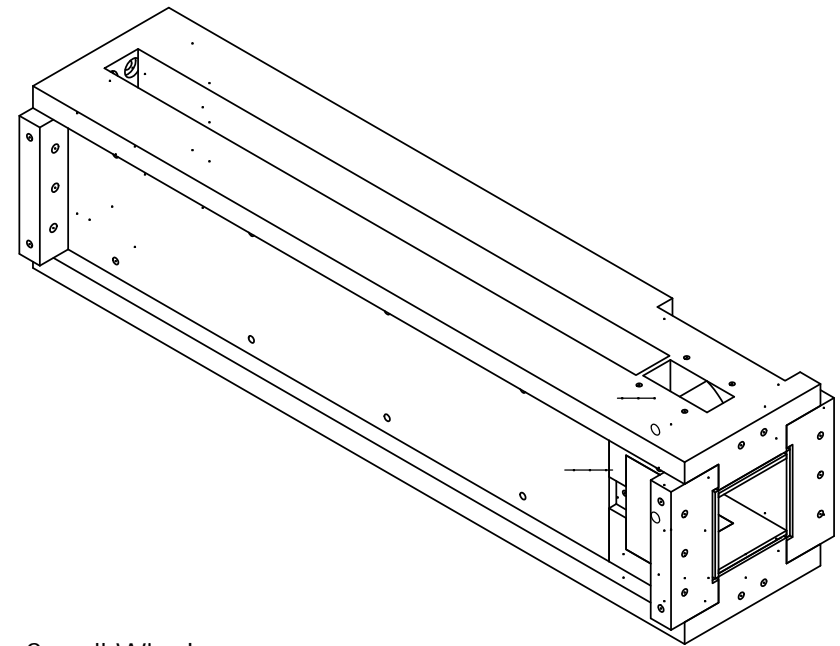
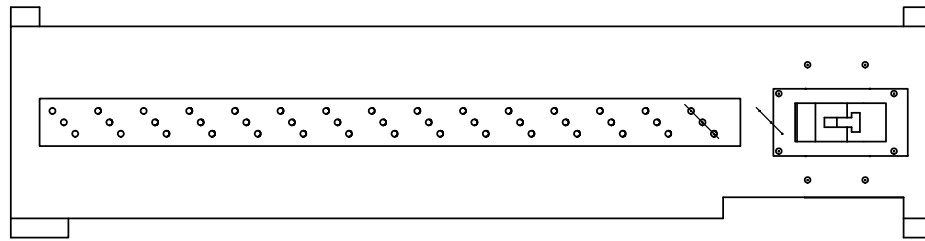
E = Young's modulus (psi) = 464000 psi

t = thickness (inch) = 0.729 inch

$$y_{\max} = \frac{\alpha q b^4}{E t^3} = \frac{0.0284 \cdot 35.5 \cdot 4.4062^4}{464000 \cdot 0.729^3} = 0.00211 \text{ (inch)}$$

In this calculation, 35.5 psig was chosen to be the maximum pressure acting on the window, but in this experiment, 35.5 psig would be never reached.

Appendix C. Test facility engineering drawings

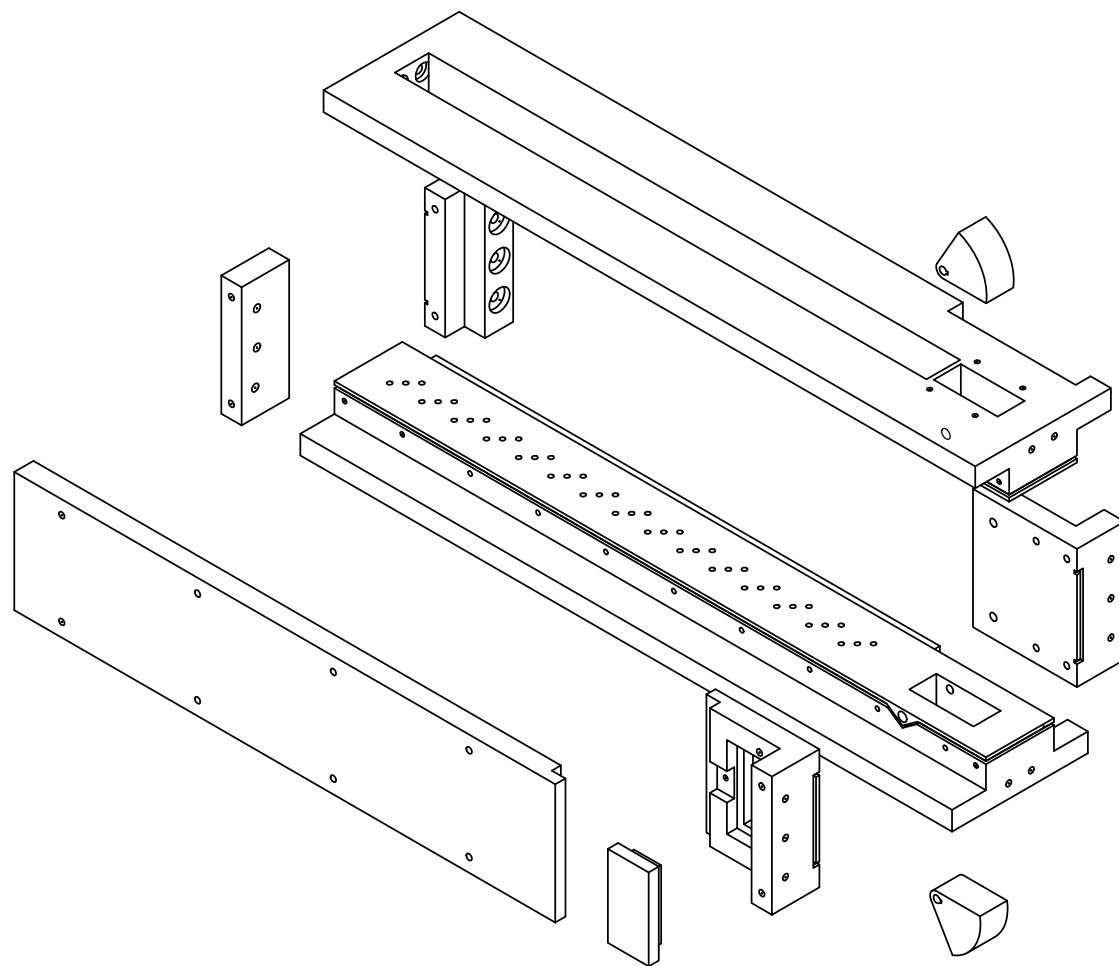


TITLE:

Test Section Assembly

MATERIAL:

Aluminum & Plexiglass



TITLE:

Assembly Drawing

MATERIAL:

Aluminum & Plexiglass

5

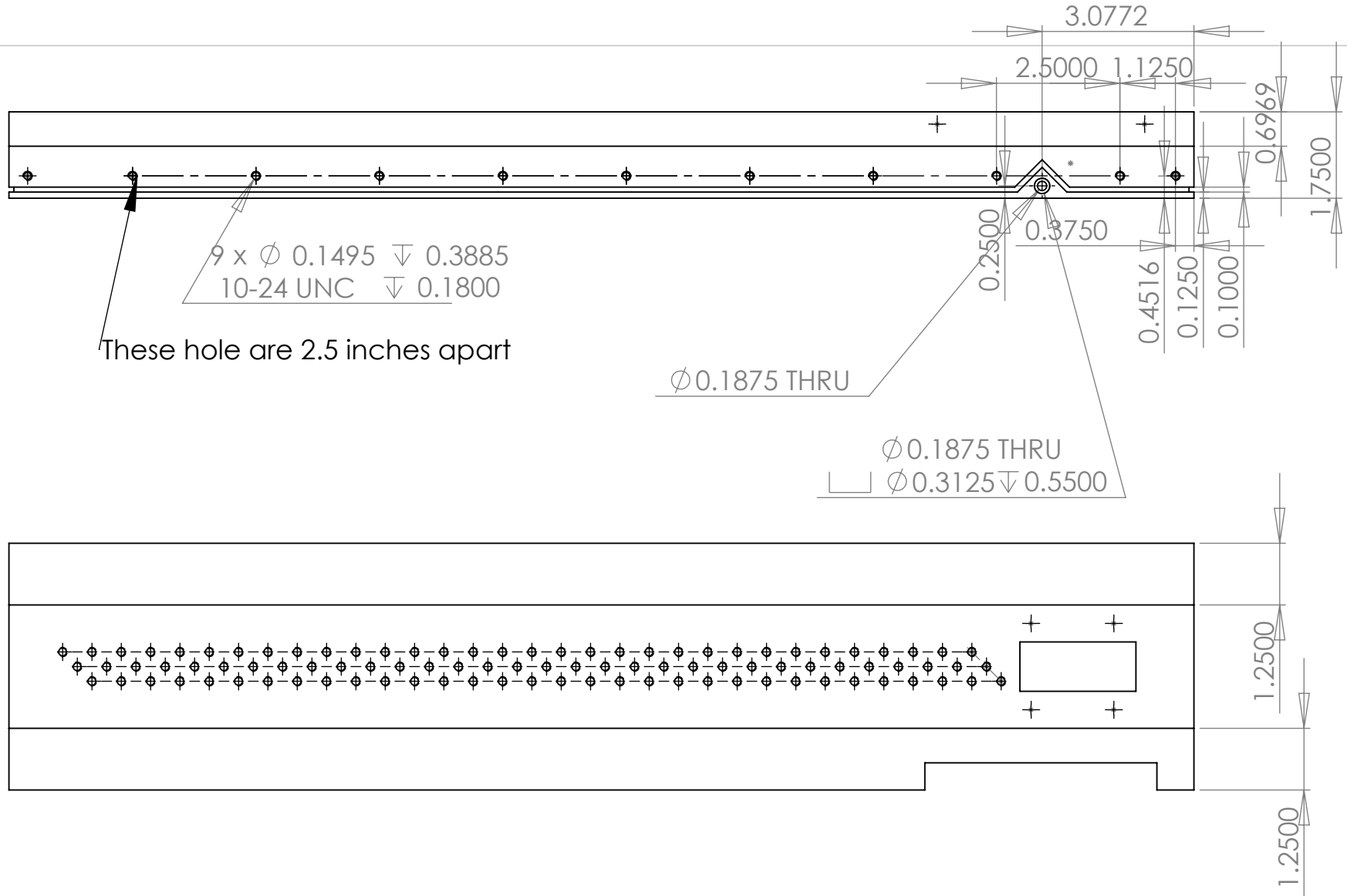


4

3

2

1



PROPRIETARY AND CONFIDENTIAL

THE INFORMATION CONTAINED IN THIS DRAWING IS THE SOLE PROPERTY OF <INSERT COMPANY NAME HERE>. ANY REPRODUCTION IN PART OR AS A WHOLE WITHOUT THE WRITTEN PERMISSION OF <INSERT COMPANY NAME HERE> IS PROHIBITED.

		UNLESS OTHERWISE SPECIFIED:		NAME	DATE	TITLE: Top plate (PT exposed) Bottom view			
		DIMENSIONS ARE IN INCHES TOLERANCES: +/-0.001 FRACTIONAL ± ANGULAR: MACH ± BEND ± TWO PLACE DECIMAL ± THREE PLACE DECIMAL ±	DRAWN	Richard Paek	1 Mar 10				
			CHECKED						
			ENG APPR.						
			MFG APPR.						
		INTERPRET GEOMETRIC TOLERANCING PER:	Q.A.			COMMENTS:			
		MATERIAL Aluminum							
		FINISH				SIZE	DWG. NO.		REV
	NEXT ASSY	USED ON				A	201		
APPLICATION		DO NOT SCALE DRAWING				SCALE: 1:1	WEIGHT:		SHEET 1 OF 1

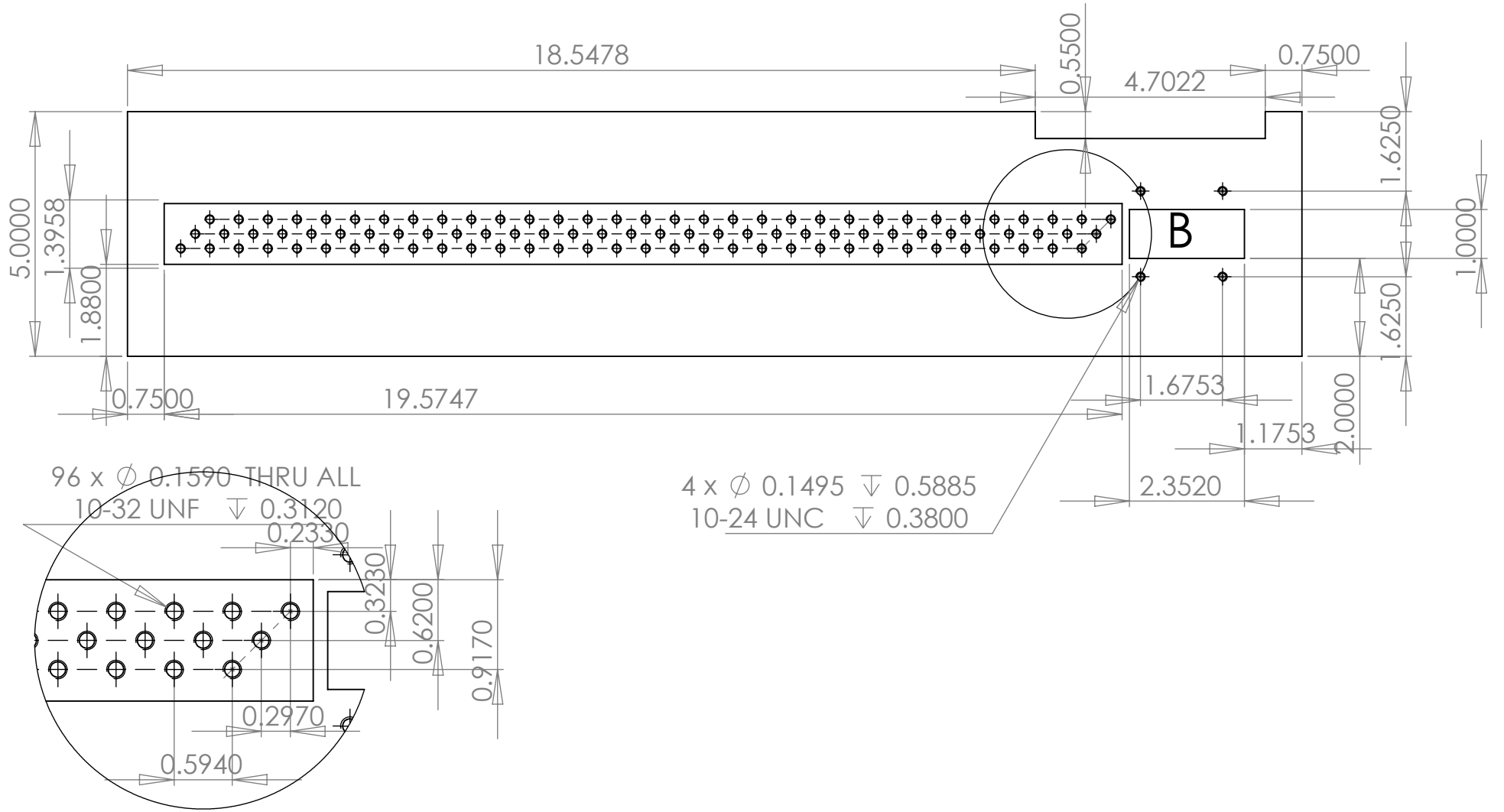
5

4

3

2

1

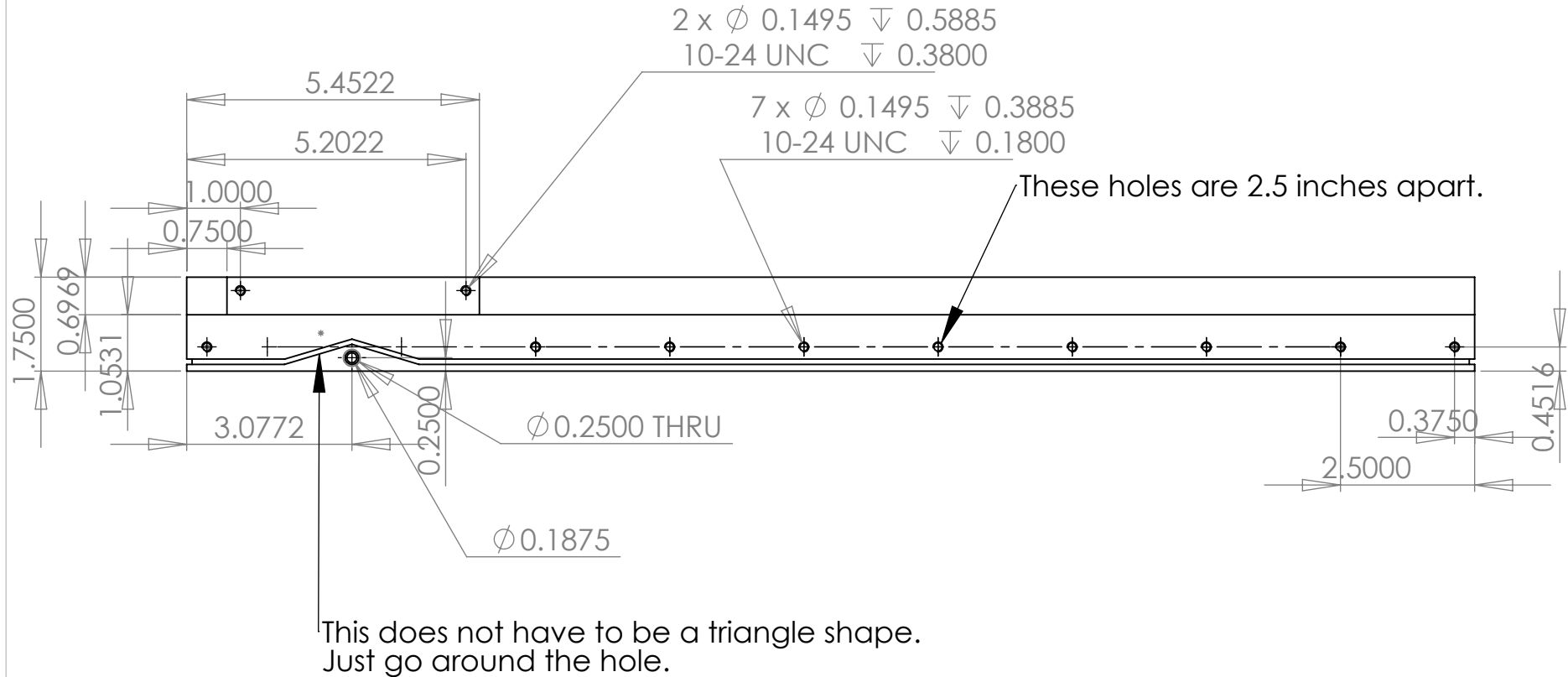


DETAIL B SCALE 2 : 3

PROPRIETARY AND CONFIDENTIAL

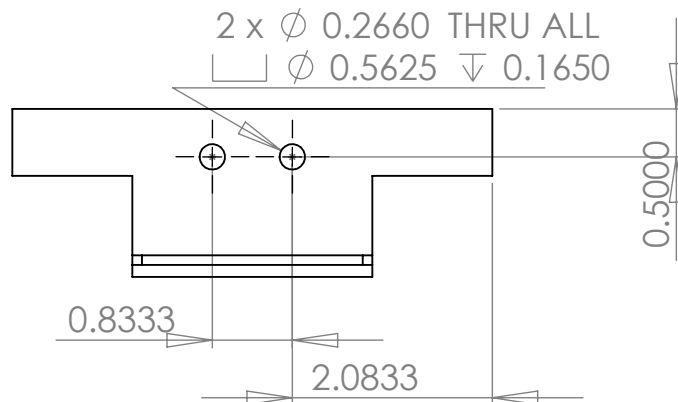
THE INFORMATION CONTAINED IN THIS DRAWING IS THE SOLE PROPERTY OF <INSERT COMPANY NAME HERE>. ANY REPRODUCTION IN PART OR AS A WHOLE WITHOUT THE WRITTEN PERMISSION OF <INSERT COMPANY NAME HERE> IS PROHIBITED.

		UNLESS OTHERWISE SPECIFIED:		NAME	DATE	TITLE: Top plate (PT exposed) Top view			
		DIMENSIONS ARE IN INCHES TOLERANCES: +/-0.001 FRACTIONAL ± ANGULAR: MACH± BEND ± TWO PLACE DECIMAL ± THREE PLACE DECIMAL ±	DRAWN	Richard Paek	1 Mar 10				
			CHECKED						
			ENG APPR.						
			MFG APPR.						
		INTERPRET GEOMETRIC TOLERANCING PER:	Q.A.			COMMENTS:			
		MATERIAL Aluminum							
		FINISH				SIZE A	DWG. NO. 200		REV
NEXT ASSY	USED ON					SCALE: 1:1	WEIGHT:	SHEET 1 OF 1	
APPLICATION		DO NOT SCALE DRAWING							

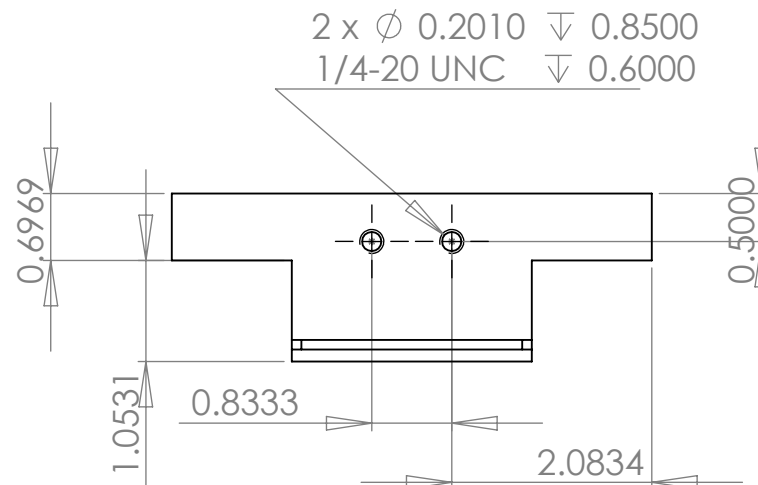


PROPRIETARY AND CONFIDENTIAL
THE INFORMATION CONTAINED IN THIS
DRAWING IS THE SOLE PROPERTY OF
<INSERT COMPANY NAME HERE>. ANY
REPRODUCTION IN PART OR AS A WHOLE
WITHOUT THE WRITTEN PERMISSION OF
<INSERT COMPANY NAME HERE> IS
PROHIBITED.

		UNLESS OTHERWISE SPECIFIED:		NAME	DATE	TITLE: Top plate (PT exposed) Back view		
		DIMENSIONS ARE IN INCHES TOLERANCES: +/-0.001 FRACTIONAL ± ANGULAR: MACH± BEND ± TWO PLACE DECIMAL ± THREE PLACE DECIMAL ±	DRAWN	Richard Paek	1 Mar 10			
			CHECKED					
			ENG APPR.					
			MFG APPR.					
		INTERPRET GEOMETRIC TOLERANCING PER:	Q.A.			SIZE DWG. NO. REV A 203		
		MATERIAL Aluminum	COMMENTS:					
		FINISH						
NEXT ASSY	USED ON					SCALE: 1:1 WEIGHT: SHEET 1 OF 1		
APPLICATION		DO NOT SCALE DRAWING						

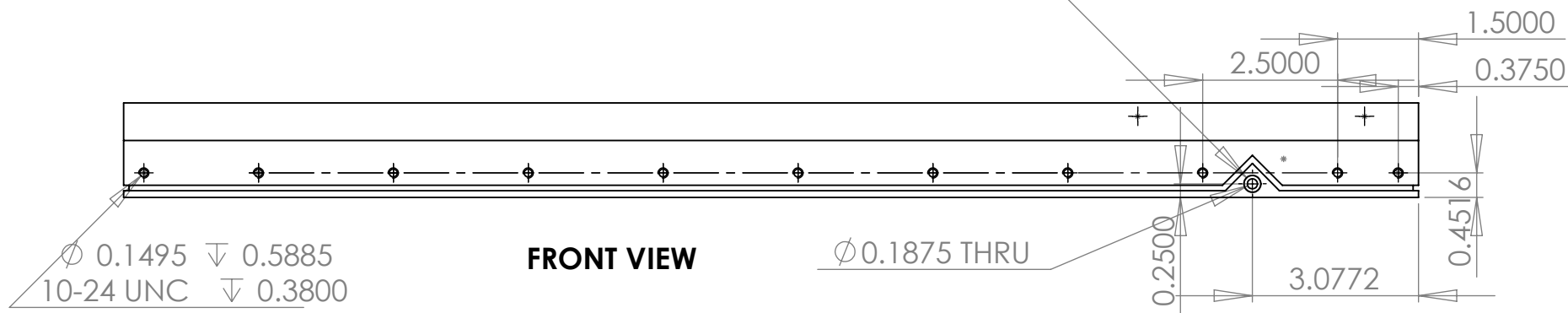


LEFT VIEW



RIGHT VIEW

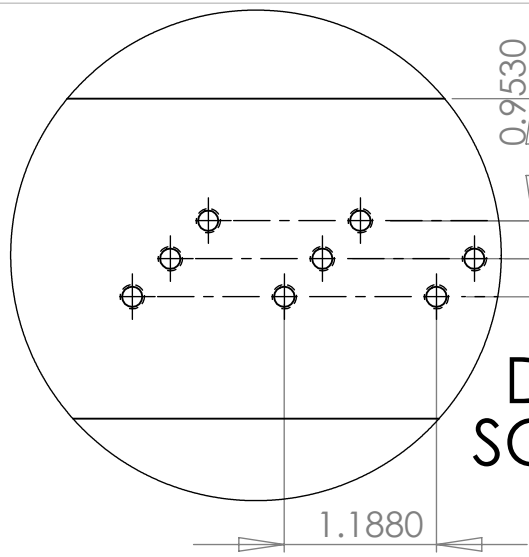
\varnothing 0.1875 THRU
 \square \varnothing 0.3125 ∇ 0.5500



FRONT VIEW

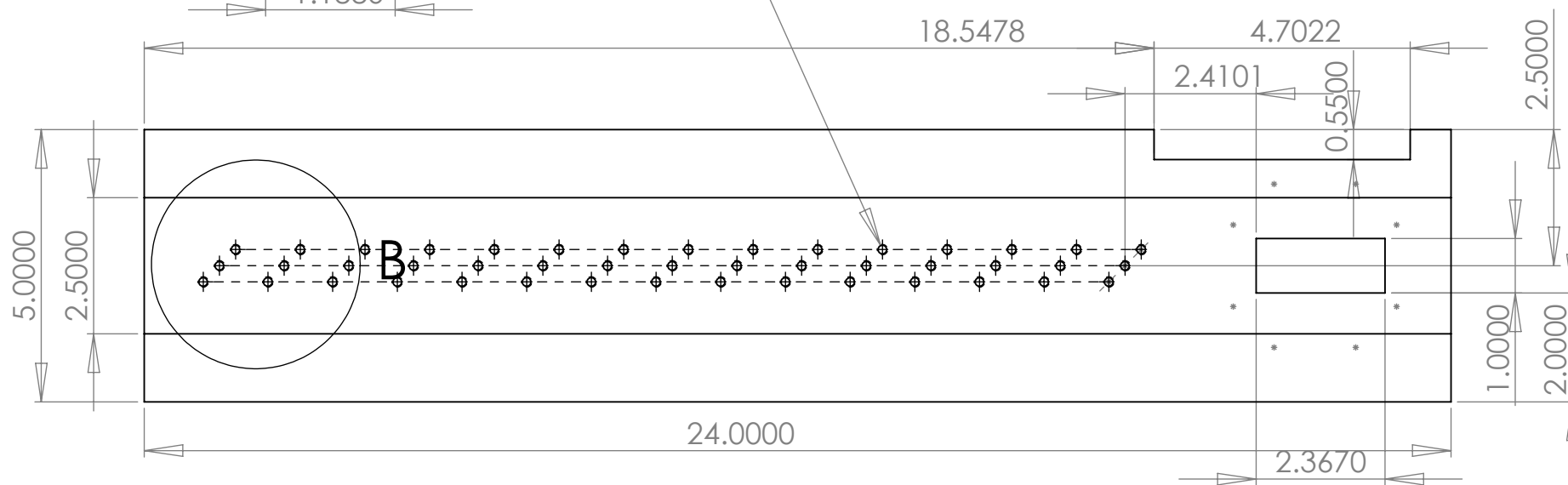
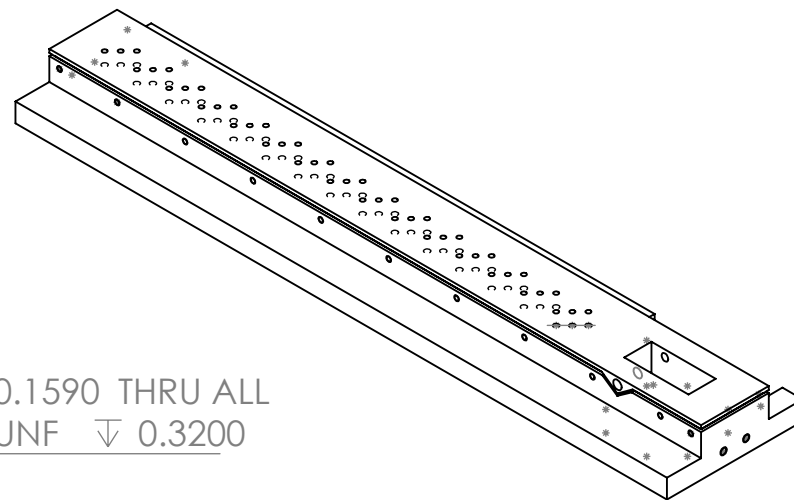
PROPRIETARY AND CONFIDENTIAL
 THE INFORMATION CONTAINED IN THIS DRAWING IS THE SOLE PROPERTY OF <INSERT COMPANY NAME HERE>. ANY REPRODUCTION IN PART OR AS A WHOLE WITHOUT THE WRITTEN PERMISSION OF <INSERT COMPANY NAME HERE> IS PROHIBITED.

		UNLESS OTHERWISE SPECIFIED:		NAME	DATE	TITLE: Top plate (PT exposed) Front, right, left view		
		DIMENSIONS ARE IN INCHES TOLERANCES: +/- 0.001	DRAWN	Richard Paek	1 Mar 10			
		FRACTIONAL ±	CHECKED					
		ANGULAR: MACH ± BEND ±	ENG APPR.					
		TWO PLACE DECIMAL ±	MFG APPR.					
		THREE PLACE DECIMAL ±				SIZE DWG. NO. REV A 202		
		INTERPRET GEOMETRIC TOLERANCING PER:	Q.A.					
		MATERIAL Aluminum	COMMENTS:					
		FINISH						
NEXT ASSY	USED ON					SCALE: 1:1 WEIGHT: SHEET 1 OF 1		
APPLICATION		DO NOT SCALE DRAWING						



DETAIL B
SCALE 2 : 3

45 x Ø 0.1590 THRU ALL
10-32 UNF ∇ 0.3200



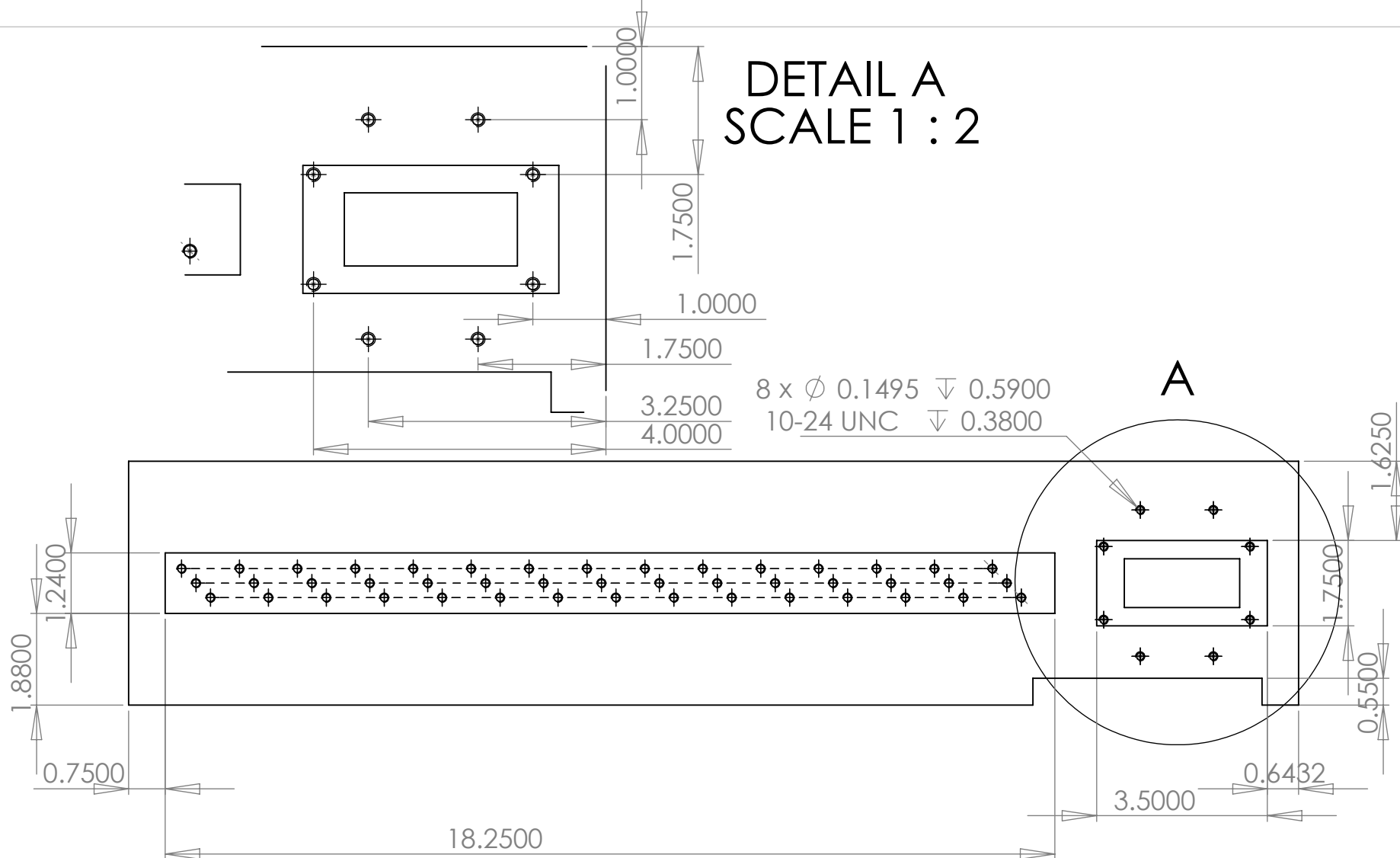
PROPRIETARY AND CONFIDENTIAL
THE INFORMATION CONTAINED IN THIS DRAWING IS THE SOLE PROPERTY OF <INSERT COMPANY NAME HERE>. ANY REPRODUCTION IN PART OR AS A WHOLE WITHOUT THE WRITTEN PERMISSION OF <INSERT COMPANY NAME HERE> IS PROHIBITED.

		UNLESS OTHERWISE SPECIFIED:		NAME	DATE
		DIMENSIONS ARE IN INCHES TOLERANCES: +/-0.001 FRACTIONAL ± ANGULAR: MACH ± BEND ± TWO PLACE DECIMAL ± THREE PLACE DECIMAL ±		DRAWN Richard Paek	1 Mar 10
				CHECKED	
				ENG APPR.	
				MFG APPR.	
		INTERPRET GEOMETRIC TOLERANCING PER:		Q.A.	
		MATERIAL Aluminum		COMMENTS:	
		FINISH			
NEXT ASSY	USED ON				
APPLICATION		DO NOT SCALE DRAWING			

TITLE:
Bottom plate (PT exposed)
Top view

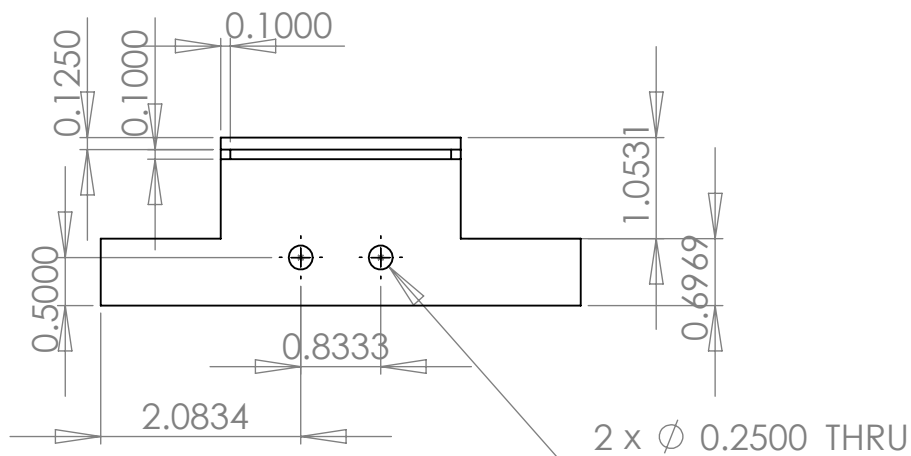
SIZE A	DWG. NO. 100	REV
SCALE: 1:5	WEIGHT:	SHEET 1 OF 1

DETAIL A
SCALE 1 : 2

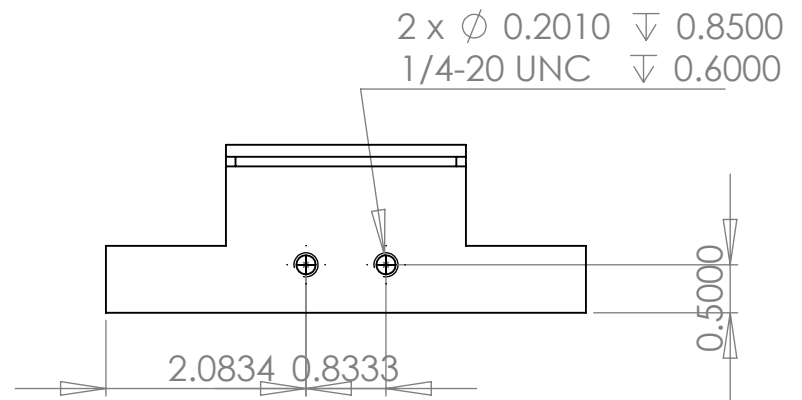


PROPRIETARY AND CONFIDENTIAL
THE INFORMATION CONTAINED IN THIS DRAWING IS THE SOLE PROPERTY OF <INSERT COMPANY NAME HERE>. ANY REPRODUCTION IN PART OR AS A WHOLE WITHOUT THE WRITTEN PERMISSION OF <INSERT COMPANY NAME HERE> IS PROHIBITED.

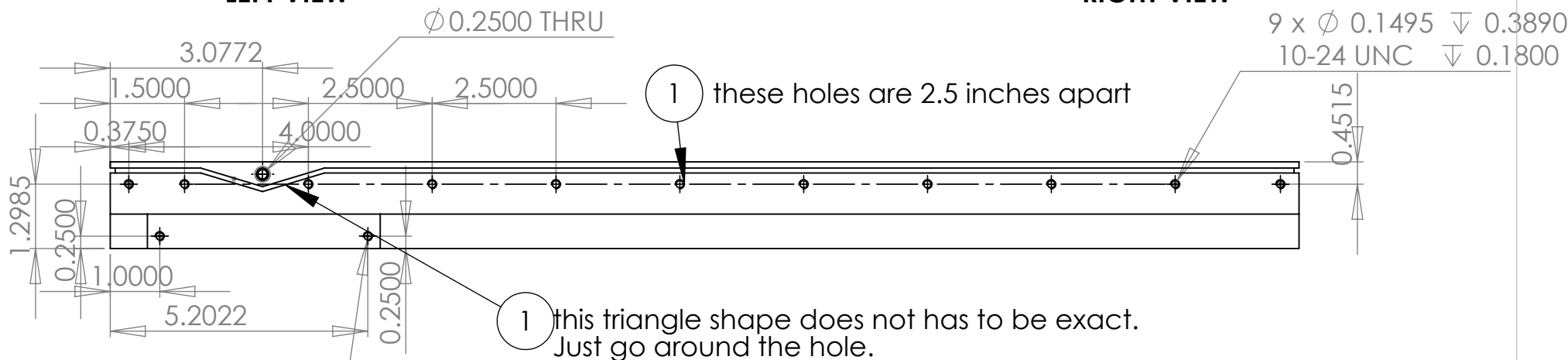
		UNLESS OTHERWISE SPECIFIED:		NAME	DATE	TITLE: Bottom Plate (PT exposed) Bottom view	
		DIMENSIONS ARE IN INCHES TOLERANCES: +/-0.0001 FRACTIONAL ± ANGULAR: MACH ± BEND ± TWO PLACE DECIMAL ± THREE PLACE DECIMAL ±	DRAWN	Richard Paek	1 Mar 10		
			CHECKED				
			ENG APPR.				
		INTERPRET GEOMETRIC TOLERANCING PER:	MFG APPR.			SIZE DWG. NO. REV A 101	
		MATERIAL Aluminum	Q.A.				
		FINISH	COMMENTS:				
NEXT ASSY	USED ON					SCALE: 1:5	WEIGHT:
APPLICATION		DO NOT SCALE DRAWING				SHEET 1 OF 1	



LEFT VIEW



RIGHT VIEW

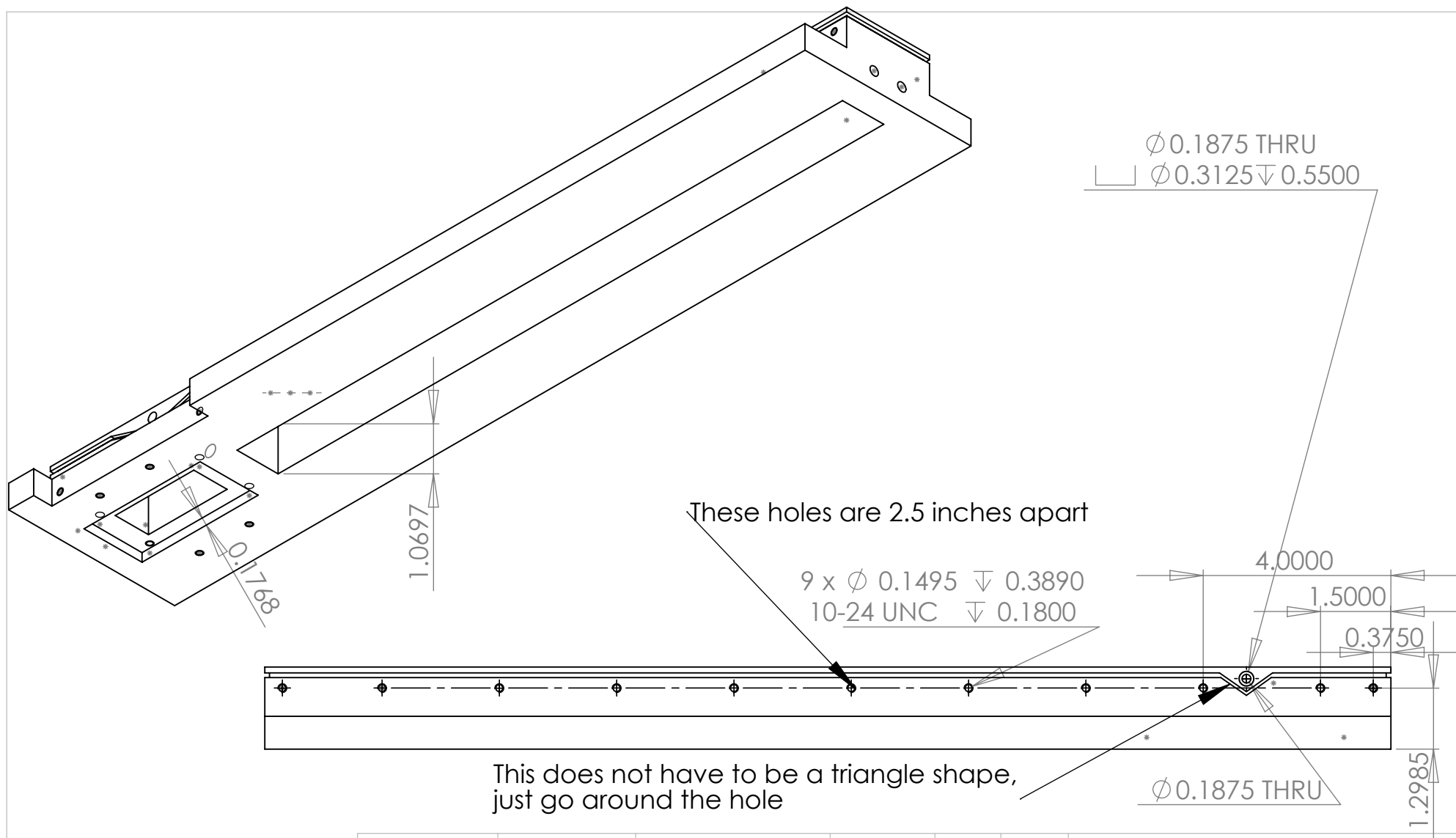


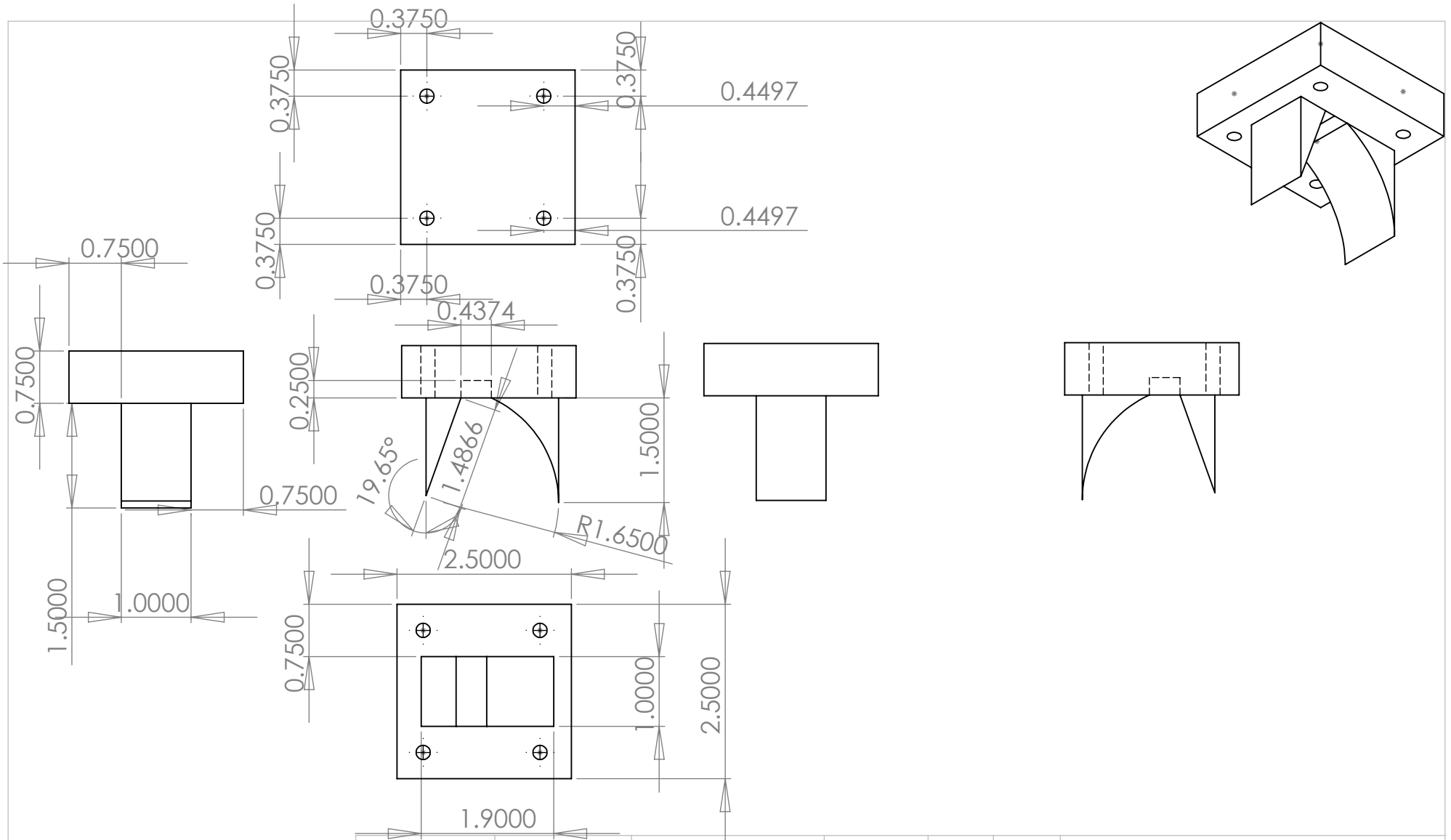
BACK VIEW

2 x Ø 0.1495 ± 0.3890
10-24 UNC ± 0.1800

PROPRIETARY AND CONFIDENTIAL
THE INFORMATION CONTAINED IN THIS DRAWING IS THE SOLE PROPERTY OF <INSERT COMPANY NAME HERE>. ANY REPRODUCTION IN PART OR AS A WHOLE WITHOUT THE WRITTEN PERMISSION OF <INSERT COMPANY NAME HERE> IS PROHIBITED.

		UNLESS OTHERWISE SPECIFIED:		NAME	DATE	TITLE: Bottom plate (PT exposed) Back, left, right view		
		DIMENSIONS ARE IN INCHES TOLERANCES: +/-0.0001 FRACTIONAL ± ANGULAR: MACH± BEND ± TWO PLACE DECIMAL ± THREE PLACE DECIMAL ±	DRAWN	Richard Paek	1 Mar 10			
			CHECKED					
			ENG APPR.					
			MFG APPR.					
		INTERPRET GEOMETRIC TOLERANCING PER:	Q.A.			COMMENTS:		
		MATERIAL Aluminum						
NEXT ASSY	USED ON	FINISH				SIZE A	DWG. NO. 102	REV
APPLICATION		DO NOT SCALE DRAWING				SCALE: 1:1	WEIGHT:	SHEET 1 OF 1





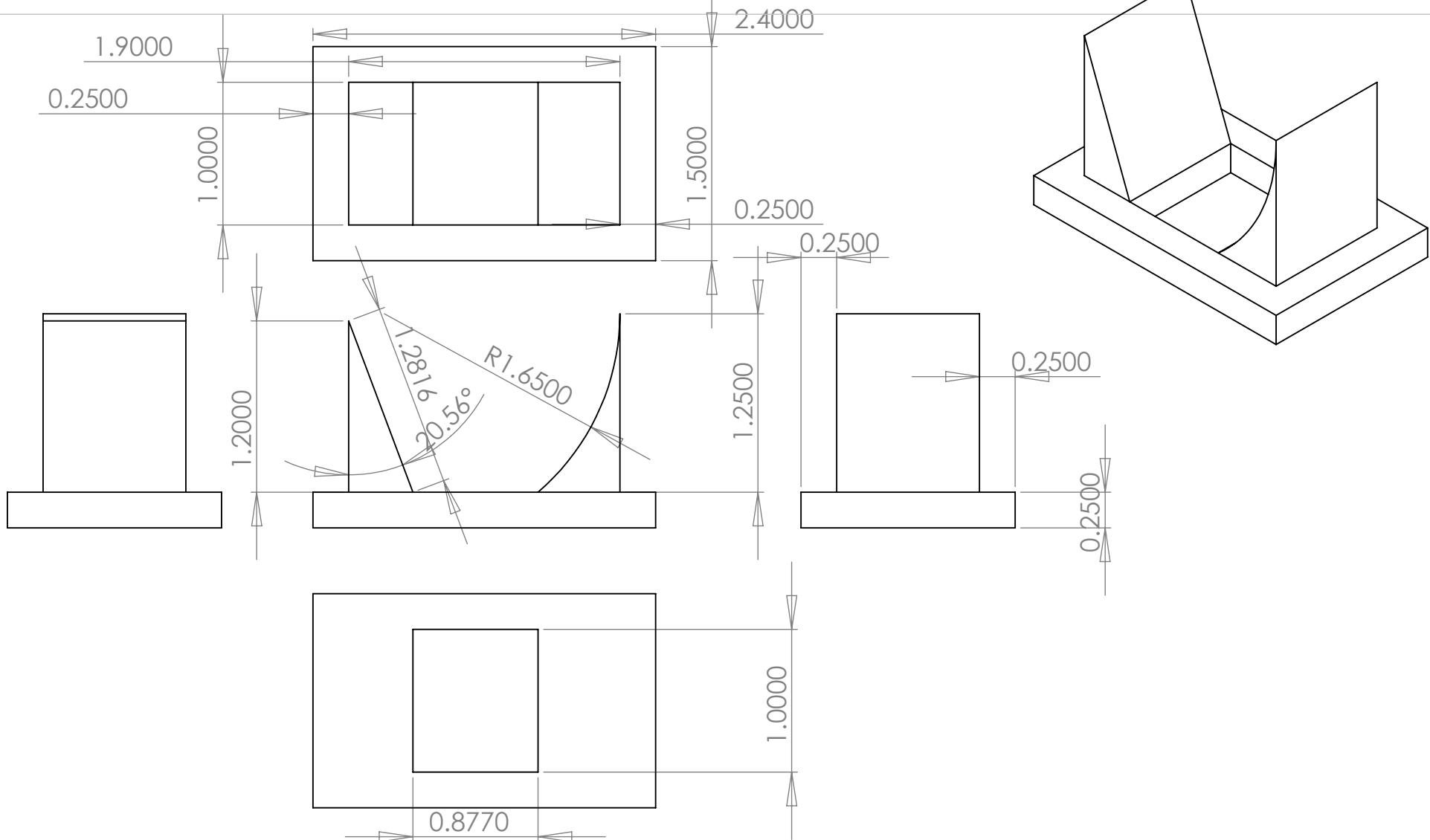
PROPRIETARY AND CONFIDENTIAL
 THE INFORMATION CONTAINED IN THIS DRAWING IS THE SOLE PROPERTY OF <INSERT COMPANY NAME HERE>. ANY REPRODUCTION IN PART OR AS A WHOLE WITHOUT THE WRITTEN PERMISSION OF <INSERT COMPANY NAME HERE> IS PROHIBITED.

NEXT ASSY	USED ON
APPLICATION	

UNLESS OTHERWISE SPECIFIED:
DIMENSIONS ARE IN INCHES
TOLERANCES:
FRACTIONAL ± 0.002
ANGULAR: MACH \pm BEND \pm
TWO PLACE DECIMAL \pm
THREE PLACE DECIMAL \pm
INTERPRET GEOMETRIC TOLERANCING PER:
MATERIAL: Aluminum
FINISH
DO NOT SCALE DRAWING

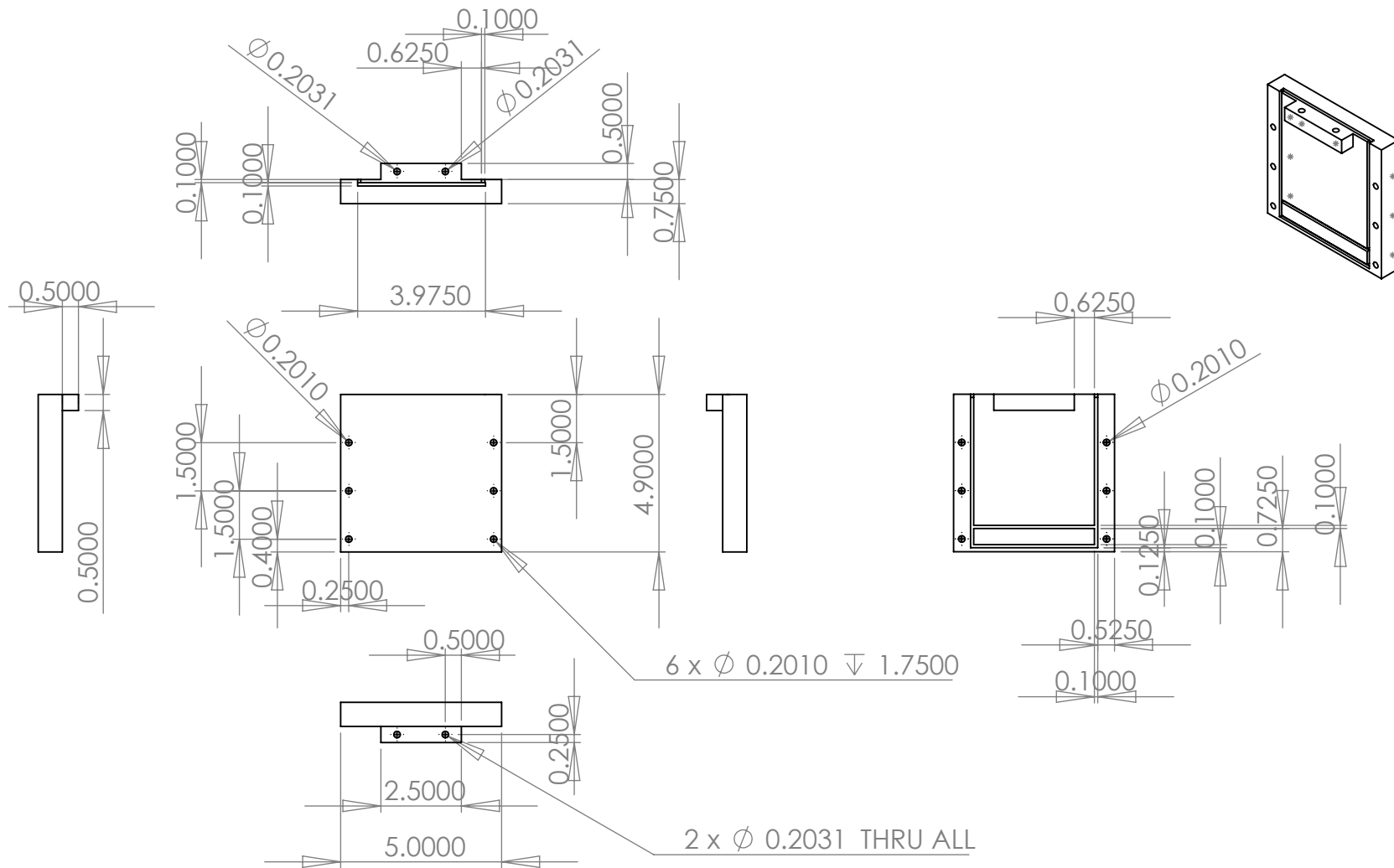
	NAME	DATE
DRAWN	Richard Paek	26 Oct 09
CHECKED		
ENG APPR.		
MFG APPR.		
Q.A.		
COMMENTS:		

TITLE:		
Top insert		
SIZE	DWG. NO.	REV
A	Drawing 16A	
SCALE: 1:2	WEIGHT:	SHEET 1 OF 1



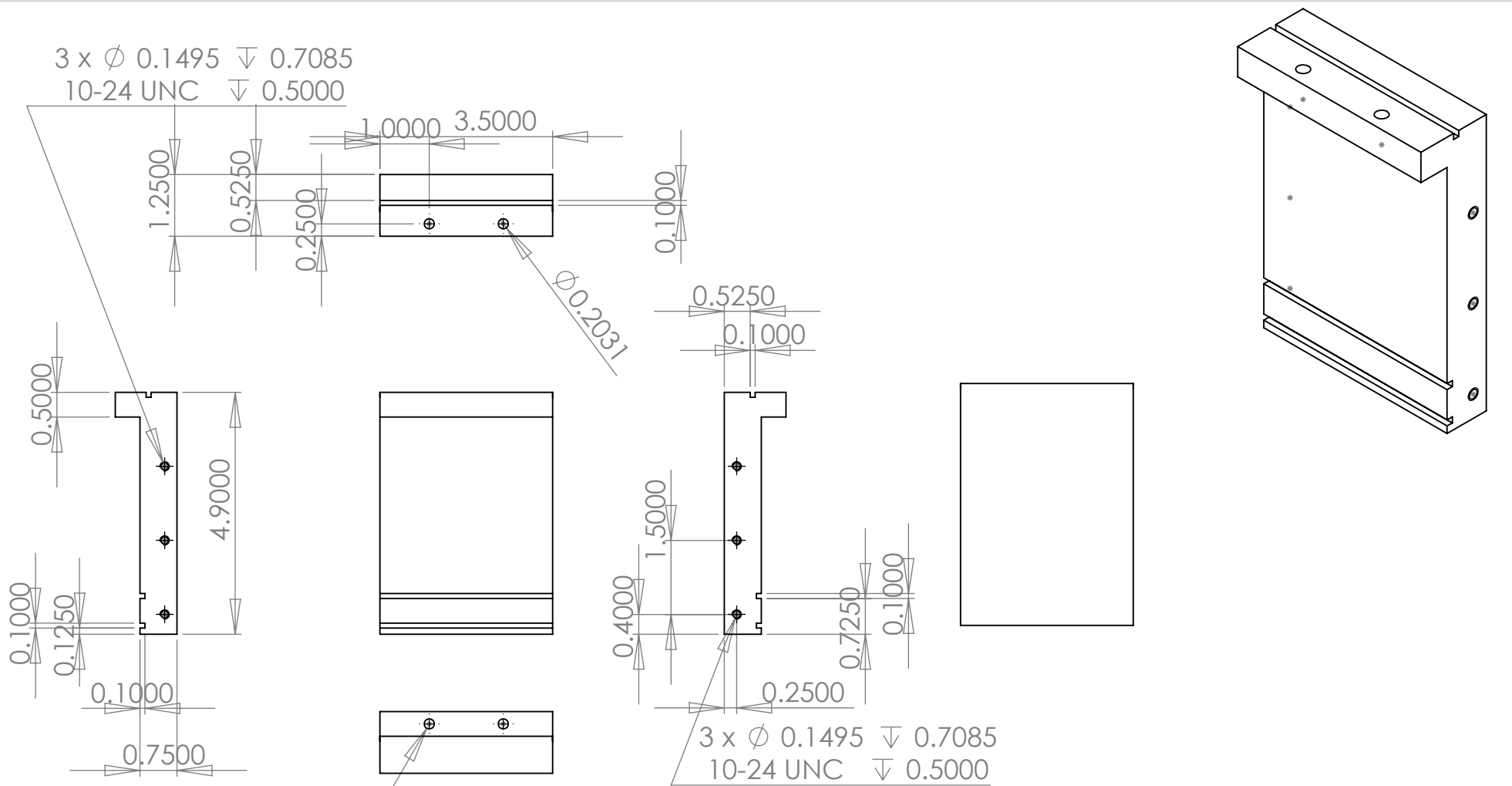
PROPRIETARY AND CONFIDENTIAL
THE INFORMATION CONTAINED IN THIS
DRAWING IS THE SOLE PROPERTY OF
<INSERT COMPANY NAME HERE>. ANY
REPRODUCTION IN PART OR AS A WHOLE
WITHOUT THE WRITTEN PERMISSION OF
<INSERT COMPANY NAME HERE> IS
PROHIBITED.

		UNLESS OTHERWISE SPECIFIED:		NAME	DATE	TITLE: Bottom Insert		
		DIMENSIONS ARE IN INCHES TOLERANCES: FRACTIONAL ±0.002 ANGULAR: MACH ± BEND ± TWO PLACE DECIMAL ± THREE PLACE DECIMAL ±	DRAWN	Richard Paek	26 Oct 09			
			CHECKED					
			ENG APPR.					
			MFG APPR.					
		INTERPRET GEOMETRIC TOLERANCING PER:	Q.A.			SIZE DWG. NO. REV A Drawing 17A		
		MATERIAL: Aluminum	COMMENTS:					
		FINISH						
NEXT ASSY	USED ON							
APPLICATION		DO NOT SCALE DRAWING				SCALE: 1:1 WEIGHT: SHEET 1 OF 1		



PROPRIETARY AND CONFIDENTIAL
THE INFORMATION CONTAINED IN THIS DRAWING IS THE SOLE PROPERTY OF <INSERT COMPANY NAME HERE>. ANY REPRODUCTION IN PART OR AS A WHOLE WITHOUT THE WRITTEN PERMISSION OF <INSERT COMPANY NAME HERE> IS PROHIBITED.

		UNLESS OTHERWISE SPECIFIED:	NAME	DATE	TITLE: Hydraulic Box Front &Back		
		DIMENSIONS ARE IN INCHES TOLERANCES: FRACTIONAL ± 0.002 ANGULAR: MACH \pm BEND \pm TWO PLACE DECIMAL \pm THREE PLACE DECIMAL \pm	DRAWN Richard Paek	19 Oct 09			
		INTERPRET GEOMETRIC TOLERANCING PER:	CHECKED				
		MATERIAL Aluminum	ENG APPR.				
		FINISH	MFG APPR.		SIZE DWG. NO. REV A Drawing 1		
NEXT ASSY	USED ON		Q.A.				
APPLICATION		DO NOT SCALE DRAWING	COMMENTS: Make 2.		SCALE: 1:1	WEIGHT:	SHEET 1 OF 1



2 x \varnothing 0.2031 THRU ALL

PROPRIETARY AND CONFIDENTIAL
THE INFORMATION CONTAINED IN THIS DRAWING IS THE SOLE PROPERTY OF <INSERT COMPANY NAME HERE>. ANY REPRODUCTION IN PART OR AS A WHOLE WITHOUT THE WRITTEN PERMISSION OF <INSERT COMPANY NAME HERE> IS PROHIBITED.

		UNLESS OTHERWISE SPECIFIED:		NAME	DATE	TITLE: Hydraulic Box Left & Right	
		DIMENSIONS ARE IN INCHES TOLERANCES: FRACTIONAL \pm 0.002 ANGULAR: MACH \pm BEND \pm TWO PLACE DECIMAL \pm THREE PLACE DECIMAL \pm	DRAWN	Richard Paek	19 Oct 09		
			CHECKED				
			ENG APPR.				
		INTERPRET GEOMETRIC TOLERANCING PER:	MFG APPR.			SIZE DWG. NO. REV A Drawing 2 1	
		MATERIAL: Aluminum	Q.A.				
		FINISH	COMMENTS:	Make 2		SCALE: 1:1	WEIGHT:
NEXT ASSY	USED ON						SHEET 1 OF 1
APPLICATION		DO NOT SCALE DRAWING					

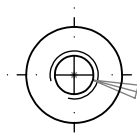
5

4

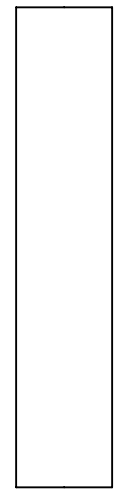
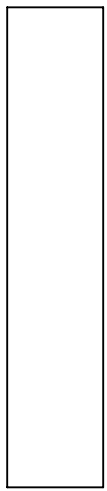
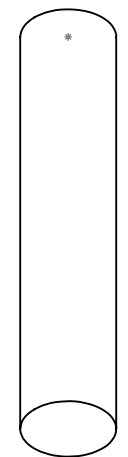
3

2

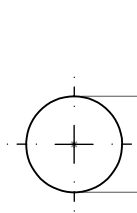
1



Ø 0.2010 ∇ 1.2500
1/4-20 UNC ∇ 1.0000



2.5000

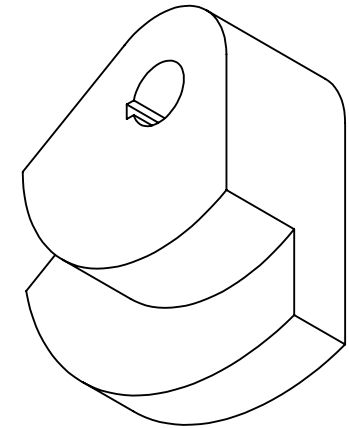
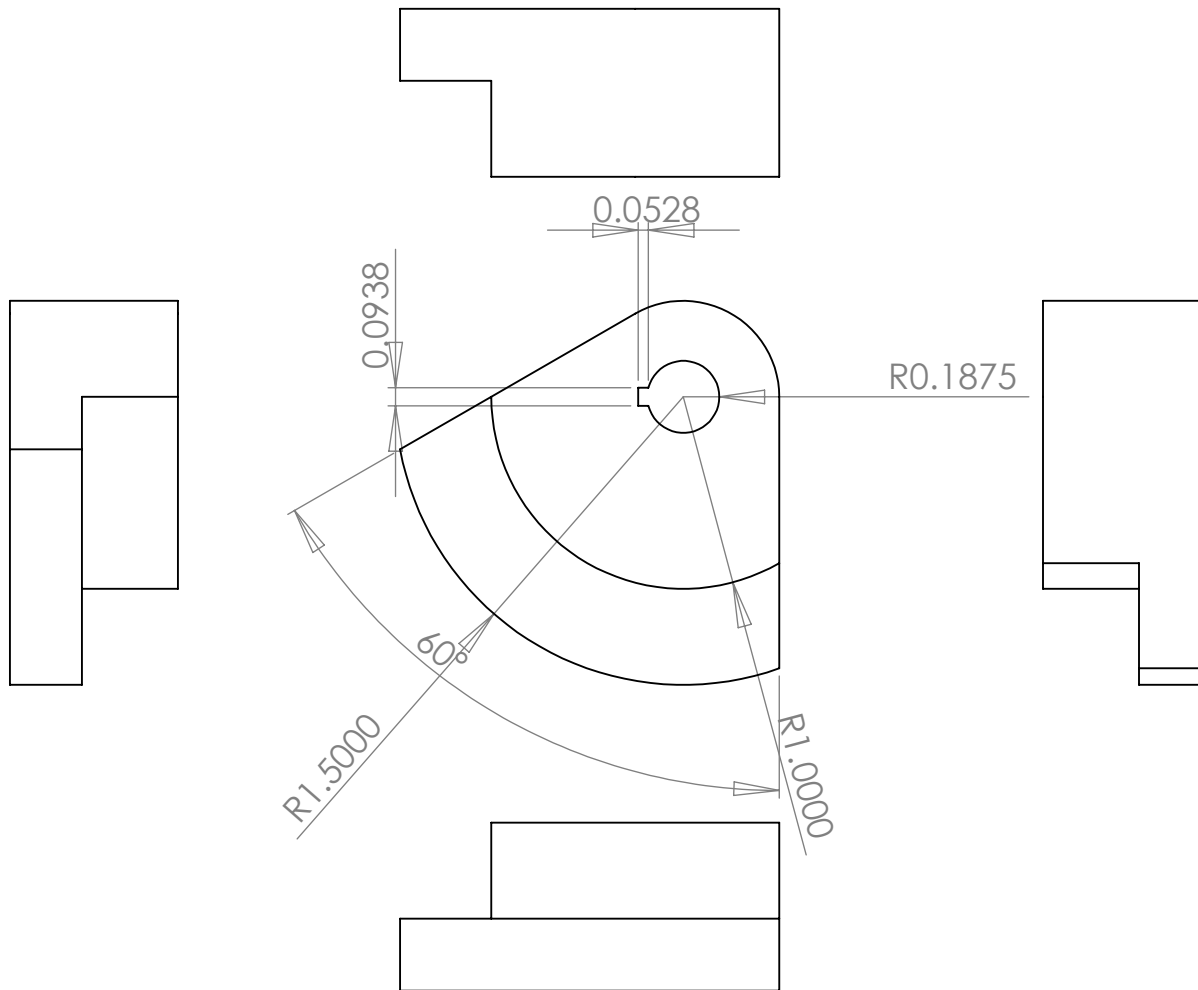


Ø 0.5000

This is supposed to be full-thread rod. This rod will be give to you. also see comments below.

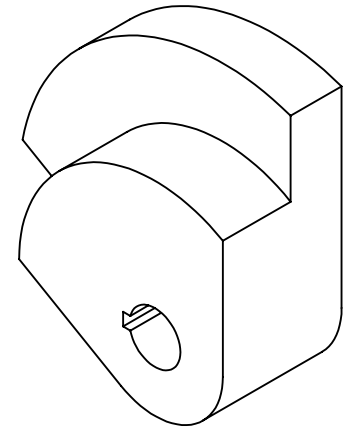
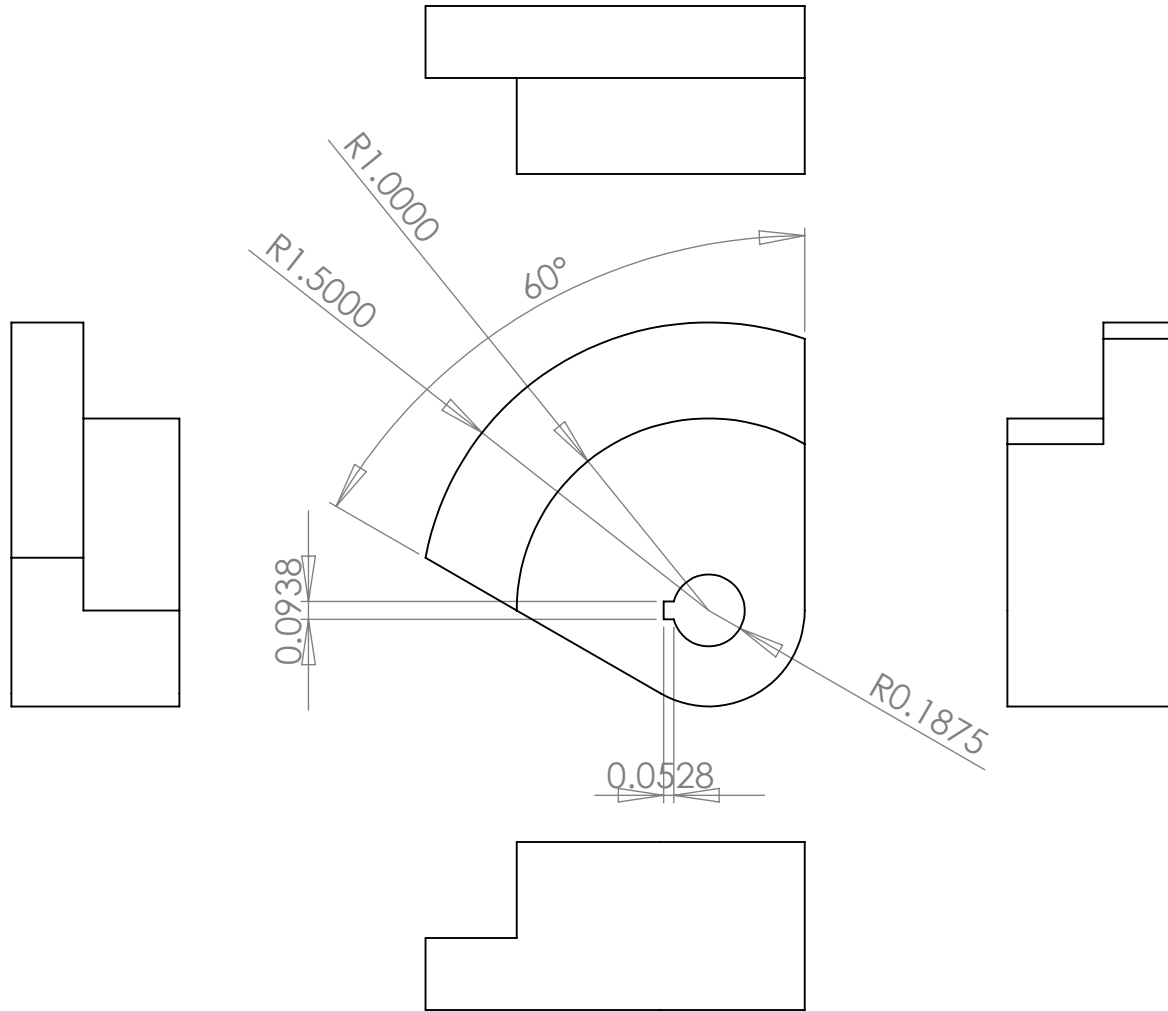
PROPRIETARY AND CONFIDENTIAL
THE INFORMATION CONTAINED IN THIS DRAWING IS THE SOLE PROPERTY OF <INSERT COMPANY NAME HERE>. ANY REPRODUCTION IN PART OR AS A WHOLE WITHOUT THE WRITTEN PERMISSION OF <INSERT COMPANY NAME HERE> IS PROHIBITED.

		UNLESS OTHERWISE SPECIFIED:		NAME	DATE	TITLE: Connector between hydraulic actuator and T-bar		
		DIMENSIONS ARE IN INCHES TOLERANCES: FRACTIONAL ±0.002 ANGULAR: MACH ± BEND ± TWO PLACE DECIMAL ± THREE PLACE DECIMAL ±	DRAWN	Richard Paek	20 Oct 09			
			CHECKED					
			ENG APPR.					
			MFG APPR.					
		INTERPRET GEOMETRIC TOLERANCING PER:	Q.A.			SIZE DWG. NO. REV A Drawing 8		
		MATERIAL: Stainless Steel	COMMENTS: 12" length 1/2"-20 thread stainless rod will be given. cut in 2.5" and make a tapped hole at one end.					
		FINISH						
NEXT ASSY	USED ON							
APPLICATION		DO NOT SCALE DRAWING						



PROPRIETARY AND CONFIDENTIAL
THE INFORMATION CONTAINED IN THIS DRAWING IS THE SOLE PROPERTY OF <INSERT COMPANY NAME HERE>. ANY REPRODUCTION IN PART OR AS A WHOLE WITHOUT THE WRITTEN PERMISSION OF <INSERT COMPANY NAME HERE> IS PROHIBITED.

		UNLESS OTHERWISE SPECIFIED:		NAME	DATE	TITLE: Japanese fan shape gear - top		
		DIMENSIONS ARE IN INCHES TOLERANCES: FRACTIONAL ± ANGULAR: MACH ± BEND ± TWO PLACE DECIMAL ± THREE PLACE DECIMAL ±	DRAWN	Richard Paek	20 Oct 09			
			CHECKED					
			ENG APPR.					
			MFG APPR.					
		INTERPRET GEOMETRIC TOLERANCING PER:	Q.A.			SIZE DWG. NO. REV A Drawing 9		
		MATERIAL: Steel	COMMENTS: A circular gear will be given to you. just cut it in 60 degree fan shape.					
		FINISH						
NEXT ASSY	USED ON							
APPLICATION		DO NOT SCALE DRAWING	SCALE: 1:1				WEIGHT:	SHEET 1 OF 1



PROPRIETARY AND CONFIDENTIAL
THE INFORMATION CONTAINED IN THIS
DRAWING IS THE SOLE PROPERTY OF
<INSERT COMPANY NAME HERE>. ANY
REPRODUCTION IN PART OR AS A WHOLE
WITHOUT THE WRITTEN PERMISSION OF
<INSERT COMPANY NAME HERE> IS
PROHIBITED.

		UNLESS OTHERWISE SPECIFIED:		NAME	DATE	TITLE: Japanese fan shape gear - bottom	
		DIMENSIONS ARE IN INCHES TOLERANCES: FRACTIONAL ± ANGULAR: MACH ± BEND ± TWO PLACE DECIMAL ± THREE PLACE DECIMAL ±	DRAWN	Richard Paek	20 Oct 09		
		INTERPRET GEOMETRIC TOLERANCING PER:	CHECKED				
		MATERIAL: Steel	ENG APPR.				
		FINISH	MFG APPR.			SIZE DWG. NO. REV A Drawing 10	
			Q.A.				
			COMMENTS: Circular gear will be given to you. Cut it in 60 degree japanese fan shape.			SCALE: 1:1	WEIGHT:
							SHEET 1 OF 1

1.0000

R0.2500

R0.1250

0.0560

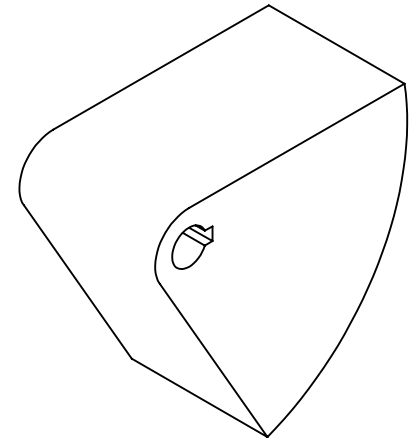
0.0938

0.2500

0.2500

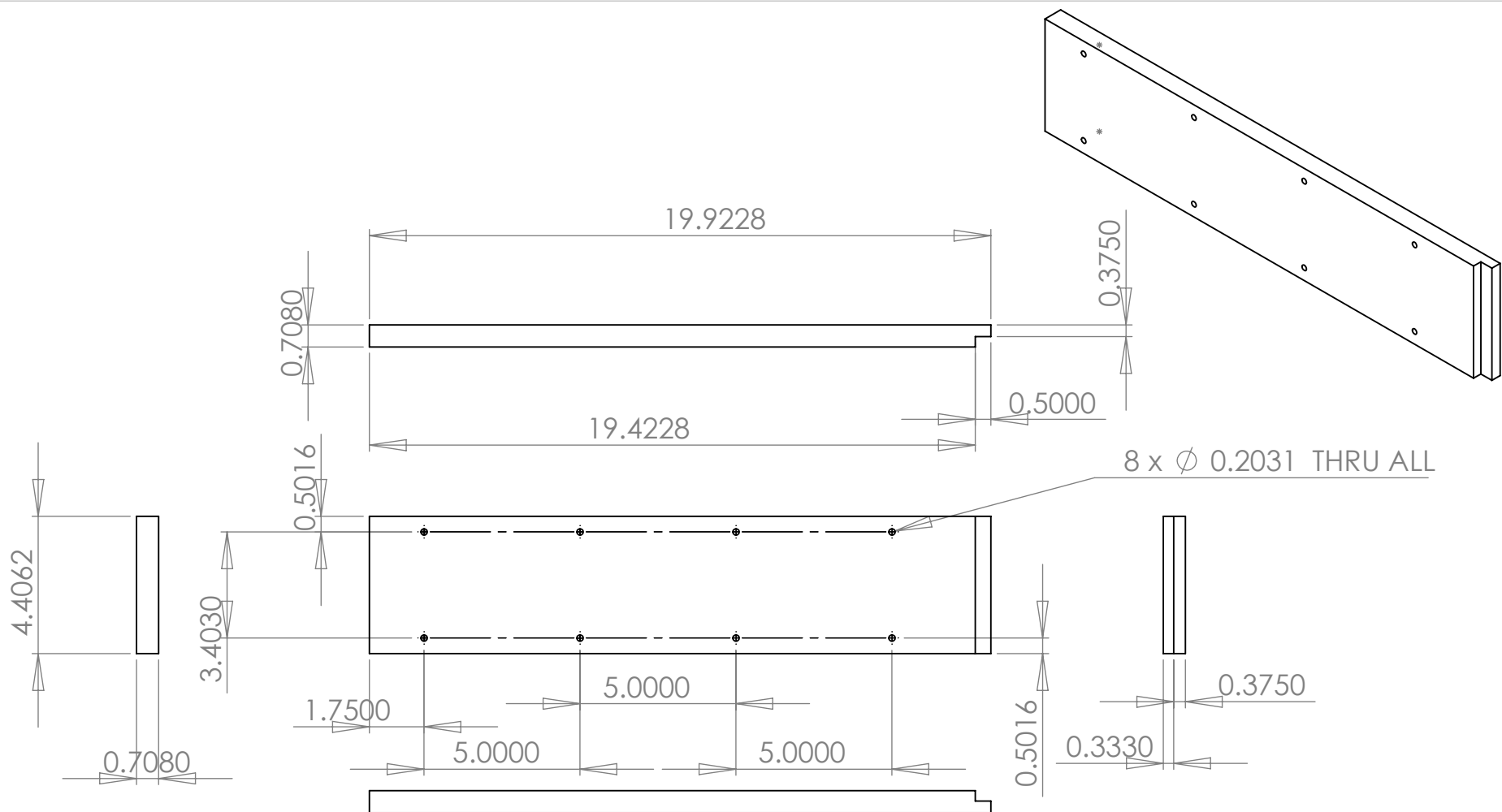
60°

R1.6071



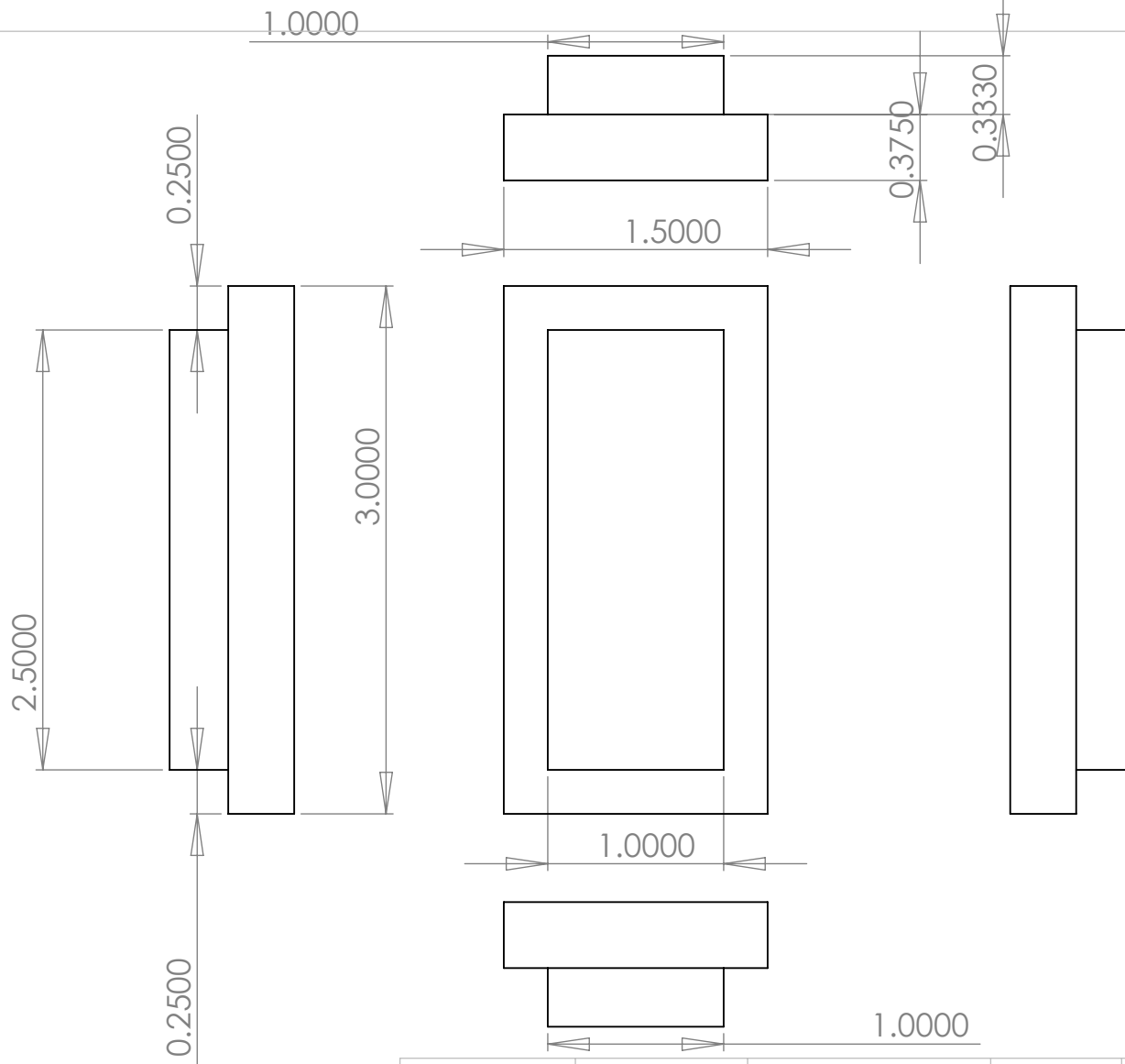
PROPRIETARY AND CONFIDENTIAL
THE INFORMATION CONTAINED IN THIS
DRAWING IS THE SOLE PROPERTY OF
<INSERT COMPANY NAME HERE>. ANY
REPRODUCTION IN PART OR AS A WHOLE
WITHOUT THE WRITTEN PERMISSION OF
<INSERT COMPANY NAME HERE> IS
PROHIBITED.

		UNLESS OTHERWISE SPECIFIED:	NAME	DATE	TITLE: Ramp (top)						
		DIMENSIONS ARE IN INCHES	DRAWN	Richard Paek				26 Oct 09			
		TOLERANCES:	CHECKED								
		FRACTIONAL ±0.002	ENG APPR.								
		ANGULAR: MACH± BEND ±	MFG APPR.								
		TWO PLACE DECIMAL ±	COMMENTS:			SIZE		DWG. NO.		REV	
		THREE PLACE DECIMAL ±				Drawing 11A					
		INTERPRET GEOMETRIC TOLERANCING PER:									
		MATERIAL: Aluminum									
NEXT ASSY	USED ON	FINISH									
APPLICATION		DO NOT SCALE DRAWING	SCALE: 1:1 WEIGHT: SHEET 1 OF 1								



PROPRIETARY AND CONFIDENTIAL
 THE INFORMATION CONTAINED IN THIS
 DRAWING IS THE SOLE PROPERTY OF
 <INSERT COMPANY NAME HERE>. ANY
 REPRODUCTION IN PART OR AS A WHOLE
 WITHOUT THE WRITTEN PERMISSION OF
 <INSERT COMPANY NAME HERE> IS
 PROHIBITED.

		UNLESS OTHERWISE SPECIFIED:									
		DIMENSIONS ARE IN INCHES TOLERANCES: FRACTIONAL ±0.002 ANGULAR: MACH ± BEND ± TWO PLACE DECIMAL ± THREE PLACE DECIMAL ±	DRAWN	Richard Paek	19 Oct 09	TITLE: Acrylic Side Walls					
			CHECKED								
			ENG APPR.								
			MFG APPR.								
		INTERPRET GEOMETRIC TOLERANCING PER:	Q.A.								
		MATERIAL: Cast Acrylic	COMMENTS:								
		FINISH	Make 2								
NEXT ASSY	USED ON										
APPLICATION		DO NOT SCALE DRAWING	SIZE						DWG. NO.		REV
			A						Drawing 4		
			SCALE: 1:1						WEIGHT:		SHEET 1 OF 1



PROPRIETARY AND CONFIDENTIAL
THE INFORMATION CONTAINED IN THIS DRAWING IS THE SOLE PROPERTY OF <INSERT COMPANY NAME HERE>. ANY REPRODUCTION IN PART OR AS A WHOLE WITHOUT THE WRITTEN PERMISSION OF <INSERT COMPANY NAME HERE> IS PROHIBITED.

		UNLESS OTHERWISE SPECIFIED:		NAME	DATE	TITLE: Small Window		
		DIMENSIONS ARE IN INCHES	DRAWN	Richard Paek	19 Oct 09			
		TOLERANCES:	CHECKED					
		FRACTIONAL ± 0.002	ENG APPR.					
		ANGULAR: MACH \pm BEND \pm	MFG APPR.					
		TWO PLACE DECIMAL \pm	Q.A.			SIZE	DWG. NO.	REV
		THREE PLACE DECIMAL \pm	COMMENTS:			A	Drawing 5	
		INTERPRET GEOMETRIC TOLERANCING PER:				SCALE: 1:1	WEIGHT:	SHEET 1 OF 1
		MATERIAL: Cast Acrylic						
NEXT ASSY	USED ON	FINISH						
APPLICATION		DO NOT SCALE DRAWING						

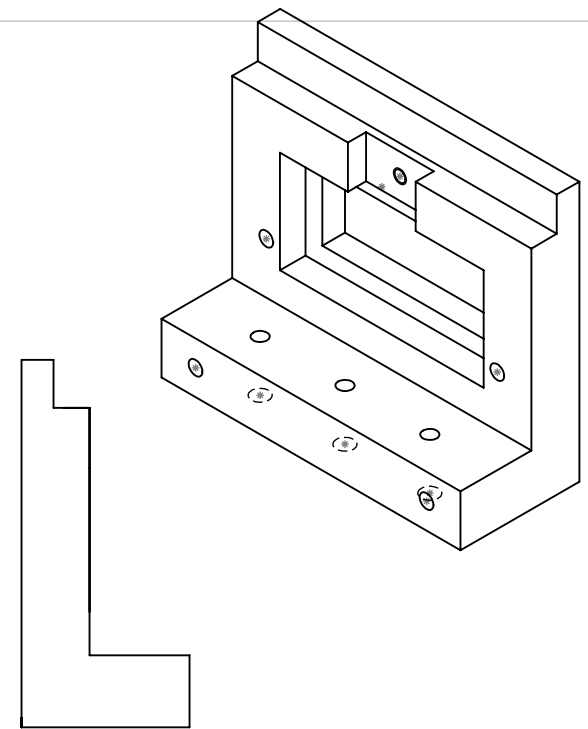
5

4

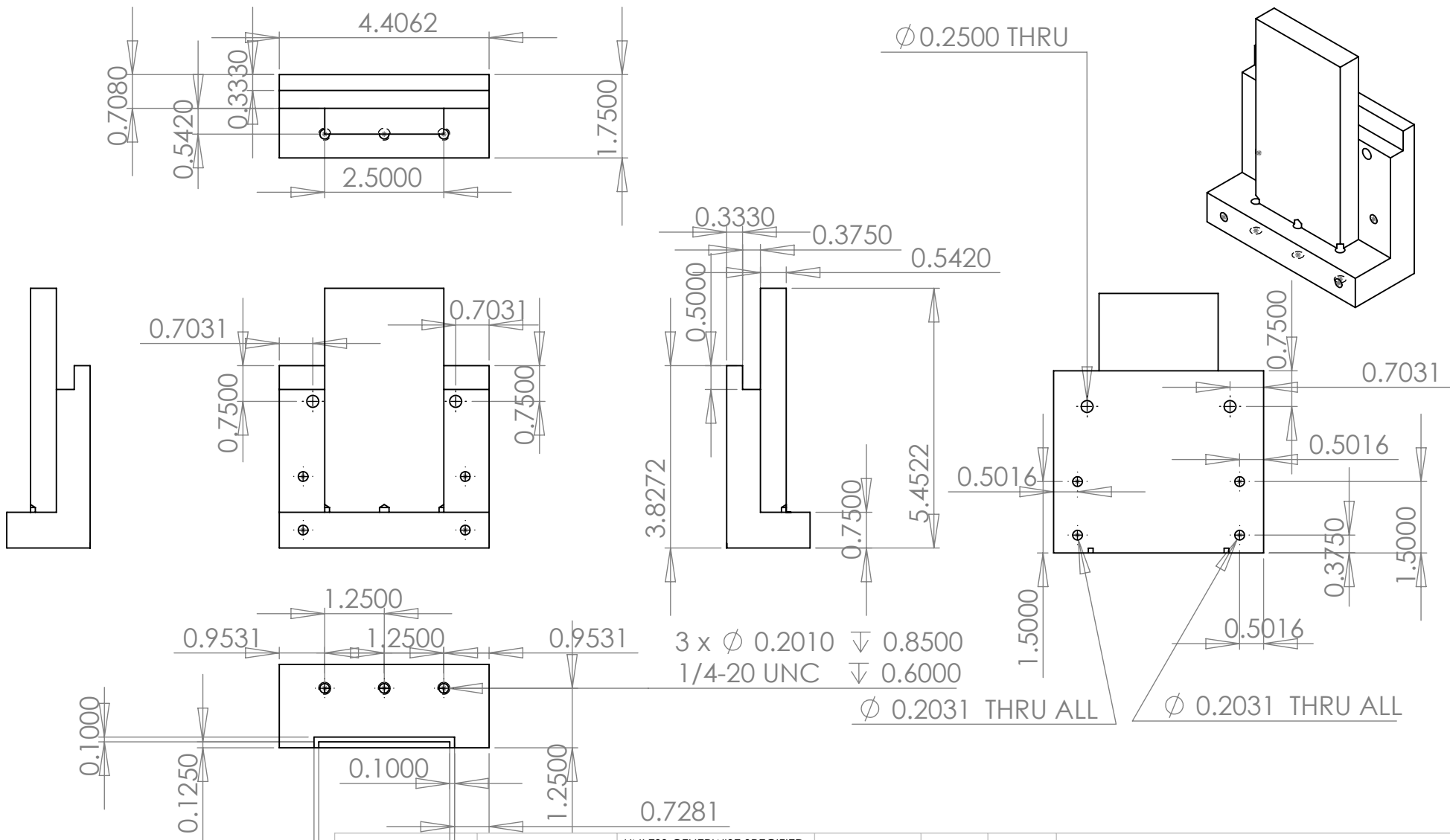
3

2

1



SHEET 1 OF 1



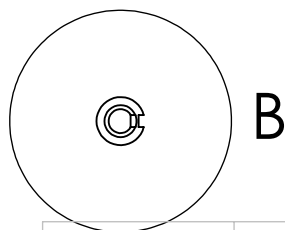
PROPRIETARY AND CONFIDENTIAL

THE INFORMATION CONTAINED IN THIS DRAWING IS THE SOLE PROPERTY OF <INSERT COMPANY NAME HERE>. ANY REPRODUCTION IN PART OR AS A WHOLE WITHOUT THE WRITTEN PERMISSION OF <INSERT COMPANY NAME HERE> IS PROHIBITED.

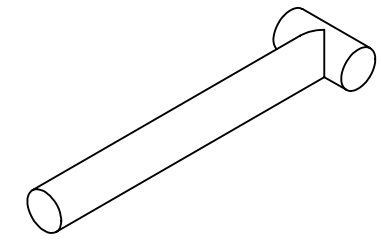
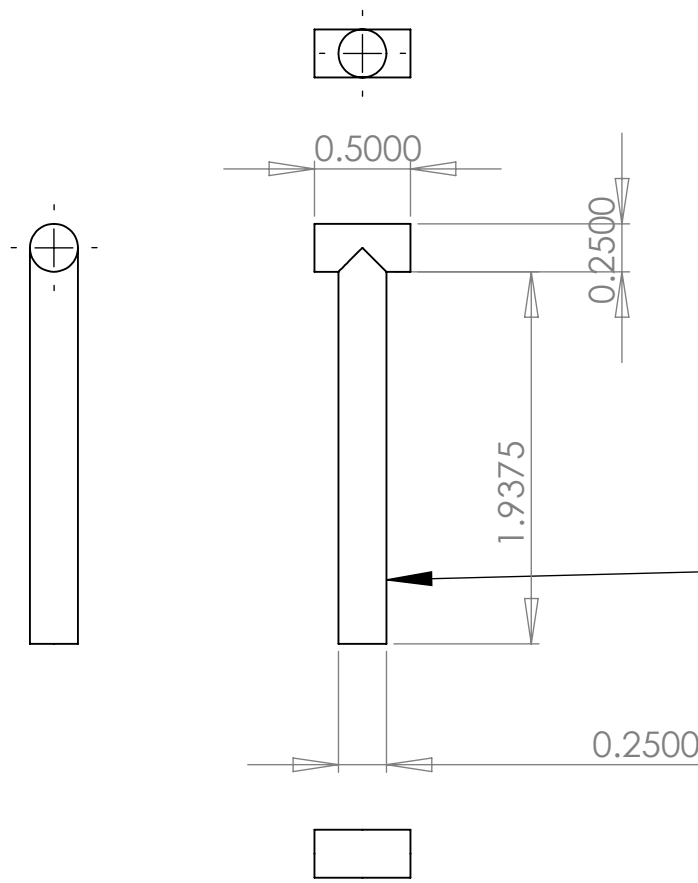
UNLESS OTHERWISE SPECIFIED:	
DIMENSIONS ARE IN INCHES	
TOLERANCES:	
FRACTIONAL ±0.002	
ANGULAR: MACH ± BEND ±	
TWO PLACE DECIMAL ±	
THREE PLACE DECIMAL ±	
INTERPRET GEOMETRIC TOLERANCING PER:	
MATERIAL: Aluminum	
FINISH	
NEXT ASSY	USED ON
APPLICATION	
DO NOT SCALE DRAWING	

NAME	DATE
DRAWN	Richard Paek 24 Oct 09
CHECKED	
ENG APPR.	
MFG APPR.	
Q.A.	
COMMENTS:	

TITLE:		
Rear Elbow Right		
SIZE	DWG. NO.	REV
A	Drawing 14	
SCALE: 1:1	WEIGHT:	SHEET 1 OF 1



<div>PROPRIETARY AND CONFIDENTIAL</div> <div>THE INFORMATION CONTAINED IN THIS DRAWING IS THE SOLE PROPERTY OF <INSERT COMPANY NAME HERE>. ANY REPRODUCTION IN PART OR AS A WHOLE WITHOUT THE WRITTEN PERMISSION OF <INSERT COMPANY NAME HERE> IS PROHIBITED.</div>			UNLESS OTHERWISE SPECIFIED:		NAME	DATE	TITLE: Keyed Shaft with 3 different diameters		
			DIMENSIONS ARE IN INCHES TOLERANCES: FRACTIONAL ±0.002 ANGULAR: MACH ± BEND ± TWO PLACE DECIMAL ± THREE PLACE DECIMAL ±	DRAWN	Richard Paek	21 Oct 09			
				CHECKED					
				ENG APPR.					
				MFG APPR.			SIZE DWG. NO. REV A Drawing 15		
			INTERPRET GEOMETRIC TOLERANCING PER:	Q.A.					
			MATERIAL: Steel	COMMENTS: Make 2. 3/8" diameter steel keyed shafts will be given to you.					
		NEXT ASSY	USED ON	FINISH	SCALE: 1:2 WEIGHT: SHEET 1 OF 1				
APPLICATION		DO NOT SCALE DRAWING							
5	4	3	2	1					



This end of rod will be male thread.
Thread: 1/4-20
Length: 1 inch

A long .25 inch diameter stainless steel will be given to you. Cut one in 0.5 inch and cut one in 1.9375 inch and make a T-bar as shown.

PROPRIETARY AND CONFIDENTIAL
THE INFORMATION CONTAINED IN THIS DRAWING IS THE SOLE PROPERTY OF <INSERT COMPANY NAME HERE>. ANY REPRODUCTION IN PART OR AS A WHOLE WITHOUT THE WRITTEN PERMISSION OF <INSERT COMPANY NAME HERE> IS PROHIBITED.

		UNLESS OTHERWISE SPECIFIED:		NAME	DATE	TITLE: T-Bar		
		DIMENSIONS ARE IN INCHES	DRAWN	Richard Paek	20 Oct 09			
		TOLERANCES:	CHECKED					
		FRACTIONAL ±0.002	ENG APPR.					
		ANGULAR: MACH± BEND ±	MFG APPR.			SIZE DWG. NO. REV A Drawing 7		
		TWO PLACE DECIMAL ±	Q.A.					
		THREE PLACE DECIMAL ±	COMMENTS:					
		INTERPRET GEOMETRIC TOLERANCING PER:						
		MATERIAL: Stainless Steel						
		FINISH						
	NEXT ASSY	USED ON				SCALE: 1:1 WEIGHT: SHEET 1 OF 1		
APPLICATION		DO NOT SCALE DRAWING						

Appendix D. Endevco pressure sensor/amplifier in-house calibration results

$$y = a \cdot x + b$$

y = pressure applied on the sensors (psi)

a = sensitivity (psi/V)

x = voltage out from the amplifier (V)

b = offset (psi)

Table 7. Endevco pressure sensor/amplifier in-house calibration results

Amplifier #	Sensor #	Calibration results
1	1	$y = 0.198 x + 0.0014$
	2	$y = 0.2015 x + 0.23$
	3	$y = 0.2024 x - 0.4672$
2	1	$y = 0.2019 x - 0.2252$
	2	$y = 0.201 x + 0.0566$
	3	$y = 0.2034 x + 0.1279$
3	1	$y = 0.2 x + 0.1785$
	2	$y = 0.2019 x + 0.1441$
	3	$y = 0.2001 x - 0.11$
4	1	$y = 0.2001 x + 0.0132$
	2	$y = 0.201 x + 0.076$
	3	$y = 0.2013 x - 0.66$

Appendix E. Unit conversion from MTS reading

1. The ratio of the MTS reading to the true length is 0.643:0.99974.

2. Converting from true actuator height to ramp angle.

$$\begin{aligned} & \text{converting_from_actuator_height_to_ramp_angle} \\ & \theta = \text{ramp_angle(deg)} \\ & \Delta h_{act} = \text{actuator_height(inch)} \\ & \theta = 60 - \tan^{-1} \left(\frac{0.99974 - \Delta h_{act}}{0.5772} \right) \end{aligned}$$

3. Converting from ramp angle to ramp edge height.

$$\begin{aligned} & \text{converting_from_ramp_angle_to_ramp_edge_height} \\ & \Delta h_{ramp} = \text{ramp_height(inch)} \\ & \Delta h_{ramp} = 1.5875 \cdot \sin \theta - 0.25 + 0.25 \cdot \cos \theta \end{aligned}$$

4. Calculating area blocked from the ramp edge height.

$$\begin{aligned} & \text{calculating_area_blocked_from_ramp_edge_height} \\ & A = 1 \cdot \Delta h_{ramp} \cdot 2 \end{aligned}$$

5. Percentage of the area blocked to the total area

$$\begin{aligned} & \text{Percent_of_area_blocked_is:} \\ & \% A = \frac{A}{6.25} \cdot 100 \end{aligned}$$

6. The air flow area is:

$$A_{flow} = A_{Total} - A_{blocked}$$

7. The percentage of the flow area to the total area is:

$$\% A_{flow} = \frac{A_{flow}}{A_{Total}}$$

See the following pages for the tabulated results.

Table 8. Unit conversion from MTS reading

MTS reading	true length ($\Delta h_{\text{actuator}}$)	ramp angle (deg)	$\Delta h_{\text{ramp_edge}}$ (inch)	Area blocked (inch ²)	% area blocked	Flow area (inch ²)	%Flow area
0	0.0000	0.000	0.000	0.000	0.00%	6.250	100.00%
0.001	0.0016	0.039	0.001	0.002	0.03%	6.248	99.97%
0.002	0.0031	0.077	0.002	0.004	0.07%	6.246	99.93%
0.003	0.0047	0.116	0.003	0.006	0.10%	6.244	99.90%
0.004	0.0062	0.155	0.004	0.009	0.14%	6.241	99.86%
0.005	0.0078	0.194	0.005	0.011	0.17%	6.239	99.83%
0.006	0.0093	0.233	0.006	0.013	0.21%	6.237	99.79%
0.007	0.0109	0.272	0.008	0.015	0.24%	6.235	99.76%
0.008	0.0124	0.312	0.009	0.017	0.28%	6.233	99.72%
0.009	0.0140	0.351	0.010	0.019	0.31%	6.231	99.69%
0.01	0.0155	0.390	0.011	0.022	0.35%	6.228	99.65%
0.011	0.0171	0.430	0.012	0.024	0.38%	6.226	99.62%
0.012	0.0187	0.470	0.013	0.026	0.42%	6.224	99.58%
0.013	0.0202	0.509	0.014	0.028	0.45%	6.222	99.55%
0.014	0.0218	0.549	0.015	0.030	0.49%	6.220	99.51%
0.015	0.0233	0.589	0.016	0.033	0.52%	6.217	99.48%
0.016	0.0249	0.629	0.017	0.035	0.56%	6.215	99.44%
0.017	0.0264	0.669	0.019	0.037	0.59%	6.213	99.41%
0.018	0.0280	0.709	0.020	0.039	0.63%	6.211	99.37%
0.019	0.0295	0.750	0.021	0.041	0.66%	6.209	99.34%
0.02	0.0311	0.790	0.022	0.044	0.70%	6.206	99.30%
0.021	0.0327	0.831	0.023	0.046	0.74%	6.204	99.26%
0.022	0.0342	0.871	0.024	0.048	0.77%	6.202	99.23%
0.023	0.0358	0.912	0.025	0.050	0.81%	6.200	99.19%
0.024	0.0373	0.953	0.026	0.053	0.84%	6.197	99.16%
0.025	0.0389	0.993	0.027	0.055	0.88%	6.195	99.12%
0.026	0.0404	1.034	0.029	0.057	0.92%	6.193	99.08%
0.027	0.0420	1.076	0.030	0.060	0.95%	6.190	99.05%
0.028	0.0435	1.117	0.031	0.062	0.99%	6.188	99.01%
0.029	0.0451	1.158	0.032	0.064	1.02%	6.186	98.98%
0.03	0.0466	1.199	0.033	0.066	1.06%	6.184	98.94%
0.031	0.0482	1.241	0.034	0.069	1.10%	6.181	98.90%
0.032	0.0498	1.282	0.035	0.071	1.13%	6.179	98.87%
0.033	0.0513	1.324	0.037	0.073	1.17%	6.177	98.83%
0.034	0.0529	1.366	0.038	0.076	1.21%	6.174	98.79%
0.035	0.0544	1.408	0.039	0.078	1.25%	6.172	98.75%
0.036	0.0560	1.450	0.040	0.080	1.28%	6.170	98.72%
0.037	0.0575	1.492	0.041	0.082	1.32%	6.168	98.68%
0.038	0.0591	1.534	0.042	0.085	1.36%	6.165	98.64%
0.039	0.0606	1.576	0.044	0.087	1.39%	6.163	98.61%
0.04	0.0622	1.618	0.045	0.089	1.43%	6.161	98.57%
0.041	0.0637	1.661	0.046	0.092	1.47%	6.158	98.53%
0.042	0.0653	1.704	0.047	0.094	1.51%	6.156	98.49%

MTS reading	true length ($\Delta h_{\text{actuator}}$)	ramp angle (deg)	$\Delta h_{\text{ramp_edge}}$ (inch)	Area blocked (inch ²)	% area blocked	Flow area (inch ²)	%Flow area
0.043	0.0669	1.746	0.048	0.097	1.54%	6.153	98.46%
0.044	0.0684	1.789	0.049	0.099	1.58%	6.151	98.42%
0.045	0.0700	1.832	0.051	0.101	1.62%	6.149	98.38%
0.046	0.0715	1.875	0.052	0.104	1.66%	6.146	98.34%
0.047	0.0731	1.918	0.053	0.106	1.70%	6.144	98.30%
0.048	0.0746	1.961	0.054	0.108	1.73%	6.142	98.27%
0.049	0.0762	2.004	0.055	0.111	1.77%	6.139	98.23%
0.05	0.0777	2.048	0.057	0.113	1.81%	6.137	98.19%
0.051	0.0793	2.091	0.058	0.116	1.85%	6.134	98.15%
0.052	0.0808	2.135	0.059	0.118	1.89%	6.132	98.11%
0.053	0.0824	2.179	0.060	0.120	1.93%	6.130	98.07%
0.054	0.0840	2.222	0.061	0.123	1.96%	6.127	98.04%
0.055	0.0855	2.266	0.063	0.125	2.00%	6.125	98.00%
0.056	0.0871	2.310	0.064	0.128	2.04%	6.122	97.96%
0.057	0.0886	2.355	0.065	0.130	2.08%	6.120	97.92%
0.058	0.0902	2.399	0.066	0.132	2.12%	6.118	97.88%
0.059	0.0917	2.443	0.067	0.135	2.16%	6.115	97.84%
0.06	0.0933	2.488	0.069	0.137	2.20%	6.113	97.80%
0.061	0.0948	2.532	0.070	0.140	2.24%	6.110	97.76%
0.062	0.0964	2.577	0.071	0.142	2.28%	6.108	97.72%
0.063	0.0980	2.622	0.072	0.145	2.32%	6.105	97.68%
0.064	0.0995	2.667	0.074	0.147	2.35%	6.103	97.65%
0.065	0.1011	2.712	0.075	0.150	2.39%	6.100	97.61%
0.066	0.1026	2.757	0.076	0.152	2.43%	6.098	97.57%
0.067	0.1042	2.802	0.077	0.155	2.47%	6.095	97.53%
0.068	0.1057	2.847	0.079	0.157	2.51%	6.093	97.49%
0.069	0.1073	2.893	0.080	0.160	2.55%	6.090	97.45%
0.07	0.1088	2.938	0.081	0.162	2.59%	6.088	97.41%
0.071	0.1104	2.984	0.082	0.165	2.63%	6.085	97.37%
0.072	0.1119	3.030	0.084	0.167	2.67%	6.083	97.33%
0.073	0.1135	3.076	0.085	0.170	2.71%	6.080	97.29%
0.074	0.1151	3.122	0.086	0.172	2.75%	6.078	97.25%
0.075	0.1166	3.168	0.087	0.175	2.80%	6.075	97.20%
0.076	0.1182	3.214	0.089	0.177	2.84%	6.073	97.16%
0.077	0.1197	3.261	0.090	0.180	2.88%	6.070	97.12%
0.078	0.1213	3.307	0.091	0.182	2.92%	6.068	97.08%
0.079	0.1228	3.354	0.092	0.185	2.96%	6.065	97.04%
0.08	0.1244	3.400	0.094	0.187	3.00%	6.063	97.00%
0.081	0.1259	3.447	0.095	0.190	3.04%	6.060	96.96%
0.082	0.1275	3.494	0.096	0.193	3.08%	6.057	96.92%
0.083	0.1290	3.541	0.098	0.195	3.12%	6.055	96.88%
0.084	0.1306	3.588	0.099	0.198	3.16%	6.052	96.84%
0.085	0.1322	3.636	0.100	0.200	3.21%	6.050	96.79%
0.086	0.1337	3.683	0.101	0.203	3.25%	6.047	96.75%
0.087	0.1353	3.731	0.103	0.206	3.29%	6.044	96.71%

MTS reading	true length ($\Delta h_{\text{actuator}}$)	ramp angle (deg)	$\Delta h_{\text{ramp_edge}}$ (inch)	Area blocked (inch ²)	% area blocked	Flow area (inch ²)	%Flow area
0.088	0.1368	3.778	0.104	0.208	3.33%	6.042	96.67%
0.089	0.1384	3.826	0.105	0.211	3.37%	6.039	96.63%
0.09	0.1399	3.874	0.107	0.213	3.41%	6.037	96.59%
0.091	0.1415	3.922	0.108	0.216	3.46%	6.034	96.54%
0.092	0.1430	3.970	0.109	0.219	3.50%	6.031	96.50%
0.093	0.1446	4.018	0.111	0.221	3.54%	6.029	96.46%
0.094	0.1462	4.067	0.112	0.224	3.58%	6.026	96.42%
0.095	0.1477	4.115	0.113	0.227	3.62%	6.023	96.38%
0.096	0.1493	4.164	0.115	0.229	3.67%	6.021	96.33%
0.097	0.1508	4.213	0.116	0.232	3.71%	6.018	96.29%
0.098	0.1524	4.261	0.117	0.235	3.75%	6.015	96.25%
0.099	0.1539	4.310	0.119	0.237	3.80%	6.013	96.20%
0.1	0.1555	4.359	0.120	0.240	3.84%	6.010	96.16%
0.101	0.1570	4.409	0.121	0.243	3.88%	6.007	96.12%
0.102	0.1586	4.458	0.123	0.245	3.92%	6.005	96.08%
0.103	0.1601	4.508	0.124	0.248	3.97%	6.002	96.03%
0.104	0.1617	4.557	0.125	0.251	4.01%	5.999	95.99%
0.105	0.1633	4.607	0.127	0.253	4.05%	5.997	95.95%
0.106	0.1648	4.657	0.128	0.256	4.10%	5.994	95.90%
0.107	0.1664	4.707	0.129	0.259	4.14%	5.991	95.86%
0.108	0.1679	4.757	0.131	0.262	4.19%	5.988	95.81%
0.109	0.1695	4.807	0.132	0.264	4.23%	5.986	95.77%
0.11	0.1710	4.857	0.134	0.267	4.27%	5.983	95.73%
0.111	0.1726	4.908	0.135	0.270	4.32%	5.980	95.68%
0.112	0.1741	4.958	0.136	0.273	4.36%	5.977	95.64%
0.113	0.1757	5.009	0.138	0.275	4.41%	5.975	95.59%
0.114	0.1772	5.060	0.139	0.278	4.45%	5.972	95.55%
0.115	0.1788	5.111	0.140	0.281	4.49%	5.969	95.51%
0.116	0.1804	5.162	0.142	0.284	4.54%	5.966	95.46%
0.117	0.1819	5.213	0.143	0.286	4.58%	5.964	95.42%
0.118	0.1835	5.265	0.145	0.289	4.63%	5.961	95.37%
0.119	0.1850	5.316	0.146	0.292	4.67%	5.958	95.33%
0.12	0.1866	5.368	0.147	0.295	4.72%	5.955	95.28%
0.121	0.1881	5.420	0.149	0.298	4.76%	5.952	95.24%
0.122	0.1897	5.472	0.150	0.300	4.81%	5.950	95.19%
0.123	0.1912	5.524	0.152	0.303	4.85%	5.947	95.15%
0.124	0.1928	5.576	0.153	0.306	4.90%	5.944	95.10%
0.125	0.1944	5.628	0.154	0.309	4.94%	5.941	95.06%
0.126	0.1959	5.681	0.156	0.312	4.99%	5.938	95.01%
0.127	0.1975	5.733	0.157	0.315	5.03%	5.935	94.97%
0.128	0.1990	5.786	0.159	0.318	5.08%	5.932	94.92%
0.129	0.2006	5.839	0.160	0.320	5.13%	5.930	94.87%
0.13	0.2021	5.892	0.162	0.323	5.17%	5.927	94.83%
0.131	0.2037	5.945	0.163	0.326	5.22%	5.924	94.78%
0.132	0.2052	5.998	0.165	0.329	5.26%	5.921	94.74%

MTS reading	true length ($\Delta h_{\text{actuator}}$)	ramp angle (deg)	$\Delta h_{\text{ramp_edge}}$ (inch)	Area blocked (inch ²)	% area blocked	Flow area (inch ²)	%Flow area
0.133	0.2068	6.051	0.166	0.332	5.31%	5.918	94.69%
0.134	0.2083	6.105	0.167	0.335	5.36%	5.915	94.64%
0.135	0.2099	6.159	0.169	0.338	5.40%	5.912	94.60%
0.136	0.2115	6.212	0.170	0.341	5.45%	5.909	94.55%
0.137	0.2130	6.266	0.172	0.344	5.50%	5.906	94.50%
0.138	0.2146	6.320	0.173	0.346	5.54%	5.904	94.46%
0.139	0.2161	6.375	0.175	0.349	5.59%	5.901	94.41%
0.14	0.2177	6.429	0.176	0.352	5.64%	5.898	94.36%
0.141	0.2192	6.483	0.178	0.355	5.68%	5.895	94.32%
0.142	0.2208	6.538	0.179	0.358	5.73%	5.892	94.27%
0.143	0.2223	6.593	0.181	0.361	5.78%	5.889	94.22%
0.144	0.2239	6.648	0.182	0.364	5.83%	5.886	94.17%
0.145	0.2254	6.703	0.184	0.367	5.87%	5.883	94.13%
0.146	0.2270	6.758	0.185	0.370	5.92%	5.880	94.08%
0.147	0.2286	6.813	0.187	0.373	5.97%	5.877	94.03%
0.148	0.2301	6.869	0.188	0.376	6.02%	5.874	93.98%
0.149	0.2317	6.925	0.190	0.379	6.07%	5.871	93.93%
0.15	0.2332	6.980	0.191	0.382	6.11%	5.868	93.89%
0.151	0.2348	7.036	0.193	0.385	6.16%	5.865	93.84%
0.152	0.2363	7.092	0.194	0.388	6.21%	5.862	93.79%
0.153	0.2379	7.148	0.196	0.391	6.26%	5.859	93.74%
0.154	0.2394	7.205	0.197	0.394	6.31%	5.856	93.69%
0.155	0.2410	7.261	0.199	0.397	6.36%	5.853	93.64%
0.156	0.2425	7.318	0.200	0.400	6.41%	5.850	93.59%
0.157	0.2441	7.375	0.202	0.403	6.45%	5.847	93.55%
0.158	0.2457	7.432	0.203	0.406	6.50%	5.844	93.50%
0.159	0.2472	7.489	0.205	0.410	6.55%	5.840	93.45%
0.16	0.2488	7.546	0.206	0.413	6.60%	5.837	93.40%
0.161	0.2503	7.603	0.208	0.416	6.65%	5.834	93.35%
0.162	0.2519	7.661	0.209	0.419	6.70%	5.831	93.30%
0.163	0.2534	7.719	0.211	0.422	6.75%	5.828	93.25%
0.164	0.2550	7.777	0.213	0.425	6.80%	5.825	93.20%
0.165	0.2565	7.835	0.214	0.428	6.85%	5.822	93.15%
0.166	0.2581	7.893	0.216	0.431	6.90%	5.819	93.10%
0.167	0.2597	7.951	0.217	0.434	6.95%	5.816	93.05%
0.168	0.2612	8.009	0.219	0.438	7.00%	5.812	93.00%
0.169	0.2628	8.068	0.220	0.441	7.05%	5.809	92.95%
0.17	0.2643	8.127	0.222	0.444	7.10%	5.806	92.90%
0.171	0.2659	8.186	0.223	0.447	7.15%	5.803	92.85%
0.172	0.2674	8.245	0.225	0.450	7.20%	5.800	92.80%
0.173	0.2690	8.304	0.227	0.453	7.25%	5.797	92.75%
0.174	0.2705	8.363	0.228	0.456	7.30%	5.794	92.70%
0.175	0.2721	8.423	0.230	0.460	7.35%	5.790	92.65%
0.176	0.2736	8.483	0.231	0.463	7.41%	5.787	92.59%
0.177	0.2752	8.542	0.233	0.466	7.46%	5.784	92.54%

MTS reading	true length ($\Delta h_{\text{actuator}}$)	ramp angle (deg)	$\Delta h_{\text{ramp_edge}}$ (inch)	Area blocked (inch ²)	% area blocked	Flow area (inch ²)	%Flow area
0.178	0.2768	8.602	0.235	0.469	7.51%	5.781	92.49%
0.179	0.2783	8.663	0.236	0.472	7.56%	5.778	92.44%
0.18	0.2799	8.723	0.238	0.476	7.61%	5.774	92.39%
0.181	0.2814	8.783	0.239	0.479	7.66%	5.771	92.34%
0.182	0.2830	8.844	0.241	0.482	7.72%	5.768	92.28%
0.183	0.2845	8.905	0.243	0.485	7.77%	5.765	92.23%
0.184	0.2861	8.966	0.244	0.489	7.82%	5.761	92.18%
0.185	0.2876	9.027	0.246	0.492	7.87%	5.758	92.13%
0.186	0.2892	9.088	0.248	0.495	7.92%	5.755	92.08%
0.187	0.2907	9.150	0.249	0.499	7.98%	5.751	92.02%
0.188	0.2923	9.211	0.251	0.502	8.03%	5.748	91.97%
0.189	0.2939	9.273	0.253	0.505	8.08%	5.745	91.92%
0.19	0.2954	9.335	0.254	0.508	8.13%	5.742	91.87%
0.191	0.2970	9.397	0.256	0.512	8.19%	5.738	91.81%
0.192	0.2985	9.459	0.257	0.515	8.24%	5.735	91.76%
0.193	0.3001	9.522	0.259	0.518	8.29%	5.732	91.71%
0.194	0.3016	9.584	0.261	0.522	8.35%	5.728	91.65%
0.195	0.3032	9.647	0.262	0.525	8.40%	5.725	91.60%
0.196	0.3047	9.710	0.264	0.528	8.45%	5.722	91.55%
0.197	0.3063	9.773	0.266	0.532	8.51%	5.718	91.49%
0.198	0.3079	9.836	0.268	0.535	8.56%	5.715	91.44%
0.199	0.3094	9.900	0.269	0.538	8.61%	5.712	91.39%
0.2	0.3110	9.963	0.271	0.542	8.67%	5.708	91.33%
0.201	0.3125	10.027	0.273	0.545	8.72%	5.705	91.28%
0.202	0.3141	10.091	0.274	0.549	8.78%	5.701	91.22%
0.203	0.3156	10.155	0.276	0.552	8.83%	5.698	91.17%
0.204	0.3172	10.219	0.278	0.555	8.89%	5.695	91.11%
0.205	0.3187	10.284	0.279	0.559	8.94%	5.691	91.06%
0.206	0.3203	10.348	0.281	0.562	9.00%	5.688	91.00%
0.207	0.3218	10.413	0.283	0.566	9.05%	5.684	90.95%
0.208	0.3234	10.478	0.285	0.569	9.10%	5.681	90.90%
0.209	0.3250	10.543	0.286	0.573	9.16%	5.677	90.84%
0.21	0.3265	10.608	0.288	0.576	9.22%	5.674	90.78%
0.211	0.3281	10.674	0.290	0.579	9.27%	5.671	90.73%
0.212	0.3296	10.740	0.291	0.583	9.33%	5.667	90.67%
0.213	0.3312	10.805	0.293	0.586	9.38%	5.664	90.62%
0.214	0.3327	10.871	0.295	0.590	9.44%	5.660	90.56%
0.215	0.3343	10.938	0.297	0.593	9.49%	5.657	90.51%
0.216	0.3358	11.004	0.298	0.597	9.55%	5.653	90.45%
0.217	0.3374	11.070	0.300	0.600	9.61%	5.650	90.39%
0.218	0.3389	11.137	0.302	0.604	9.66%	5.646	90.34%
0.219	0.3405	11.204	0.304	0.607	9.72%	5.643	90.28%
0.22	0.3421	11.271	0.305	0.611	9.77%	5.639	90.23%
0.221	0.3436	11.338	0.307	0.614	9.83%	5.636	90.17%
0.222	0.3452	11.406	0.309	0.618	9.89%	5.632	90.11%

MTS reading	true length ($\Delta h_{\text{actuator}}$)	ramp angle (deg)	$\Delta h_{\text{ramp_edge}}$ (inch)	Area blocked (inch ²)	% area blocked	Flow area (inch ²)	%Flow area
0.223	0.3467	11.473	0.311	0.622	9.94%	5.628	90.06%
0.224	0.3483	11.541	0.313	0.625	10.00%	5.625	90.00%
0.225	0.3498	11.609	0.314	0.629	10.06%	5.621	89.94%
0.226	0.3514	11.677	0.316	0.632	10.12%	5.618	89.88%
0.227	0.3529	11.746	0.318	0.636	10.17%	5.614	89.83%
0.228	0.3545	11.814	0.320	0.639	10.23%	5.611	89.77%
0.229	0.3561	11.883	0.322	0.643	10.29%	5.607	89.71%
0.23	0.3576	11.952	0.323	0.647	10.35%	5.603	89.65%
0.231	0.3592	12.021	0.325	0.650	10.40%	5.600	89.60%
0.232	0.3607	12.090	0.327	0.654	10.46%	5.596	89.54%
0.233	0.3623	12.159	0.329	0.658	10.52%	5.592	89.48%
0.234	0.3638	12.229	0.331	0.661	10.58%	5.589	89.42%
0.235	0.3654	12.299	0.332	0.665	10.64%	5.585	89.36%
0.236	0.3669	12.369	0.334	0.668	10.70%	5.582	89.30%
0.237	0.3685	12.439	0.336	0.672	10.75%	5.578	89.25%
0.238	0.3700	12.509	0.338	0.676	10.81%	5.574	89.19%
0.239	0.3716	12.580	0.340	0.680	10.87%	5.570	89.13%
0.24	0.3732	12.651	0.342	0.683	10.93%	5.567	89.07%
0.241	0.3747	12.722	0.343	0.687	10.99%	5.563	89.01%
0.242	0.3763	12.793	0.345	0.691	11.05%	5.559	88.95%
0.243	0.3778	12.864	0.347	0.694	11.11%	5.556	88.89%
0.244	0.3794	12.936	0.349	0.698	11.17%	5.552	88.83%
0.245	0.3809	13.007	0.351	0.702	11.23%	5.548	88.77%
0.246	0.3825	13.079	0.353	0.706	11.29%	5.544	88.71%
0.247	0.3840	13.151	0.355	0.709	11.35%	5.541	88.65%
0.248	0.3856	13.224	0.357	0.713	11.41%	5.537	88.59%
0.249	0.3871	13.296	0.358	0.717	11.47%	5.533	88.53%
0.25	0.3887	13.369	0.360	0.721	11.53%	5.529	88.47%
0.251	0.3903	13.442	0.362	0.724	11.59%	5.526	88.41%
0.252	0.3918	13.515	0.364	0.728	11.65%	5.522	88.35%
0.253	0.3934	13.588	0.366	0.732	11.71%	5.518	88.29%
0.254	0.3949	13.661	0.368	0.736	11.77%	5.514	88.23%
0.255	0.3965	13.735	0.370	0.740	11.83%	5.510	88.17%
0.256	0.3980	13.809	0.372	0.743	11.89%	5.507	88.11%
0.257	0.3996	13.883	0.374	0.747	11.96%	5.503	88.04%
0.258	0.4011	13.957	0.376	0.751	12.02%	5.499	87.98%
0.259	0.4027	14.032	0.377	0.755	12.08%	5.495	87.92%
0.26	0.4042	14.106	0.379	0.759	12.14%	5.491	87.86%
0.261	0.4058	14.181	0.381	0.763	12.20%	5.487	87.80%
0.262	0.4074	14.256	0.383	0.766	12.26%	5.484	87.74%
0.263	0.4089	14.332	0.385	0.770	12.33%	5.480	87.67%
0.264	0.4105	14.407	0.387	0.774	12.39%	5.476	87.61%
0.265	0.4120	14.483	0.389	0.778	12.45%	5.472	87.55%
0.266	0.4136	14.559	0.391	0.782	12.51%	5.468	87.49%
0.267	0.4151	14.635	0.393	0.786	12.58%	5.464	87.42%

MTS reading	true length ($\Delta h_{\text{actuator}}$)	ramp angle (deg)	$\Delta h_{\text{ramp_edge}}$ (inch)	Area blocked (inch ²)	% area blocked	Flow area (inch ²)	%Flow area
0.268	0.4167	14.711	0.395	0.790	12.64%	5.460	87.36%
0.269	0.4182	14.788	0.397	0.794	12.70%	5.456	87.30%
0.27	0.4198	14.864	0.399	0.798	12.76%	5.452	87.24%
0.271	0.4214	14.941	0.401	0.802	12.83%	5.448	87.17%
0.272	0.4229	15.018	0.403	0.806	12.89%	5.444	87.11%
0.273	0.4245	15.096	0.405	0.810	12.95%	5.440	87.05%
0.274	0.4260	15.173	0.407	0.814	13.02%	5.436	86.98%
0.275	0.4276	15.251	0.409	0.818	13.08%	5.432	86.92%
0.276	0.4291	15.329	0.411	0.822	13.14%	5.428	86.86%
0.277	0.4307	15.407	0.413	0.826	13.21%	5.424	86.79%
0.278	0.4322	15.485	0.415	0.830	13.27%	5.420	86.73%
0.279	0.4338	15.564	0.417	0.834	13.34%	5.416	86.66%
0.28	0.4353	15.643	0.419	0.838	13.40%	5.412	86.60%
0.281	0.4369	15.722	0.421	0.842	13.47%	5.408	86.53%
0.282	0.4385	15.801	0.423	0.846	13.53%	5.404	86.47%
0.283	0.4400	15.880	0.425	0.850	13.60%	5.400	86.40%
0.284	0.4416	15.960	0.427	0.854	13.66%	5.396	86.34%
0.285	0.4431	16.040	0.429	0.858	13.72%	5.392	86.28%
0.286	0.4447	16.120	0.431	0.862	13.79%	5.388	86.21%
0.287	0.4462	16.200	0.433	0.866	13.86%	5.384	86.14%
0.288	0.4478	16.281	0.435	0.870	13.92%	5.380	86.08%
0.289	0.4493	16.361	0.437	0.874	13.99%	5.376	86.01%
0.29	0.4509	16.442	0.439	0.878	14.05%	5.372	85.95%
0.291	0.4524	16.524	0.441	0.882	14.12%	5.368	85.88%
0.292	0.4540	16.605	0.443	0.886	14.18%	5.364	85.82%
0.293	0.4556	16.687	0.445	0.891	14.25%	5.359	85.75%
0.294	0.4571	16.768	0.447	0.895	14.32%	5.355	85.68%
0.295	0.4587	16.850	0.449	0.899	14.38%	5.351	85.62%
0.296	0.4602	16.933	0.452	0.903	14.45%	5.347	85.55%
0.297	0.4618	17.015	0.454	0.907	14.52%	5.343	85.48%
0.298	0.4633	17.098	0.456	0.911	14.58%	5.339	85.42%
0.299	0.4649	17.181	0.458	0.916	14.65%	5.334	85.35%
0.3	0.4664	17.264	0.460	0.920	14.72%	5.330	85.28%
0.301	0.4680	17.347	0.462	0.924	14.78%	5.326	85.22%
0.302	0.4696	17.431	0.464	0.928	14.85%	5.322	85.15%
0.303	0.4711	17.515	0.466	0.932	14.92%	5.318	85.08%
0.304	0.4727	17.599	0.468	0.937	14.98%	5.313	85.02%
0.305	0.4742	17.683	0.470	0.941	15.05%	5.309	84.95%
0.306	0.4758	17.768	0.473	0.945	15.12%	5.305	84.88%
0.307	0.4773	17.852	0.475	0.949	15.19%	5.301	84.81%
0.308	0.4789	17.937	0.477	0.954	15.26%	5.296	84.74%
0.309	0.4804	18.022	0.479	0.958	15.32%	5.292	84.68%
0.31	0.4820	18.108	0.481	0.962	15.39%	5.288	84.61%
0.311	0.4835	18.193	0.483	0.966	15.46%	5.284	84.54%
0.312	0.4851	18.279	0.485	0.971	15.53%	5.279	84.47%

MTS reading	true length ($\Delta h_{\text{actuator}}$)	ramp angle (deg)	$\Delta h_{\text{ramp_edge}}$ (inch)	Area blocked (inch ²)	% area blocked	Flow area (inch ²)	%Flow area
0.313	0.4867	18.365	0.487	0.975	15.60%	5.275	84.40%
0.314	0.4882	18.452	0.490	0.979	15.67%	5.271	84.33%
0.315	0.4898	18.538	0.492	0.984	15.74%	5.266	84.26%
0.316	0.4913	18.625	0.494	0.988	15.81%	5.262	84.19%
0.317	0.4929	18.712	0.496	0.992	15.87%	5.258	84.13%
0.318	0.4944	18.799	0.498	0.996	15.94%	5.254	84.06%
0.319	0.4960	18.887	0.500	1.001	16.01%	5.249	83.99%
0.32	0.4975	18.975	0.503	1.005	16.08%	5.245	83.92%
0.321	0.4991	19.063	0.505	1.010	16.15%	5.240	83.85%
0.322	0.5006	19.151	0.507	1.014	16.22%	5.236	83.78%
0.323	0.5022	19.239	0.509	1.018	16.29%	5.232	83.71%
0.324	0.5038	19.328	0.511	1.023	16.36%	5.227	83.64%
0.325	0.5053	19.417	0.514	1.027	16.43%	5.223	83.57%
0.326	0.5069	19.506	0.516	1.031	16.50%	5.219	83.50%
0.327	0.5084	19.595	0.518	1.036	16.57%	5.214	83.43%
0.328	0.5100	19.685	0.520	1.040	16.64%	5.210	83.36%
0.329	0.5115	19.775	0.522	1.045	16.72%	5.205	83.28%
0.33	0.5131	19.865	0.525	1.049	16.79%	5.201	83.21%
0.331	0.5146	19.955	0.527	1.054	16.86%	5.196	83.14%
0.332	0.5162	20.046	0.529	1.058	16.93%	5.192	83.07%
0.333	0.5178	20.136	0.531	1.062	17.00%	5.188	83.00%
0.334	0.5193	20.228	0.533	1.067	17.07%	5.183	82.93%
0.335	0.5209	20.319	0.536	1.071	17.14%	5.179	82.86%
0.336	0.5224	20.410	0.538	1.076	17.21%	5.174	82.79%
0.337	0.5240	20.502	0.540	1.080	17.29%	5.170	82.71%
0.338	0.5255	20.594	0.542	1.085	17.36%	5.165	82.64%
0.339	0.5271	20.686	0.545	1.089	17.43%	5.161	82.57%
0.34	0.5286	20.779	0.547	1.094	17.50%	5.156	82.50%
0.341	0.5302	20.872	0.549	1.098	17.57%	5.152	82.43%
0.342	0.5317	20.965	0.551	1.103	17.65%	5.147	82.35%
0.343	0.5333	21.058	0.554	1.107	17.72%	5.143	82.28%
0.344	0.5349	21.151	0.556	1.112	17.79%	5.138	82.21%
0.345	0.5364	21.245	0.558	1.117	17.86%	5.133	82.14%
0.346	0.5380	21.339	0.561	1.121	17.94%	5.129	82.06%
0.347	0.5395	21.433	0.563	1.126	18.01%	5.124	81.99%
0.348	0.5411	21.528	0.565	1.130	18.08%	5.120	81.92%
0.349	0.5426	21.623	0.567	1.135	18.16%	5.115	81.84%
0.35	0.5442	21.718	0.570	1.139	18.23%	5.111	81.77%
0.351	0.5457	21.813	0.572	1.144	18.30%	5.106	81.70%
0.352	0.5473	21.908	0.574	1.149	18.38%	5.101	81.62%
0.353	0.5488	22.004	0.577	1.153	18.45%	5.097	81.55%
0.354	0.5504	22.100	0.579	1.158	18.52%	5.092	81.48%
0.355	0.5520	22.196	0.581	1.162	18.60%	5.088	81.40%
0.356	0.5535	22.293	0.584	1.167	18.67%	5.083	81.33%
0.357	0.5551	22.389	0.586	1.172	18.75%	5.078	81.25%

MTS reading	true length ($\Delta h_{\text{actuator}}$)	ramp angle (deg)	$\Delta h_{\text{ramp_edge}}$ (inch)	Area blocked (inch ²)	% area blocked	Flow area (inch ²)	%Flow area
0.358	0.5566	22.486	0.588	1.176	18.82%	5.074	81.18%
0.359	0.5582	22.584	0.590	1.181	18.90%	5.069	81.10%
0.36	0.5597	22.681	0.593	1.186	18.97%	5.064	81.03%
0.361	0.5613	22.779	0.595	1.190	19.04%	5.060	80.96%
0.362	0.5628	22.877	0.597	1.195	19.12%	5.055	80.88%
0.363	0.5644	22.975	0.600	1.200	19.19%	5.050	80.81%
0.364	0.5659	23.074	0.602	1.204	19.27%	5.046	80.73%
0.365	0.5675	23.172	0.605	1.209	19.34%	5.041	80.66%
0.366	0.5691	23.271	0.607	1.214	19.42%	5.036	80.58%
0.367	0.5706	23.371	0.609	1.218	19.49%	5.032	80.51%
0.368	0.5722	23.470	0.612	1.223	19.57%	5.027	80.43%
0.369	0.5737	23.570	0.614	1.228	19.65%	5.022	80.35%
0.37	0.5753	23.670	0.616	1.233	19.72%	5.017	80.28%
0.371	0.5768	23.770	0.619	1.237	19.80%	5.013	80.20%
0.372	0.5784	23.871	0.621	1.242	19.87%	5.008	80.13%
0.373	0.5799	23.972	0.623	1.247	19.95%	5.003	80.05%
0.374	0.5815	24.073	0.626	1.252	20.03%	4.998	79.97%
0.375	0.5831	24.174	0.628	1.256	20.10%	4.994	79.90%
0.376	0.5846	24.276	0.631	1.261	20.18%	4.989	79.82%
0.377	0.5862	24.377	0.633	1.266	20.25%	4.984	79.75%
0.378	0.5877	24.480	0.635	1.271	20.33%	4.979	79.67%
0.379	0.5893	24.582	0.638	1.275	20.41%	4.975	79.59%
0.38	0.5908	24.685	0.640	1.280	20.48%	4.970	79.52%
0.381	0.5924	24.787	0.643	1.285	20.56%	4.965	79.44%
0.382	0.5939	24.891	0.645	1.290	20.64%	4.960	79.36%
0.383	0.5955	24.994	0.647	1.295	20.72%	4.955	79.28%
0.384	0.5970	25.098	0.650	1.300	20.79%	4.950	79.21%
0.385	0.5986	25.202	0.652	1.304	20.87%	4.946	79.13%
0.386	0.6002	25.306	0.655	1.309	20.95%	4.941	79.05%
0.387	0.6017	25.410	0.657	1.314	21.02%	4.936	78.98%
0.388	0.6033	25.515	0.659	1.319	21.10%	4.931	78.90%
0.389	0.6048	25.620	0.662	1.324	21.18%	4.926	78.82%
0.39	0.6064	25.725	0.664	1.329	21.26%	4.921	78.74%
0.391	0.6079	25.831	0.667	1.333	21.34%	4.917	78.66%
0.392	0.6095	25.937	0.669	1.338	21.41%	4.912	78.59%
0.393	0.6110	26.043	0.672	1.343	21.49%	4.907	78.51%
0.394	0.6126	26.149	0.674	1.348	21.57%	4.902	78.43%
0.395	0.6141	26.256	0.676	1.353	21.65%	4.897	78.35%
0.396	0.6157	26.362	0.679	1.358	21.73%	4.892	78.27%
0.397	0.6173	26.470	0.681	1.363	21.80%	4.887	78.20%
0.398	0.6188	26.577	0.684	1.368	21.88%	4.882	78.12%
0.399	0.6204	26.685	0.686	1.373	21.96%	4.877	78.04%
0.4	0.6219	26.792	0.689	1.377	22.04%	4.873	77.96%
0.401	0.6235	26.901	0.691	1.382	22.12%	4.868	77.88%
0.402	0.6250	27.009	0.694	1.387	22.20%	4.863	77.80%

MTS reading	true length ($\Delta h_{\text{actuator}}$)	ramp angle (deg)	$\Delta h_{\text{ramp_edge}}$ (inch)	Area blocked (inch ²)	% area blocked	Flow area (inch ²)	%Flow area
0.403	0.6266	27.118	0.696	1.392	22.28%	4.858	77.72%
0.404	0.6281	27.227	0.699	1.397	22.36%	4.853	77.64%
0.405	0.6297	27.336	0.701	1.402	22.43%	4.848	77.57%
0.406	0.6313	27.446	0.704	1.407	22.51%	4.843	77.49%
0.407	0.6328	27.555	0.706	1.412	22.59%	4.838	77.41%
0.408	0.6344	27.665	0.709	1.417	22.67%	4.833	77.33%
0.409	0.6359	27.776	0.711	1.422	22.75%	4.828	77.25%
0.41	0.6375	27.886	0.713	1.427	22.83%	4.823	77.17%
0.411	0.6390	27.997	0.716	1.432	22.91%	4.818	77.09%
0.412	0.6406	28.108	0.718	1.437	22.99%	4.813	77.01%
0.413	0.6421	28.220	0.721	1.442	23.07%	4.808	76.93%
0.414	0.6437	28.331	0.723	1.447	23.15%	4.803	76.85%
0.415	0.6452	28.443	0.726	1.452	23.23%	4.798	76.77%
0.416	0.6468	28.555	0.728	1.457	23.31%	4.793	76.69%
0.417	0.6484	28.668	0.731	1.462	23.39%	4.788	76.61%
0.418	0.6499	28.781	0.733	1.467	23.47%	4.783	76.53%
0.419	0.6515	28.894	0.736	1.472	23.55%	4.778	76.45%
0.42	0.6530	29.007	0.738	1.477	23.63%	4.773	76.37%
0.421	0.6546	29.120	0.741	1.482	23.71%	4.768	76.29%
0.422	0.6561	29.234	0.743	1.487	23.79%	4.763	76.21%
0.423	0.6577	29.348	0.746	1.492	23.87%	4.758	76.13%
0.424	0.6592	29.463	0.748	1.497	23.95%	4.753	76.05%
0.425	0.6608	29.577	0.751	1.502	24.03%	4.748	75.97%
0.426	0.6623	29.692	0.754	1.507	24.11%	4.743	75.89%
0.427	0.6639	29.807	0.756	1.512	24.19%	4.738	75.81%
0.428	0.6655	29.923	0.759	1.517	24.27%	4.733	75.73%
0.429	0.6670	30.039	0.761	1.522	24.36%	4.728	75.64%
0.43	0.6686	30.155	0.764	1.527	24.44%	4.723	75.56%
0.431	0.6701	30.271	0.766	1.532	24.52%	4.718	75.48%
0.432	0.6717	30.387	0.769	1.537	24.60%	4.713	75.40%
0.433	0.6732	30.504	0.771	1.542	24.68%	4.708	75.32%
0.434	0.6748	30.621	0.774	1.547	24.76%	4.703	75.24%
0.435	0.6763	30.739	0.776	1.553	24.84%	4.697	75.16%
0.436	0.6779	30.856	0.779	1.558	24.92%	4.692	75.08%
0.437	0.6795	30.974	0.781	1.563	25.00%	4.687	75.00%
0.438	0.6810	31.092	0.784	1.568	25.08%	4.682	74.92%
0.439	0.6826	31.211	0.786	1.573	25.17%	4.677	74.83%
0.44	0.6841	31.329	0.789	1.578	25.25%	4.672	74.75%
0.441	0.6857	31.448	0.792	1.583	25.33%	4.667	74.67%
0.442	0.6872	31.567	0.794	1.588	25.41%	4.662	74.59%
0.443	0.6888	31.687	0.797	1.593	25.49%	4.657	74.51%
0.444	0.6903	31.807	0.799	1.598	25.57%	4.652	74.43%
0.445	0.6919	31.927	0.802	1.603	25.65%	4.647	74.35%
0.446	0.6934	32.047	0.804	1.609	25.74%	4.641	74.26%
0.447	0.6950	32.167	0.807	1.614	25.82%	4.636	74.18%

MTS reading	true length ($\Delta h_{\text{actuator}}$)	ramp angle (deg)	$\Delta h_{\text{ramp_edge}}$ (inch)	Area blocked (inch ²)	% area blocked	Flow area (inch ²)	%Flow area
0.448	0.6966	32.288	0.809	1.619	25.90%	4.631	74.10%
0.449	0.6981	32.409	0.812	1.624	25.98%	4.626	74.02%
0.45	0.6997	32.531	0.814	1.629	26.06%	4.621	73.94%
0.451	0.7012	32.652	0.817	1.634	26.14%	4.616	73.86%
0.452	0.7028	32.774	0.820	1.639	26.23%	4.611	73.77%
0.453	0.7043	32.896	0.822	1.644	26.31%	4.606	73.69%
0.454	0.7059	33.019	0.825	1.649	26.39%	4.601	73.61%
0.455	0.7074	33.142	0.827	1.654	26.47%	4.596	73.53%
0.456	0.7090	33.265	0.830	1.660	26.55%	4.590	73.45%
0.457	0.7105	33.388	0.832	1.665	26.64%	4.585	73.36%
0.458	0.7121	33.511	0.835	1.670	26.72%	4.580	73.28%
0.459	0.7137	33.635	0.837	1.675	26.80%	4.575	73.20%
0.46	0.7152	33.759	0.840	1.680	26.88%	4.570	73.12%
0.461	0.7168	33.883	0.843	1.685	26.96%	4.565	73.04%
0.462	0.7183	34.008	0.845	1.690	27.04%	4.560	72.96%
0.463	0.7199	34.133	0.848	1.695	27.13%	4.555	72.87%
0.464	0.7214	34.258	0.850	1.701	27.21%	4.549	72.79%
0.465	0.7230	34.383	0.853	1.706	27.29%	4.544	72.71%
0.466	0.7245	34.509	0.855	1.711	27.37%	4.539	72.63%
0.467	0.7261	34.635	0.858	1.716	27.45%	4.534	72.55%
0.468	0.7276	34.761	0.861	1.721	27.54%	4.529	72.46%
0.469	0.7292	34.887	0.863	1.726	27.62%	4.524	72.38%
0.47	0.7308	35.014	0.866	1.731	27.70%	4.519	72.30%
0.471	0.7323	35.141	0.868	1.736	27.78%	4.514	72.22%
0.472	0.7339	35.268	0.871	1.741	27.86%	4.509	72.14%
0.473	0.7354	35.396	0.873	1.747	27.95%	4.503	72.05%
0.474	0.7370	35.523	0.876	1.752	28.03%	4.498	71.97%
0.475	0.7385	35.651	0.878	1.757	28.11%	4.493	71.89%
0.476	0.7401	35.779	0.881	1.762	28.19%	4.488	71.81%
0.477	0.7416	35.908	0.884	1.767	28.27%	4.483	71.73%
0.478	0.7432	36.037	0.886	1.772	28.35%	4.478	71.65%
0.479	0.7448	36.166	0.889	1.777	28.44%	4.473	71.56%
0.48	0.7463	36.295	0.891	1.782	28.52%	4.468	71.48%
0.481	0.7479	36.425	0.894	1.788	28.60%	4.462	71.40%
0.482	0.7494	36.554	0.896	1.793	28.68%	4.457	71.32%
0.483	0.7510	36.684	0.899	1.798	28.76%	4.452	71.24%
0.484	0.7525	36.815	0.901	1.803	28.85%	4.447	71.15%
0.485	0.7541	36.945	0.904	1.808	28.93%	4.442	71.07%
0.486	0.7556	37.076	0.907	1.813	29.01%	4.437	70.99%
0.487	0.7572	37.207	0.909	1.818	29.09%	4.432	70.91%
0.488	0.7587	37.338	0.912	1.823	29.17%	4.427	70.83%
0.489	0.7603	37.470	0.914	1.828	29.25%	4.422	70.75%
0.49	0.7619	37.602	0.917	1.833	29.33%	4.417	70.67%
0.491	0.7634	37.734	0.919	1.839	29.42%	4.411	70.58%
0.492	0.7650	37.866	0.922	1.844	29.50%	4.406	70.50%

MTS reading	true length ($\Delta h_{\text{actuator}}$)	ramp angle (deg)	$\Delta h_{\text{ramp_edge}}$ (inch)	Area blocked (inch ²)	% area blocked	Flow area (inch ²)	%Flow area
0.493	0.7665	37.999	0.924	1.849	29.58%	4.401	70.42%
0.494	0.7681	38.131	0.927	1.854	29.66%	4.396	70.34%
0.495	0.7696	38.264	0.929	1.859	29.74%	4.391	70.26%
0.496	0.7712	38.398	0.932	1.864	29.82%	4.386	70.18%
0.497	0.7727	38.531	0.934	1.869	29.90%	4.381	70.10%
0.498	0.7743	38.665	0.937	1.874	29.98%	4.376	70.02%
0.499	0.7758	38.799	0.940	1.879	30.07%	4.371	69.93%
0.5	0.7774	38.933	0.942	1.884	30.15%	4.366	69.85%
0.501	0.7790	39.068	0.945	1.889	30.23%	4.361	69.77%
0.502	0.7805	39.203	0.947	1.894	30.31%	4.356	69.69%
0.503	0.7821	39.338	0.950	1.899	30.39%	4.351	69.61%
0.504	0.7836	39.473	0.952	1.904	30.47%	4.346	69.53%
0.505	0.7852	39.608	0.955	1.909	30.55%	4.341	69.45%
0.506	0.7867	39.744	0.957	1.914	30.63%	4.336	69.37%
0.507	0.7883	39.880	0.960	1.919	30.71%	4.331	69.29%
0.508	0.7898	40.016	0.962	1.924	30.79%	4.326	69.21%
0.509	0.7914	40.153	0.965	1.929	30.87%	4.321	69.13%
0.51	0.7930	40.289	0.967	1.934	30.95%	4.316	69.05%
0.511	0.7945	40.426	0.970	1.940	31.03%	4.310	68.97%
0.512	0.7961	40.563	0.972	1.945	31.11%	4.305	68.89%
0.513	0.7976	40.701	0.975	1.950	31.19%	4.300	68.81%
0.514	0.7992	40.838	0.977	1.954	31.27%	4.296	68.73%
0.515	0.8007	40.976	0.980	1.959	31.35%	4.291	68.65%
0.516	0.8023	41.114	0.982	1.964	31.43%	4.286	68.57%
0.517	0.8038	41.252	0.985	1.969	31.51%	4.281	68.49%
0.518	0.8054	41.391	0.987	1.974	31.59%	4.276	68.41%
0.519	0.8069	41.530	0.990	1.979	31.67%	4.271	68.33%
0.52	0.8085	41.669	0.992	1.984	31.75%	4.266	68.25%
0.521	0.8101	41.808	0.995	1.989	31.83%	4.261	68.17%
0.522	0.8116	41.947	0.997	1.994	31.91%	4.256	68.09%
0.523	0.8132	42.087	1.000	1.999	31.99%	4.251	68.01%
0.524	0.8147	42.227	1.002	2.004	32.06%	4.246	67.94%
0.525	0.8163	42.367	1.004	2.009	32.14%	4.241	67.86%
0.526	0.8178	42.507	1.007	2.014	32.22%	4.236	67.78%
0.527	0.8194	42.648	1.009	2.019	32.30%	4.231	67.70%
0.528	0.8209	42.788	1.012	2.024	32.38%	4.226	67.62%
0.529	0.8225	42.929	1.014	2.029	32.46%	4.221	67.54%
0.53	0.8240	43.070	1.017	2.033	32.54%	4.217	67.46%
0.531	0.8256	43.212	1.019	2.038	32.61%	4.212	67.39%
0.532	0.8272	43.353	1.022	2.043	32.69%	4.207	67.31%
0.533	0.8287	43.495	1.024	2.048	32.77%	4.202	67.23%
0.534	0.8303	43.637	1.026	2.053	32.85%	4.197	67.15%
0.535	0.8318	43.779	1.029	2.058	32.92%	4.192	67.08%
0.536	0.8334	43.922	1.031	2.063	33.00%	4.187	67.00%
0.537	0.8349	44.064	1.034	2.067	33.08%	4.183	66.92%

MTS reading	true length ($\Delta h_{\text{actuator}}$)	ramp angle (deg)	$\Delta h_{\text{ramp_edge}}$ (inch)	Area blocked (inch ²)	% area blocked	Flow area (inch ²)	%Flow area
0.538	0.8365	44.207	1.036	2.072	33.16%	4.178	66.84%
0.539	0.8380	44.350	1.038	2.077	33.23%	4.173	66.77%
0.54	0.8396	44.493	1.041	2.082	33.31%	4.168	66.69%
0.541	0.8411	44.637	1.043	2.087	33.39%	4.163	66.61%
0.542	0.8427	44.780	1.046	2.091	33.46%	4.159	66.54%
0.543	0.8443	44.924	1.048	2.096	33.54%	4.154	66.46%
0.544	0.8458	45.068	1.050	2.101	33.61%	4.149	66.39%
0.545	0.8474	45.212	1.053	2.106	33.69%	4.144	66.31%
0.546	0.8489	45.357	1.055	2.110	33.77%	4.140	66.23%
0.547	0.8505	45.501	1.058	2.115	33.84%	4.135	66.16%
0.548	0.8520	45.646	1.060	2.120	33.92%	4.130	66.08%
0.549	0.8536	45.791	1.062	2.124	33.99%	4.126	66.01%
0.55	0.8551	45.936	1.065	2.129	34.07%	4.121	65.93%
0.551	0.8567	46.081	1.067	2.134	34.14%	4.116	65.86%
0.552	0.8583	46.227	1.069	2.139	34.22%	4.111	65.78%
0.553	0.8598	46.373	1.072	2.143	34.29%	4.107	65.71%
0.554	0.8614	46.518	1.074	2.148	34.37%	4.102	65.63%
0.555	0.8629	46.664	1.076	2.152	34.44%	4.098	65.56%
0.556	0.8645	46.811	1.079	2.157	34.51%	4.093	65.49%
0.557	0.8660	46.957	1.081	2.162	34.59%	4.088	65.41%
0.558	0.8676	47.104	1.083	2.166	34.66%	4.084	65.34%
0.559	0.8691	47.250	1.085	2.171	34.73%	4.079	65.27%
0.56	0.8707	47.397	1.088	2.175	34.81%	4.075	65.19%
0.561	0.8722	47.544	1.090	2.180	34.88%	4.070	65.12%
0.562	0.8738	47.692	1.092	2.185	34.95%	4.065	65.05%
0.563	0.8754	47.839	1.095	2.189	35.03%	4.061	64.97%
0.564	0.8769	47.987	1.097	2.194	35.10%	4.056	64.90%
0.565	0.8785	48.134	1.099	2.198	35.17%	4.052	64.83%
0.566	0.8800	48.282	1.101	2.203	35.24%	4.047	64.76%
0.567	0.8816	48.430	1.104	2.207	35.31%	4.043	64.69%
0.568	0.8831	48.578	1.106	2.212	35.39%	4.038	64.61%
0.569	0.8847	48.727	1.108	2.216	35.46%	4.034	64.54%
0.57	0.8862	48.875	1.110	2.221	35.53%	4.029	64.47%
0.571	0.8878	49.024	1.112	2.225	35.60%	4.025	64.40%
0.572	0.8893	49.173	1.115	2.229	35.67%	4.021	64.33%
0.573	0.8909	49.322	1.117	2.234	35.74%	4.016	64.26%
0.574	0.8925	49.471	1.119	2.238	35.81%	4.012	64.19%
0.575	0.8940	49.620	1.121	2.243	35.88%	4.007	64.12%
0.576	0.8956	49.769	1.123	2.247	35.95%	4.003	64.05%
0.577	0.8971	49.919	1.126	2.251	36.02%	3.999	63.98%
0.578	0.8987	50.069	1.128	2.256	36.09%	3.994	63.91%
0.579	0.9002	50.219	1.130	2.260	36.16%	3.990	63.84%
0.58	0.9018	50.368	1.132	2.264	36.23%	3.986	63.77%
0.581	0.9033	50.519	1.134	2.268	36.30%	3.982	63.70%
0.582	0.9049	50.669	1.136	2.273	36.36%	3.977	63.64%

MTS reading	true length ($\Delta h_{\text{actuator}}$)	ramp angle (deg)	$\Delta h_{\text{ramp_edge}}$ (inch)	Area blocked (inch ²)	% area blocked	Flow area (inch ²)	%Flow area
0.583	0.9065	50.819	1.139	2.277	36.43%	3.973	63.57%
0.584	0.9080	50.970	1.141	2.281	36.50%	3.969	63.50%
0.585	0.9096	51.120	1.143	2.285	36.57%	3.965	63.43%
0.586	0.9111	51.271	1.145	2.290	36.63%	3.960	63.37%
0.587	0.9127	51.422	1.147	2.294	36.70%	3.956	63.30%
0.588	0.9142	51.573	1.149	2.298	36.77%	3.952	63.23%
0.589	0.9158	51.724	1.151	2.302	36.84%	3.948	63.16%
0.59	0.9173	51.875	1.153	2.306	36.90%	3.944	63.10%
0.591	0.9189	52.026	1.155	2.310	36.97%	3.940	63.03%
0.592	0.9204	52.178	1.157	2.315	37.03%	3.935	62.97%
0.593	0.9220	52.329	1.159	2.319	37.10%	3.931	62.90%
0.594	0.9236	52.481	1.161	2.323	37.16%	3.927	62.84%
0.595	0.9251	52.633	1.163	2.327	37.23%	3.923	62.77%
0.596	0.9267	52.785	1.165	2.331	37.29%	3.919	62.71%
0.597	0.9282	52.936	1.167	2.335	37.36%	3.915	62.64%
0.598	0.9298	53.089	1.169	2.339	37.42%	3.911	62.58%
0.599	0.9313	53.241	1.171	2.343	37.49%	3.907	62.51%
0.6	0.9329	53.393	1.173	2.347	37.55%	3.903	62.45%
0.601	0.9344	53.545	1.175	2.351	37.61%	3.899	62.39%
0.602	0.9360	53.698	1.177	2.355	37.68%	3.895	62.32%
0.603	0.9375	53.850	1.179	2.359	37.74%	3.891	62.26%
0.604	0.9391	54.003	1.181	2.363	37.80%	3.887	62.20%
0.605	0.9407	54.156	1.183	2.366	37.86%	3.884	62.14%
0.606	0.9422	54.308	1.185	2.370	37.93%	3.880	62.07%
0.607	0.9438	54.461	1.187	2.374	37.99%	3.876	62.01%
0.608	0.9453	54.614	1.189	2.378	38.05%	3.872	61.95%
0.609	0.9469	54.767	1.191	2.382	38.11%	3.868	61.89%
0.61	0.9484	54.920	1.193	2.386	38.17%	3.864	61.83%
0.611	0.9500	55.073	1.195	2.389	38.23%	3.861	61.77%
0.612	0.9515	55.227	1.197	2.393	38.29%	3.857	61.71%
0.613	0.9531	55.380	1.198	2.397	38.35%	3.853	61.65%
0.614	0.9547	55.533	1.200	2.401	38.41%	3.849	61.59%
0.615	0.9562	55.687	1.202	2.404	38.47%	3.846	61.53%
0.616	0.9578	55.840	1.204	2.408	38.53%	3.842	61.47%
0.617	0.9593	55.994	1.206	2.412	38.59%	3.838	61.41%
0.618	0.9609	56.147	1.208	2.415	38.64%	3.835	61.36%
0.619	0.9624	56.301	1.209	2.419	38.70%	3.831	61.30%
0.62	0.9640	56.455	1.211	2.423	38.76%	3.827	61.24%
0.621	0.9655	56.609	1.213	2.426	38.82%	3.824	61.18%
0.622	0.9671	56.762	1.215	2.430	38.87%	3.820	61.13%
0.623	0.9686	56.916	1.217	2.433	38.93%	3.817	61.07%
0.624	0.9702	57.070	1.218	2.437	38.99%	3.813	61.01%
0.625	0.9718	57.224	1.220	2.440	39.04%	3.810	60.96%
0.626	0.9733	57.378	1.222	2.444	39.10%	3.806	60.90%
0.627	0.9749	57.532	1.224	2.447	39.15%	3.803	60.85%

MTS reading	true length ($\Delta h_{\text{actuator}}$)	ramp angle (deg)	$\Delta h_{\text{ramp_edge}}$ (inch)	Area blocked (inch ²)	% area blocked	Flow area (inch ²)	%Flow area
0.628	0.9764	57.686	1.225	2.451	39.21%	3.799	60.79%
0.629	0.9780	57.840	1.227	2.454	39.26%	3.796	60.74%
0.63	0.9795	57.994	1.229	2.457	39.32%	3.793	60.68%
0.631	0.9811	58.149	1.230	2.461	39.37%	3.789	60.63%
0.632	0.9826	58.303	1.232	2.464	39.43%	3.786	60.57%
0.633	0.9842	58.457	1.234	2.467	39.48%	3.783	60.52%
0.634	0.9857	58.611	1.235	2.471	39.53%	3.779	60.47%
0.635	0.9873	58.765	1.237	2.474	39.58%	3.776	60.42%
0.636	0.9889	58.920	1.239	2.477	39.64%	3.773	60.36%
0.637	0.9904	59.074	1.240	2.481	39.69%	3.769	60.31%
0.638	0.9920	59.228	1.242	2.484	39.74%	3.766	60.26%
0.639	0.9935	59.383	1.244	2.487	39.79%	3.763	60.21%
0.64	0.9951	59.537	1.245	2.490	39.84%	3.760	60.16%
0.641	0.9966	59.691	1.247	2.493	39.89%	3.757	60.11%
0.642	0.9982	59.846	1.248	2.497	39.94%	3.753	60.06%
0.643	0.9997	60.000	1.250	2.500	39.99%	3.750	60.01%

The actuator shaft pushes the ramp vertically under the ramp. As it rises, the T-bar pushes the ramp up and the head of T-bar slides within the T-slot. See the Figure 115 on the following page.

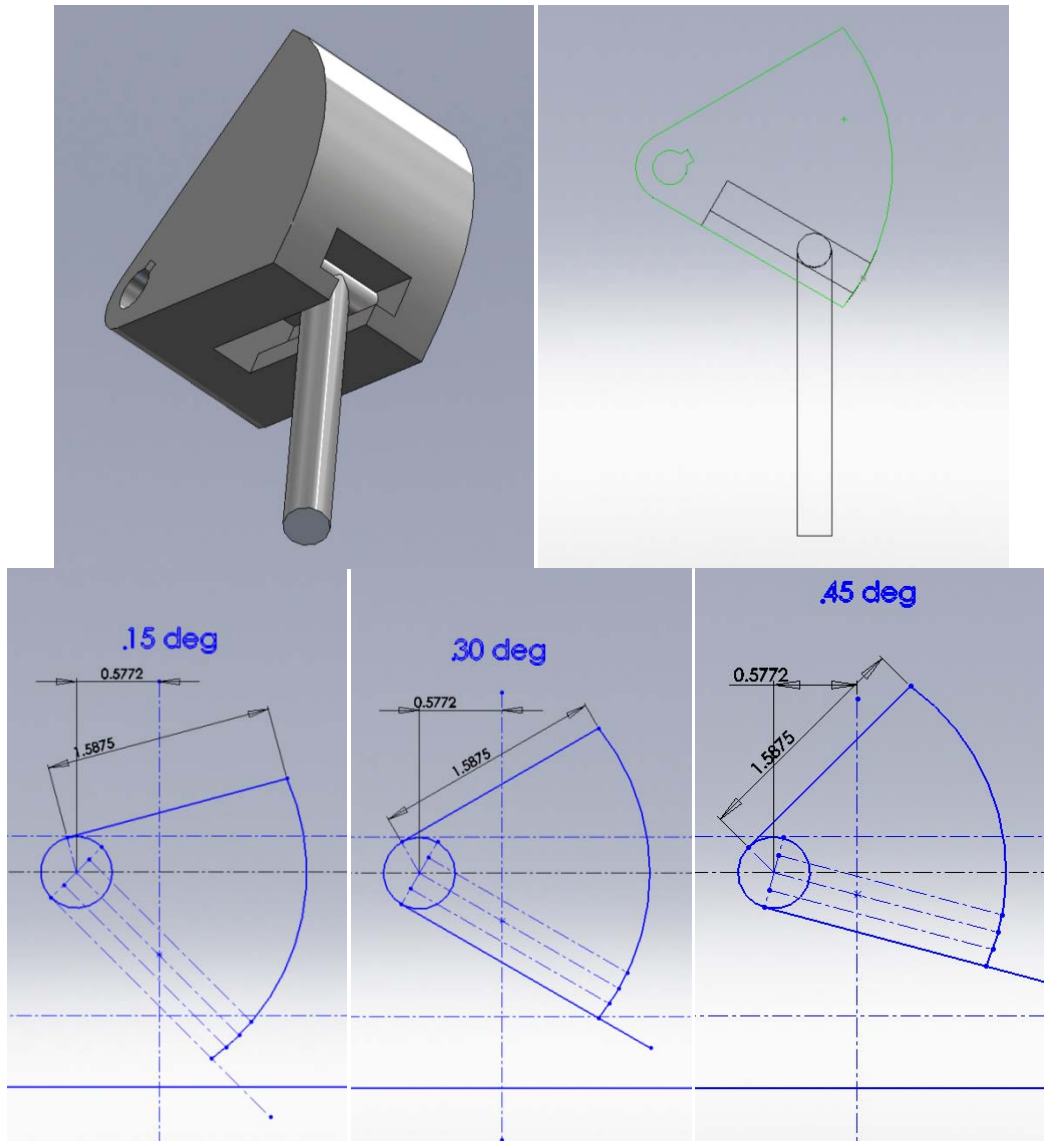


Figure 115. Ramp and T-bar and their relative motion

Because the T-slot does not coincide with the centerline of the pivot of the ramp, the linear increase in the actuator height does not mean the linear increase in the ramp angle, the area blocked, nor the flow area. Their non-linear relationships are shown in three figures on the following pages.

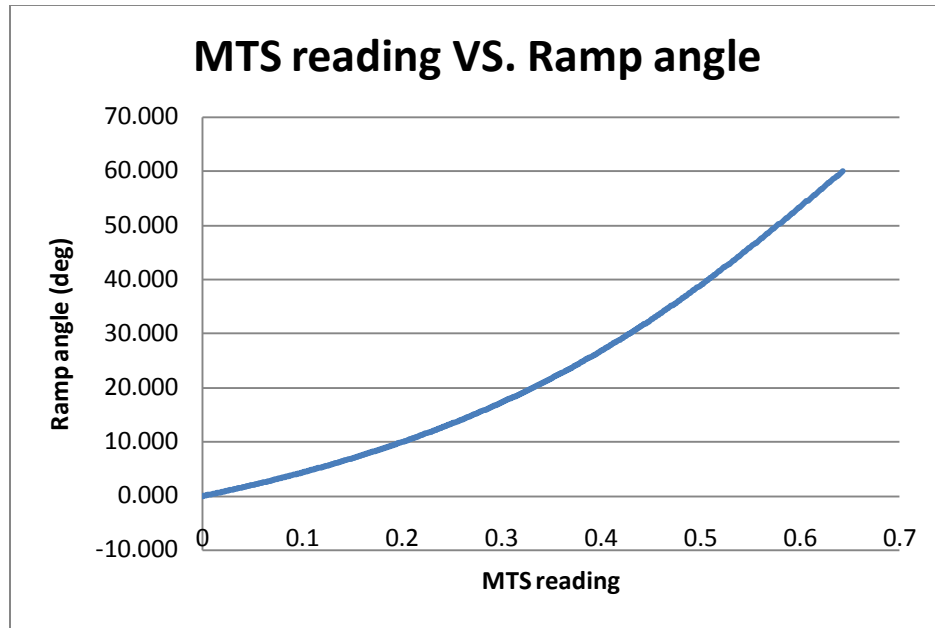


Figure 116. MTS reading increase VS. Ramp angle increase

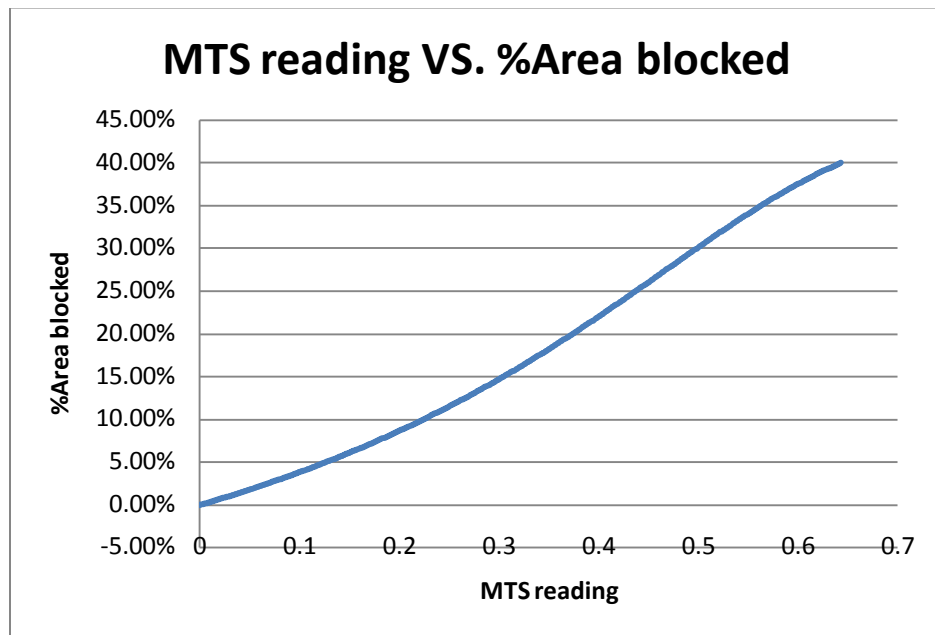


Figure 117. MTS reading increase VS. %Area blocked increase

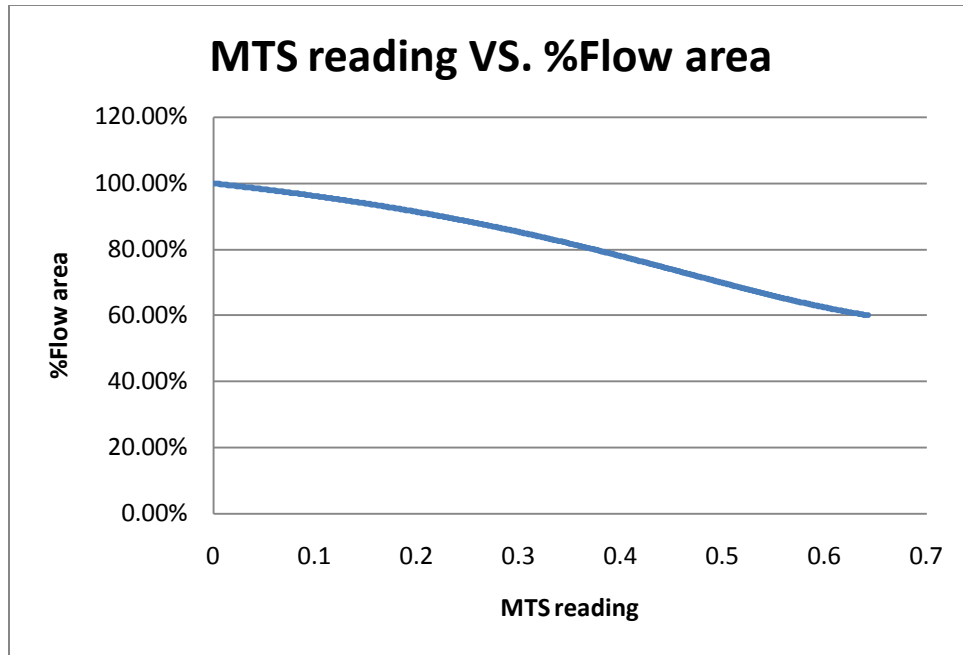


Figure 118. MTS reading increase VS. %Flow area decrease

Bibliography

1. *A Scramjet Engine Model Including Effects of Precombustion Shocks and Dissociation.* **Torrez, Sean M., et al.** AIAA 2008-4619, Hartford CT : AIAA, 2008 , 21 - 23-July, 44th AIAA/ASME/SAE/ASEE Joint Propulsion Conference & Exhibit.
2. *Modeling for Control of a Generic Airbreathing Hypersonic Vehicle.* **Mirmirani, Maj, et al.** AIAA 2005-6256, San Francisco CA : AIAA Pub, 2005 , 15 - 18-August, AIAA Guidance, Navigation, and Control Conference and Exhibit.
3. *Dynamics and control of hypersonic vehicles, The integration challenge for the 1990s.* **Schmidt, D. K., Mamich, H. and Chavez, F.** s.l. : AIAA Paper 91-5057, 1991 , December.
4. *Milestones in the history of scramjets.* s.l. : UQ News, 2002 , 27-July.
5. Scramjet. *Wikipedia.* [Online] Wikipedia. [Cited: 2010 , 28-February.] <http://en.wikipedia.org/wiki/Scramjet>.
6. *Preliminary Study of Shock Train in a Curved Variable-Section Diffuser.* **Tan, Hui-jun and Sun, Shu.** 2, 2008 , March - April, Journal of Propulsion And Power, Vol. 24.
7. *Aerodynamic Performance Analysis of a Hypersonic Inlet Isolator Using Computation and Experiment.* **Reinartz, Birgit U., Herrmann, Carsten D. and Ballmann, Josef.** 5, 2003 , September - October, Journal of Propulsion and Power, Vol. 19.
8. *An Experimental Investigation of Supersonic Inlet Unstart.* **Wagner, J. L., et al.** 2007-4352, Miami FL : AIAA, 2007 ,, 37th AIAA Fluid Dynamics Conference and Exhibit.
9. *Unsteady Pressure Behavior in a Ramjet/Scramjet Inlet.* **Rodi, P. E., Emami, S. and Trexler, C. A.** 3, 1996 ,, Journal of Propulsion and Power, Vol. 12, pp. 486-493.
10. *Shock Train Leading Edge Detection in a Dual-Mode Scramjet.* **Lee, D., et al.** Reno NV : AIAA, 2006 , January, 44th AIAA Aerospace Sciences Meeting and Exhibit.
11. **Weiting, A. R.** *Exploratory Study of Transient Unstart Phenomena in a Three-Dimensional Fixed-Geometry Scramjet Engine.* TN, NASA. 1976. D-8156.
12. *Load Oscillations Caused by Unstart of Hypersonic Wind Tunnels and Engines.* **Shimura, T., et al.** 3, 1998 ,, Journal of Propulsion and Power, Vol. 14, pp. 348-353.

13. *Research on Supersonic Combustion*. **Billing, F. S.** AIAA-92-0001, Reno NV : AIAA, 1992 , 6 - 9-January, 30th Aerospace Sciences Meeting & Exhibit.
14. *Evaluation of the X-43A Scramjet Engine Controller Performance by Monte Carlo Technique*. **Jones, P. T. and Baumann, E.** s.l. : AIAA, 2003 ,. AIAA Paper 2003-5192.
15. **auBuchon, Mark D., et al.** *RAMJET/SCRAMJET INLET ISOLATOR UNSTART PREVENTION*. 5,806,301 United States, 1998 , 15-September. Hartford CT: United Technologies Corporation, 11 December 1995.
16. *Investigation of Two-Dimensional Scramjet Inlet Flowfield at Mach 7*. **Haberle, J. and Gulhan, A.** 3, 2008 , May - June, Journal of Propulsion and Power, Vol. 24.
17. **Emami, S., et al.** *Experimental Investigation of Inlet-Combustor Isolators for a Dual Mode Scramjet at a Mach Number of 4*. NASA. 1995. TP-3502.
18. *Starting Characteristics of Supersonic Inlets*. **Van Wie, D. M., Kwok, F. T. and Walsh, R. F.** AIAA Paper 96-2914, s.l. : AIAA, 1996 , July.
19. *Two-Dimensional Generic Inlet Unstart Detection at Mach 2.5 - 5.0*. **Hawkins, W. R. and Marquart, E. J.** AIAA 95-6016, s.l. : AIAA, 1995 , April.
20. *Nonlinear Longitudinal Dynamical Model of an Air-Breathing Hypersonic Vehicle*. **Bolender, Michael A. and Doman, David B.** 2, 2007 , March - April, Journal of Spacecraft and Rockets, Vol. 44.
21. *Some Flow-Structure Features of Scramjet Isolator*. **Shang, J. S.** Reno NV : AIAA, 2008. 46th AIAA Aerospace Sciences Meeting and Exhibit. AIAA 2008-722.
22. **Anderson, John D.** *Fundamental of Aerodynamics*. Third Edition. New York : McGraw-Hill, 2001.
23. **Hibbeler, R. C.** *Mechanics of materials*. Fourth Edition. New Jersey : Prentice Hall, 2000.
24. *National Instruments - Test and Measurements*. [Online] National Instruments. [Cited: 2010 , 28-February.] <http://www.ni.com>.
25. *Endevco - Welcome to Endevco.com*. [Online] Endevco. [Cited: 2010 , 28-February.] <http://www.endevco.com/>.

26. **Saad, Michel A.** *Compressible Fluid Flow*. New Jersey : Prentice-Hall, 1985.
27. *Characterization of Shock Train Structures inside Constant-Area Isolators of Model Scramjet Combustors*. **Lin, K. C., et al.** Reno, Nevada : AIAA, January 9-12, 2006, 44th AIAA Aerospace Sciences Meeting and Exhibit. 2006-816.
28. **Pope, Alan and Goin, Kenneth L.** *High-speed wind tunnel testing*. New York : John Wiley & Sons, Inc., 1965.
29. Professional plastics / cast acrylic. *Professional plastics*. [Online] Professional plastics. [Cited: 2010 , 7-March.]
<http://www.professionalplastics.com/professionalplastics/content/castacrylic.pdf>.
30. Elastic properties of Young modulus for some materials. *The Engineering toolbox*. [Online] The Engineering toolbox. [Cited: 2010 , 7-March.]
http://www.engineeringtoolbox.com/young-modulus-d_417.html.
31. **Young, Warren C. and Budynas, Richard G.** *Roak's formula for stress and strain*. 7th Edition. s.l. : McGraw-Hill, 2002.

Vita

Captain Richard I. Paek graduated from Joel E. Ferris High School in Spokane, WA in 2000 as a valedictorian. He completed his Bachelor of Science degree in Astronautical Engineering at University of Washington, Seattle, WA in 2004. After graduation, he was admitted to U.S. Air Force Officer Training School and received his commission in November 2004.

His first assignment was a flight test operational engineer at 419th Bomber Flight Test Squadron in Edwards Air Force Base, California. In 2007, he was assigned to the Hypersonic Flight Combined Test Force at the same base where he served as an X-51 lead project engineer. In September 2008, he received an admission to the department of Aeronautics and Astronautics at AFIT in 2008. Upon completion of his degree, he will follow-on to the Air Force Research Laboratory, Propulsion Directorate, Technology Branch (AFRL/RZAT).

REPORT DOCUMENTATION PAGE				Form Approved OMB No. 074-0188	
<p>The public reporting burden for this collection of information is estimated to average 1 hour per response, including the time for reviewing instructions, searching existing data sources, gathering and maintaining the data needed, and completing and reviewing the collection of information. Send comments regarding this burden estimate or any other aspect of the collection of information, including suggestions for reducing this burden to Department of Defense, Washington Headquarters Services, Directorate for Information Operations and Reports (0704-0188), 1215 Jefferson Davis Highway, Suite 1204, Arlington, VA 22202-4302. Respondents should be aware that notwithstanding any other provision of law, no person shall be subject to a penalty for failing to comply with a collection of information if it does not display a currently valid OMB control number.</p> <p>PLEASE DO NOT RETURN YOUR FORM TO THE ABOVE ADDRESS.</p>					
1. REPORT DATE (DD-MM-YYYY) 25-03-2010		2. REPORT TYPE Master's Thesis		3. DATES COVERED (From - To) September 2008 - March 2010	
TITLE AND SUBTITLE Back-pressure effect on shock-train location in a scramjet engine isolator				5a. CONTRACT NUMBER	
				5b. GRANT NUMBER	
				5c. PROGRAM ELEMENT NUMBER	
6. AUTHOR(S) Paek, Richard I., Captain, USAF				5d. PROJECT NUMBER JON:10ENY107	
				5e. TASK NUMBER	
				5f. WORK UNIT NUMBER	
7. PERFORMING ORGANIZATION NAMES(S) AND ADDRESS(S) Air Force Institute of Technology Graduate School of Engineering and Management (AFIT/ENY) 2950 Hobson Way, Building 640 WPAFB OH 45433-8865				8. PERFORMING ORGANIZATION REPORT NUMBER AFIT/GAE/ENY/10-M17	
9. SPONSORING/MONITORING AGENCY NAME(S) AND ADDRESS(ES) Jeffrey M. Donbar Air Force Research Laboratory/Propulsion Directorate 1950 Fifth Street, WPAFB, OH 45433-7251 COMM (937)255-1996, DSN 785-1995 Jeffrey.donbar@wpafb.af.mil				10. SPONSOR/MONITOR'S ACRONYM(S) AFRL/RZA	
				11. SPONSOR/MONITOR'S REPORT NUMBER(S)	
12. DISTRIBUTION/AVAILABILITY STATEMENT APPROVED FOR PUBLIC RELEASE; DISTRIBUTION UNLIMITED.					
13. SUPPLEMENTARY NOTES					
14. ABSTRACT <p>The isolator of the scramjet decelerates the incoming high Mach flow to a lower Mach number and stabilizes the flow before it enters the combustor. Because of the unsteady combustion phenomenon and inconsistent completeness of the combustion, pressures within the combustor can vary drastically. These pressure variations can propagate forward and affect the flow field in the isolator - worst case un-starting the inlet. In this research, the shock train location VS. the back-pressure is examined experimentally. The back-pressure is artificially created by symmetric (top & bottom) ramps that can close the flow area. Raising/lowering ramps result in higher/lower back-pressure. Higher back-pressure moves the shock train forward, with too high a back-pressure causing un-start. This experiment is conducted for a variation in Reynolds number, ramp angle, and two incoming Mach #s, and will result in a relationship between back-pressure and shock train location for various airflow conditions.</p>					
15. SUBJECT TERMS <p>Scramjet, isolator, shock-train, back-pressure, un-start</p>					
16. SECURITY CLASSIFICATION OF:			17. LIMITATION OF ABSTRACT	18. NUMBER OF PAGES	19a. NAME OF RESPONSIBLE PERSON
a. REPORT	b. ABSTRACT	c. THIS PAGE			Paul I. King, Dr.
U	U	U	UU	195	19b. TELEPHONE NUMBER (Include area code) (937) 255-3636, ext 4628 (pking@afit.edu)

Standard Form 298 (Rev. 8-98)
Prescribed by ANSI Std. Z39-18